POLYTECHNIQUE MONTRÉAL
affiliée à l'Université de Montréal

Raman Scattering From Hyperbolic Phonon-Polaritons in 2D Materials

ALARIC BERGERON
Département de génie physique

Thèse présentée en vue de l'obtention du diplôme de *Philosophiæ Doctor*
Génie physique

Août 2020

POLYTECHNIQUE MONTRÉAL
affiliée à l'Université de Montréal

Cette thèse intitulée :

Raman Scattering From Hyperbolic Phonon-Polaritons in 2D Materials

présentée par **BERGERON Alaric**
en vue de l'obtention du diplôme de *Philosophiæ Doctor*
a été dûment acceptée par le jury d'examen constitué de :

MÉNARD David, président
FRANCOEUR Sébastien, membre et directeur de recherche
LEONELLI Richard, membre et codirecteur de recherche
SELETSKIY Denis, membre
RUEDIGER Andreas, membre externe

DEDICATION

"When you're thinking about something that you don't understand, you have a terrible, uncomfortable feeling called confusion. It's a very difficult and unhappy business. And so most of the time you're rather unhappy, actually, with this confusion. You can't penetrate this thing. Now, is the confusion's because we're all some kind of apes that are kind of stupid working against this, trying to figure out [how] to put the two sticks together to reach the banana and we can't quite make it, the idea? And I get this feeling all the time that I'm an ape trying to put two sticks together, so I always feel stupid. Once in a while, though, the sticks go together on me and I reach the banana."

— ***Richard Feynman***

"Genuine scientific progress is a slow climb, which requires a stable society to support thinkers and theorists over many generations."

— ***Peter F. Hamilton***, *Pandora's Star*

"Yesterday's weirdness is tomorrow's reason why."

— ***Hunter S. Thompson***, *The Curse of Lono*

"But this is it, the deed is done
Silence drowns the sound
Before I leaped, I should have seen
The view from halfway down
I really should've thought about
The view from halfway down
I wish I could've known about
The view from halfway down"

— ***Alison Tafel***, *Bojack Horseman*

À ma très chère maman,
merci pour tout,
du fond du coeur.

ACKNOWLEDGEMENTS

First, I would like to thank my lab colleagues Jab, Philibert, Anne-Lau, John, and Alex, with whom I've shared countless enriching discussions, a few of them being related to physics. They've all in their own way played a great part to help me accomplish the work described in this thesis. I also thank my colleague Alexandra for the good reading suggestions.

I would also like to extend special acknowledgement to Evgueni Babian, whose passion and fabrication skills played a major part in the realization of custom apparatus used in this work. Exchanging ideas with Evgueni over the years helped me refine my approach to mechanical design and fabrication, and I am grateful for it.

I am greatly indebted to my research advisor, professor Sébastien Francoeur, who hired me as a summer intern almost twelve years ago, and has had to endure my trials and tribulations ever since, yet always providing insightful advice and pointed questions to guide my research endeavors at every step. Our countless meetings discussing theoretical models, scrutinizing noisy spectra, and debating the aesthetics of recirculating water cooling systems or bicycle frame materials not only have played a major part in the development of the work presented in this thesis, but also in that of its author.

I also want to thank my co-advisor, professor Richard Leonelli, not only for providing me access to a hidden treasure trove of crystals grown in the 1970's and 1980's, but also for contributing insightful perspectives when discussing my research project.

Finally, I want to thank all of my close friends and family, who supported me throughout all these years, and in particular both my roommates, as well as my partner, who have remained supportive despite having to endure me over the last few months of writing this thesis in the midst of the current pandemic lockdown. I am sincerely sorry to all of you for leaving you marooned for so many months, and I hope this thesis can, at least in part, be worth the toll it took to forge it.

RÉSUMÉ

Les états polaritoniques supportés par les matériaux bi-dimensionnels (2D) suscitent beaucoup d'intérêt de par leur capacité de fortement confiner la lumière. Parmi ceux-ci, les phonons-polaritons hyperboliques (PPH) semblent particulièrement prometteurs pour la réalisation de dispositifs nano-phononiques accordables à haute efficacité dans l'infrarouge lointain. Afin d'étudier et de contrôler ces polaritons, une multitude de méthodes basées sur un couplage résonant sont couramment employées avec grand succès. Cependant, seuls les polaritons ayant des énergies supérieures à environ $500\,\mathrm{cm}^{-1}$ ($60\,\mathrm{meV}$) sont accessibles par ces méthodes étant donné l'instrumentation disponible. Ceci limite largement l'étendue des matériaux 2D pouvant être étudiés, la majorité possédant des phonons en deçà de cette limite. Ainsi, l'introduction d'une technique pouvant caractériser les PPH à basse énergie dans les matériaux 2D permettrait de grandement élargir le catalogue de polaritons hyperboliques.

Dans cette thèse, la spectroscopie Raman est proposée comme une alternative simple et efficace permettant d'accéder aux modes PPH dans les matériaux 2D, et ce à l'aide d'instrumentation communément disponible dans les laboratoires de recherche sur les matériaux 2D. Le GaSe est sélectionné à titre d'exemple pour démontrer cette approche étant donné ses fortes résonances polaires, mais la technique est applicable à une large gamme de matériaux 2D. Cette thèse comprend quatre contributions scientifiques majeures, décrites ci-dessous.

La première contribution est une étude approfondie du processus de photo-oxydation, afin de déterminer les conditions expérimentales nécessaires pour préserver l'intégrité des échantillons durant une mesure optique. Une dégradation rapide est observée sous exposition simultanée à de l'oxygène, de l'humidité et de la lumière, et le retrait d'un de ces trois éléments freine le processus. Il est démontré que l'apparition du mode A_1 du Ga_2Se_3 ($155\,\mathrm{cm}^{-1}$) et du mode A_g du Ga_2O_3 ($161\,\mathrm{cm}^{-1}$) est un signe précurseur de la dégradation, pouvant servir à identifier l'oxidation d'un échantillon et à sélectionner des échantillons de haute qualité.

La seconde et principale contribution de cette thèse est la démonstration de la diffusion Raman rétrograde provenant de polaritons confinés dans des échantillons de GaSe en deçà d'un micromètre d'épaisseur. Étant donné le confinement élevé des PPH et l'épaisseur restreinte des échantillons, la relaxation de la conservation de quantité de mouvement permetent l'observation d'un fort signal Raman en géométrie rétrograde. Ces résultats confirment que les PPH confinés peuvent être observés à l'aide de cette technique, ce qui ouvre la porte à l'étude de PPH confinés dans une multitude de nouveaux matériaux 2D. De plus, ils soulignent la nécessité de considérer la présence de polaritons confinés dans l'analyse de tout spectre

Raman provenant de matériaux 2D polaires, ce qui pourrait aider à résoudre l'attribution de certains modes Raman observés dans d'autres matériaux 2D. Finalement, il est démontré que la dépendance en épaisseur de la dispersion des polaritons observés pourrait servir à estimer rapidement l'épaisseur d'échantillons allant jusqu'à 1000 nm.

La troisième contribution de cette thèse est le développement d'un modèle numérique permettant de calculer la diffusion Raman de polaritons confinés dans des systèmes multi-couches anisotropes. Ce modèle exploite la relation directe entre les déplacements atomiques et le champ électromagnétique des polaritons afin d'exprimer le spectre Raman en fonction d'une distribution de champ électrique. Un formalisme matriciel 4×4 est utilisé pour déterminer cette distribution de champ, et la section efficace Raman est ensuite déterminée à l'aide de tenseurs Raman modifiés. Ce modèle s'avère un outil puissant pour l'analyse de la diffusion Raman provenant de systèmes multi-couches complexes comme des matériaux 2D exfoliés sur divers substrats, ou encore des hétérostructures complexes de matériaux 2D.

Finalement, la quatrième contribution concerne l'usage de Raman quasi-résonant pour étudier des polaritons confinés en trois dimensions dans des échantillons de GaSe exfoliés. Les résultats présentés révèlent la présence de polaritons confinés anisotropiquement, et permettent pour la première fois d'estimer une borne inférieure pour la figure de mérite de propagation des polaritons dans le GaSe à $\gamma^{-1} \geq 39$. Cette valeur se compare favorablement aux valeurs démontrées dans le h-BN, ce qui indique que le GaSe est une plate-forme intéressante pour le développement de dispositifs nano-photoniques dans l'infrarouge lointain.

ABSTRACT

Polaritons in two-dimensional (2D) materials have attracted attention in recent years given their potential for extreme optical field confinement. In particular, hyperbolic phonon-polaritons (HPPs) have shown great potential for developing tunable infrared and THz nanophotonic devices with low propagation losses. An ever-growing list of methods are used to study and control these polaritons with an impressive level of precision, specificity, and sensitivity. These techniques rely on resonant coupling to the studied polaritons, therefore their applicability is limited to polaritons with energies above $500\,\mathrm{cm}^{-1}$ (60 meV) due to instrumentation availability. However, most 2D materials exhibit HPPs with energies below this limit, thus their study would require further development of current methods, or the introduction of a different approach.

In this thesis, it is demonstrated for the first time that Raman spectroscopy is a convenient and powerful tool for the investigation of a wide range of strongly confined hyperbolic phonon-polariton states in 2D materials. Raman scattering is almost universally available in 2D materials research labs, effectively lifting the energy limitations imposed by current resonance-based techniques. For this demonstration, Gallium selenide (GaSe) was chosen as a prototypical material owing to its strong polar resonances, but the technique should translate to a large number of 2D materials. This thesis reports four important contributions, as listed below.

The first contribution of this work is a thorough study of its photo-oxidation, conducted to determine ideal experimental conditions for preserving sample integrity. The reported results offer valuable insight into the photo-chemical processes involved in the rapid photo-oxidation of thin GaSe flakes, which is a common issue with 2D materials. The concomitant presence of oxygen, humidity and light is shown to trigger rapid oxidation, which is inhibited by removal of any of these three elements. Earliest signs of GaSe sample degradation are also reported as Ga_2Se_3 and Ga_2O_3 Raman modes at $155\,\mathrm{cm}^{-1}$ and $161\,\mathrm{cm}^{-1}$, respectively, and can be used to identify sample degradation or to select high quality samples. In this work, samples are prepared in an inert oxygen-free atmosphere and measured in vacuum optical cells to ensure optimal sample quality.

The second and most significant original contribution of this thesis is the demonstration that sub-micron thin GaSe flakes exhibit strong polariton backscattering signal due to momentum conservation relaxation. This phenomenon is especially important in hyperbolic materials given the deep subwavelength confinement of polaritons. The compounded effects

of relaxed momentum conservation and hyperbolic confinement yields a strong backscattering Raman signal. This result could have a significant impact in the 2D materials scientific community, since it confirms that confined hyperbolic polaritons can be observed and characterized from backscattering Raman measurements, enabling their study in a large number of new materials. Furthermore, it indicates that polariton scattering has to be taken into account when analyzing Raman spectra from polar 2D materials, which could help resolving conflicting assignment of phonon modes in other polar 2D materials, where the presence of polaritons may have gone unsuspected. Finally, the dispersion of confined polariton states is thickness-dependent, which extends the range where Raman spectra can be used to estimate the sample thickness up to 1000 nm.

The third major contribution is the development of a numerical model to assist in the interpretation of scattering from polariton modes in multi-layer anisotropic media. This model exploits the direct relation between the lattice displacement and electromagnetic field of polaritons which enables a complete determination of Raman spectra from the distribution of the electric field in the sample. A 4×4 transfer matrix optical waveguide model is used to model the polariton electric field distribution. Polariton Raman cross-section is then determined from the computed field, using modified polariton Raman tensors. The resulting original numerical model is a powerful tool to analyze scattering spectra from complex anisotropic multilayer structures, such as exfoliated 2D materials supported by various substrates, as well as complex 2D material heterostructures.

Finally, the fourth contribution is the use of near-resonant Raman scattering to study 3D-confined polariton states in exfoliated GaSe flakes. The original results presented show evidence of anisotropic laterally confined polariton states. From these results, very low polariton propagation losses in GaSe are estimated, and a lower bound on the propagation figure of merit of $\gamma^{-1} \geq 39$ is reported for the first time in GaSe, which is as high as state-of-the-art values reported in h-BN. This indicates that GaSe is a very promising material for applications in far-infrared subwavelength nanophotonic devices.

TABLE OF CONTENTS

LIST OF TABLES

LIST OF FIGURES

CHAPTER 1 INTRODUCTION

When an electromagnetic wave propagates through a material, its interaction with the various dipolar degrees of freedom in the propagation medium induces a polarization response and the propagating wave thus becomes a combination of the external electric field and induced polarization response. In the case where the electromagnetic wave's frequency neighbors that of a dipolar oscillator's resonance in the material, the radiation and excited modes become strongly coupled and the resultant hybrid wave is called a polariton.

These hybrid quasiparticles have been reported for a multitude of polar oscillators, such as plasmons, excitons, and phonons. They have attracted the interest of the scientific community for the last few decades as they exhibit mixed light-matter properties and enable unique levels of manipulation, confinement, and control of material and light properties. Research on polaritons has yielded many impressive results, especially in the field of exciton-polaritons, where polaritonic effects have been the most studied. For instance, experimental demonstrations of Bose-Einstein polariton condensation [1], polariton lasing [2], and sub-diffraction imaging [3] are reported in the literature.

A specific type of polariton known as hyperbolic polaritons can be observed in strongly anisotropic materials. Indeed, when polar resonance along different crystal lattice directions have different energies, a so-called hyperbolic energy band occurs where dielectric permittivity has opposite signs along two directions. Such hyperbolic energy bands can theoretically sustain extremely confined propagating polariton modes with low propagation losses [4, 5]. Initially, only meta-materials were thought to support hyperbolic polaritons [6], but the observation of hyperbolic phonon-polaritons in hexagonal boron nitride (h-BN) [4,5,7] revealed for the first time the existence of highly-confined hyperbolic polaritons in a natural material. Since then, 2D materials and their heterostructures have been the subject of intense scrutiny in the search for new hyperbolic polariton states [8]. So far, phonon-polaritons in MoO_3 [9,10] and plasmon-polaritons in WTe_2 [11] are the only confined hyperbolic polaritons reported in natural 2D materials.

With the exception of recent results in MoO_3, h-BN is the only 2D material where confined hyperbolic phonon-polaritons have been extensively studied in recent years. A wide variety of experimental techniques were used in order to study the properties of these hyperbolic polaritons, the most common being scattering-type scanning near-field optical microscopy (s-SNOM) [12]. Using these techniques, several remarkable properties of these phonon-polaritons states have been reported in the last five years, underlining their great potential

for applications in polaritonic systems [13–16]. These reports will be detailed in the literature review.

1.1 Research question

2D materials have been the subject of considerable interest of the materials community in the last decade. Given the outstanding properties of 2D-confined hyperbolic polaritons reported in recent years, it is surprising that phonon-polaritons have only been reported in two materials among the ever-growing library of known 2D materials. Indeed, a wide array of these materials exhibit strongly anisotropic polar lattice modes and thus naturally exhibit hyperbolic energy bands. The reason why so few of these materials were investigated may relate to the instrumental difficulty in exciting and detecting phonon-polaritons. Up to now, all measurement techniques used to study phonon-polaritons in 2D materials were based on absorption, requiring excitation and detection energies at or near resonance, which is in the mid- to far-infrared [12]. This poses a serious problem since high quality light sources, collimation, beam-splitting and polarization optics, and detectors are often lacking in the far-infrared. Hence, materials exhibiting stiff polar phonon modes with energies above the current $\sim$500 cm^{-1} to 1000 cm^{-1} limit readily accessible using Fourier transform infrared spectroscopy and quantum cascade laser sources, respectively [17]. Indeed, phonon-polaritons in *h*-BN and MoO_3 are found between 750 cm^{-1} and 1575 cm^{-1} [5] and between 545 cm^{-1} and 1010 cm^{-1} [10], respectively. However, most 2D materials have polar phonon modes below that limit. This includes including transition-metal mono- and di-chalcogenides such as GaSe and MoS_2 [18, 19].

Great strides have been made in recent years with the development of far-infrared and terahertz light sources and detectors [17]. Some proposed approaches even exploiting phonon-polaritons in AlAs [20], and nonlinear effects in GaSe [21, 22]. Nevertheless, the lack of available experimental methods to study phonon-polariton states in these materials, which have already demonstrated a wide range of unique properties and applications in almost every field of material science, highlights a need for further development in this regard.

Rather than focusing on the aforementioned sophisticated modern techniques that currently dominate the study of hyperbolic phonon polaritons in 2D materials, this thesis harkens back to the very beginnings of the field of polaritonics. In 1965, Henry and Hopfield reported the first experimental observation of polaritons by measuring near-forward Raman scattering from phonon-polaritons in GaP [23]. In the following decades, Raman scattering from phonon-polaritons was the subject of many extensive theoretical and experimental works. However, the rise in popularity of plasmon-polaritons and exciton-polaritons seemingly led

to the technique being largely ignored in the field of polaritonics in the last few decades, especially in the context of 2D materials.

The current resurgence of phonon-polaritons in hyperbolic 2D materials as a promising platform for nanophotonics is being held back by the availability and characteristics of current experimental methods. Could Raman spectroscopy, using commonly available instrumentation, prove to be a useful tool to advance and broaden the field of nanophotonics in 2D materials? Previous reports of polariton Raman scattering from a multitude of materials, including guided polaritons in GaSe [24], indicate that it may be the case. This thesis aims to demonstrate this claim, using GaSe as a prototypical polar 2D material.

1.2 Research Objectives

In order to realize this goal, the first objective is to develop a means to identify phonon-polariton features in Raman spectra. This is necessary not only to distinguish them from mechanical phonon scattering, but also to provide the correct mode assignments. In order to do so, a theoretical model of Raman scattering from confined polariton states needs to be developed, since they exhibit intricate dispersion relations that depend on multiple parameters.

The second objective is to demonstrate unambiguous observation of these polariton states in experimental Raman scattering data. In order to realize this, it is critical to first ascertain the integrity of the prepared samples. It is hypothesized that GaSe, like most 2D materials, is sensitive to photo-oxidation processes. Therefore, a systematic study of the stability of thin GaSe under various experimental conditions will be conducted to establish the necessary measures for sample stability during optical measurements. Having established these parameters, a series of near-forward and backward Raman scattering measurements over a range of scattering angles will be carried out, based on the hypothesis that strongly-confined phonon-polariton modes will exhibit visible dispersion in backward scattering data, while near-forward scattering should confirm the results reported in the literature.

Finally, the third objective is to demonstrate other applications of Raman spectroscopy to characterize relevant properties of these phonon-polariton states. For instance, demonstration of lateral polariton propagation, waveguiding, or reflection would firmly establish the technique as a useful tool in the field of hyperbolic polariton nanophotonics research. Laterally confining polaritons by cleaving or micro-fabricating cavities should provide a suitable test platform to test the capabilities of Raman scattering in this regard.

1.3 Thesis outline

Following this introduction, Chapter 2 presents a brief overview of the literature on GaSe, followed by a survey of the literature pertaining to hyperbolic phonon-polaritons and Raman scattering by polaritons.

Chapters 3 to 5 describe the many theories and concepts that were combined to develop the numerical model used to theoretically compute Raman spectra. Chapter 3 presents the basic concepts of uniaxial lattice vibrational mode dispersion, as well as the associated ordinary and hyperbolic phonon-polariton dispersion. The theory of Raman scattering from these polariton states, based largely on the model of Mills and Burstein [25] adapted to uniaxial crystals by Irmer [26], is presented in Chapter 4. The first part of Chapter 5 then presents the theoretical dispersion relation of confined polaritons in thin GaSe 2D slabs, as described by Sasaki and Ushioda [24, 27]. The second part of Chapter 5 details the numerical 4×4 transfer matrix formalism developed by Passler [28], which was used to compute the spatial electric field distribution of the polariton states. Finally, the process of Raman scattering spectrum computation using a combination of the aforementioned concepts is described.

Chapter 6 then presents a detailed description of experimental methods and techniques used in this work. Sample preparation and characterization, experimental setups, and calibration procedures are presented for both backscattering and near-forward measurements.

Before moving on to polariton scattering results, Chapter 7 presents a detailed study of the photo-oxidation process of GaSe as observed with Raman scattering. Time-dependent oxidation dynamics are reported under different atmospheres to identify causes and telltale signs of sample degradation, and a photo-chemical model of the oxidation process is introduced. The work presented this chapter has been the subject of a publication in *Applied Physics Letters* [29].

Chapter 8 presents all experimental Raman scattering results from phonon-polaritons in GaSe. The first section presents near-forward polariton Raman scattering results using k-space spectral imaging. The data is compared to predictions of the numerical model and the presence of several polariton features is discussed. Angle-resolved and thickness-dependent Raman backscattering results from exfoliated GaSe flakes on Si/SiO_2 substrates are presented in the next section, clear evidence of polariton scattering is discussed with the help of the numerical model. The last sections of Chapter 8 study the effect of near-resonant excitation and sample anisotropy on polariton scattering, pointing to evidence of lateral confinement.

Finally, the Conclusion summarizes the original contributions reported throughout the thesis and their anticipated impact on the research on phonon-polaritons. Then key limitations of

these contributions are identified, as well as promising research avenues to build upon them.

CHAPTER 2 LITERATURE REVIEW

This section presents a brief overview of the most relevant scientific literature and historical context related to the work presented in this thesis. First, a general overview of the material properties of gallium selenide is presented, followed by a bird's eye view of the history and recent advances in the field of hyperbolic phonon-polaritons. Finally, the evolution of the use of Raman scattering as a powerful tool to study polaritons, dating back to the very first observation of polariton states in the 1960's, is summarized.

2.1 Gallium selenide

Gallium selenide, first reported in 1934 [30], is a III-IV mono-chalcogenide semiconductor with a layered hexagonal structure. It is well-known as an optical nonlinear medium with a wide usable bandwidth from near infrared to THz regimes [31–33]. Along with other layered mono-chalcogenide materials like GaS [34] and InSe [35], atomic layers of GaSe have recently garnered a lot of attention in the 2D materials scientific community owing to their excellent photoelectric properties [36,37], as well as their large thickness-, strain- and alloying-dependent bandgap tunability [38–40], high second harmonic coefficient [41], and interesting spin physics [42, 43].

This section presents a brief overview of the current literature pertaining to three critical aspects of GaSe relevant to this work, namely its crystalline structure, electronic band structure and nonlinear properties. Note that discussion of vibrational modes and Raman spectroscopy, being a core element of this thesis, is omitted here as it will be covered in detail in Chapter 4.

2.1.1 Crystal structure

GaSe has a hexagonal layered lattice structure (see Fig. 2.1), with each monolayer consisting of two opposed tetrahedral layers of gallium and selenium in a Se-Ga-Ga-Se sequence. The unit cell of the monolayer contains four atoms and has a D_{3h} symmetry. The hexagonal lattice constant of the monolayer are $a = 3.755\,\text{Å}$ and $c = 15.95\,\text{Å}$ [44]. In the bulk material, monolayers are bound together by weak van der Waals forces, enabling them to be exfoliated into 2D monolayers while maintaining their crystalline integrity [45].

The stacking order of the monolayers determines the polytype of the bulk material, the most commonly identified in the literature being ϵ-Gase, with D^1_{3h} space group symmetry and a

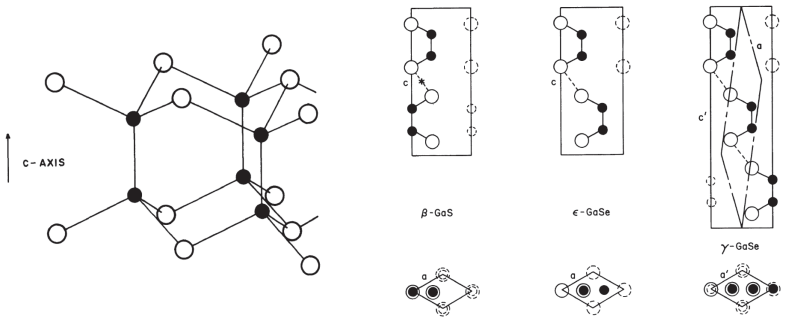

Figure 2.1 Crystal structure of GaSe hexagonal monolayer and unit cells of the β, ϵ, and γ bulk polytypes projected along the (110) and (001) planes. Dark circles represent Ga atoms and white circles Se atoms. Adapted from from Ref. [46] © 1981 Wiley-VCH Verlag GmbH & Co. KGaA, Weinheim.

ABA stacking order, with an interlayer spacing of 0.798 nm [18, 47–50]. This polytype lacks an inversion symmetry center and has four molecular units per unit cell, yielding a total of 24 normal lattice vibrational modes. The larger number of atoms in the unit cell compared to the monolayer yields a large number of vibrational modes, but many of these tend to be energetically quasi-degenerate with the monolayer modes, and have not been observed experimentally in the literature, as will be discussed in chapter 4.

The γ-GaSe and β-GaSe polytypes, with C_{3v}^5 and D_{6h}^4 space groups, respectively, have been identified by some authors in the literature, but the general lack of consistency in the reported vibrational mode assignments has led to some controversy with regards to their identification from Raman and IR spectra. Due to the weak inter-layer interactions, all polytypes have very similar electronic and vibrational energies [46,49,51,52] and can thus be difficult to distinguish from such measurements since the splittings are lower than the phonon linewidths. The main differences between polytypes originate from the existence of an inversion symmetry center or lack thereof, which determines second-order non-linear optical properties, as well as some critical Raman scattering and infrared absorption selection rules, which will be discussed in chapter 4. Large, high quality Bridgeman-grown crystals such as those used in this work are generally known to be ϵ-GaSe, although some evidence suggests that stacking faults in these samples may lead to a small fraction of γ-GaSe content [18, 47, 53].

2.1.2 Band structure and optical properties

Bulk GaSe presents a direct band gap with an energy of $E_g = 2.02\,\text{eV}$ [54] located at the Brillouin zone Γ point (see Fig. 2.2(a)). The upper valence bands are predominantly derived from the Se $4p$ orbitals [55, 56], while the lower conduction band is formed by the Ga $4s$

orbitals [56,57]. The strong crystalline anisotropy lifts the p_z component of the upper valence band almost 1 eV above the $p_{x,y}$ components. This anisotropy gives rise to strong dipolar selection rules wherein optical transitions at E_g are only allowed for an optical electric field $\mathbf{E} \parallel \mathbf{c}$, as evidenced by the polarized absorption coefficients shown on Fig. 2.2(b).

For $\mathbf{E} \perp \mathbf{c}$ optical fields, spin-orbit coupling enables selection-rule breaking transitions at E_g, albeit with a cross-section that is about two orders of magnitude smaller than the allowed transition [58]. The out-of-plane optically-active dipoles result in a strongly anisotropic coupling to light, which is both dependent on light propagation direction and polarization [42, 59–61].

The bandgap of atomically-thin GaSe has been predicted to increase dramatically, with an increase from the bulk direct $E_g = 2.02$ eV to a quasi direct $E_g \sim 3.2$ eV in the monolayer, the valence maximum shifting slightly away from the Γ point [63]. This quasi-direct bandgap in the monolayer has recently been confirmed by ARPES measurements [64].

Due to the rapid oxidation of thin layers when exposed to ambient conditions [29] (see Chapter 7), photoluminescence (PL) measurements from thin flakes have mostly failed to demonstrate this bandgap increase, despite many efforts [65, 66]. Recently published PL measurements [39] from pristine encapsulated flakes down to the bilayer (see Fig. 2.3) show the marked PL energy increase for few-layer flakes, in good agreement with the predicted behavior of the bandgap. Fig. 2.3(a) also highlights the reduced PL efficiency for thin flakes due to the weak spin-orbit-mediated coupling to in-plane polarized light. So far, no PL results from a single GaSe layer have been published, most likely because the bandgap becomes quasi-direct, further reducing the PL efficiency.

2.1.3 Non-linear optical properties

GaSe is one of the best nonlinear crystals for operation in the near- to far-infrared, owing to its high transparency over an extremely broad wavelength range from the near infrared (0.62 µm) up the far infrared (20 µm), and even up to THz regimes 500 µm with the exception of some polar resonance bands [22]. It also exhibits high birefringence in the far IR and THz regimes, as well as a strong second order nonlinear coefficient ($d_{22} = 54$ pm V^{-1} at 10 µm) [31], more than one order of magnitude above common nonlinear crystals such as β-BaB_2O_4 (BBO), LiB_3O_5, $LiNbO_3$, or $KTiOPO_4$ (KTP) [31]. Coupled with its very high laser damage threshold and advantageous thermal properties [44, 67], along with the vast domain of isovalent (S, In, Te, Al, Er) and heterovalent (Ag) doping combinations preserving the ϵ polytype structure, these properties position GaSe as an extremely promising nonlinear crystal over an extremely large frequency band.

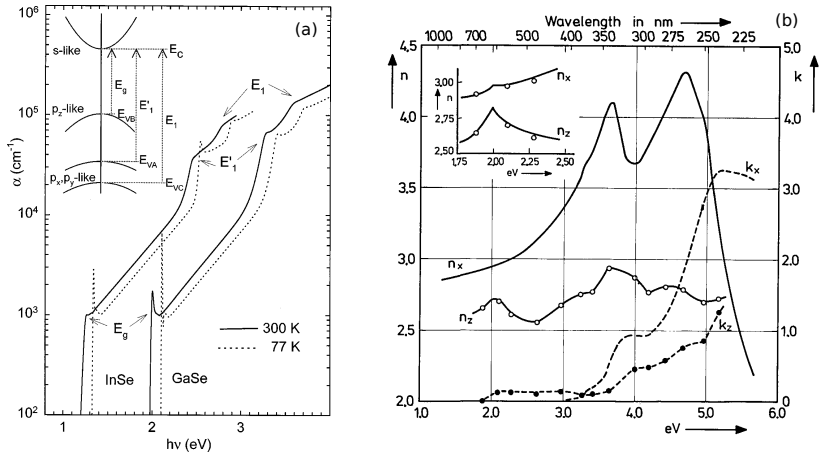

Figure 2.2 (a) Absorption coefficient of GaSe from 1.2 to 4 eV at room temperature and liquid nitrogen temperature. Inset shows a schematical illustration of the band structure near the Brillouin zone center, illustrating the p_z-like valence band to s-like conduction band transition at E_g, which is only allowed for photons polarized as $\mathbf{E} \parallel z$. The E_1 and E_1' transitions, visible in the absorption spectrum, occur more than 1 eV above the direct band gap. Reprinted with permission from Ref. [62] © 1997 American Physical Society (b) Anisotropic refraction index $n_{x,z}$ and absorption coefficient $k_{x,z}$ of GaSe at room temperature. k_z exhibits a very weak absorption edge at $E_g = 2\,\text{eV}$, while k_x shows an absorption edge at $E_1' = 3.25\,\text{eV}$ as well as a sharp resonance at $E_1' = 3.85\,\text{eV}$. Reprinted with permission from Ref. [54] © 1973 Optical Society of America.

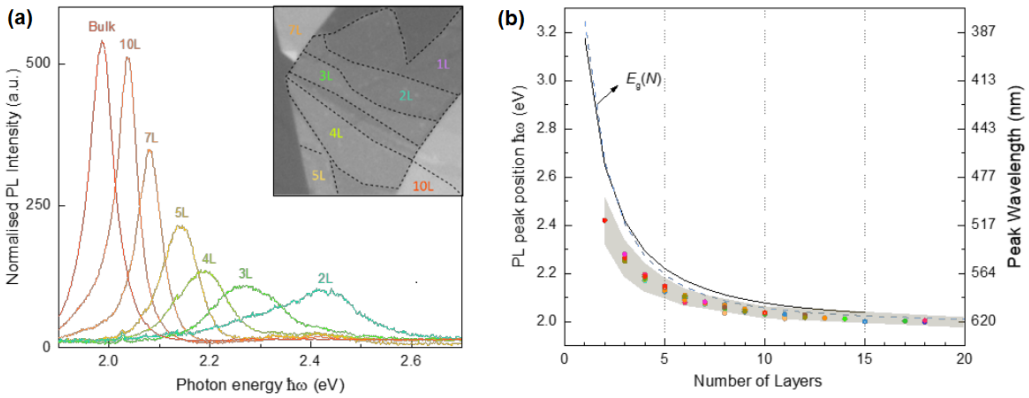

Figure 2.3 (a) Photoluminescence (PL) spectra for various GaSe flake thicknesses, normalized against flake thickness. (b) PL peak intensity as a function of the number of layers for various samples (colored dots) compared to DFT modeling (black line) and $k \cdot p$ tight binding modeling (blue line) of the GaSe bandgap. Adapted with permission from Ref. [39] © 2018 IOP Publishing Ltd.

In the case of atomically thin layers, many studies have shown the strikingly strong second harmonic generation from monolayer hegagonal crystals such as graphene [68], h-BN [69, 70] and transition metal dichalchogenides (TMDs) such as MoS_2 [70–73], which appears in few-layer samples due to the broken inversion symmetry in odd-numbered atomic layer stacks, and is amplified by the very strong unscreened excitonic resonances in these materials [74, 75]. ϵ-GaSe, on the other hand, presents strong nonlinear coefficients even in bulk form, and monolayer second-harmonic generation (SHG) has been shown to be 1-2 orders of magnitude more efficient than in other 2D materials studied so far [41] with the exception of InSe, a very closely related layered monochalchogenide compound with similarly intense SHG [76]. In few-layer materials, nonlinear effects have proven an invaluable tool for detemining stacking order [41, 70, 76, 77] due to their high sensitivity to long-range lattice symmetry, as well as opening the door to the implementation of nanoscale nonlinear optoelectronic devices [78–80].

As will be discussed in the next chapters, the strong nonlinear coefficients within this family of layered monochalchogenide compounds translate into high Raman scattering efficiency from long-range polarization waves, which will prove to be a critical element of the work presented in this thesis.

2.2 Hyperbolic phonon-polaritons

Tolpygo [81] and Huang [82] independently introduced the theoretical concept of polariton in 1950 and 1951, respectively, presenting the first quantum description of the polar resonance contributions to a material's complex permittivity, forming mixed photon-matter excitation states. Soon after, Hopfield [83] introduced the name "polariton" and formalized the theory of exciton-polaritons, defining coefficients describing the 'exciton content' and 'photon content' of the polariton states, now known as the Hopfield coefficients. Some years later, the first experimental observation of polaritonic effects was reported by Henry and Hopfield [23]. Using near-forward Raman scattering, they demonstrated the existence of low-wave vector phonon-polaritons in GaP and measured their dispersion (see Fig. 2.4).

Many polar oscillations, such as plasmons, excitons, magnons, or phonons, can interact with electromagnetic waves and form polariton states. They may occur over different energy ranges and exhibit different dispersive behaviors due to the nature of the polar oscillators involved, but all of these hybrid light-matter quasi-particles involve similar physics. In the rest of this work, the term 'polariton' shall be understood to refer to phonon-polaritons. When referring to other types of polaritons, the full name (plasmon-polariton, exciton-polaritons, etc.) will be used.

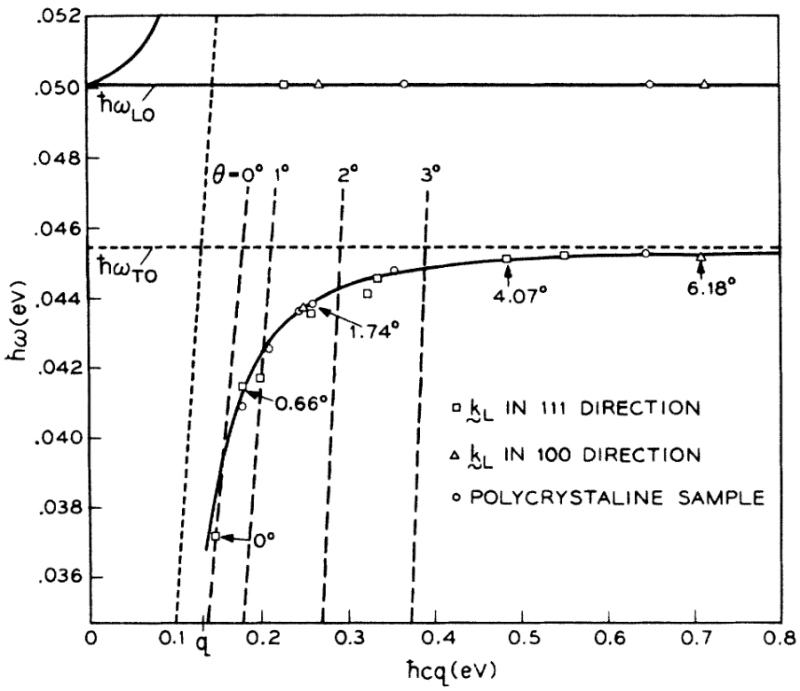

Figure 2.4 Dispersion relation of phonon-polaritons in GaP (solid lines). Oblique dashed lines illustrate momentum conservation relations for various near-forward Raman scattering angles. Raman scattering data points are illustrated by the empty points. Reprinted with permission from Ref. [23] © 1965 American Physical Society.

In order to limit the scope of this section to the most relevant works, emphasis has been put onto literature pertaining to phonon-polaritons in thin films, especially hyperbolic phonon-polaritons in 2D materials.

2.2.1 Confined polaritons

The two leftmost columns of Fig. 2.5 illustrate the dispersion relations of plasmon-polaritons in a conductor and of phonon-polaritons in polar dielectrics, for both semi-infinite (a,c,e) and thin samples (b,d,f). In the semi-infinite case, there exists an upper polariton branch above the negative permittivity region that becomes photon-like at high wave vectors, and a surface polariton (identified by the red curve). Polar insulators also exhibit a lower polariton branch that becomes phonon-like at high wave vectors. Note that the LO phonon does not couple to electromagnetic fields and thus exhibits no dispersion. For thin samples, the upper and lower branches split into multiple guided waves inside the slab, whereas both surface modes interact with each other, lifting their degenerescence and resulting in symmetric and asymmetric guided modes.

In hyperbolic materials, crystalline anisotropy gives rise to frequency bands where oscillators along a certain cristallographic axis exhibit a Reststrahlen band while other crystalline directions have positive permittivity. In uniaxial crystals, Reststrahlen bands along the ordinary axes are known as type I hyperbolic, while extraordinary Reststrahlen bands are known as type II. The rightmost column of Fig. 2.5 shows the phonon-polariton dispersion curve of a uniaxial material with a type II hyperbolic dispersion relation.

As will be shown in the next chapters, these hyperbolic regions, in addition to supporting surface polariton states, can support highly confined guided hyperbolic polariton modes. A note should be made here that several authors refer to guided hyperbolic phonon-polariton as surface polaritons, even though they possess real propagative wave vectors inside the material. This nomenclature is confusing and should be avoided, as guided hyperbolic modes exhibit very different dispersion behaviors than surface modes, especially in sub-wavelength slabs.

2.2.2 Hyperbolic polaritons : applications and control

Hyperbolic materials, sometimes referred to as indefinite permittivity media, were first demonstrated for RF waves in a magnetized plasma in 1969 [85]. In the first decade of this century, interest in these materials surged due to the advent of engineered optical metamaterials [6, 86]. Using these 2D and 3D nanostructured hyperbolic metamaterials, researchers

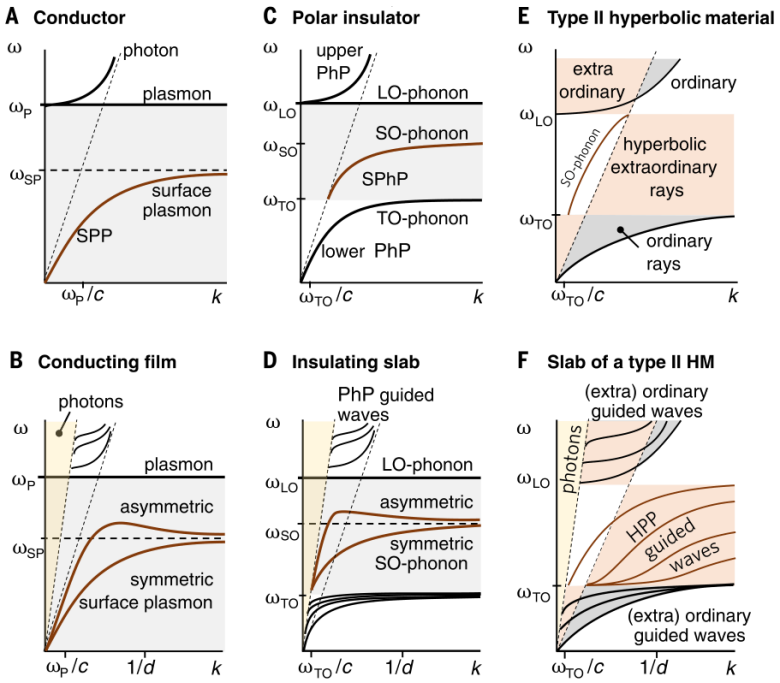

Figure 2.5 Polariton dispersion relation of bulk (a,c,e) and thin slabs (b,d,f) of different materials. (a,b) Plasmon polariton dispersion of a conductor, with a surface plasmon mode indicated by the red line. The diagonal dotted lines represent the photon dispersion curves in vacuum and in the material. (c,d) Phonon-polariton dispersion in a polar dielectric, showing TO and LO phonons, as well as a surface mode (labeled SO here). Near the light line (dashed diagonal), there are a lower polariton, upper polariton and surface-polariton dispersive branches. (e,f) Phonon-polariton in a type II hyperbolic material, with dispersive upper, lower, and surface polariton branches. Note that in (f), there are multiple guided hyperbolic modes (red curves) in the Reststrahlen band between ω_{TO} and ω_{LO}. Reprinted from Ref. [84] © 2016, American Association for the Advancement of Science.

demonstrated multiple effects such as subwavelength imaging [3, 87] and focusing using [88], spontaneous emission enhancement [89], and extreme field enhancement in hyperbolic waveguides [90]. Some natural uniaxial crystals were already known to exhibit hyperbolic properties [91–93], and the observation of confined, low-loss phonon-polaritons in hexagonal boron nitride by Dai *et al.* in 2014 [4] sparked a great level of interest for 2D materials in the nanophotonics community [14, 15, 84, 94, 95].

Since then, several impressive properties and applications of h-BN-confined hyperbolic polaritons were reported, including nanofocusing in tapered h-BN slabs [96], polariton propagation control and steering along h-BN waveguides [97], and polariton launching from plasmonic antennas on h-BN slabs [98]. Up until 2018, h-BN was the only 2D compound in which hyperbolic phonon-polaritons had been reported, and though the material presents great figure of merits, it can only support polaritons in its two Reststrahlen bands (760-825 cm^{-1} and 1360-1610 cm^{-1} [99]). In 2018, hyperbolic polaritons were reported in the biaxial layered layered material α-MoO_3 [100]. In light of the wide array of naturally hyperbolic layered materials currently undergoing intense scientific scrutiny on multiple fronts [16], as well as the promising opportunities from hybridized polaritons from 2D heterostructures [84, 101, 102], it is only a matter of time before other hyperbolic 2D materials become focal points of interest.

2.2.3 Near-field experimental techniques

Due to the non-propagative nature of surface and guided phonon-polaritons modes outside the host material, no direct photon-polariton coupling can be achieved using an external radiating field, and any interaction with these states relies on some form of indirect coupling either to the evanescent electromagnetic field or to the associated polar oscillator.

In order to couple external propagating fields to the evanescent field states of the polaritons near the sample interface, some scheme must be employed to overcome the momentum mismatch between the confined and free-space fields. A large majority of experimental works studying confined phonon-polaritons in thin films use near-field coupling to access the polariton states. Scattering-type apertureless scanning near-field optical microscopy (s-SNOM) [55, 103, 104], exploiting field confinement from the surface plasmons of a metallized AFM cantilever tip [105], has been shown to enable imaging of polar oscillators with lateral resolution in the tens of nanometers [106]. The method has notably been used to map surface field distributions of polaritons in silicon carbide [107], hexagonal boron nitride [4], and more recently α-MoO_3, a biaxial hyperbolic layered compound [100]. From these spatial field imaging measurements, polariton propagative behavior, confinement ratio, dispersion relations, and decay length can be extracted, as is shown on Fig. 2.6.

In order to image the field distribution, a metallized AFM tip is scanned over the sample surface and illuminated with a bright infrared beam. Surface plasmons are excited on the small tip radius, acting as an 'optical antenna' [104], which results in a strong evanescent field between the tip and sample, which has the necessary momentum to launch polaritons into the sample. These polaritons propagate away from the tip in all directions until they are reflected by a medium boundary such as a sample edge. These reflected waves form a standing wave field pattern between the tip and the boundary, which can be mapped by measuring the intensity of elastically scattered IR light from the tip as it is moved toward that boundary. Measuring the distance between these wavefronts enables direct determination of the polariton wavelength and wave vector inside the sample.

In order to distinguish the weak tip-scattered signal from the background elastically scattered light, lock-in detection schemes must be used. Since the tip-scattered signal intensity is highly sensitive to the tip to sample spacing, modulation from the cantilever oscillation has been used as a lock-in reference with some success, although some form of heterodyne [108] or pseudo-heterodyne [109] detection is necessary to achieve background-free images, the most commonly used being a pseudo-heterodyne detection scheme using a phase-modulated reference wave [92, 109].

s-SNOM has proven to be an invaluable tool to study confined polariton states in 2D materials with sub-wavelength spatial resolution, providing a direct window into the real-space field distribution of these polariton states. Some degree of control over the probed wave vectors can be obtained by tuning the tip to sample distance [110], but resolution is quite limited. The direct wavelength observation technique illustrated in Fig. 2.6 enables precise wave vector determination, however it can only be applied to modes with large enough decay lengths and wavelengths, as it requires the ability to observe and resolve at least two wavefronts. Also, it can only be applied near a boundary that can reflect polaritons toward the AMF tip to create standing wave patterns, such as a flake edge or terrace, or the edge a deposited metal layer. The technique realizes a very high lateral resolution, but it can only couple to fields with a vertical polarization (normal to the surface) due to the geometry of the system, and is only sensitive to field distributions at the sample surface.

Coupling of free-space radiation to high-momentum confined polariton states can also be achieved by the use of surface gratings or periodic arrays of nanostructures, as was demonstrated in silicon carbide [111] and h-BN [5]. This method yields strong signals and allows for precise wave vector selectivity, although accessible wave vectors are defined by the nanostructure and array geometries, requiring extensive microfabrication to determine dispersion behavior.

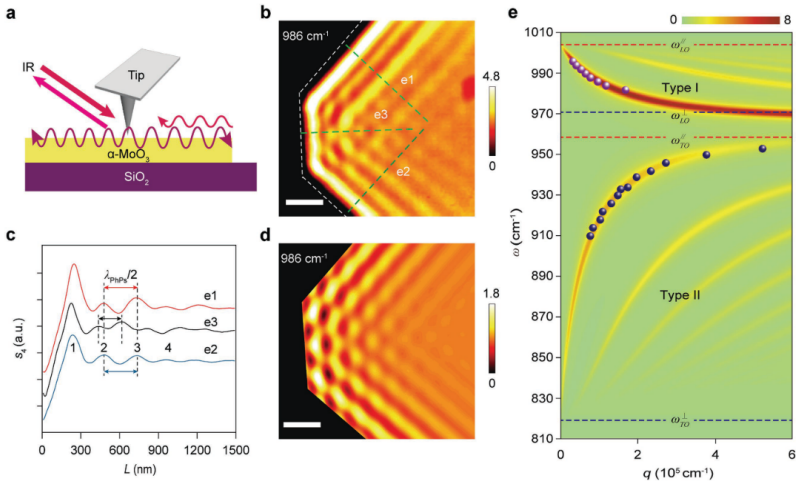

Figure 2.6 Scattering-type apertureless scanning near-field optical microscopy measurement from a 102 nm flake of α-MoO_3. (a) Schematic illustration of the experimental method. (b) s-SNOM image of the flake with excitation frequency of 986 cm^{-1} (scale bar is 500 nm). (c) Field amplitude profiles along the three dashed lines in (b), revealing polariton stationary waves in the flake. (d) Simulated field distribution in the flake. (e) Simulated dispersion relation of hyperbolic polaritons in α-MoO_3. Data points correspond to the wavenumber-wavelength pairs extracted from field profiles for various excitation frequencies. Reprinted from Ref. [100] CC BY-NC 4.0.

Attenuated total internal reflection (ATR) inside a prism suspended above the sample (Otto configuration) [112] allows for precise wave vector control of the probed states, and has been used to study several polariton features in thin films using free electron laser sources [113–115], although it suffers from a lack of spatial resolution.

All of the aforementioned techniques rely on external light sources in resonance with the probed polaritons, and although recent progress has been achieved with tunable quantum cascade lasers (QCLs), continuum IR lasers, synchrotron sources, and photoconductive antennas [116–118], direct spectroscopy in the far-IR range remains limited due to the availability of high-brightness tunable sources and fast detectors in this energy range. A comprehensive review of the various experimental techniques used to probe mid- to far-infrared polaritons is given in Ref. [17].

So far, the only reports of hyperbolic phonon-polaritons using these methods in 2D materials are in hexagonal boron nitride (h-BN) and α-MoO_3, although all layered dipolar materials should in theory exhibit hyperbolic dispersion due to their extreme anisotropy. Both these materials have stiff phonon resonances in the 900-1500 cm^{-1} range, where tunable QCL sources are commercially available. However, polar oscillators in transition metal dichal-

chogenides such as MoS_2 are in the 300-400 cm^{-1} range [119], and those of GaSe in the 200-400 cm^{-1} range, outside the currently accessible tuning range of QCLs.

2.3 Raman spectroscopy of polaritons

Phonon-polariton states, due to their part-phonon nature, can in some cases be accessed via Raman scattering, such as in the landmark 1965 experiment of Henry and Hopfield, where they observed bulk phonon-polariton states in GaP using near-forward Raman scattering (see Fig. 2.4). Raman scattering from polaritons can be observed in polar crystals with no inversion center, where polar modes can be Raman-active. However, due to the large momentum of the incident and scattered photons (usually in the visible range) compared to the mid- to far-infrared polariton states, only near-forward scattering geometries, where incident and scattered photons are nearly colinear, enable observation of polariton dispersion from bulk samples, as is shown by the shallow scattering angles used by Henry and Hopfield (see Fig. 2.4). Conversely, right-angle or backscattering geometries, with an angle of 90 or 180° between incident and scattered photons, require a large momentum contribution from the phonon, precluding observation of the low-momentum dispersive polariton states.

Surface polaritons

Raman scattering of surface polariton dispersion was reported for the first time in 1973 by Evans, Ushioda and McMullen [120]. Surface polariton dispersion in thick (semi-infinite) samples in vacuum occurs over a very narrow wave vector range, rapidly converging to an energy that is close to the LO phonon. In order to facilitate their measurement, Evans *et al.* used a thin GaAs film on a sapphire substrate, where both the sapphire's high refractive index and confinement effects in the thin film contributed to flatten the dispersion of the lower (symmetric) surface polariton toward lower energies and higher wave vectors, respectively. Two years later, Prieur and Ushioda [121] reported observation of scattering from the upper (anti-symmetric) surface mode in the same sample by immersing it in benzene to alter the refractive index at the second interface of the GaAs film (see Fig. 2.7). Direct scattering from single-interface surface polaritons in a GaP sample was achieved a few years later by Valdez and Ushioda [122] exploiting resonant Raman enhancement from the argon-ion laser absorption. The effects of the surrounding dielectric environment, confinement in thin slabs, and resonant enhancement used in these initial experiments are central elements of this work, and will be discussed in detail in the following chapters.

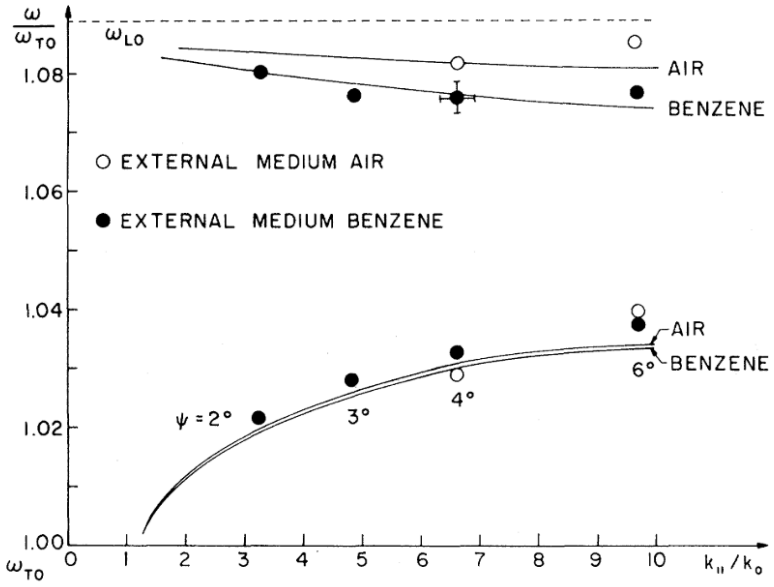

Figure 2.7 Calculated dispersion curves of the upper and lower surface polariton modes in a thin GaAs film on a sapphire substrate in air and immerged in benzene. Circles represent near-forward Raman scattering data. Reprinted with permission from Ref. [121] © 1975 American Physical Society.

Guided polaritons

After theoretical predictions of Raman activity from guided polariton modes [123], Valdez, Mattei and Ushioda reported the first observation of Raman scattering from guided polaritons in 30 µm GaP films [124], identifying multiple guided modes in the scattered spectra. Building upon these results, Sasaki and Ushioda [24] reported the first experimental study of Raman scattering by guided hyperbolic polaritons, using cleaved ϵ-GaSe samples with thicknesses between 2.7 and 6.5 µm. They observed the thickness dependency of the polariton dispersion in GaSe slabs (see Fig. 2.8) and modeled their results using an electromagnetic waveguide model and a field density-based Raman cross section model similar to the one used in this work, which is described in detail in Chapters 4 and 5. However, due to the relatively large thickness of the samples they used, polaritons were only weakly confined in the slabs, restricting their dispersive regimes to low wave vectors.

Recent uses of Raman in polaritonics

In recent years, very little work pertaining to polariton coupling via Raman scattering has been published, and the technique is conspicuously absent from most literature reviews de-

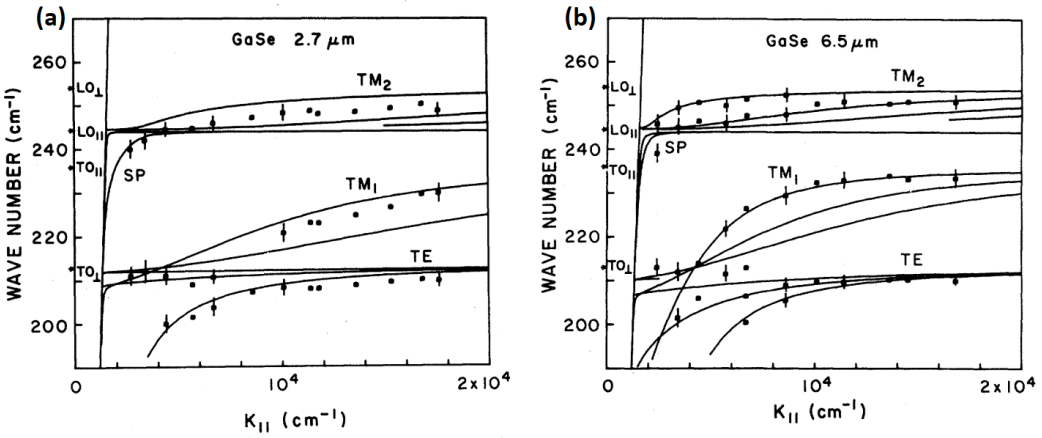

Figure 2.8 Calculated dispersion curves of the surface (SP) and guided ordinary (TE) and guided extraordinary/hyperbolic (TM) polariton modes in (a) 2.7 μm and (b) 6.5 μm GaSe films in air. Black circles represent near-forward Raman scattering data. Adapted with permission from Ref. [24] © 1983 American Physical Society.

scribing the study of phonon-polaritons [12, 17]. Some notable exceptions include the use of impulsive stimulated Raman scattering (ISRS) to generate large populations of guided hyperbolic polaritons in the THz regime in nonlinear media [125–127]. Features in the Raman spectrum of SiC nanopillar arrays were also identified as originating from localized surface polaritons [111]. The polarization sensitivity of Raman scattering has also been exploited to study modal profiles of confined polaritons in a suspended rectangular waveguide of InP [128] and to observe evidence of lasing behavior from an electrically pumped polariton laser [20]. In contrast to the groundbreaking demonstrations of Raman scattering as a tool to completely characterize polariton dispersion, most of these reports do not fully exploit the potential of Raman spectroscopy in the study of confined polaritons, being often used as a complementary technique to FTIR or THz measurements.

In summary, Raman scattering, providing indirect probing of polaritons via nonlinear interaction with the electro-mechanical polaritonic wave, enables remote access to confined polariton states using external propagative fields, in contrast to near-field techniques that rely on in-situ evanescent fields to couple to the polariton electromagnetic field. This obviates the requirement for high-quality light sources and detectors in the far-IR and THz or complex experimental setups, allowing the study of polaritons using conventional laser sources, optics, and detectors. Raman scattering also enables observation of in-plane polarized modes, and is a polarization-sensitive technique, as opposed to the commonly used s-SNOM. This simple, noninvasive technique has been seldom exploited in recent years, likely because near-forward scattering, which is generally understood as the only way to observe Raman scattering from

polaritons, is not straightforward to carry out on thin or 2D flakes. In this thesis, it will be demonstrated that Raman spectroscopy, both in the near-forward and backscattering configurations, proves to be a powerful tool to study surface and guided hyperbolic polariton modes in 2D films and waveguides.

CHAPTER 3 PHONONS AND PHONON-POLARITONS IN UNIAXIAL CRYSTALS

In any crystalline lattice, there exists a variety of normal vibrational modes, each associated with an atomic displacement degree of freedom in the unit cell. For example, a diatomic three-dimensional unit cell crystal structure has $2 \times 3 = 6$ degrees of freedom, thus 6 normal modes. Among these normal modes, there are three so-called acoustic modes, and the rest are known as optical modes.

The three acoustic modes represent in-phase displacements of all the unit cell atoms along the same direction. These acoustic modes, or acoustic phonons, only exist in a propagating state, as a non-propagating (or infinite wavelength) acoustic mode is really just a rigid displacement of the whole lattice, as opposed to a crystalline vibrational mode, and thus their frequency tends to zero as $k \to 0$.

Optical vibrational modes comprise all of the remaining out of phase atomic displacements, and only occur in crystals with two or more atoms in the unit cell. Contrary to acoustic modes, optical modes have finite frequency as $k \to 0$, as they do not represent a rigid displacement of the unit cell, but rather an oscillation within each respective unit cell. The frequency of these normal mechanical oscillator modes are determined in general by the short-range atomic bond strength and atomic masses. Dispersive effects arising from the lattice structure do not affect small-k phonons, and the optical phonon dispersion curves have a vanishing derivative (usually a quadratic dispersion) at the zone center (see Fig. 3.1).

In the following sections, the effect of the dipole moments in polar crystals on the vibrational mode dispersion relation near the Brillouin zone center is presented. In order to be consistent with the literature, vibrational modes near the zone center ($k \ll \frac{\pi}{a}$) but far beyond the light cone ($k \gg \frac{\omega}{c}$) will be referred to as zone-center phonons, whereas vibrational modes in the vicinity of the light cone are referred to as polaritons.

3.1 Phonons in polar crystals

In ionic or polar crystals, relative displacements within the unit cell can yield oscillating dipole moments. These dipole moments can interact with each other and add a long-range Coulomb contribution to the effective oscillator restoring force. This long-range interaction depends on the dipole orientation relative to the propagation direction. For longitudinal dipole orientations, the interaction between adjacent dipoles adds up at a macroscopic level,

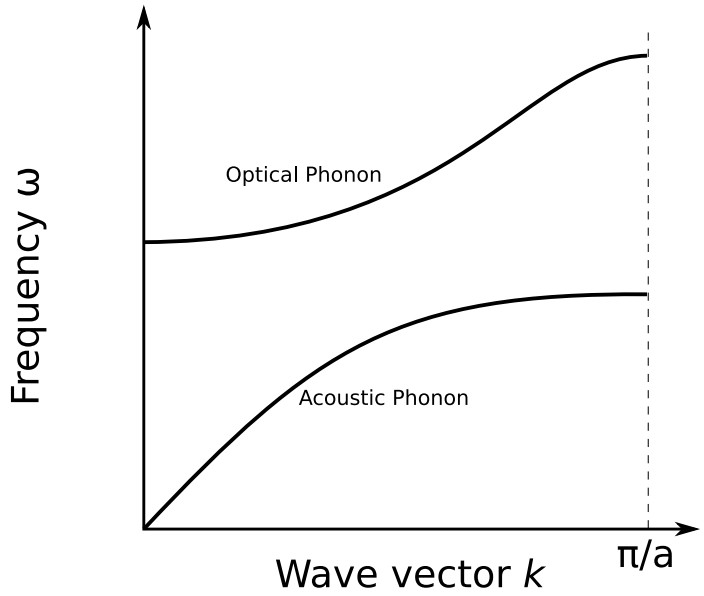

Figure 3.1 Acoustic and optical phonon dispersion over the full extent of the Brillouin zone ($0 < k < \frac{\pi}{a}$) for a crystal with lattice parameter a.

contributing an additional electrostatic component to the oscillator energy. For transverse dipole orientations, the macroscopic electric field vanishes, and there is no long-range contribution to the oscillator energy. Because of this, longitudinal optical (LO) phonons have a higher energy than their transverse counterparts (TO phonons) despite possessing similar mechanical displacements. Therefore, each polar vibrational mode can exhibit two different vibration frequencies depending on the relative orientation of its direction of propagation and atomic displacement. The magnitude of the TO-LO splitting is specific to each polar phonon in a material and depends on the mode dipole strength and lattice dielectric screening. Note here that since the origin of this energy splitting is a long-range interaction, its effects also apply to long-wavelength phonons ($k \ll \frac{\pi}{a}$), where a is the lattice parameter.

Near the very center of the Brillouin zone, the transverse dipole oscillations couple with electromagnetic wave modes that have wave vectors of $q = \frac{\omega}{c}$ and exhibit strongly dispersive behavior. These polariton mixed states will be discussed in more detail later, but for now only the purely mechanical zone-center phonons will be considered.

3.1.1 Uniaxial phonon dispersion

In cubic polar crystals, the Coulomb interaction is isotropic, therefore the TO-LO splitting for the zone-center phonons is uniform in all directions. For uniaxial crystals however, Coulomb interaction has pronounced effects on the directional dispersion of polar phonons. Not only is

every polar mode split into a TO and LO version, but the long-range nature of the Coulomb interaction means that dispersion effects can be observed much closer to the Brillouin zone center than in non-polar crystals.

For uniaxial crystals, the extraordinary axis (conventionally named the c axis) differs from the two others, and normal vibrational modes with atomic displacements along that axis have a frequency $\omega_{/\!/}$ that differs from the frequency $\omega_{\perp}$ of the twofold degenerate modes with atomic displacements perpendicular to c. The zone-center phonons propagating in the plane perpendicular to this axis have well-defined symmetries relating to the lattice symmetry, as for cubic crystal phonons. However, zone-center phonons that propagate at an angle $\theta \notin \{0, \frac{\pi}{2}\}$ relative to the extraordinary axis exhibit a mixed character, since even a small wave vector can reduce their symmetry below that of the lattice because of the long-ranging effects of the Coulomb interaction [129]. When varying the propagation direction between two principal axes, they smoothly change from one character to another, forming a phonon branch between these two axes.

The dispersion of these so-called oblique phonons involves both an electrostatic contribution and the crystalline anisotropy of the material. The electrostatic contribution originates from the long-range Coulomb interaction that induces the LO-TO energy splitting, while the crystalline anisotropy accounts for the differing energies between out-of-plane ($/\!/$ or A-type) and in-plane ($\perp$ or E-type) displacements. Indeed, while the vibrational modes are well defined by their A, E, TO and LO characters for propagation directions $\theta = 0$ and $\frac{\pi}{2}$, the dispersion branches between these vary greatly depending on the relative magnitudes of the electrostatic and crystalline contributions [130–132].

Loudon [131] highlights two canonical types of uniaxial crystals : those with dominant crystalline anisotropy and those with dominant Coulomb interaction. In the case of dominant anisotropy, the modes will maintain their symmetry character at both extremities of the branch but their electric field orientation will gradually change from TO to LO or vice versa. In crystals where the Coulomb interaction is dominant, the modes will instead maintain their TO or LO character, and the atomic displacement symmetry will differ on both extremities. In both cases, the change in character of the modes along the branch is accompanied by a consequent vibrational frequency dispersion as a function of propagation angle.

The phonon dispersion relations for a Coulomb-dominant crystal like GaSe are given by

[18, 131]

$$\omega^2_{\mathrm{To}}(\theta) = \omega^2_{\mathrm{TO}\perp}, \tag{3.1}$$

$$\omega^2_{\mathrm{Te}}(\theta) = \omega^2_{\mathrm{TO}\perp}\cos^2\theta + \omega^2_{\mathrm{TO}/\!/}\sin^2\theta, \tag{3.2}$$

$$\omega^2_{\mathrm{Le}}(\theta) = \omega^2_{\mathrm{LO}/\!/}\cos^2\theta + \omega^2_{\mathrm{LO}\perp}\sin^2\theta. \tag{3.3}$$

From inspection of these equations, the three phonon dispersion branches can be identified as transverse ordinary (To), transverse extraordinary (Te) and longitudinal extraordinary (Le). This nomenclature is exact for the ordinary branch, as it involves no long-range electric field and remains a transverse E mode for all angles θ, but the extraordinary branches do not possess strictly defined symmetries, as they have non-zero long-range fields and therefore their symmetry is lower than that of the lattice. The resulting dispersion for the three branches is plotted of Fig. 3.2 for GaSe.

3.2 Polariton dispersion

This section presents the polariton dispersion relations near the light cone ($k \sim \frac{\omega}{c}$) for cubic and uniaxial polar crystals based on a simple charged harmonic oscillator model.

3.2.1 Cubic crystals

In the simple case of a cubic lattice with a single polar vibrational mode, which we model as a damped harmonic oscillator interacting with the electromagnetic field through its dipolar moment, the dispersion relation for TO phonons near the Brillouin zone center is given by [131–133]:

$$\frac{k^2c^2}{\omega^2} = \epsilon(\omega) = \epsilon_\infty + \frac{\epsilon_s - \epsilon_\infty}{\omega^2_{\mathrm{TO}} - \omega^2 - \iota\Gamma\omega}\omega^2_{\mathrm{TO}} \tag{3.4}$$

In this relation, ϵ_s and ϵ_∞ represent the static and high-frequency relative permittivity, respectively, ω_{TO} the transverse lattice mode frequency and Γ the anharmonic component of the mode oscillation, which corresponds to a damping rate. For the following discussion, the damping factor will be omitted for simplicity, and it will be reintroduced in the general numerical model presented in §5.3 by substituting[1] $\omega^2 \to \omega^2 + \iota\Gamma\omega$. The resulting effective permittivity is plotted on Fig. 3.3 for $\Gamma = 0$, showing a diverging value when $\omega \to \omega_{\mathrm{TO}}$, and

[1]The Greek letter ι is used in this work to denote the imaginary unit $\iota \equiv \sqrt{-1}$ to avoid confusion with the letter i used as indices and subscripts.

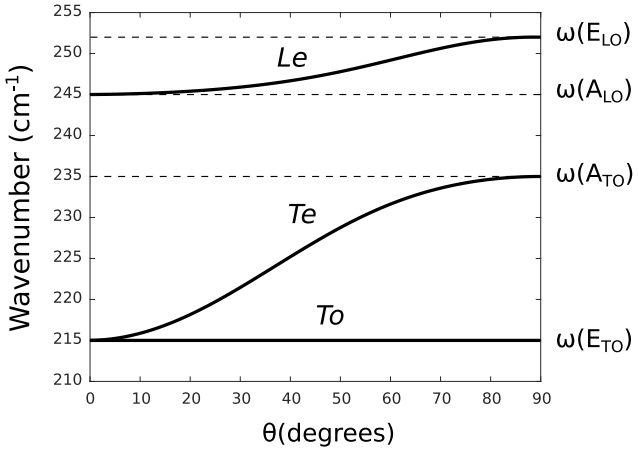

Figure 3.2 Angular dispersion of the zone center ($\omega/c \ll k \ll \frac{\pi}{a}$) phonon modes of GaSe. There is a lower transverse ($\mathrm{E_{TO}} \rightarrow \mathrm{A_{TO}}$) and an upper longitudinal ($\mathrm{E_{LO}} \rightarrow \mathrm{A_{LO}}$) extraordinary phonon branch as well as an ordinary transverse branch ($\mathrm{E_{TO}} \rightarrow \mathrm{E_{TO}}$). This indicates a dominant Coulomb interaction in GaSe since the extraordinary branches retain their TO or LO character at both extremities.

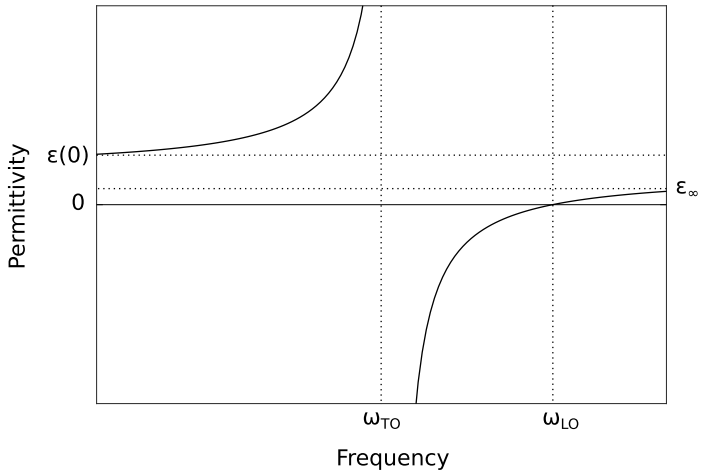

Figure 3.3 Permittivity as a function of frequency in a cubic crystal with a single polar phonon, as described by equation (3.4) (with $\Gamma = 0$). The permittivity at low frequency is ϵ_s, then diverges to a large value at ω_{TO}. Between ω_{TO} and ω_{LO}, ϵ is negative, and then tends toward ϵ_∞, which is lower than ϵ_s as there is one less mechanism that can contribute to the polarization of the material, as the polar phonon cannot respond to frequencies much larger than ω_{LO}.

a region of negative permittivity between ω_{TO} and ω_{LO} which is known as a Reststrahlen band.

Setting $\omega = \omega_{\mathrm{LO}}$ in the previous equation, with ω_{LO} defined as $\epsilon(\omega_{\mathrm{LO}}) \equiv 0$, yields the Lyddane-Sachs-Teller relation [134] between the LO and TO frequencies :

$$\frac{\omega_{\mathrm{LO}}^2}{\omega_{\mathrm{TO}}^2} = \frac{\epsilon_s}{\epsilon_\infty}. \tag{3.5}$$

From the previous equation, equation (3.4) can take the form

$$\frac{k^2c^2}{\omega^2} = \epsilon(\omega) = \epsilon_\infty \left(\frac{\omega_{\mathrm{LO}}^2 - \omega^2}{\omega_{\mathrm{TO}}^2 - \omega^2} \right). \tag{3.6}$$

This relation only shows dispersive behavior near the very center of the Brillouin zone, where $k \sim \frac{\omega}{c}$. In this momentum region, the polar mechanical vibrations couple strongly with electromagnetic waves that have momentum $q = \frac{\omega}{c}$. This coupling yields hybrid photon-phonon modes called phonon-polaritons (PhPs) that simultaneously exhibit phonon-like and photon-like characteristics. Figure 3.4 shows the dispersion relation of a simple cubic crystal with a single polar mode. The LO mode shows no dispersive behavior as electromagnetic waves are transverse in nature, while the TO mode exhibits an anti-crossing behavior with the low- and high-frequency photon modes, which are represented by the dashed lines.

The upper TO branch starts out at $k = 0$ as a transverse mechanical vibration with frequency ω_{LO} and gradually transitions into a high-frequency photon propagating in the media with permittivity ϵ_∞. Between these two limits, it propagates as a polaritonic wave, which is known as the upper polariton branch. The lower polariton branch starts at $k = 0$ as a photon propagating in a ϵ_s dielectric medium and gradually transitions into a transverse mechanical mode, eventually becoming a fully mechanical TO phonon at higher k.

3.2.2 Uniaxial crystals

Uniaxial crystal such as GaSe present a crystalline anisotropy where one axis (extraordinary axis) exhibits a different permittivity, which is equivalent along the two other axes (ordinary axes). In the case of GaSe, the extraordinary axis is the c axis (out-of-plane) with permittivity $\epsilon_{/\!/}$, and the in-plane permittivity $\epsilon_\perp$ is isotropic in the ab plane.

For polar anisotropic phonons, normal modes classified according to the lattice point group symmetry propagate in certain directions in the lattice. For example, a longitudinal 'E' mode ($\mathrm{E_{LO}}$) cannot propagate along the c axis, as the associated lattice displacement and

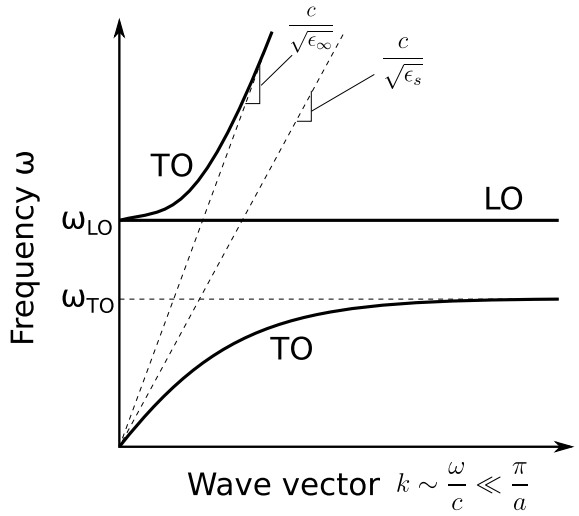

Figure 3.4 Schematic representation of the Brillouin zone center dispersion of a polaritons in a cubic crystal illustrating the LO branch, the upper and lower TO branches, and the uncoupled phonon and photon dispersion curves (dashed lines)

dipole moment are both in the *ab* plane and the phonon propagation and dipole moment are defined as co-linear for an LO mode. Conversely, the associated transverse mode (E_{TO}) can propagate in any direction in the crystal, as there is always an in-plane displacement vector that is perpendicular (or 'transverse') to a given propagation direction. This mode is known as an ordinary wave, and exhibits the same dispersion relation as for a cubic crystal :

$$\epsilon_{\perp}(\omega) = \epsilon_{\infty\perp}\left(\frac{\omega_{LO\perp}^2 - \omega^2}{\omega_{TO\perp}^2 - \omega^2}\right). \tag{3.7}$$

Similarly for the out-of-plane modes,

$$\epsilon_{/\!/}(\omega) = \epsilon_{\infty/\!/}\left(\frac{\omega_{LO/\!/}^2 - \omega^2}{\omega_{TO/\!/}^2 - \omega^2}\right). \tag{3.8}$$

Equation (3.7) describes the dispersion of ordinary transverse polaritons. Equation (3.8) applies to extraordinary polaritons propagating in the *ab* plane. These dispersion relations are illustrated on figure Fig. 3.5 for GaSe. Note that there are two distinct Reststrahlen bands applying to in-plane and out of plane vibrations. The general dispersion relation for arbitrary wave vector direction of extraordinary waves depends on both wavelength and

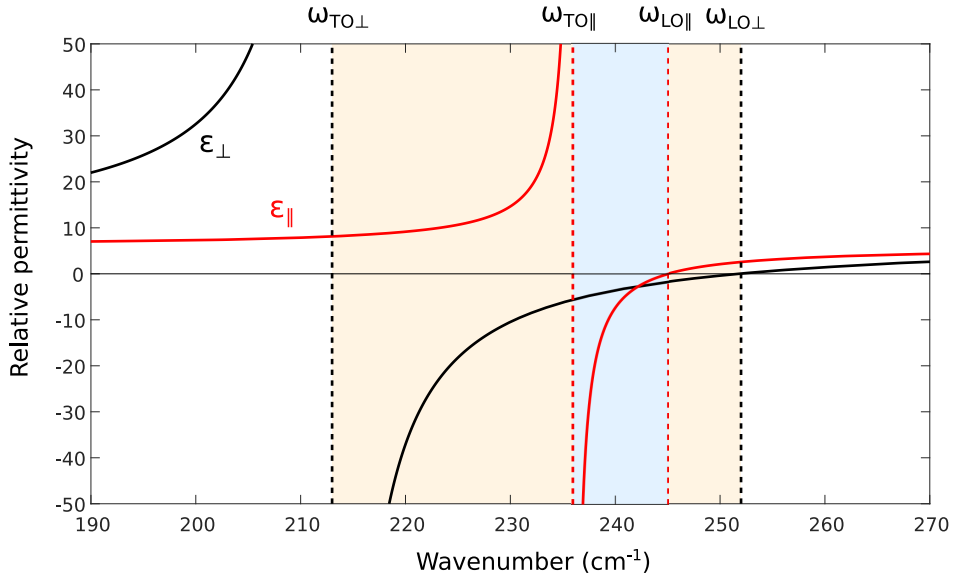

Figure 3.5 Permittivity as a function of frequency for the two principal directions in gallium selenide, as described by equations (3.7) and (3.8). The frequency regions in which one of the permittivities is negative (Type II hyperbolic with $\epsilon_\perp < 0$ in the case of GaSe) are highlighted in orange. The region shaded in blue is the double Reststrahlen region, where both permittivities are negative.

propagation angle θ relative to the c axis [131]:

$$\frac{k^2c^2}{\omega^2} = \epsilon_e(\omega,\theta) = \frac{\epsilon_\perp(\omega)\epsilon_{/\!/}(\omega)}{\epsilon_\perp(\omega)\sin\theta^2 + \epsilon_{/\!/}(\omega)\cos\theta^2}, \tag{3.9}$$

which can also be expressed as

$$\frac{\omega^2}{c^2} = \frac{k_\perp^2}{\epsilon_\perp} + \frac{k_{/\!/}^2}{\epsilon_{/\!/}}. \tag{3.10}$$

Both longitudinal frequencies can be obtained via their respective versions of (3.5)

$$\frac{\omega_{\mathrm{LO}\perp}^2}{\omega_{\mathrm{TO}\perp}^2} = \frac{\epsilon_{0\perp}}{\epsilon_{\infty\perp}} \quad \text{and} \quad \frac{\omega_{\mathrm{LO}/\!/}^2}{\omega_{\mathrm{TO}/\!/}^2} = \frac{\epsilon_{0/\!/}}{\epsilon_{\infty/\!/}}. \tag{3.11}$$

For positive $\epsilon_\perp$ and $\epsilon_{/\!/}$, the dispersion relation (3.10) can describe a revolution ellipsoid, which is the typical uniaxial dispersion. For negative $\epsilon_{/\!/}$ and positive $\epsilon_\perp$, in the out of plane Reststrahlen region, it describes a one-sheeted revolution hyperboloid, known as a Type I hyperbolic dispersion. When $\epsilon_\perp$ is negative and $\epsilon_{/\!/}$ positive, (3.10) describes a two-sheeted revolution hyperboloid, known as Type II hyperbolic dispersion. All three cases are illustrated on Fig. 3.6. Frequency regions where both permittivities are negative are double Reststrahlen

bands, similar to the Reststrahlen band in cubic crystals. In general, the relative positions of $\omega_{\mathrm{TO}\perp}$, $\omega_{\mathrm{LO}\perp}$, $\omega_{\mathrm{TO}\parallel}$ and $\omega_{\mathrm{LO}\parallel}$ can define multiple combinations of Type I, Type II and double Reststrahlen regions in an anisotropic polar material.

It is important to note here that all of the dispersion relations presented in this chapter were only defined for cubic crystals with a single triply degenerate polar resonance at frequency ω_{TO}, or for uniaxial crystals with a single group of one singly degenerate A and a doubly degenerate E polar resonances. In more complex crystals such as GaSe, there are multiple polar phonons, and the complete expression for the dispersion relation involves coupling between all the n_λ optical modes along a particular direction λ [135] :

$$\epsilon_\lambda(\omega) = \epsilon_{\lambda\infty} \prod_{i=1}^{n_\lambda} \left(\frac{\omega_{\mathrm{LO}\lambda i}^2 - \omega^2}{\omega_{\mathrm{TO}\lambda i}^2 - \omega^2} \right). \tag{3.12}$$

In the case of bulk GaSe, there are two groups of three polar modes $2 \times (1\mathrm{A} + 2\mathrm{E})$. The first group is at very low energies and consists of 'rigid layer modes', which are out-of-phase acoustic modes (see Table 4.2). The transverse frequency of the low-energy E mode is relatively well established from Raman [18, 47, 53, 136–138] and THz measurements [22] at $\omega_{\mathrm{TO}\perp} = 19.5\,\mathrm{cm}^{-1}$. The low-frequency A mode is less well-documented, but infrared absorption [53, 139] and numerical computations [136] indicate that it has a wavenumber of around $\omega_{\mathrm{TO}/\!/} = 36\,\mathrm{cm}^{-1}$. However, there is no data in the literature indicating the corresponding longitudinal frequency of these modes. Nevertheless, these resonances are very weak [22, 46] and do not affect the permittivity at higher energies and thus they were not included in the modeling of the permittivity of GaSe in this work.

The group of three higher-frequency polar modes, which are very well documented in the literature and exhibit strong resonances [18, 22, 47, 48, 53, 139–141], were used to model the permittivity. Table 3.1 lists the corresponding energies and high-frequency permittivities that are used in this work.

	ω_{TO} (cm^{-1})	ω_{LO} (cm^{-1})	ϵ_∞
In-plane $\mathrm{E}'(2^{1,2})$ mode	213.5	254	7.44
Out-of-plane $\mathrm{A}_2''(2)$ mode	236	244.5	5.76

Table 3.1 Transverse and longitudinal frequencies and high-frequency permittivities for the in-plane and out-of plane polar phonons in GaSe (values taken from the Handbook of Optical Constants in Solids vol. III [142]).

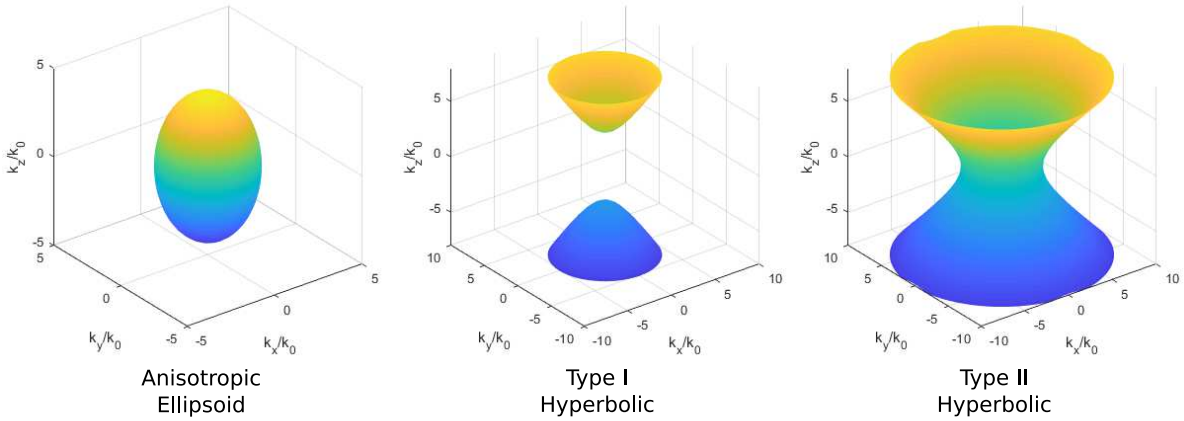

Figure 3.6 Typical isofrequency surfaces of the dispersion relation of a uniaxial material with positive uniaxial ellipsoidal dispersion (with $\epsilon_{\parallel} > \epsilon_{\perp}$), Type I hyperbolic dispersion and Type II hyperbolic dispersion.

CHAPTER 4 RAMAN SCATTERING BY PHONONS AND POLARITONS

4.1 Raman scattering by phonons

Excitations in a crystal lattice can induce fluctuations in the electric susceptibility of the crystal via multiple mechanisms, such as lattice displacements inducing oscillations in the periodic electronic structure. These susceptibility fluctuations can in turn scatter photons inelastically, wherein the lattice excitations and the scattering photons exchange energy.

4.1.1 The Raman tensor and selection rules

In a semi-classical approach, Raman scattering in a crystal can be viewed as a two-step process, with an incident electromagnetic field $\boldsymbol{E}$ inducing an electric polarization $\boldsymbol{P}$ in the material, according to the electronic susceptibility tensor $\overleftrightarrow{\chi}$

$$\boldsymbol{P} = \epsilon_0 \overleftrightarrow{\chi} \boldsymbol{E}. \tag{4.1}$$

The induced polarization field then radiates light at an intensity proportional to $|\boldsymbol{P}|^2$, which can be modulated by fluctuations in the susceptibility.

The electronic states that define the susceptibility tensor can be affected by lattice displacements through the electron-lattice interaction. In a crystal, the susceptibility can be expressed as a Taylor series of the atomic displacements around their equilibrium positions [131]

$$\overleftrightarrow{\chi} = \overleftrightarrow{\chi}_0 + \sum_{\lambda} \left(\frac{\partial \overleftrightarrow{\chi}}{\partial Q_\lambda} \right)_{Q_\lambda = 0} Q_\lambda + \frac{1}{2} \sum_{\lambda,\beta} \left(\frac{\partial^2 \overleftrightarrow{\chi}}{\partial Q_\lambda \partial Q_\beta} \right)_{Q_{\lambda,\beta}=0} Q_\lambda Q_\beta + \ldots, \tag{4.2}$$

where $Q_{\lambda,\beta}$ represent normal coordinates of the lattice atomic displacements.

The second term in this expression corresponds to the first order Raman tensor $\overleftrightarrow{R}_\lambda \equiv \left(\frac{\partial \overleftrightarrow{\chi}}{\partial Q_\lambda} \right)_{Q_\lambda = 0}$. The scattering efficiency of non-polar phonons can be expressed through the well known relation [131]

$$I_\lambda = A \left(\hat{e}_i \cdot \overleftrightarrow{R}_\lambda \cdot \hat{e}_s \right)^2, \tag{4.3}$$

where $\hat{e_i}, \hat{e_s}$ are unit vectors in the direction of polarization of the incident and scattered photons, respectively, and A is a constant. The Raman tensors for all crystal symmetry classes are tabulated with corrected errors in Ref. [133]. The selection rules for Raman scattering,

which describe the polarization of the incident and scattered for which scattering events can occur, can be obtained from equation(4.3). Eq. (4.3) accurately describes scattering efficiency from non-polar phonons far from any resonances, but more detailed model, presented in §4.3, must be considered to treat polar phonons, polaritons and resonance phenomena.

4.1.2 The Porto notation

A commonly used method of expressing scattering configuration is the Porto notation [143], which specifies the directions of the incident and scattered wave vectors and polarizations for the normal crystal coordinates in a compact form. The notation is structured as $\hat{k}_i(\hat{e}_i\hat{e}_s)\hat{k}_s$, where $\hat{k}_{i,s}$ represent the incident and scattered propagation directions and $\hat{e}_{i,s}$ are their respective polarizations. The notation is further simplified by only defining these orientations for scattering geometries where both the incident and scattered photon propagation directions and polarizations are coincident with the crystal lattice axes $x, y,$ and z, with negative values being denoted as $\bar{x}, \bar{y},$ and $\bar{z}$.

As an example, for an incident photon propagating along the crystal's z axis and polarized along the y axis, scattering configurations in the Porto notation might be $\bar{z}(yy)z$ for co-polarized backscattering, $z(yx)z$, for cross-polarized near-forward scattering, or $z(yx)y$ for right-angle scattering, where the scattered photon propagates along the y axis.

4.1.3 Raman and infrared selection rules

Non-polar modes can be either acoustic, optically inactive or Raman active, but polar modes can also be active in infrared absorption (IR) through direct dipole interaction with the electromagnetic radiation. Raman active modes interact with light by affecting the polarizability tensor $\overleftrightarrow{\alpha}$ of the electronic states of the crystal via the electron-lattice interaction. The periodic variation of the polarizability of the crystal induced by the lattice vibration causes a small fraction of the incident light of frequency ω_i to be scattered at a frequency $\omega_s = \omega_i \pm \omega_{\text{ph}}$, with ω_{ph} being the phonon frequency.

In crystals possessing an inversion center, it can be shown that Raman activity and IR activity are mutually exclusive, as polar modes do not induce a variation of the crystal polarizability and vice-versa. However, in non-centrosymmetric crystals such as GaSe, some modes can be simultaneously Raman and IR active, which will be shown to be of critical importance for the Raman scattering observation of phonon-polaritons.

4.2 Symmetry and vibrational modes of GaSe

Vibrational crystal modes can be classified according to the point space group of the crystal lattice, and the respective irreducible representations of the atomic displacements involved in each vibrational mode. The 12 vibrational modes of the monolayer of GaSe, which has a D_{3h} point group and four atoms per unit cell, are represented schematically by the eight diagrams in 4.1, taking into account the double degeneracy of the four in-plane E modes.

In the bulk $\epsilon-$GaSe polytype, with D_{3h} symmetry, the unit cell spans two monolayers, and contains 8 atoms, for a total of 24 vibrational modes. Therefore, the normal modes bear the same symmetry representations as those of the monolayer, but each mode is now split into two Davydov doublets [47], where one mode has both layers oscillating in phase, with a replica being out of phase. Owing to the very weak interlayer interaction in GaSe [47, 145, 146], the Davydov doublets are nearly degenerate for the high-energy optical modes studied in this work. One thing to note is that the acoustic modes also gain Davydov replicas in the bulk material, which become optical vibrations owing to their out-of phase lattice displacements, but they lie at very low energies and have weak oscillator strengths and thus can be ignored in the context of this work. Table 4.2 lists the 12 optical normal modes of bulk $\epsilon-$GaSe (omitting the degenerate Davydov replicas), along with their reported energies and selection rules.

The Raman tensor components for each of the normal modes of $\epsilon-$GaSe are as follows [133]:

$$\overset{\leftrightarrow}{R}^{(1)}_{\mathrm{E}''} = \begin{pmatrix} 0 & 0 & 0 \\ 0 & 0 & c \\ 0 & c & 0 \end{pmatrix}, \qquad \overset{\leftrightarrow}{R}^{(2)}_{\mathrm{E}''} = \begin{pmatrix} 0 & 0 & -c \\ 0 & 0 & 0 \\ -c & 0 & 0 \end{pmatrix}, \qquad \overset{\leftrightarrow}{R}_{\mathrm{A}'_1} = \begin{pmatrix} a & 0 & 0 \\ 0 & a & 0 \\ 0 & 0 & b \end{pmatrix} \tag{4.4}$$

$$\overset{\leftrightarrow}{R}_{\mathrm{E}'_1}(x) = \begin{pmatrix} 0 & d & 0 \\ d & 0 & 0 \\ 0 & 0 & 0 \end{pmatrix}, \qquad \overset{\leftrightarrow}{R}_{\mathrm{E}'_1}(y) = \begin{pmatrix} d & 0 & 0 \\ 0 & -d & 0 \\ 0 & 0 & 0 \end{pmatrix}, \qquad \overset{\leftrightarrow}{R}_{\mathrm{A}''_2}(z) = 0, \tag{4.5}$$

where a, b, c and d are constants, and the Cartesian coordinate in parenthesis identifies the polarization direction for polar modes, which will become relevant in §4.3.

4.3 Raman scattering by polar phonons and polaritons

In contrast to pure mechanical phonons, Raman scattering from polaritons exhibits a richer structure, as the electromagnetic component of the wave is highly dispersive in the region where $k \sim \frac{\omega}{c}$.

$E'(1)$	$A_2''(1)$	$E''(1)$	$A_1'(1)$	$E''(2)$	$E'(2)$	$A_2''(2)$	$A_1'(2)$
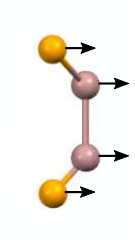	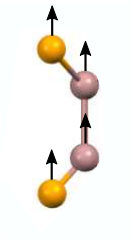	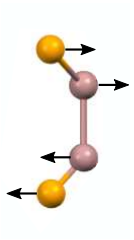	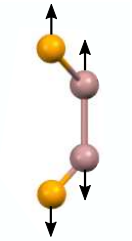	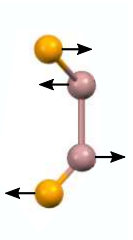	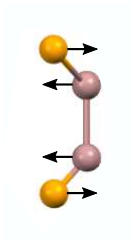	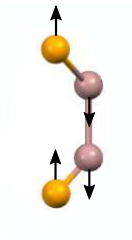	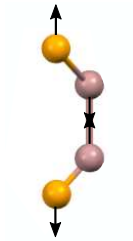
(Acoustic)	(Acoustic)	Raman	Raman	Raman	Raman Infrared	Infrared	Raman
-	-	$\bar{x}(yz)x$ $\bar{y}(xz)y$	$\bar{x}(yy)x$ $\bar{x}(zz)x$ $\bar{y}(xx)y$ $\bar{y}(zz)y$ $\bar{z}(xx)z$ $\bar{z}(yy)z$	$\bar{x}(yz)x$ $\bar{y}(xz)y$	$\bar{x}(yy)x$ [LO] $\bar{y}(xx)y$ [TO] $\bar{z}(xx)z$ [TO] $\bar{z}(xy)z$ [TO] $\bar{z}(yy)z$ [TO]	-	$\bar{x}(yy)x$ $\bar{x}(zz)x$ $\bar{y}(xx)y$ $\bar{y}(zz)y$ $\bar{z}(xx)z$ $\bar{z}(yy)z$

Table 4.1 Normal vibrational modes of the GaSe monolayer. For each normal mode, from top to bottom are the Mulliken symbols [144], schematic atomic displacements within the unit cell, mode activity, and Raman selection rules.

$E'(1^2)$	$A_2''(1^2)$	$E''(1^{1,2})$	$A_1'(1^{1,2})$	$E''(2^{1,2})$	$E'(2^{1,2})$	$A_2''(2^{1,2})$	$A_1'(2^{1,2})$
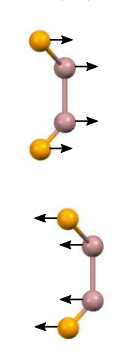	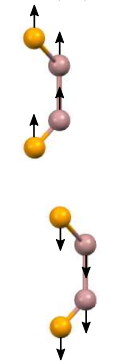	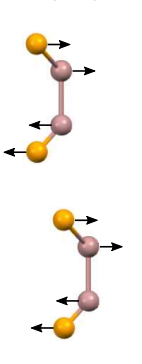	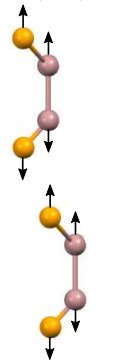	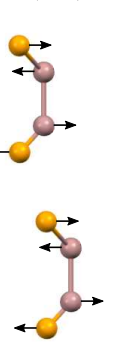	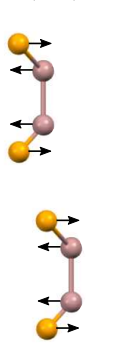	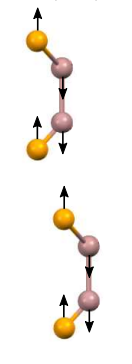	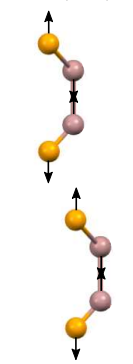
$19.0\,\mathrm{cm}^{-1}$	$36.7\,\mathrm{cm}^{-1}$	$60\,\mathrm{cm}^{-1}$	$134\,\mathrm{cm}^{-1}$	$209\,\mathrm{cm}^{-1}$	TO:$213\,\mathrm{cm}^{-1}$ LO:$254\,\mathrm{cm}^{-1}$	TO:$236\,\mathrm{cm}^{-1}$ LO:$244.5\,\mathrm{cm}^{-1}$	$308\,\mathrm{cm}^{-1}$
Raman Infrared	Infrared	Raman	Raman	Raman	Raman Infrared	Infrared	Raman
-	-	$\bar{x}(yz)x$ $\bar{y}(xz)y$	$\bar{x}(yy)x$ $\bar{x}(zz)x$ $\bar{y}(xx)y$ $\bar{y}(zz)y$ $\bar{z}(xx)z$ $\bar{z}(yy)z$	$\bar{x}(yz)x$ $\bar{y}(xz)y$	$\bar{x}(yy)x$ [LO] $\bar{y}(xx)y$ [TO] $\bar{z}(xx)z$ [TO] $\bar{z}(xy)z$ [TO] $\bar{z}(yy)z$ [TO]	-	$\bar{x}(yy)x$ $\bar{x}(zz)x$ $\bar{y}(xx)y$ $\bar{y}(zz)y$ $\bar{z}(xx)z$ $\bar{z}(yy)z$

Table 4.2 Normal vibrational modes of bulk ϵ-GaSe. For each normal mode, from top to bottom are the Mulliken symbols [144], schematic atomic displacements within the unit cell, mode activity, and Raman selection rules. Frequency values and mode assignments from Ref. [18]. Davydov replicas (with the bottom layer in opposite phase to the one pictured) are omitted for simplicity.

A general approach to model the polariton Raman scattering response is presented by Irmer [26], based on the Born-Huang model of phonon-polaritons [82]. The separate contributions of the atomic displacement and electric field are projected onto the normal lattice modes to obtain a complete description of the effective Raman tensor which considers both the mechanical phonon Raman tensors as well as an additional term from the electro-optic contribution to the polarizability, which is proportional to the electric field. In this section, the derivation of the Raman scattering intensity as a function of the polariton electric field is presented, based on the works of Loudon [131], Claus, Merten and Brandmuller [133], Mills and Burstein [25], and inspired largely by the approach presented by Irmer *et al.* [26].

4.3.1 Raman selection rules of polaritons

Owing to their accompanying electric fields and reduced symmetry compared to the crystal lattice, phonon-polaritons may exhibit different Raman selection rules than pure mechanical phonons. In this section, the Raman selection rules for oblique-propagating polaritons are determined as a function of the wave vector orientation.

As was presented in §4.1, the susceptibility of a material can be affected by atomic displacements, but it also depends on the macroscopic electric field in the material. In the case of polar phonons or polaritons, the susceptibility can be expressed as a power series of the macroscopic electric field $\boldsymbol{E}$ accompanying the lattice displacements

$$\overleftrightarrow{\chi} = \overleftrightarrow{\chi}_0 + \sum_\lambda \left(\frac{\partial \overleftrightarrow{\chi}}{\partial E_\lambda}\right)_{E_\lambda=0} E_\lambda + \frac{1}{2}\sum_{\lambda,\beta}\left(\frac{\partial^2 \overleftrightarrow{\chi}}{\partial E_\lambda \partial E_\beta}\right)_{E_{\lambda,\beta}=0} E_\lambda E_\beta + \ldots \tag{4.6}$$

$$\overleftrightarrow{\chi} = \overleftrightarrow{\chi}^{(1)} + 2\sum_\lambda \overleftrightarrow{\chi}^{(2)}_\lambda E_\lambda + 3\sum_{\lambda,\beta} \overleftrightarrow{\chi}^{(3)}_{\lambda\beta} E_\lambda E_\beta + \ldots, \tag{4.7}$$

where $\overleftrightarrow{\chi}^{(1)}$, $\overleftrightarrow{\chi}^{(2)}$ and $\overleftrightarrow{\chi}^{(3)}$ are the linear, second- and third-order susceptibility tensors of the material as defined in nonlinear optics (with implicit summation over repeated indices) [147]:

$$\boldsymbol{P} = \boldsymbol{P}_0 + \epsilon_0 \sum_\lambda \left[\overleftrightarrow{\chi}^{(1)}_{\lambda,i} E_i(\omega_1) + \overleftrightarrow{\chi}^{(2)}_{\lambda,ij} E_i(\omega_1) E_j(\omega_2) + \overleftrightarrow{\chi}^{(3)}_{\lambda,ijk} E_i(\omega_1) E_j(\omega_2) E_k(\omega_3) + \ldots\right], \tag{4.8}$$

where explicit frequency dependencies $\overleftrightarrow{\chi}^{(1)}(\omega_s)$, $\overleftrightarrow{\chi}^{(2)}(\omega_s;\omega_1,\omega_2)$, and $\overleftrightarrow{\chi}^{(3)}(\omega_s;\omega_1,\omega_2,\omega_3)$ have been omitted for brevity. The frequency ω_s in the expression for $\overleftrightarrow{\chi}^{(2)}$ corresponds to the Stokes Raman scattered photon frequency, $\omega_1 = \omega_i$ is the incident laser frequency, $\omega_2 = -\omega$ the polariton frequency and $\omega_3 = \omega_a$ is the anti-Stokes Raman scattered frequency. This expression highlights the fact that Raman scattering can be interpreted as a third-order difference frequency generation, wherein the third driving optical field $E_j(\omega_2)$ comes from

the thermal excitations in the crystal rather than from an external source.

Polariton branches do not exhibit the same symmetries as the crystal lattice as they propagate obliquely in the crystal. In order to express the resulting first-order effect of the polariton on the susceptibility of the material, the polariton normal coordinates $\{To, Te, Le\}$ can be projected onto lattice coordinates $\{x, y, z\}$.

With the polariton wave vector orientation in the lattice coordinates defined as

$$\boldsymbol{k} = k\left(\sin\theta\cos\phi, \sin\theta\sin\phi, \cos\theta\right), \tag{4.9}$$

the polariton normal coordinates are defined so that $\hat{To} \perp (\hat{z}, \boldsymbol{k})$, $\hat{Te} \perp (\hat{To}, \boldsymbol{k})$ and $\hat{Le} /\!\!/ \boldsymbol{k}$. The projection matrix,

$$W = \begin{pmatrix} \hat{To}\cdot\hat{x} & \hat{To}\cdot\hat{y} & \hat{To}\cdot\hat{z} \\ \hat{Te}\cdot\hat{x} & \hat{Te}\cdot\hat{y} & \hat{Te}\cdot\hat{z} \\ \hat{Le}\cdot\hat{x} & \hat{Le}\cdot\hat{y} & \hat{Le}\cdot\hat{z} \end{pmatrix} = \begin{pmatrix} -\sin\phi & \cos\phi & 0 \\ -\cos\theta\cos\phi & -\cos\theta\sin\phi & \sin\theta \\ \sin\theta\cos\phi & \sin\theta\sin\phi & \cos\theta \end{pmatrix}, \tag{4.10}$$

can then be used to project polariton coordinates onto the lattice coordinates so that

$$\begin{pmatrix} \overleftrightarrow{R}_{To} \\ \overleftrightarrow{R}_{Te} \\ \overleftrightarrow{R}_{Le} \end{pmatrix} = W \begin{pmatrix} \overleftrightarrow{R}_{x} \\ \overleftrightarrow{R}_{y} \\ \overleftrightarrow{R}_{z} \end{pmatrix} \qquad \text{and} \qquad \begin{pmatrix} \overleftrightarrow{\chi}^{(2)}_{To} \\ \overleftrightarrow{\chi}^{(2)}_{Te} \\ \overleftrightarrow{\chi}^{(2)}_{Le} \end{pmatrix} = W \begin{pmatrix} \overleftrightarrow{\chi}^{(2)}_{x} \\ \overleftrightarrow{\chi}^{(2)}_{y} \\ \overleftrightarrow{\chi}^{(2)}_{z} \end{pmatrix}. \tag{4.11}$$

The total first-order effect of the polariton on the material susceptibility can then be written as

$$\delta\overleftrightarrow{\chi}_N = \overleftrightarrow{R}_N Q_N + 2\overleftrightarrow{\chi}^{(2)}_N E_N, \tag{4.12}$$

with N indicating the polariton normal coordinates $\{To, Te, Le\}$, and Q_N and E_N the polariton displacements and electric fields.

These electric fields are directly linked to the lattice displacements by the Born-Huang lattice equation of motion [26, 82]

$$-\omega^2 Q_\perp = B^{11}_\perp Q_\perp + B^{12}_\perp E_\perp \tag{4.13}$$

$$-\omega^2 Q_{/\!/} = B^{11}_{/\!/} Q_{/\!/} + B^{12}_{/\!/} E_{/\!/}, \tag{4.14}$$

where $\perp$ and $/\!/$ indicate the in-plane and out-of-plane components of the displacement and

electric fields. The coefficients $B^{11}_{\perp,/\!/}$ and $B^{12}_{\perp,/\!/}$ can be expressed as functions of the static and high frequency permittivities and transverse frequency of the normal modes, yielding [148]

$$E_{\perp,/\!/} = \frac{\omega^2_{\mathrm{TO};\perp,/\!/} - \omega^2}{\omega_{\mathrm{TO};\perp,/\!/}\sqrt{\epsilon_0(\epsilon_{s;\perp,/\!/} - \epsilon_{\infty;\perp,/\!/})}} Q_{\perp,/\!/} = \frac{1}{K_{\perp,/\!/}} Q_{\perp,/\!/}, \tag{4.15}$$

defining $K_{\perp,/\!/} \equiv Q_{\perp,/\!/}/E_{\perp,/\!/}$. This relation establishes a direct proportionality the electric and atomic displacement fields, and the variation of the polarizability can then be expressed as a function of the atomic displacements

$$\delta\overleftrightarrow{\chi}_N = \left(\overleftrightarrow{R}_N + \frac{2}{K_N}\overleftrightarrow{\chi}^{(2)}_N\right) Q_N, \tag{4.16}$$

or conversely, as a function of the electric field

$$\delta\overleftrightarrow{\chi}_N = \left(K_N\overleftrightarrow{R}_N + 2\overleftrightarrow{\chi}^{(2)}_N\right) E_N, \tag{4.17}$$

with $K_{To,Te} = K_\perp$ and $K_{Le} = K_{/\!/}$. Note here that K_N diverges for $\omega = \omega_{\mathrm{TO}}$, as the electric field vanishes at the transverse frequency.

The Raman tensors for normal lattice modes GaSe, given in §4.1 can then be projected onto the polariton coordinates to obtain the expressions for $\overleftrightarrow{R}_N$. E'_1 is the only Raman-allowed polar mode, therefore the Raman tensors in the polariton basis are given by

$$\overleftrightarrow{R}_{To} = \left(W\overleftrightarrow{R}^{E'_1}\right)_{To} = d\begin{pmatrix} \cos\phi & -\sin\phi & 0 \\ -\sin\phi & -\cos\phi & 0 \\ 0 & 0 & 0 \end{pmatrix}, \tag{4.18}$$

$$\overleftrightarrow{R}_{Te} = \left(W\overleftrightarrow{R}^{E'_1}\right)_{Te} = d\cos\theta\begin{pmatrix} -\sin\phi & -\cos\phi & 0 \\ -\cos\phi & \sin\phi & 0 \\ 0 & 0 & 0 \end{pmatrix}, \tag{4.19}$$

$$\overleftrightarrow{R}_{Le} = \left(W\overleftrightarrow{R}^{E'_1}\right)_{Le} = d\sin\theta\begin{pmatrix} \sin\phi & \cos\phi & 0 \\ \cos\phi & -\sin\phi & 0 \\ 0 & 0 & 0 \end{pmatrix}. \tag{4.20}$$

The electro-optic tensor elements $\chi^{(2)}_{\lambda ij}$ used here can be obtained directly from the second harmonic generation tensor $d_{\lambda,ij}$ as $\chi^{(2)}_{\lambda ij} = 2d_{\lambda,ij}$ [149]. Note here that this electro-optic tensor differs from the one often used when describing the Pockels effect, which is defined as $r_{\lambda,ij} = 2\chi^{(2)}_{\lambda ij}/n^4_\lambda$, where n_λ is the refractive index at wavelength λ [150].

The noncentrosymmetric D_{3h} crystal structure second order susceptibility tensor is, in the contracted Kleinmann notation [151]:

$$\overleftrightarrow{d}_{\mathrm{D_{3h}}} = \begin{pmatrix} 0 & 0 & 0 & 0 & 0 & -d_{22} \\ -d_{22} & d_{22} & 0 & 0 & 0 & 0 \\ 0 & 0 & 0 & 0 & 0 & 0 \end{pmatrix}, \tag{4.21}$$

from which the tensor components for every polarization direction can be obtained (note that they have the same form as the Raman tensor elements) :

$$\overleftrightarrow{d}_{\mathrm{D_{3h}}x} = \begin{pmatrix} 0 & -d_{22} & 0 \\ -d_{22} & 0 & 0 \\ 0 & 0 & 0 \end{pmatrix}, \qquad \overleftrightarrow{d}_{\mathrm{D_{3h}}y} = \begin{pmatrix} -d_{22} & 0 & 0 \\ 0 & d_{22} & 0 \\ 0 & 0 & 0 \end{pmatrix}, \qquad \overleftrightarrow{d}_{\mathrm{D_{3h}}z} = 0. \tag{4.22}$$

Projecting these tensors onto the normal polariton modes and multiplying by 4 yields the corresponding electro-optic tensor elements

$$\overleftrightarrow{\chi}^{(2)}_{To} = 2\left(W\overleftrightarrow{d}_{\mathrm{D_{3h}}}\right)_{To} = 2d_{22}\begin{pmatrix} \cos\phi & -\sin\phi & 0 \\ -\sin\phi & -\cos\phi & 0 \\ 0 & 0 & 0 \end{pmatrix}, \tag{4.23}$$

$$\overleftrightarrow{\chi}^{(2)}_{Te} = 2\left(W\overleftrightarrow{d}_{\mathrm{D_{3h}}}\right)_{Te} = 2d_{22}\cos\theta\begin{pmatrix} \sin\phi & -\cos\phi & 0 \\ -\cos\phi & \sin\phi & 0 \\ 0 & 0 & 0 \end{pmatrix}, \tag{4.24}$$

$$\overleftrightarrow{\chi}^{(2)}_{Le} = 2\left(W\overleftrightarrow{d}_{\mathrm{D_{3h}}}\right)_{Le} = 2d_{22}\sin\theta\begin{pmatrix} \sin\phi & \cos\phi & 0 \\ \cos\phi & -\sin\phi & 0 \\ 0 & 0 & 0 \end{pmatrix}. \tag{4.25}$$

The Raman scattering intensity, expressed at the beginning of this section as

$$I_\lambda = A\left(\hat{e_i}\cdot\overleftrightarrow{R}_\lambda\cdot\hat{e_s}\right)^2, \tag{4.26}$$

can now be modified to include the electro-optic contribution

$$I_\lambda = A\left(\hat{e_i}\cdot\left[\overleftrightarrow{R}_\lambda + \frac{2}{K_\lambda}\overleftrightarrow{\chi}^{(2)}_\lambda\right]\cdot\hat{e_s}\right)^2, \tag{4.27}$$

and expressed in the normal coordinates of the polariton modes

$$I_N = A\left(\hat{e_i}\cdot\left[\overleftrightarrow{R}_N + \frac{2}{K_N}\overleftrightarrow{\chi}^{(2)}_N\right]\cdot\hat{e_s}\right)^2. \tag{4.28}$$

Equation (4.28) can be used to determine the polarization selection rules for bulk polaritons, which turn out to be the same as those for mechanical oblique phonons, since the tensors $\overleftrightarrow{R}$ and $\overleftrightarrow{\chi}^{(2)}$ have the same symmetries. However, the relative importance of the contributions of the mechanical and electromagnetic components of the polariton to the scattering efficiency are of particular interest.

4.3.2 Scattering efficiency of polaritons : the Faust-Henry and Hopfield coefficients

In this section, the relative contributions of the mechanical and electromagnetic components of the polaritons to their scattering efficiencies is expressed as a function of the Faust-Henry and Hopfield coefficients of the material.

The ratio $\overleftrightarrow{R}_{\lambda,ij}/\overleftrightarrow{\chi}^{(2)}_{\lambda,ij}$ is proportional to the Faust-Henry coefficients $\overleftrightarrow{C}^{\mathrm{FH}}_{\lambda,ij}$ [152],

$$\frac{R_{\lambda,ij}}{\chi^{(2)}_{\lambda,ij}} = C^{\mathrm{FH}}_{\lambda,ij}\frac{2\omega_{\mathrm{TO}\lambda}}{\sqrt{\epsilon_0(\epsilon_{s\lambda}-\epsilon_{\infty\lambda})}}, \tag{4.29}$$

the value of which can be determined by evaluating the relative Raman scattering intensities of the pure phonon ($k \gg \frac{\omega}{c}$) LO and TO modes. This can be understood by considering that equation (4.28) also applies to pure phonon modes, and since LO modes exhibit a macroscopic electric field, their Raman scattering efficiency includes an additional electro-optic contribution that the TO modes lack. This effect has in fact been demonstrated as a means to precisely determine the electro-optic and second harmonic coefficients of non-centrosymmetric materials from Raman measurements [149].

As mentioned earlier, the Faust-Henry coefficient can be expressed as a function of the ratio of scattering intensities $\frac{I_{\mathrm{LO}\lambda}}{I_{\mathrm{TO}\lambda}}$. In order to derive this relation, a more complete expression of the Raman scattering efficiency must be used. Mills and Burstein [25] define the Stokes Raman scattering intensity by unit solid angle as (assuming that the incident and scattered photons have energies lower than the electronic bandgap)

$$\frac{\mathrm{d}I_N}{\mathrm{d}\Omega} = \left(\frac{\omega_s}{c}\right)^4 VL\left|\left\langle 1+n_\omega\left|\hat{e_i}\cdot\delta\overleftrightarrow{\chi}_N\cdot\hat{e_i}\right|n_\omega\right\rangle\right|^2, \tag{4.30}$$

where $\omega_{i,s}$ are the incident and scattered photon frequencies, ω is the scattering phonon

frequency, c is the speed of light in vacuum, V is the scattering volume, L the scattering length, and n_ω is the polariton occupation number, or, in the following treatment, the Bose-Einstein factor.

This expression was originally derived in a very similar form by Loudon [153], modeling Raman scattering as a three step perturbative process, where the scattering probability W of an incident photon with frequency ω_i and wave vector $\boldsymbol{q}_i$ is proportional to

$$W \propto \sum_{\boldsymbol{k},\boldsymbol{q}_s} \sum_{a,b} \left| \frac{\langle n_1 - 1, n_2 + 1; 1 + n_\omega; 0 \left| H_{ER} \right| a \rangle \langle a \left| H_{EL} \right| b \rangle \langle b \left| H_{ER} \right| n_1, n_2; n_\omega; 0 \rangle}{(\omega_a - \omega_i)(\omega_b - \omega_i)} \right|^2 \times \delta(\omega_i - \omega - \omega_0), \quad (4.31)$$

where $n_{1,2}$ are the incident and scattered photon populations, n_ω the polariton population before the scattering event, and the 0 in the initial and final states represents the electronic ground state. In this expression, the three matrix elements represent each of the interaction steps, that is, from right to left,

1. Absorption of a photon of frequency ω_i by the electronic transition from the ground state $|0\rangle$ to a virtual excited state $|b\rangle$ via the electron-radiation interaction Hamiltonian H_{ER}.

2. Transition of the virtual electronic state $|b\rangle$ into a new virtual state $|a\rangle$ by the emission of a polariton described by the electron-lattice interaction Hamiltonian $H_{EL} = H_{EL}^M + H_{EL}^e$, where H_{EL}^M represents the lattice mechanical deformation potential and H_{EL}^e is the additional electron-lattice electro-optic or Fröhlich interaction for modes with a net macroscopic electric field.

3. Emission of a photon of frequency ω_s by the electronic transition from the virtual state $|a\rangle$ back to the ground state via the electron-radiation interaction Hamiltonian H_{ER}.

The summation (or integration) over all intermediate virtual states $|a\rangle$ and $|b\rangle$ and over all phonon wave vectors k and scattered wave vectors q_s within the collection solid angle $\mathrm{d}\Omega$ yields the matrix element in (4.30) along with a momentum conservation term $\delta(\boldsymbol{q}_i - \boldsymbol{k} - \boldsymbol{q}_i)$, which will be discussed in more detail later. The electron-lattice interaction terms stemming from the mechanical deformation potential and electro-optic interaction contribute to the resulting susceptibility modulation $\delta\overleftrightarrow{\chi}$.

This expression can be split into a polarization selection rule term and a transition matrix element, as both contributions to the electron-lattice interaction are modeled as linear in

Q_N and E_N (see equations (4.16) and (4.17)). Using these relations, equation (4.30) can be expressed as

$$I_N(\omega) = \left(\frac{\omega_s}{c}\right)^4 VL \left|\hat{e}_i \cdot \left(\overleftrightarrow{R}_N + \frac{2}{K_N}\overleftrightarrow{\chi}_N^{(2)}\right) \cdot \hat{e}_s\right|^2 |\langle 1 + n_\omega | Q_N | n_\omega \rangle|^2 \tag{4.32}$$

or

$$I_N(\omega) = \left(\frac{\omega_s}{c}\right)^4 VL \left|\hat{e}_i \cdot \left(K_N \overleftrightarrow{R}_N + 2\overleftrightarrow{\chi}_N^{(2)}\right) \cdot \hat{e}_s\right|^2 |\langle 1 + n_\omega | E_N | n_\omega \rangle|^2 . \tag{4.33}$$

The first squared term in these expressions corresponds to the first-order effect of the polariton mechanical and electromagnetic components on the material's susceptibility, and defines the polarization selection rules for a given mode N. The second term is a transition matrix element of the displacement or electric field operators

The matrix elements $|\langle 1 + n_\omega | Q_N | n_\omega \rangle|^2$ for the uniaxial crystal are given by Mills and Burstein [25] as

$$|\langle 1 + n_\omega | Q_\lambda | n_\omega \rangle|^2 = \left(\frac{\hbar(1 + n_\omega)}{2V}\right) \frac{h^p(\omega)}{\omega_{\mathrm{TO}}}, \tag{4.34}$$

where the Bose-Einstein occupation factor is evaluated as

$$n_\omega = \frac{1}{e^{\frac{\hbar\omega}{k_B T}} - 1}, \tag{4.35}$$

and $h^p(\omega)$ is the coefficient defined by Hopfield [83] that characterizes the proportion of the polariton's energy stored in the mechanical lattice vibrations

$$h^p(\omega) = \frac{\omega\omega_{\mathrm{TO}}(\omega_{\mathrm{LO}}^2 - \omega_{\mathrm{TO}}^2)}{(\omega_{\mathrm{TO}}^2 - \omega^2)^2 + \omega_{\mathrm{TO}}^2(\omega_{\mathrm{LO}}^2 - \omega_{\mathrm{TO}}^2)}. \tag{4.36}$$

Similarly for the electric field expression,

$$|\langle 1 + n_\omega | E_\lambda | n_\omega \rangle|^2 = \left(\frac{\hbar\omega(1 + n_\omega)}{2\epsilon_0 V}\right) \frac{h^E(\omega)}{\epsilon_\infty}, \tag{4.37}$$

introducing the Hopfield coefficient $h^E(\omega)$ representing the fraction of the energy of the wave stored in the electromagnetic field

$$h^E(\omega) = \left(1 + \frac{\omega_{\mathrm{TO}^2}(\omega_{\mathrm{LO}}^2 - \omega_{\mathrm{TO}}^2)}{(\omega_{\mathrm{TO}}^2 - \omega^2)^2}\right)^{-1}. \tag{4.38}$$

In uniaxial crystals, the matrix elements and Hopfield coefficients for the electric field have been derived in Ref. [26] :

$$|\langle 1+n_\omega|E_{To}|n_\omega\rangle|^2 = \left(\frac{\hbar\omega(1+n_\omega)}{2\epsilon_0 V}\right)\frac{h^E_\perp}{\epsilon_{\infty\perp}}, \tag{4.39}$$

$$|\langle 1+n_\omega|E_{Te}|n_\omega\rangle|^2 = \left(\frac{\hbar\omega(1+n_\omega)}{2\epsilon_0 V}\right)\left(\frac{h^E_\perp\cos^2\theta}{\epsilon_{\infty\perp}}+\frac{h^E_{/\!/}\sin^2\theta}{\epsilon_{\infty/\!/}}\right), \tag{4.40}$$

$$|\langle 1+n_\omega|E_{Le}|n_\omega\rangle|^2 = \left(\frac{\hbar\omega(1+n_\omega)}{2\epsilon_0 V}\right)\left(\frac{h^E_\perp\sin^2\theta}{\epsilon_{\infty\perp}}+\frac{h^E_{/\!/}\cos^2\theta}{\epsilon_{\infty/\!/}}\right), \tag{4.41}$$

$$h^E_\perp = \left(1+\frac{\omega^2_{\mathrm{TO}\perp}(\omega^2_{\mathrm{LO}\perp}-\omega^2_{\mathrm{TO}\perp})}{(\omega^2_{\mathrm{TO}\perp}-\omega^2)^2}\right)^{-1}, \tag{4.42}$$

$$h^E_{/\!/} = \left(1+\frac{\omega^2_{\mathrm{TO}/\!/}(\omega^2_{\mathrm{LO}/\!/}-\omega^2_{\mathrm{TO}/\!/})}{(\omega^2_{\mathrm{TO}/\!/}-\omega^2)^2}\right)^{-1}. \tag{4.43}$$

The scattering efficiency can then be written as

$$I_N(\omega) = \left(\frac{\omega_s}{c}\right)^4\left(\frac{\hbar\omega(1+n_\omega)L}{2\epsilon_0}\right)\left|\hat{e}_i\cdot\left(K_N\overleftrightarrow{R}_N+2\overleftrightarrow{\chi}^{(2)}_N\right)\cdot\hat{e}_s\right|^2 H^E_N(\omega,\theta), \tag{4.44}$$

where $H^E_N(\omega,\theta)$ represents the appropriate version of the last term of equations (4.39)-(4.41). A similar process can be used to obtain the expression

$$I_N(\omega) = \left(\frac{\omega_s}{c}\right)^4\left(\frac{\hbar(1+n_\omega)L}{2}\right)\left|\hat{e}_i\cdot\left(\overleftrightarrow{R}_N+\frac{2}{K_N}\overleftrightarrow{\chi}^{(2)}_N\right)\cdot\hat{e}_s\right|^2 H^p_N(\omega,\theta), \tag{4.45}$$

Finally, the ratio of the pure phonon LO and TO modes can be expressed (in the cartesian lattice coordinates λ) as

$$\frac{I^{ij}_{LO,\lambda}}{I^{ij}_{TO,\lambda}} = \frac{\omega_{\mathrm{TO},\lambda}(n_{\omega\mathrm{LO},\lambda}+1)}{\omega_{\mathrm{LO},\lambda}(n_{\omega\mathrm{TO},\lambda}+1)}\left|1+\frac{2}{K_N}\frac{\overleftrightarrow{\chi}^{(2)}_{\lambda,ij}}{\overleftrightarrow{R}_{\lambda,ij}}\right|^2 \tag{4.46}$$

$$= \frac{\omega_{\mathrm{TO},\lambda}(n_{\omega\mathrm{LO},\lambda}+1)}{\omega_{\mathrm{LO},\lambda}(n_{\omega\mathrm{TO},\lambda}+1)}\left|1+\frac{\omega^2_{\mathrm{TO},\lambda}-\omega^2_{\mathrm{LO},\lambda}}{C^{\mathrm{FH}}_{\lambda,ij}\omega^2_{\mathrm{TO},\lambda}}\right|^2 \tag{4.47}$$

where $I^{i,j}_{\mathrm{TO;LO},\lambda}$ represent the Raman scattering intensities for the λ polarized mode with i,j incident and scattered field polarizations.

4.3.3 Resonant Raman scattering

The model of Raman scattering proposed by Loudon (see Eq. (4.31)) and developed in the previous sections considers all intermediate electron-hole states that can interact with the lattice and light. If the energy of the incident or scattered photon approaches the energy of an electronic transition in the material, the sum is determined by only one or a few terms and the resulting Raman tensor contains divergent terms which can result in an increase in scattering efficiency.

Resonant Raman, where either the incoming or outgoing photon is in resonance with an interband transition affects the scattering intensity in two ways :

(1) The second-order perturbation defined for non-resonant Raman is enhanced, and this efficiency increase is linked to the electron-photon interaction terms in Eq. (4.31). The intensity gain due to this effect is correlated to the absorption coefficient and/or photoluminescence lifetime, as it also relates directly to the electronic dipole strength governing the light-matter interaction.

(2) The intermediate state that is involved in the electron-lattice interaction is now a real electronic state, which can enable additional scattering mechanisms in the electron-lattice Hamiltonian.

Martin [154] presented a model of Raman scattering considering the intermediate states as excitons rather than electron-hole pairs, which is necessary to accurately model the electron-lattice interaction near excitonic resonances [155]. Their model predicts a significant increase of the effective Raman tensor $(K_N \overset{\leftrightarrow}{R}_N + 2\overset{\leftrightarrow}{\chi}^{(2)}_N)$ proportional to $(\hbar\omega_i - E_g)^{-1}$ when $\hbar\omega_i \to E_g$, the material's bandgap, as expected from point (1) mentioned above. Furthermore, for $\hbar\omega_i \sim E_g - E_1$ (where E_1 is the exciton binding energy), Martin predicts that an additional 'forbidden' $\boldsymbol{k}$-dependent intraband Frölich interaction becomes significant, and can become the dominant scattering mechanism for near-resonant scattering, with a cross-section scaling as $(\hbar\omega_i - E_g - E_1)^{-3}$ [156].

The Hamiltonian describing the Fröhlich exciton-lattice interaction can be expressed as a combination of the Fröhlich interaction of an electron and a hole [155, 157, 158]

$$H^F = \frac{C_F}{k}\left(\frac{1}{(1+[p_h a_0 k/2]^2)^2} - \frac{1}{(1+[p_e a_0 k/2]^2)^2}\right), \tag{4.48}$$

where

$$C_F = e\sqrt{\frac{2\pi\hbar\omega_{LO}}{NV}(\epsilon_\infty{}^{-1} - \epsilon_s^{-1})} \quad , \quad p_e = \frac{m_e}{m_e + m_h} \quad \text{and} \quad p_h = \frac{m_h}{m_e + m_h}. \tag{4.49}$$

In the above expressions, a_0 is the exciton Bohr radius, e the electron charge, and $m_{e,h}$ the electron and hole effective masses at the direct exciton point, and C_F can be treated as a constant. For small values of k relative to the Brillouin zone size, this expression can be simplified to

$$H^F \simeq C_F k a_0^2 \frac{m_e - m_h}{m_e + m_h}. \tag{4.50}$$

The matrix element $\left\langle a|H^F|b\right\rangle$ only takes on nonzero values for intraband transitions of excitonic states [155, 157] and so only two resonant terms (incoming and outgoing) contribute to the 'forbidden' k-dependent Fröhlich Raman tensor

$$\overleftrightarrow{R^F}_\lambda \propto \left|\left\langle a|H^F|b\right\rangle\right| = C_F(ka_0)\begin{pmatrix}1&0&0\\0&1&0\\0&0&1\end{pmatrix} = \begin{pmatrix}a^F&0&0\\0&a^F&0\\0&0&a^F\end{pmatrix}, \tag{4.51}$$

which is diagonal in the lattice normal coordinates for all polar modes [156]. The total Raman scattering efficiency for the polariton modes near resonance now becomes

$$I_N(\omega, \boldsymbol{q}) \propto \left|\hat{e}_i \cdot \left(K_N \overleftrightarrow{R}_N + \overleftrightarrow{\chi}^{(2)}_N + \overleftrightarrow{R^F}_N\right) \cdot \hat{e}_s\right|^2 H^E_N(\omega, \theta). \tag{4.52}$$

Using the transformation matrix W defined in section 4.3 for a polariton wave vector $\boldsymbol{k} = k(\sin\theta\cos\phi, \sin\theta\sin\phi, \cos\theta)$,

$$\overleftrightarrow{R^F}_{To} = (\cos\phi - \sin\phi)\begin{pmatrix}a^F&0&0\\0&a^F&0\\0&0&a^F\end{pmatrix} \tag{4.53}$$

$$\overleftrightarrow{R^F}_{Te} = \sin\theta - \cos\theta(\cos\phi + \sin\phi)\begin{pmatrix}a^F&0&0\\0&a^F&0\\0&0&a^F\end{pmatrix} \tag{4.54}$$

$$\overleftrightarrow{R^F}_{Le} = \cos\theta + \sin\theta(\cos\phi + \sin\phi)\begin{pmatrix}a^F&0&0\\0&a^F&0\\0&0&a^F\end{pmatrix} \tag{4.55}$$

Hoff and Irwin [18, 140] observed resonant enhancement of both the E(LO) and A2"(LO) modes of GaSe, demonstrating the polarization selection rule breakdown predicted by Martin, both for Raman-allowed and Raman-forbidden modes due to the $\boldsymbol{k}$-dependent Fröhlich interaction. They also observed a significant antiresonance of the nonpolar A modes below the resonant energy, which is not directly explained by Martin's model, but might be understood by considering interference effects between various scattering processes [159].

Recent reports of the Fröhlich interaction-mediated Raman efficiency enhancement near resonance in semiconductor nanostructures [160, 161] and 2D transition metal dichalcogenides MoS_2 [162] and WS_2 [163] highlight the importance of the Fröhlich interaction in the two-dimensional limit [164, 165].

This additional term is the dominant contribution to Raman scattering efficiency near excitonic resonances, and explains the redefined selection rules observed around resonance. Its effects will be discussed in more detail in the context of the resonant Raman scattering results presented in chapter 8.

4.3.4 Raman scattering from thin films

The expressions derived in the previous sections assume a sample size that is large compared to the scattering volume, and therefore only describe scattering from polaritons inside a bulk (infinite) crystal.

When considering scattering from finite-size samples, several key differences must be considered. Not only can the scattering volume be limited by the sample size, but the sample surfaces add additional boundary conditions to the system. The confined polariton eigenstates inside the crystal are modified by this boundary, and additional surface states can exist under certain conditions.

The expression of scattering efficiency and momentum conservation in the case of confined polaritons requires a more detailed analysis which is based on the same principles as those presented so far in this chapter, but treatment of the spatial boundary condition rapidly becomes very complex and cumbersome. The derivation is not carried out in this work, but a brief overview of the approach, along with the principal results reported in the literature are presented.

Mills, Chen, and Burstein [166] developed a model of Raman scattering by surface polaritons in thin films wherein the incident and scattered light are described in terms of the electromagnetic Green's functions with the film boundary conditions. The scattering efficiency is then expressed as a function of the polariton's electric field distribution in the film, using

similar arguments as those presented in §4.3.1. Now, the Green's functions that are used to describe the scattered light also describe the polariton electric field, as they are also normal modes of the dielectric film, albeit at vastly different frequencies. The resulting scattering efficiency is then expressed as a function of the spectral density of the electric field in the film.

Subbaswamy and Mills [123] revisited the results of Mills, Chen, and Burstein and, along with correcting a few critical errors, show that the general expression of the scattering efficiency derived in [166] not only describes scattering by surface polaritons, but also from guided-wave polaritons in the film. From these results, Ushioda [167] expresses the polarization selection rules as a function of the electric field and of the effective Raman tensor

$$I_N(\omega) = A|(\hat{e}_i \cdot \widetilde{R}_N \cdot \hat{e}_s)\langle E_N(z)\rangle|^2, \tag{4.56}$$

where the effective Raman tensor, including the electro-optic and $\boldsymbol{k}$-dependent Fröhlich interaction contributions is defined as

$$\widetilde{R}_N \equiv K_N \overleftrightarrow{R}_N + 2\overleftrightarrow{\chi}_N^{(2)} + \overleftrightarrow{R^F}_N, \tag{4.57}$$

and $\langle E_N(z)\rangle$ is the time-averaged root mean squared value of the electric field along the polariton normal coordinate. The total scattering intensity can then be expressed by including the relaxed wave vector conservation condition for a thin film, spanning from $-d/2$ to $d/2$ in the z dimension, which yields [24]

$$I_N(\omega) = \frac{C(n_\omega + 1)}{d} \left| (\hat{e}_i \cdot \widetilde{R}_N \cdot \hat{e}_s) \int_{-d/2}^{d/2} e^{\iota \Delta \boldsymbol{q}_\perp z} \langle E_N(z)\rangle \mathrm{d}z \right|^2 \delta(\Delta \boldsymbol{q}_{/\!/} - k_{/\!/}) H_N^E(\omega, \theta) \tag{4.58}$$

where $\Delta \boldsymbol{q} = \boldsymbol{q_i} - \boldsymbol{q_s}$, and C is a constant.

CHAPTER 5 NUMERICAL MODELING OF CONFINED POLARITONS

Given the fact that polaritons possess a photonic component, it is particularly convenient to use a classical electromagnetic wave model to determine the polariton modes in a sample of finite dimensions, viewing it as an optical cavity. In this chapter, the dispersion relations of polariton in finite samples are modeled as optical modes in a slab cavity. §5.1 presents the general properties and boundary conditions of confined modes in a slab waveguide, §5.2 presents the analytical determination of the guided modes in a slab of GaSe, highlighting the unique properties of confined hyperbolic modes and §5.3 introduces a general 4×4 matrix formalism of electromagnetic wave propagation in multilayer dielectric slab systems that enables efficient numerical computation of the guided mode dispersion and electric field distribution. These computed field distributions are then used to model the Raman scattering efficiency of the confined polaritons using the approach presented in chapter 4.

5.1 Confined polariton modes : the waveguide model

When confined along one or more dimensions, photons can be guided within the confined area, such as in an optical fiber. In such a waveguide, several modes can propagate with different field distributions which can be modeled as different propagation orientations of light rays, which experience total internal reflection (TIR) at the waveguide boundaries and propagate along the non-confined directions. In order to sustain a guided mode, the magnitude of the wave vector must be larger inside the dielectric medium than it is outside of it, that is to say, it has to have a larger permittivity $\epsilon_{\text{in}} > \epsilon_{\text{out}}$.

This criterion can be understood by considering the wave vectors on either side of the interface. TIR conditions impose an evanescent propagation away from the waveguide, therefore the wave vector orthogonal from the surface $k_{\text{out}\perp}$ is imaginary. In order to satisfy these requirements, the tangential wave vector component $k_{\text{out}/\!/}$ has to be greater than the norm of the free-space wave vector $k_{\text{out}} = \sqrt{\epsilon_{\text{out}}}\omega/c$, since $k_{\text{out}}^2 = k_{\text{out}\perp}^2 + k_{\text{out}/\!/}^2$.

5.1.1 Isotropic waveguide

The propagation of a guided wave propagating with angle θ relative to the surface normal in a dielectric slab waveguide is illustrated on Fig. 5.1. In order to support a guided mode, the phase accumulated by the wave between two reflections $\phi = \frac{kd}{\cos\theta}$ must be an integer multiple

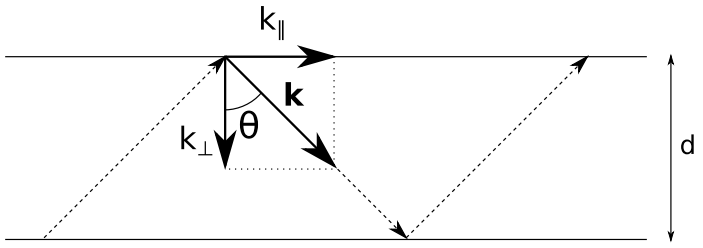

Figure 5.1 Schematic representation of a propagating wave in a dielectric slab waveguide at angle θ relative to the surface normal, which is also the lattice c axis.

of π. The magnitude of $\boldsymbol{k}$ is given by

$$k^2 = \epsilon_{\text{in}} \frac{\omega^2}{c^2}, \tag{5.1}$$

with $k_\perp = k\cos\theta$ and $k_{/\!/} = k\sin\theta$. Knowing that the tangential wave vector is conserved through a dielectric interface, the tangential component inside the waveguide $k_{/\!/} = k_{\text{out}/\!/} > k_{\text{out}}$, therefore, for any propagative mode with real $k_\perp$ inside the waveguide, $k_{/\!/} > \sqrt{\epsilon_{\text{out}}}\frac{\omega}{c}$, therefore the propagation angle must satisfy the condition $\theta > \sin^{-1}\sqrt{\frac{\epsilon_{\text{out}}}{\epsilon_{\text{in}}}}$.

For very small d, only a single mode can be supported in the slab, with $k_{/\!/} \to \sqrt{\epsilon_{\text{in}}}\frac{\omega}{c}$ and $\theta \to \frac{\pi}{2}$. For larger values of d, more guided modes can propagate, each with an associated propagation angle and tangential wave vector component, up to the limit of very large d where there is a continuum of guided modes with

$$\sin^{-1}\sqrt{\frac{\epsilon_{\text{out}}}{\epsilon_{\text{in}}}} < \theta < \frac{\pi}{2} \qquad \text{and} \qquad \sqrt{\epsilon_{\text{out}}}\frac{\omega}{c} < k_{/\!/} < \sqrt{\epsilon_{\text{in}}}\frac{\omega}{c}. \tag{5.2}$$

The photonic part of a polariton wave can be guided in a slab waveguide in the fashion described above, but the polaritonic coupling with phonons occurs at energies near the polar phonon resonance, where the permittivity diverges. Below the TO frequency, ϵ becomes very large, and more guided modes with higher values of $k_{/\!/}$ can be sustained for a given waveguide thickness.

The frequency range between the TO and LO frequencies is known as a Reststrahlen band, where the permittivity is negative and there are no propagative waves in the medium. However, for imaginary $k_\perp$, there can be solutions to $k_{in}^2 = k_\perp^2 + k_{/\!/}^2 > k_{\text{out}}^2$ that correspond to electromagnetic waves propagating along the interface with evanescent fields inside and outside the medium, known as surface waves. For a waveguide with two interfaces, there can exist two surface waves that are degenerate for large d and that split into an upper and lower

surface mode when the distance between the interfaces becomes comparable to the inverse of the evanescent wave's decay constant $-\iota k_\perp$.

5.1.2 Anisotropic waveguide

For an uniaxial anisotropic waveguide with the extraordinary axis perpendicular to the interfaces, the relationship between $k_{/\!/}$ and $k_\perp$ takes the form

$$\epsilon_\perp \frac{\omega^2}{c^2} = k_{/\!/}^2 + k_\perp^2 \tag{5.3}$$

for ordinary waves, which behave exactly as waves in an isotropic medium, since only one permittivity applies to them. For extraordinary waves,

$$\frac{\omega^2}{c^2} = \frac{k_{/\!/}^2}{\epsilon_{/\!/}} + \frac{k_\perp^2}{\epsilon_\perp}, \tag{5.4}$$

and the guided modes show significant differences from the isotropic case.

When both permittivities are positive, the waveguiding conditions as a function of d are essentially the same as those described above for an isotropic waveguide, and guided extraordinary modes can exist if $\epsilon_{/\!/} > \epsilon_{\text{out}}$ and $\epsilon_\perp > \epsilon_{\text{out}}$.

Frequency ranges where both of the anisotropic permittivities are negative are called double Reststrahlen bands, and two surface modes can be guided by the slab, as in the isotropic case described previously.

Reststrahlen bands that apply only to one polarization directions correspond to Type I or Type II hyperbolic bands. For these frequencies, only one of the permittivities is negative, and the waveguide can support up to two surface modes with imaginary $k_\perp$ as well as guided modes with real $k_\perp$.

An arbitrarily large number of guided modes with real $k_\perp$ can exist in these hyperbolic bands since equation (5.4) does not impose an upper limit on the magnitude of $k_{/\!/}$ or $k_\perp$, as long as the positive permittivity is greater than ϵ_{out}. Contrary to the standard dielectric waveguide case, reducing the waveguide dimension d increases the magnitude of both $k_{/\!/}$ and $k_\perp$, and in the limit of large k, the propagation angle converges to

$$\theta(k \gg \omega/c) = \arctan\sqrt{\left|\frac{\epsilon_{/\!/}}{\epsilon_\perp}\right|}. \tag{5.5}$$

These photonic waveguide effects can be used to precisely tailor the wave vector of the polaritons by tuning the waveguide thickness d. The detailed relationships between $k_{/\!/}$, $k_\perp$

and d for hyperbolic polaritons will be developed in the next section.

5.2 Analytical solution of guided and surface polariton modes

As has been established in the previous section, polariton dispersion curves can be significantly altered by spatial confinement. In this section, the analytical solution to polariton guided-wave and surface mode dispersion relations in a slab waveguide of GaSe are derived from Maxwell's equations and the anisotropic dispersion relations presented in §3.2.2.

5.2.1 Wave propagation in an anisotropic medium

The macroscopic Maxwell equations describe the propagation of an electromagnetic field in matter, assuming no free charges nor currents in the material :

$$\nabla \cdot \boldsymbol{D} = 0, \tag{5.6}$$

$$\nabla \cdot \boldsymbol{B} = 0, \tag{5.7}$$

$$\nabla \times \boldsymbol{E} = -\frac{\partial \boldsymbol{B}}{\partial t}, \tag{5.8}$$

$$\nabla \times \boldsymbol{H} = \frac{\partial \boldsymbol{D}}{\partial t}. \tag{5.9}$$

Assuming plane-wave oscillating electric and magnetic fields defined as

$$\boldsymbol{E}(\boldsymbol{r}, t) = \boldsymbol{E}_0 e^{\iota(\boldsymbol{k}\cdot\boldsymbol{r} - \omega t)}, \tag{5.10}$$

$$\boldsymbol{H}(\boldsymbol{r}, t) = \boldsymbol{H}_0 e^{\iota(\boldsymbol{k}\cdot\boldsymbol{r} - \omega t)}, \tag{5.11}$$

with the electric displacement and magnetic induction defined as

$$\boldsymbol{D} = \epsilon_0 \overleftrightarrow{\epsilon} \boldsymbol{E}, \tag{5.12}$$

$$\boldsymbol{B} = \mu_0 \overleftrightarrow{\mu} \boldsymbol{H}, \tag{5.13}$$

where the permittivity $\overleftrightarrow{\epsilon}$ and permeability $\overleftrightarrow{\mu}$ describe how the propagation medium interacts with the electromagnetic wave through various polarization and magnetization processes. In the context of this work, we assume $\overleftrightarrow{\mu}$ to be equal to 1, as GaSe shows no magnetic properties. The relative permittivity is a second-order tensor $\overleftrightarrow{\epsilon}$ and, for a uniaxial crystal like GaSe, it

has two distinct components [168]:

$$\overleftrightarrow{\epsilon} = \begin{pmatrix} \epsilon_\perp & 0 & 0 \\ 0 & \epsilon_\perp & 0 \\ 0 & 0 & \epsilon_{/\!/} \end{pmatrix}, \tag{5.14}$$

where $\epsilon_{/\!/}$ and $\epsilon_\perp$ are given by equations (3.8) and (3.7). Combining equations (5.8) and (5.9) yields the well-known wave equation

$$\nabla \times \nabla \times \boldsymbol{E} + \mu_0 \epsilon_0 \overleftrightarrow{\epsilon} \frac{\partial^2 \boldsymbol{E}}{\partial \boldsymbol{t}^2} = 0. \tag{5.15}$$

Since the fields are assumed to be simple harmonic waves of the form $e^{\iota(\boldsymbol{k}\cdot\boldsymbol{r}-\omega t)}$, we can replace the ∇ operator by $\iota\boldsymbol{k}$ and $\frac{\partial}{\partial t}$ by $-\iota\omega$ (using the identity $\nabla \times \nabla \times \boldsymbol{x} = \nabla(\nabla \cdot \boldsymbol{x}) - \nabla^2 \boldsymbol{x}$) :

$$\nabla(\nabla \cdot \boldsymbol{E}) = -\boldsymbol{k}(\boldsymbol{k} \cdot \boldsymbol{E}) \tag{5.16}$$

$$\nabla^2 \boldsymbol{E} = -|\boldsymbol{k}|^2 \boldsymbol{E}, \tag{5.17}$$

which yields the anisotropic wave equation (with $\mu_0\epsilon_0 = 1/c^2$) :

$$\boldsymbol{k}(\boldsymbol{k} \cdot \boldsymbol{E}) - |\boldsymbol{k}|^2 \boldsymbol{E} + \frac{\omega^2}{c^2} \overleftrightarrow{\epsilon} \boldsymbol{E} = 0. \tag{5.18}$$

Before moving further, it is important to consider the relationship between the wave vector direction and amplitude. In an isotropic material, the divergence term in (5.18) is equal to zero and to obtain nontrivial solutions the following relation must hold true :

$$\frac{c^2 k^2}{\omega^2} - \epsilon_r = 0. \tag{5.19}$$

The relationship between $|\boldsymbol{k}|$ and ω in anisotropic materials is more complex, as the permittivity is not a scalar and the electric field is not always perpendicular to the wave vector k, thus its divergence is not equal to zero. In the case of a uniaxial crystal, either the wave is extraordinary and the divergence of $\boldsymbol{E}$ is zero, or the wave is extraordinary, and the solutions to equation (5.18) must satisfy

$$\left(\frac{c^2 k^2}{\omega^2} - \epsilon_\perp\right)\left(\epsilon_\perp \frac{c^2 k_\perp^2}{\omega^2} + \epsilon_{/\!/} \frac{c^2 k_{/\!/}^2}{\omega^2} - \epsilon_{/\!/}\epsilon_\perp\right) = 0, \tag{5.20}$$

where $k_\perp$ and $k_{/\!/}$ are the components of the wave vector that are respectively perpendicular and parallel to the c axis, or optical axis, of the crystal. The first term corresponds to the

ordinary wave solutions, and the second term to the extraordinary waves.

This expression allows for two distinct wave vectors for a given frequency. The waves satisfying the first term of the equation are known as the ordinary waves, where the electric field is orthogonal to the optical axis and to the wave vector, and the effective permittivity is a scalar. The waves satisfying the second term are the extraordinary waves, where the $\boldsymbol{E} \cdot \hat{k} \neq 0$ and $\boldsymbol{E} \cdot \hat{c} \neq 0$.

5.2.2 Slab waveguide problem

In this section, the guided wave solutions in a dielectric GaSe slab of thickness d are obtained analytically by imposing the appropriate boundary conditions at the interfaces and outside the slab. Fig. 5.2 illustrates the modeled configuration and the coordinate system used.

For a slab having surfaces normal to the crystalline c axis, we can consider only waves propagating in the xz plane without restricting the generality of the obtained solutions given the uniaxial symmetry of the material.

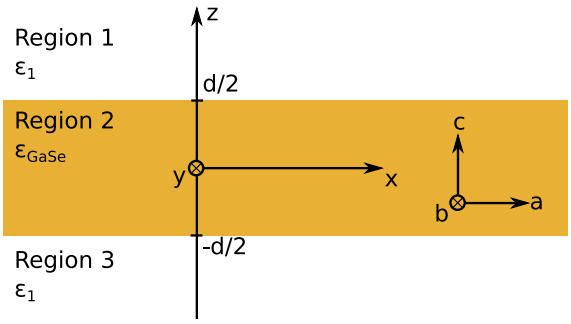

Figure 5.2 Coordinate definition for the GaSe slab considered in this section. The slab has a thickness d and is located in vacuum. The top and bottom surfaces at $z = \pm d/2$ are perpendicular to the c crystalline axis.

In the case of guided waves, the fields in regions 1 and 3 must be evanescent along the z direction, away from the crystal surface, thus the z component of their wave vectors $k_{1z} = \iota\alpha_1$ and $k_{3z} = -\iota\alpha_3$ must be imaginary, whereas inside the crystal slab k_{2z} can be either real (in the case of guided oscillatory modes) or imaginary (in the case of surface modes). The tangential component of the wave vector on either side of every interface is continuous, thus we can state that $k_{1x} = k_{2x} = k_{3x} = k_x$, which is the real propagation vector in the x direction

(parallel to the slab). These conditions thus impose the following form to the electric fields :

$$\boldsymbol{E}_1(\boldsymbol{r},t) = \boldsymbol{E}_1^* e^{-\alpha_1 z} e^{\iota(k_x x - \omega t)} \tag{5.21}$$

$$\boldsymbol{E}_2(\boldsymbol{r},t) = \left(\boldsymbol{E}_2^{*+} e^{\iota k_{2z} z} + \boldsymbol{E}_2^{*-} e^{-\iota k_{2z} z}\right) e^{\iota(k_x x - \omega t)} \tag{5.22}$$

$$\boldsymbol{E}_3(\boldsymbol{r},t) = \boldsymbol{E}_3^* e^{\alpha_3 z} e^{\iota(k_x x - \omega t)}, \tag{5.23}$$

with

$$\boldsymbol{E}_i^* = \begin{pmatrix} E_{ix} \\ E_{iy} \\ E_{iz} \end{pmatrix} \tag{5.24}$$

representing the constant field amplitude vectors in each region, using the asterisk to differentiate the propagating field from the field amplitude. The magnetic fields will have a similar plane wave form, with constant field amplitude vectors in each region

$$\boldsymbol{H}_i^* = \begin{pmatrix} H_{ix} \\ H_{iy} \\ H_{iz} \end{pmatrix} \tag{5.25}$$

with corresponding exponential propagation components

$$\boldsymbol{H}_1(\boldsymbol{r},t) = \boldsymbol{H}_1^* e^{-\alpha_1 z} e^{\iota(k_x x - \omega t)} \tag{5.26}$$

$$\boldsymbol{H}_2(\boldsymbol{r},t) = \left(\boldsymbol{H}_2^{*+} e^{\iota k_{2z} z} + \boldsymbol{H}_2^{*-} e^{-\iota k_{2z} z}\right) e^{\iota(k_x x - \omega t)} \tag{5.27}$$

$$\boldsymbol{H}_3(\boldsymbol{r},t) = \boldsymbol{H}_3^* e^{\alpha_3 z} e^{\iota(k_x x - \omega t)}. \tag{5.28}$$

The external waves in regions 1 and 3 for a given transverse wave vector k_x will give rise to two waves inside the slab with the same transverse wave vector component and two different normal vectors k_{2z}, the ordinary and extraordinary wave. The ordinary wave has an electric field perpendicular to the c axis, which in the considered xz propagation plane means that the field is in the y direction, which corresponds to a transverse electric (TE) wave. The extraordinary waves have electric fields in the xz plane and magnetic fields along the y axis, which corresponds to transverse magnetic (TM) waves. Note that the TE wave corresponds to the transverse ordinary (To) polariton branch introduced in the previous chapter, while the transverse and longitudinal extraordinary (Te and Le) polariton branches correspond to TM waves.

5.2.3 Guided mode solutions

Transverse electric waves

For the TE waves, the electric field $\boldsymbol{E} = E_y\hat{y}$, and the magnetic field is in the xy plane $\boldsymbol{H} = H_x\hat{x} + H_z\hat{z}$. Maxwell's equations (5.8) and (5.9) can be reduced to

$$\frac{\partial E_y}{\partial z} = -\iota\omega\mu_0 H_x \tag{5.29}$$

$$\iota k_x E_y = -\iota\omega\mu_0 H_z \tag{5.30}$$

$$\frac{\partial H_x}{\partial z} - \iota k_x H_z = \iota\omega\epsilon_y\epsilon_0 E_y, \tag{5.31}$$

where ϵ_y represents the effective permittivity for fields along the y axis in each region which is ϵ_0 in vacuum and $\epsilon_0\epsilon_\perp$ in GaSe.

Equations (5.29) and (5.30) can be used to express the components of the magnetic field as functions of the electric field

$$H_x = \frac{\iota}{\omega\mu_0}\frac{\partial E_y}{\partial z} \tag{5.32}$$

$$H_z = -\frac{k_x}{\omega\mu_0}E_y. \tag{5.33}$$

Substituting into equation (5.31) yields a wave equation for the electrical field

$$\frac{\partial^2 E_y}{\partial z^2} + (\epsilon_y(\omega^2/c^2) - k_x^2)E_y = 0. \tag{5.34}$$

From the form of the above wave equation, the propagation constant along the z axis k_z has to take the form

$$k_z = \sqrt{\epsilon_y(\omega^2/c^2) - k_x^2}. \tag{5.35}$$

Outside the slab, the permittivity is ϵ_0, and the propagation constant are defined as $k_{1z} = \iota\alpha_1$ and $k_{3z} = -\iota\alpha_3$, therefore $\iota\alpha_1 = -\iota\alpha_3 = \sqrt{\omega^2/c^2 - k_x^2} = \iota\alpha$.

The tangential components of $\boldsymbol{H}$ in each region

$$H_{1x} = -\frac{\iota\alpha_1}{\omega\mu_0} E_{1y} e^{-\alpha_1 z} e^{\iota(k_x x - \omega t)} \tag{5.36}$$

$$H_{2x} = -\frac{k_{2z}}{\omega\mu_0} \left(E_{2y}^{+} e^{\iota k_{2z} z} - E_{2y}^{-} e^{-\iota k_{2z} z} \right) e^{\iota(k_x x - \omega t)} \tag{5.37}$$

$$H_{3x} = \frac{\iota\alpha_3}{\omega\mu_0} E_{3y} e^{\alpha_3 z} e^{\iota(k_x x - \omega t)} \tag{5.38}$$

have to be continuous at the interfaces $z = \pm d/2$, yielding

$$-\iota\alpha_1 E_{1y} e^{-dz/2} = -k_{2z} \left(E_{2y}^{+} e^{\iota k_{2z} d/2} - E_{2y}^{-} e^{-\iota k_{2z} d/2} \right) \tag{5.39}$$

$$\iota\alpha_3 E_{3y} e^{-dz/2} = -k_{2z} \left(E_{2y}^{+} e^{-\iota k_{2z} d/2} - E_{2y}^{-} e^{\iota k_{2z} d/2} \right). \tag{5.40}$$

The tangential components of the $\boldsymbol{E}$ field are also continuous at the interfaces

$$E_{1y} e^{-dz/2} = \left(E_{2y}^{+} e^{\iota k_{2z} d/2} + E_{2y}^{-} e^{-\iota k_{2z} d/2} \right) \tag{5.41}$$

$$E_{3y} e^{-dz/2} = \left(E_{2y}^{+} e^{-\iota k_{2z} d/2} + E_{2y}^{-} e^{\iota k_{2z} d/2} \right). \tag{5.42}$$

Substituting equations (5.39) and (5.40) into the last two equations gives the following system of equations for the electric field amplitudes in the slab :

$$(-k_{2z} + \iota\alpha_1) E_{2y}^{+} e^{\iota k_{2z} d/2} + (k_{2z} + \iota\alpha_1) E_{2y}^{-} e^{-\iota k_{2z} d/2} = 0 \tag{5.43}$$

$$-(k_{2z} + \iota\alpha_3) E_{2y}^{+} e^{-\iota k_{2z} d/2} + (k_{2z} - \iota\alpha_3) E_{2y}^{-} e^{\iota k_{2z} d/2} = 0. \tag{5.44}$$

The determinant of this system of equations must be zero for non-trivial solutions :

$$(-k_{2z}^2 + \alpha_1\alpha_3 + \iota k_{2z}(\alpha_1 + \alpha_3)) e^{2\iota k_{2z} d/2} + (k_{2z}^2 - \alpha_1\alpha_3 + \iota k_{2z}(\alpha_1 + \alpha_3)) e^{-2\iota k_{2z} d/2} = 0, \tag{5.45}$$

which can be simplified to the following transcendental equation

$$\tan(k_{2z} d) = \frac{k_{2z}(\alpha_1 + \alpha_3)}{k_{2z}^2 - \alpha_1\alpha_3}, \tag{5.46}$$

where $k_{2z} = \sqrt{(\omega^2/c^2)\epsilon_\perp - k_x^2}$. This solution has the same form as the solution in a isotropic slab, as the ordinary waves only exhibit a single effective refractive index. The only solutions for this relation are real values of k_{2z}, therefore only guided propagative modes (as opposed to surface modes) exist for TE polarization [24, 167, 169].

Transverse magnetic waves

In the case of transverse magnetic waves, the non-vanishing field components are H_y, E_x and E_z. Similarly to the TE case, Maxwell's equations can be reduced to

$$\iota k_x E_z + \frac{\partial E_x}{\partial z} = \iota\omega\mu_0 H_y \tag{5.47}$$

$$\iota k_x H_y = \iota\omega\epsilon_z E_z \tag{5.48}$$

$$\frac{\partial H_y}{\partial z} = \iota\omega\epsilon_x E_x. \tag{5.49}$$

ϵ_x and ϵ_z are the permittivities in each region which apply to fields polarized along x and z, respectively. Outside the slab, $\epsilon_x = \epsilon_y = \epsilon_0$, and in the slab, $\epsilon_x = \epsilon_0\epsilon_\perp$ and $\epsilon_z = \epsilon_0\epsilon_{/\!/}$.

Using the last two equations to obtain the $\boldsymbol{E}$ field components as functions of H_y and substituting into the first equation results in a wave equation for H_y (with $\gamma = \epsilon_x/\epsilon_z$) :

$$\frac{\partial^2 H_y}{\partial z^2} + \gamma(\epsilon_z(\omega^2/c^2) - k_x^2)H_y = 0. \tag{5.50}$$

As for the TE case, the form of the above expression implies a z propagation constant of the form $k_z = \sqrt{\gamma(\epsilon_z(\omega^2/c^2) - k_x^2)}$.

Continuity of the tangential component of $\boldsymbol{H}$ at the interfaces $z = \pm d/2$ gives

$$H_{1y}e^{-\alpha_1 d/2} = \left(H_{2y}^+ e^{\iota k_{2z} d/2} + H_{2y}^- e^{-\iota k_{2z} d/2}\right) \tag{5.51}$$

$$H_{3y}e^{-\alpha_3 d/2} = \left(H_{2y}^+ e^{-\iota k_{2z} d/2} + H_{2y}^- e^{\iota k_{2z} d/2}\right). \tag{5.52}$$

The tangential $\boldsymbol{E}$ field components also have to be continuous in $z = \pm d/2$

$$E_{1x} = \frac{\iota\alpha_1}{\omega\epsilon_1} H_{1y} e^{\mp\alpha_1 d/2} e^{\iota(k_x x - \omega t)} \tag{5.53}$$

$$E_{2x} = \frac{k_{2z}}{\omega\epsilon_\perp}\left(H_{2y}^+ e^{\pm\iota k_{2z} d/2} - H_{2y}^- e^{\mp\iota k_{2z} d/2}\right) e^{\iota(k_x x - \omega t)} \tag{5.54}$$

$$E_{3x} = -\frac{\iota\alpha_3}{\omega\epsilon_3} H_{3y} e^{\mp\alpha_3 d/2} e^{\iota(k_x x - \omega t)}. \tag{5.55}$$

Combining equations (5.51) to (5.55) establishes a system of equations for the amplitudes of the $\boldsymbol{H}_2$ field :

$$(\alpha_1\epsilon_\perp + \iota\epsilon_1 k_{2z})H_{2y}^+ e^{\iota k_{2z} d/2} + (\alpha_1\epsilon_\perp - \iota\epsilon_1 k_{2z})H_{2y}^- e^{-\iota k_{2z} d/2} = 0 \tag{5.56}$$

$$(\alpha_3\epsilon_\perp - \iota\epsilon_3 k_{2z})H_{2y}^+ e^{-\iota k_{2z} d/2} + (\alpha_3\epsilon_\perp + \iota\epsilon_3 k_{2z})H_{2y}^- e^{\iota k_{2z} d/2} = 0, \tag{5.57}$$

which imposes the following relation between the parameters :

$$\tan(k_{2z}d) = \frac{\epsilon_\perp k_{2z}(\epsilon_1\alpha_3 + \epsilon_3\alpha_1)}{\epsilon_1\epsilon_3 k_{2z}^2 - \epsilon_\perp^2\alpha_1\alpha_3}. \tag{5.58}$$

Here the z propagation constant is $k_{2z} = \sqrt{\gamma(\epsilon_{/\!/}(\omega^2/c^2) - k_x^2)}$, with $\gamma = \epsilon_\perp/\epsilon_{/\!/}$.

5.2.4 Numerical solution of the transcendental equations

The transcendental equations obtained in the previous section for TE and TM modes do not have analytical solutions. In order to find the values of k_{2z} which support guided modes, both sides of the equation must be expressed as functions of a single common variable and the intersections of the curves correspond to the eigenvalues of the system.

TE solutions

Starting with the TE solutions, equation (5.46) can be rewritten as a function of the parameter $\beta = 2k_{2z}a = k_{2z}d$. The propagation constants outside the film can be expressed as the parameters η_i which are functions of β :

$$\eta_i = \alpha_i d = \sqrt{(\epsilon_\perp - \epsilon_i)\frac{\omega^2 d^2}{c^2} - \beta^2} \tag{5.59}$$

and the transcendental equation becomes

$$\tan(\beta) = \frac{\beta(\eta_1 + \eta_3)}{\beta^2 - \eta_1\eta_3}. \tag{5.60}$$

For the sake of simplicity, let's consider a GaSe slab suspended in air, with $\epsilon_1 = \epsilon_3 = 1$ and $\eta_1 = \eta_3 = \eta$:

$$\tan(\beta) = \frac{2\beta\eta}{\beta^2 - \eta^2}. \tag{5.61}$$

Plotting both sides of the equation as a function of β is a useful tool to understand the behavior of the solutions. Fig. 5.3 illustrates the guided propagative solutions obtained for two different energies, above and below the Reststrahlen bands of GaSe, in a 5 µm thick slab of GaSe in air. The green curve reveals the presence of three distinct guided modes with a wavenumber of 210 cm^{-1} and different propagation parameters β, as shown by the three intersection points with the black curve. On the other hand, a single guided mode is allowed

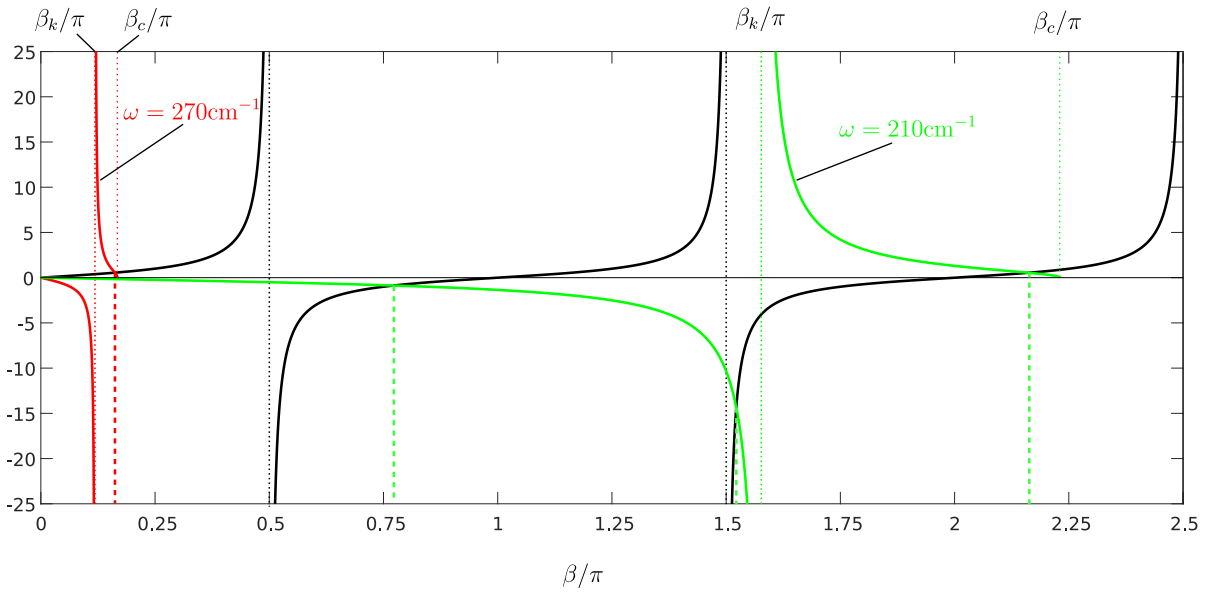

Figure 5.3 Plot of both sides of equation (5.61) in a 5 µm thick slab of GaSe. The black line is the left term of the equation, and the solid green and red plots represent the right-hand side term for wavenumbers of 210 cm^{-1} and 270 cm^{-1}, respectively. The intersections between the curves are highlighted by vertical dashed lines of the corresponding color.

for a wavenumber of 270 cm^{-1}, as shown by the red curve.

Solving numerically the transcendental equation for every wavenumber in a given region of interest yields a dispersion relation $\beta(\sigma)$ for each of the guided modes in the slab. The poles of the transcendental equation must be treated carefully to obtain meaningful results. The right-hand term has real values for $0 \leq \beta \leq \beta_c$, with

$$\beta_c = k_0 d\sqrt{\epsilon_\perp - 1} = \frac{\omega d}{c}\sqrt{\epsilon_\perp - 1} \tag{5.62}$$

corresponding to the maximal transverse propagation constant β for which the parameters $\eta = \alpha d$ outside the film are real, which corresponds to $k_x = \omega/c$. At this cutoff limit, $\eta = 0$ and the wave extends to infinity. β_c must be real and non-vanishing for the layer to support guided modes, therefore guided modes only exist in the region where $\epsilon_\perp > 1$. Equation (5.61) also reveals a pole at $\beta_k = \beta_c/\sqrt{2}$, which has to be taken into account during numerical solving. Both points of interest (β_c and β_k) are indicated on Fig. 5.3.

In order to avoid numerical issues at the poles, each solution has to be considered within a

continuous interval. The total number of allowed modes is given by

$$n = \left\lceil \frac{\beta_c}{\pi} \right\rceil, \tag{5.63}$$

with $\lceil\ \rceil$ representing the ceiling function, and each root β_i occurs in a distinct interval of length π, such that

$$i - 1 < \beta_i/\pi \leq i, \qquad \forall\ i \in [1, n]. \tag{5.64}$$

For solutions $\beta_i < \beta_k$, the interval can be further narrowed down to

$$i - 1/2 < \beta_i/\pi \leq i \tag{5.65}$$

since the right-hand term is negative in this region. Conversely, solutions where $\beta_k < \beta_i \leq \beta_c$ are restricted to the intervals

$$i - 1 < \beta_i/\pi \leq i - 1/2. \tag{5.66}$$

These intervals are now free of discontinuities, and the solutions of equation (5.61) they contain can be easily obtained numerically using the bisection method. For each wavenumber, the poles β_c and β_k are determined, along with the total number of allowed modes n. Then, each of the n unique solutions $\{\beta_1, \ldots, \beta_n\}$ for that wavenumber are computed by bisection over the intervals defined by equations (5.64)-(5.66). The results obtained for the example 5 µm GaSe slab are shown in Fig. 5.4.

TM Modes

The solutions for TM modes can be obtained using a similar approach, however equation (5.58) allows the propagation constant k_{2z} to take on imaginary values, thus there can be both real solutions and imaginary solutions. The real solutions are guided modes in the slab, that have a real propagation vector in the xz plane, throughout the whole volume of the slab. The imaginary solutions for β correspond to surface modes, which have a real propagation vector in the x direction, and an imaginary propagation vector in the z direction, which corresponds to an evanescent field inside the slab, decreasing away from the surfaces. Since the solutions also have to be evanescent outside the slab, these modes are bound to the surfaces of the slab, and are therefore called surface modes.

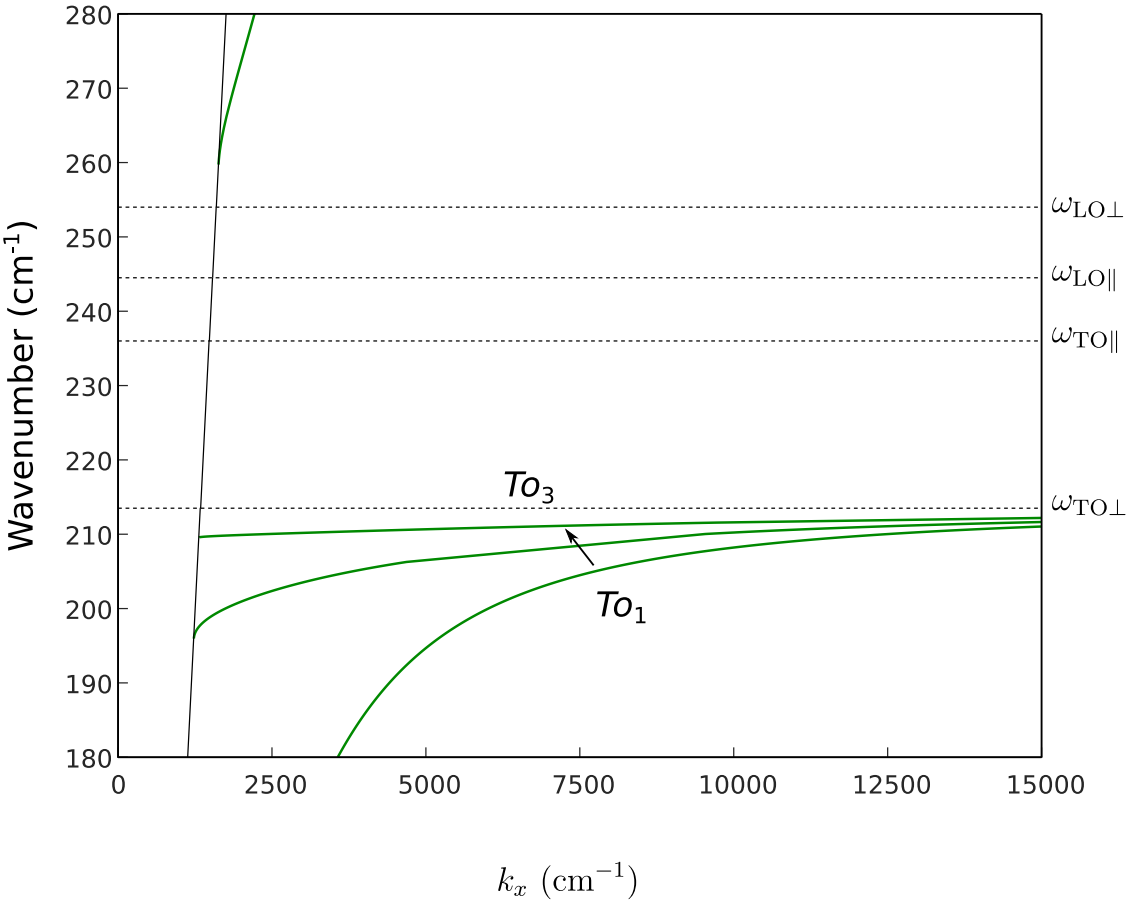

Figure 5.4 Dispersion relation of the first three guided TE modes in a 5 µm thick slab of GaSe. The TE modes correspond to the transverse ordinary (To) polariton branch, as indicated on the graph. The photon-like ordinary polariton branch above $\omega_{\mathrm{LO}\perp}$ is almost coincident with the vacuum light line (indicated by the solid oblique black line) and is of little interest in this work because of its weak confinement.

Substituting $\beta = 2k_{2z}a$ and $\eta_i = \alpha_i d$ in equation (5.58) yields the transcendental equation

$$\tan(\beta) = \frac{\epsilon_\perp \beta(\epsilon_1\eta_3 + \epsilon_3\eta_1)}{\epsilon_1\epsilon_3\beta^2 - \epsilon_\perp^2\eta_1\eta_3}. \tag{5.67}$$

For the surface mode solutions, this equation can be reformulated (with $\beta = \iota\zeta$) as

$$\tanh(\zeta) = \frac{-\epsilon_\perp \zeta(\epsilon_1\eta_3 + \epsilon_3\eta_1)}{\epsilon_1\epsilon_3\zeta^2 + \epsilon_\perp^2\eta_1\eta_3}. \tag{5.68}$$

The expression of η_i as a function of β is

$$\eta_i = \sqrt{(\epsilon_{/\!/} - \epsilon_i)\frac{\omega^2 d^2}{c^2} - \frac{1}{\gamma}\beta^2}, \tag{5.69}$$

with $\gamma = \epsilon_\perp/\epsilon_{/\!/}$.

For a freestanding slab where $\eta_1 = \eta_3 = \eta$ and $\epsilon_1 = \epsilon_3 = 1$, equation (5.67) simplifies to

$$\tan(\beta) = \frac{2\epsilon_\perp \beta\eta}{\beta^2 - \epsilon_\perp^2\eta^2} \tag{5.70}$$

This relation is very similar to the one obtained for the TE modes, with the addition that it exhibits an explicit dependence on $\epsilon_\perp$.

The signs and values of the permittivities must be carefully considered in order to determine the frequency and propagation constant ranges where non-trivial TM solutions can be supported by the slab. Guided mode solutions can be derived from the the constraint that the field outside the slab must be evanescent, thus η must be real :

$$\eta^2 = (\epsilon_{/\!/} - 1)\frac{\omega^2 d^2}{c^2} - \frac{\epsilon_{/\!/}}{\epsilon_\perp}\beta^2 > 0. \tag{5.71}$$

The cutoff parameter where $k_x = k_0 = \omega/c$ for guided TM modes is

$$\beta_c = \frac{\omega d}{c}\sqrt{\frac{\epsilon_\perp}{\epsilon_{/\!/}}(\epsilon_{/\!/} - 1)} \tag{5.72}$$

Analysis of equations (5.71) and (5.72) reveals four distinct regimes depending on the signs and values of $\epsilon_\perp$ and $\epsilon_{/\!/}$.

Case I , where $\epsilon_\perp > 0$ and $\epsilon_{/\!/} > 0$, is the standard dielectric waveguide regime, for which guided solutions must satisfy $\beta < \beta_c$, with $\epsilon_{/\!/} > 1$. Fig. 5.5 illustrates graphically the

transcendental equation. The total number of guided TM modes in this case is given by

$$n = \left\lceil \frac{\beta_c}{\pi} \right\rceil . \tag{5.73}$$

Using a similar approach to the TE case, the roots β_i can be found in distinct continuous intervals of length $\pi/2$, taking into consideration the presence of a pole at

$$\beta_k = \frac{\omega d}{c} \sqrt{\frac{\epsilon_\perp^2 (\epsilon_{/\!/} - 1)}{1 + \epsilon_\perp \epsilon_{/\!/}}}. \tag{5.74}$$

Solutions $\beta_i < \beta_k$ are found in the intervals

$$i - 1/2 < \beta_i/\pi \leq i \tag{5.75}$$

and solutions where $\beta_k < \beta_i \leq \beta_c$ are restricted to

$$i - 1 < \beta_i/\pi \leq i - 1/2. \tag{5.76}$$

Case II , where $\epsilon_\perp > 0$ and $\epsilon_{/\!/} < 0$, corresponds to a Type I hyperbolic Reststrahlen band, and guided solutions must satisfy $\beta > \beta_c$. Note here that there is no upper limit on the propagation parameter β, and the slab can support an arbitrarily large number of guided modes. This unique property of hyperbolic waveguides will be discussed in more detail in §5.2.5. In the case of GaSe, there is no frequency range with Type I hyperbolic behavior.

Case III , where $\epsilon_\perp < 0$ and $\epsilon_{/\!/} > 0$, defines a Type II hyperbolic Reststrahlen band. For $0 < \epsilon_{/\!/} < 1$, guided modes exist with $\beta > \beta_c$. For $\epsilon_{/\!/} > 1$, the cutoff parameter is imaginary, and guided propagative modes with any real $\beta > 0$ as well as surface modes with $\zeta < -\iota\beta_c$ are supported by the slab.

As for the Type I modes, there is no upper bound on the transverse wave vector, and the transcendental equation has an infinite number of propagative mode solutions. These solutions can be found once again in distinct continuous intervals. The equation has poles for real values of β_k, which induces a change of sign of the right-hand term of equation (5.70). Fig. 5.6 illustrates the three different cases for propagative solutions in a Type II hyperbolic band.

In the hyperbolic region, the transverse wave parameter can be imaginary for $\epsilon_{/\!/} > 1$, and has an upper boundary of $\zeta < -\iota\beta_c$, as is illustrated by the blue and green curves on Fig. 5.8. There are no discontinuities in (5.70) and only two solutions, therefore numerical solving

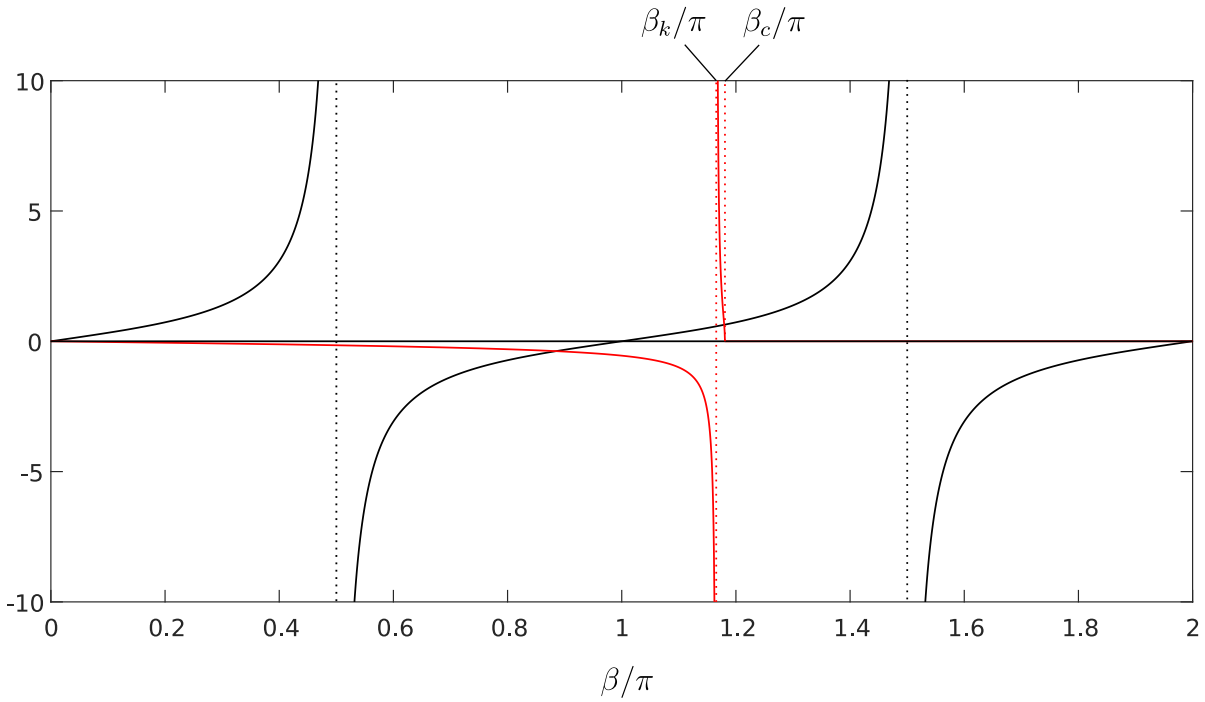

Figure 5.5 Plot of both sides of equation (5.70) in a 5 µm thick slab of GaSe. The solid black line is the left term of the equation, and the solid red plot represents the right-hand side term for a wavenumber of 500 cm^{-1}, far above any Reststrahlen band.

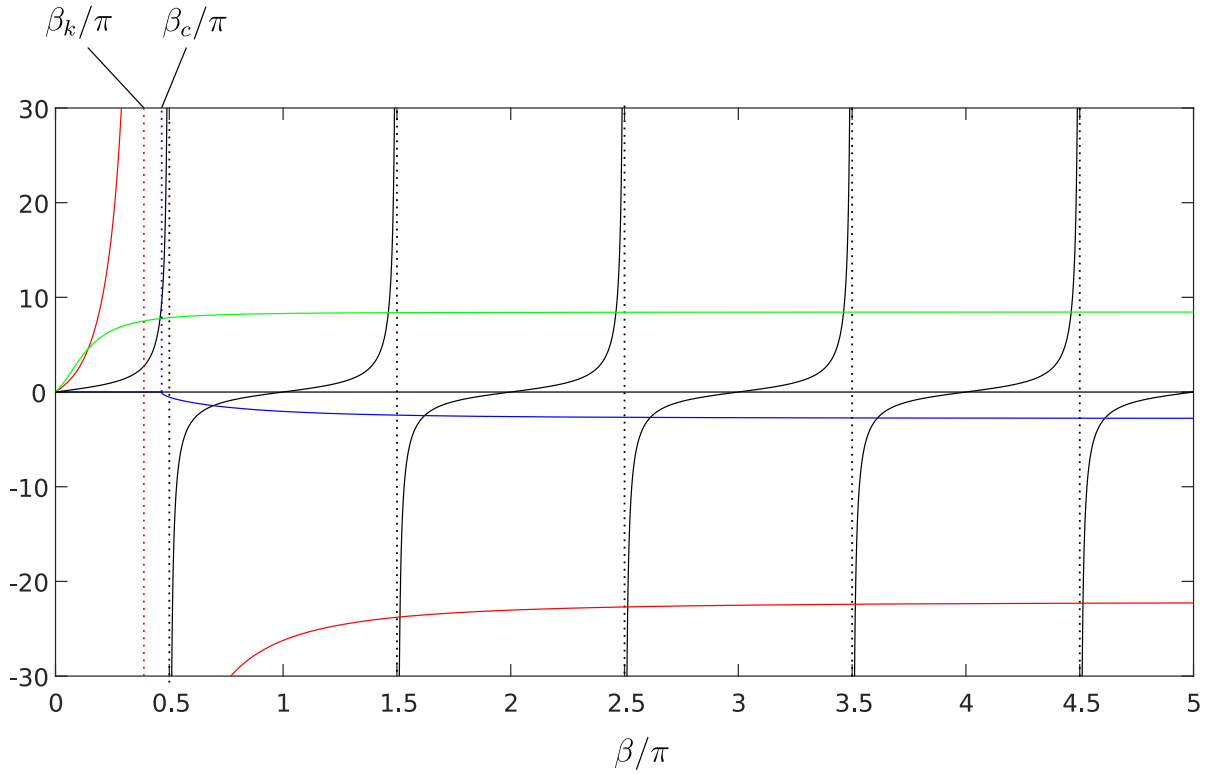

Figure 5.6 Plot of both sides of the transcendental equation in a 5 µm thick slab of GaSe. The solid black line is the left term of the equation, and the colored curves represents the right-hand side term for wavenumbers of 245.5 cm^{-1} (blue line), 247 cm^{-1} (green line) and 250 cm^{-1} (red line).

is rather simple. The resulting dispersion curves for TM modes in a 5 µm slab of GaSe are shown on Fig. 5.9.

Case IV , where $\epsilon_\perp < 0$ and $\epsilon_{/\!/} < 0$, defines a double Reststrahlen band, where no volumetric propagative solutions exist and guided surface mode solutions must satisfy $\zeta > -\iota\beta_c = \zeta_c$. In this region, there is also no limit on the magnitude of the transverse parameter β, but its value is imaginary, and the modes only propagate longitudinally at the surface and are evanescent in the volume. The slab can only guide two surface modes, therefore the magnitude of the guided modes at a given frequency is limited since there are no higher order modes possible. By selecting the right slab thickness and frequency, one could nevertheless obtain guided surface modes with extremely large longitudinal wave vectors. The resulting dispersion curves for TM modes in a 5 µm slab of GaSe are shown on Fig. 5.9.

5.2.5 Confinement limits

The solutions obtained in the previous sections are solutions for the transverse wave parameter β. Although it is a convenient parameter for the numerical solutions described above, the lateral wave vector component k_x is more useful to describe the experimental observations, as it is preserved both inside and outside the slab and remains real for all types of guided modes. The numerical results are easily converted using the relations for TE and TM modes

$$k_x^{\mathrm{TE}} = \frac{1}{d}\sqrt{\frac{\omega^2\epsilon_\perp d^2}{c^2} - \beta^2}, \tag{5.77}$$

$$k_x^{\mathrm{TM}} = \frac{1}{d}\sqrt{\frac{\omega^2\epsilon_{/\!/} d^2}{c^2} - \frac{\epsilon_{/\!/}}{\epsilon_\perp}\beta^2}. \tag{5.78}$$

It is important to note here that for a given solution β, the resulting longitudinal wave vector k_x decreases with a decrease in the slab thickness for TE modes and TM modes described by case I, whereas it increases in thinner flakes for hyperbolic and surface waves (cases II, III and IV). Coupled to the fact that there is no upper limit to the magnitude of the wave vector for hyperbolic waves, this enables extreme wave confinement to dimensions far smaller than the diffraction limit in materials that exhibit these properties.

The peculiar condition in cases II and III, for which there is no maximum value imposed on β stems from the fact that the permittivities have opposite signs, and the material exhibits

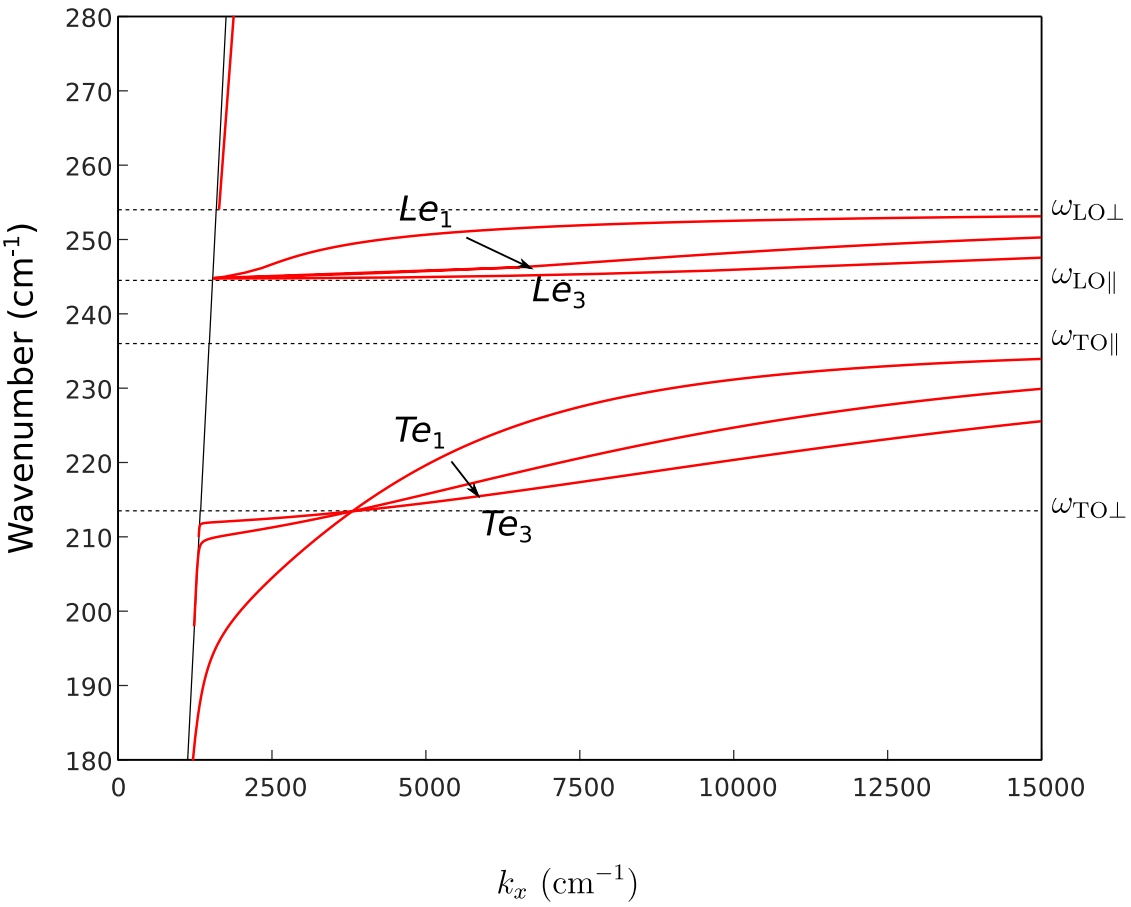

Figure 5.7 Dispersion relation of the first three guided TM modes in a 5 µm thick slab of GaSe. The upper modes correspond to the longitudinal extraordinary (Le) polariton branch and the lower modes to transverse extraordinary Te polaritons. Note the weakly-confined photon-like extraordinary polariton branch, almost coincident with the vacuum light line above $\omega_{\mathrm{LO}\perp}$.

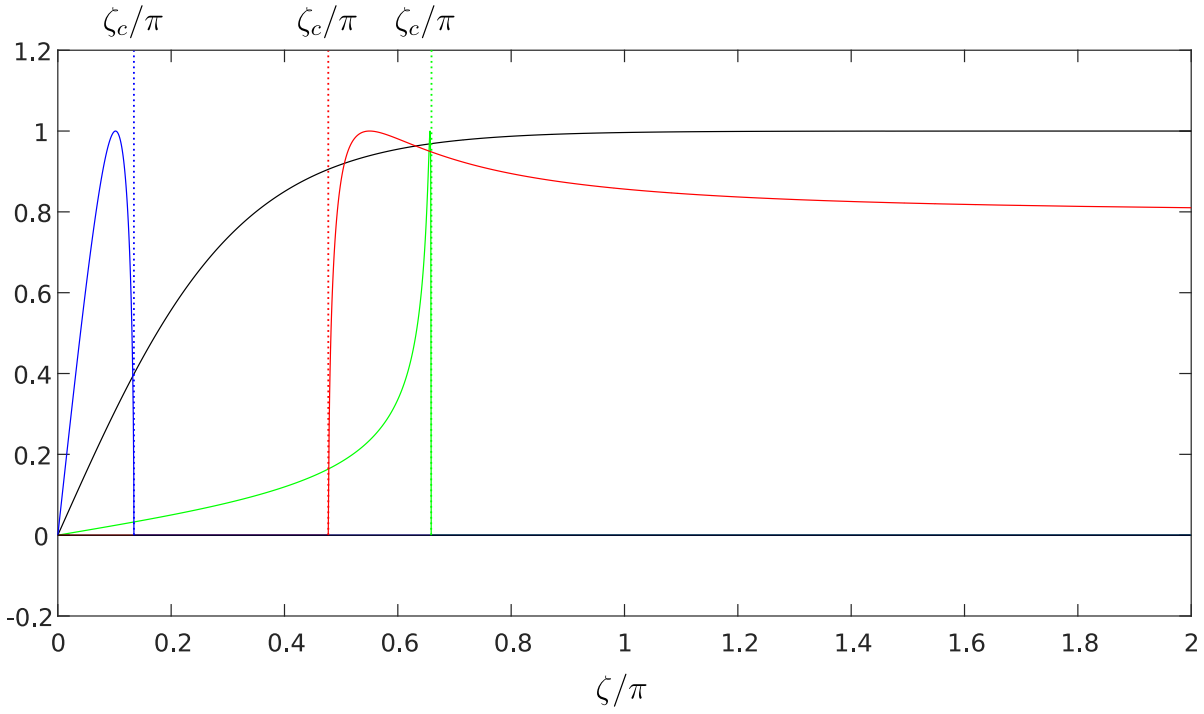

Figure 5.8 Plot of both sides of the transcendental equation in a 5 µm thick slab of GaSe. The solid black line is the left term of the equation, and the colored plots represents the right-hand side term for wavenumbers of 232 cm^{-1} (green line, Type II hyperbolic Reststrahlen), 243 cm^{-1} (red line, double Reststrahlen) and 248 cm^{-1} (blue line, Type II hyperbolic Reststrahlen). The vertical dotted lines indicate the position of the cutoff parameter ζ_c for each curve.

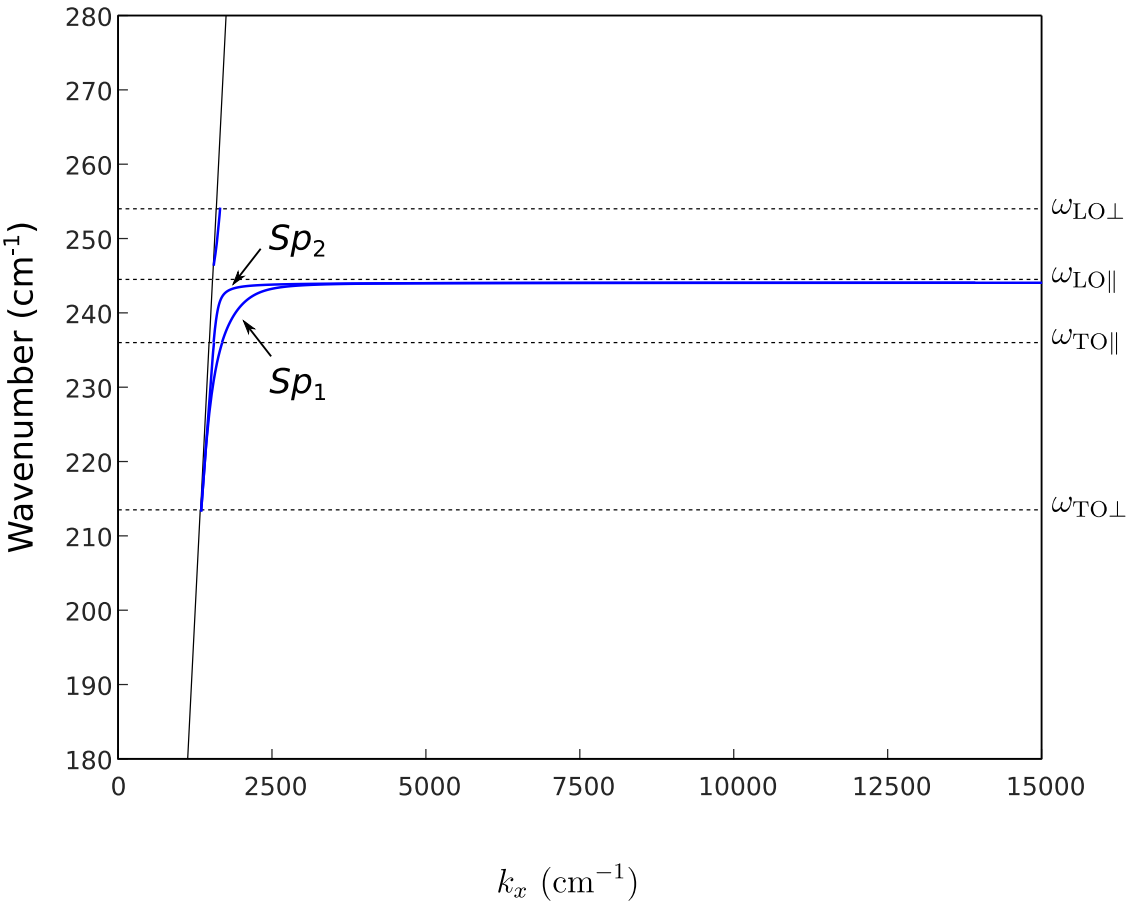

Figure 5.9 Dispersion relation of the surface polariton (Sp) modes in a 5 µm thick slab of GaSe. The two main surface modes extend below the double Reststrahlen band, as surface waves can also exist in the Type II hyperbolic regions around that band. Note that the upper wavenumber limit for the surface modes is lower than $\omega_{LO\parallel}$, since no surface waves can exist for $\epsilon_\parallel > -1$. An additional upper surface mode exists between $\omega_{LO\parallel}$ and $\omega_{LO\perp}$, but its proximity to the light line means that it is poorly confined.

a hyperbolic dispersion behavior defined by

$$\frac{k_x^2}{\epsilon_{/\!/}} + \frac{k_{2z}^2}{\epsilon_\perp} = \frac{\omega^2}{c^2}, \tag{5.79}$$

which has solutions for arbitrarily large wave vectors at a given frequency. In the case of GaSe, which only has a Type II hyperbolic band ($\epsilon_\perp < 0$ and $\epsilon_{/\!/} > 0$), equation (5.79) imposes a minimum value to the longitudinal wave vector

$$|k_x| \geq \sqrt{\frac{\omega^2 \epsilon_{/\!/}}{c^2}}, \tag{5.80}$$

for which $k_{2z} = \beta = 0$, as can be seen on Fig. 5.10. The boundary conditions in the slab require α to take on real values

$$\alpha = \sqrt{\frac{\omega^2}{c^2} - k_x^2}, \tag{5.81}$$

which imposes the condition $\beta > \beta_c$ for $\epsilon_{/\!/} < 1$.

The lack of an upper bound on β is significant as it highlights a unique property of hyperbolic materials in that waves with frequencies in the hyperbolic bands (where $\epsilon_{/\!/}(\omega)\epsilon_\perp(\omega) < 0$) can propagate with arbitrarily large wave vectors. Indeed, the dispersion relation shown on Fig. 5.10 does not restrict the magnitude of $\mathbf{k}$ as in a standard dielectric material, but rather its orientation relative to the extraordinary axis z is restricted. For large values of k, equation (5.79) describes a conical surface with angle

$$\theta = \arctan \sqrt{\left| \frac{\epsilon_{/\!/}}{\epsilon_\perp} \right|} \tag{5.82}$$

This behavior could theoretically be observed for wave vectors up to the limit of $k \sim \pi/a_0$, where the wavelength is of similar dimension to the unit cell, and the effective medium approximation breaks down. Hyperbolic materials can therefore theoretically confine electromagnetic radiation down to extremely small sub-wavelength dimensions, with confinement factors $\lambda_0/\lambda = k/k_0$ up to 10^5.

5.3 General 4x4 matrix formalism for numerical calculations

The model presented in the previous sections provides a good insight into the behavior of polariton modes guided in an anisotropic slab waveguide and its simplicity clearly reveals the different types of guided modes. In order to obtain a more accurate model of the guided

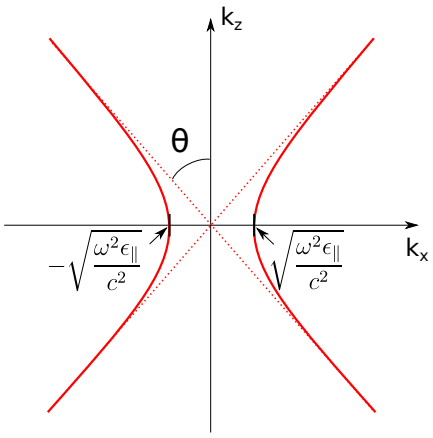

Figure 5.10 Schematic representation dispersion relation in a bulk hyperbolic material within a Type II hyperbolic band showing the minimum value $|k_x|$ specified in the text.

modes and the electric field distributions associated with them, the damping parameter Γ in the expression of the slab's permittivity as well as the substrate permittivity must be taken into account.

In this section, a general 4×4 matrix formalism based on the approach presented in Ref. [28] is used to model the electromagnetic transfer function of a multilayer dielectric medium with anisotropic and/or absorptive media. This formalism combines multiple previous attempts over the last four decades to accurately model multilayer optical films in a format that is well adapted for numerical computation. The use of a matrix formalism enables rapid solving of multiple linear equations and is well suited for the problem at hand, but great care must be taken to avoid numerical instabilities and singularities. Many previously proposed numerical models were either plagued with discontinuities and numerical instabilities, or lacked the ability to model a combination of isotropic and anisotropic media and evanescent fields.

5.3.1 Transfer matrix determination

A transfer matrix is determined for each interface and through each of the N layers of the multilayered medium using Maxwell's equation and boundary conditions in a matrix form. As in the previous derivation, a wave propagating in the xz plane can be considered without loss

of generality due to the symmetry of the system. Defining the field vectors (with $\epsilon_0 = \mu_0 = 1$)

$$\boldsymbol{G} \equiv \begin{pmatrix} E_x \\ E_y \\ E_z \\ H_x \\ H_y \\ H_z \end{pmatrix} e^{-\iota\omega t}, \qquad \boldsymbol{C} \equiv \begin{pmatrix} D_x \\ D_y \\ D_z \\ B_x \\ B_y \\ B_z \end{pmatrix} e^{-\iota\omega t}, \tag{5.83}$$

and assuming no free charges nor currents in the material, Mawxell's equations (5.8) and (5.9) can be expressed as

$$\boldsymbol{RG} = \begin{pmatrix} 0 & 0 & 0 & 0 & -\frac{\partial}{\partial z} & \frac{\partial}{\partial y} \\ 0 & 0 & 0 & \frac{\partial}{\partial z} & 0 & -\frac{\partial}{\partial x} \\ 0 & 0 & 0 & -\frac{\partial}{\partial y} & \frac{\partial}{\partial x} & 0 \\ 0 & \frac{\partial}{\partial z} & -\frac{\partial}{\partial y} & 0 & 0 & 0 \\ -\frac{\partial}{\partial z} & 0 & \frac{\partial}{\partial x} & 0 & 0 & 0 \\ \frac{\partial}{\partial y} & -\frac{\partial}{\partial x} & 0 & 0 & 0 & 0 \end{pmatrix} \begin{pmatrix} E_x \\ E_y \\ E_z \\ H_x \\ H_y \\ H_z \end{pmatrix} = -\iota\omega \begin{pmatrix} D_x \\ D_y \\ D_z \\ B_x \\ B_y \\ B_z \end{pmatrix} = -\iota\omega \boldsymbol{C} \tag{5.84}$$

The constitutive relations between $\boldsymbol{G}$ and $\boldsymbol{C}$ can be written as

$$\boldsymbol{C} = \boldsymbol{M}\boldsymbol{G} = \begin{pmatrix} \overleftrightarrow{\epsilon} & 0 \\ 0 & \overleftrightarrow{\mu} \end{pmatrix} \boldsymbol{G}, \tag{5.85}$$

where we assume $\overleftrightarrow{\mu} = \overleftrightarrow{1}$, with $\overleftrightarrow{1}$ representing the identity matrix.

Combining equations (5.84) and (5.85) and removing the E_z and H_z terms, which can be obtained from the four remaining field terms, gives a 4×4 matrix equation [170] :

$$\frac{\partial}{\partial z}\boldsymbol{\Psi} = \iota\frac{\omega}{c}\boldsymbol{\Delta}\boldsymbol{\Psi}, \tag{5.86}$$

where

$$\boldsymbol{\Psi} = \begin{pmatrix} E_x \\ H_y \\ E_y \\ -H_x \end{pmatrix}. \tag{5.87}$$

The 4×4 matrix $\boldsymbol{\Delta}$ is a function of the matrix $\boldsymbol{M}$ of the layer and of the longitudinal wave

vector component k_x, which is preserved in every layer. It is constructed by equating

$$\boldsymbol{RG} = -\iota\omega\boldsymbol{MG}, \tag{5.88}$$

replacing $\frac{\partial}{\partial x}$ by ιk_x and $\frac{\partial}{\partial y}$ by 0, and removing the z components of the fields. The resulting matrix is

$$\boldsymbol{\Delta} = \begin{pmatrix} 0 & 1 + \frac{c^2 k_x^2}{\omega^2 \epsilon_{/\!/}} & 0 & 0 \\ \epsilon_\perp & 0 & 0 & 0 \\ 0 & 0 & 0 & 1 \\ 0 & 0 & \epsilon_\perp + \frac{c^2 k_x^2}{\omega^2} & 0 \end{pmatrix} \tag{5.89}$$

In each layer i, equation (5.86) has $j = (1, 2, 3, 4)$ solutions, with eigenvalues $\frac{ck_{z,i}^j}{\omega}$, that are the dimensionless z-components of the eigenmode wave vectors, and the corresponding eigenmode field amplitudes are given by $\boldsymbol{\Psi}_i^j$ such that

$$\frac{ck_{z,i}^j}{\omega}\boldsymbol{\Delta}_i = \boldsymbol{\Psi}_i^j \boldsymbol{\Delta}_i \tag{5.90}$$

The four eigenmodes correspond to two s-polarized waves and two p-polarized waves, that each propagate in $\pm z$ directions. In order to avoid poles and discontinuities during the numerical treatment of the transfer matrices, the eigenvalues must be assigned to their corresponding polarization and propagation direction. By evaluating the sign of the imaginary parts (or their sign if they are real) of the eigenvalues $k_{z,i}^j$, the propagation direction can be established. To distinguish s- and p-polarized fields, the relative magnitude of the respective x and y electric field components is compared.

The eigenvalues are then sorted so that $k_{z,i}^1$ and $k_{z,i}^3$ correspond to p-polarized waves and $k_{z,i}^2$ and $k_{z,i}^4$ to s-polarized waves, propagating toward the positive and negative z directions, respectively. This unambiguous assignment then enables the determination of the corresponding z-component of the electric fields while avoiding singularities [171]. To do so, a dimensionless electric field vector $\boldsymbol{\gamma}_i^j$ is defined as

$$\boldsymbol{\gamma}_i^j = \begin{pmatrix} \gamma_{x,i}^j \\ \gamma_{y,i}^j \\ \gamma_{z,i}^j \end{pmatrix}, \tag{5.91}$$

so that $\gamma_{x,i}^1 = \gamma_{y,i}^2 = -\gamma_{x,i}^3 = \gamma_{y,i}^4 = 1$ and $\boldsymbol{E}_i^j = E_i^j \boldsymbol{\gamma}_i^j$. The other components of $\boldsymbol{\gamma}_i^j$ can be obtained using the relations presented in Ref. [171], that enable a computer program to

determine the electric field vectors while avoiding the singularities that arise from the general case when the eigenvalues are degenerate ($k^1_{z,i} = k^3_{z,i}$ or $k^2_{z,i} = k^4_{z,i}$). In the present case, the permittivity tensor is diagonal there are two doubly degenerate eigenvalues, and the only other nonzero components of the normalized electric fields are

$$\boldsymbol{\gamma}^1_{z,i} = \frac{k_x k^1_{z,i}}{(\omega^2/c^2)\epsilon_{/\!/} - k_x^2} \qquad \text{and} \qquad \boldsymbol{\gamma}^3_{z,i} = \frac{k_x k^3_{z,i}}{(\omega^2/c^2)\epsilon_{/\!/} - k_x^2} \tag{5.92}$$

The boundary conditions for the electric and magnetic fields at each interface can be defined as

$$\boldsymbol{A}_{i-1}\boldsymbol{E}_{i-1} = \boldsymbol{A}_i\boldsymbol{E}_i, \tag{5.93}$$

with $\boldsymbol{A}_i$ being a projection matrix onto the eigenfields expressed as a function of the sorted singularity-free electric fields $\boldsymbol{\gamma}^j_i$:

$$\boldsymbol{A}_i = \begin{pmatrix} \gamma^1_{x,i} & \gamma^2_{x,i} & \gamma^3_{x,i} & \gamma^4_{x,i} \\ \gamma^1_{y,i} & \gamma^2_{y,i} & \gamma^3_{y,i} & \gamma^4_{y,i} \\ \frac{\omega}{c}(k^1_{z,i}\gamma^1_{x,i} - k_x\gamma^1_{z,i}) & \frac{\omega}{c}(k^2_{z,i}\gamma^2_{x,i} - k_x\gamma^2_{z,i}) & \frac{\omega}{c}(k^3_{z,i}\gamma^3_{x,i} - k_x\gamma^3_{z,i}) & \frac{\omega}{c}(k^4_{z,i}\gamma^4_{x,i} - k_x\gamma^4_{z,i}) \\ \frac{\omega}{c}k^1_{z,i}\gamma^1_{y,i} & \frac{\omega}{c}k^2_{z,i}\gamma^2_{y,i} & \frac{\omega}{c}k^3_{z,i}\gamma^3_{y,i} & \frac{\omega}{c}k^4_{z,i}\gamma^4_{y,i} \end{pmatrix} \tag{5.94}$$

And the vector $\boldsymbol{E}_i$ representing the electric field amplitudes that satisfy these boundary conditions is defined as

$$\boldsymbol{E}_i = \begin{pmatrix} E^+_p \\ E^+_s \\ E^-_p \\ E^-_s \end{pmatrix}, \tag{5.95}$$

with $E^\pm_p$ and $E^\pm_s$ representing the p-polarized and s-polarized field amplitude propagating in the $\pm z$ direction, respectively. The field in layer i at the interface with layer $i-1$ as a function of the field E_{i-1} on the other side of that interface can now be defined as $\boldsymbol{L}_i \equiv \boldsymbol{A}^{-1}_{i-1}\boldsymbol{A}_i$

$$\boldsymbol{E}_{i-1} = \boldsymbol{A}^{-1}_{i-1}\boldsymbol{A}_i\boldsymbol{E}_i = \boldsymbol{I}_i\boldsymbol{E}_i. \tag{5.96}$$

Between the interfaces of layer i, which has a thickness t_i, the waves propagate along the z direction with a propagation component $e^{\iota k_z z}$. Going from interface i to interface $i-1$, the

eigenfields therefore accumulate a propagation phase that can be expressed in matrix form

$$\boldsymbol{P}_i = \begin{pmatrix} e^{-\iota k^1_{z,i} t_i} & 0 & 0 & 0 \\ 0 & e^{-\iota k^2_{z,i} t_i} & 0 & 0 \\ 0 & 0 & e^{-\iota k^3_{z,i} t_i} & 0 \\ 0 & 0 & 0 & e^{-\iota k^4_{z,i} t_i} \end{pmatrix}. \tag{5.97}$$

The total transfer matrix through layer i can then be expressed as

$$\boldsymbol{T}_i = \boldsymbol{A}_i \boldsymbol{P}_i \boldsymbol{A}_i^{-1}, \tag{5.98}$$

which contains half of the interface matrix on either sides of the layer. For all N stacked layers, we obtain

$$\boldsymbol{T} = \boldsymbol{A}_0 \left[\prod_{i=1}^{N} \boldsymbol{A}_i \boldsymbol{P}_i \boldsymbol{A}_i^{-1} \right] \boldsymbol{A}_{N+1} \tag{5.99}$$

$$= \boldsymbol{L}_1 \boldsymbol{P}_1 \boldsymbol{L}_2 \boldsymbol{P}_2 \ldots \boldsymbol{P}_{N-1} \boldsymbol{L}_N \boldsymbol{P}_N \boldsymbol{L}_{N+1} \tag{5.100}$$

to which the matrices $\boldsymbol{A}$ for the external medium on either side of the stack have been added to complete the first and last interface matrices $\boldsymbol{L}_1$ and $\boldsymbol{L}_{N+1}$. This total transfer matrix defines the relationship between the field vectors outside the multilayered structure

$$\boldsymbol{E}_0 = \boldsymbol{T} \boldsymbol{E}_{N+1}. \tag{5.101}$$

Fig. 5.11 illustrates schematically the computation steps and associated fields in the multilayer structure, along with an example of the application of the formalism to the guided polariton modes in GaSe slabs.

5.3.2 Transmission and reflection coefficients

Considering the field amplitudes on either side of the multilayered structure, Ref. [172] gives the expressions of the transmission and reflection coefficients as a function of the transfer matrix elements. However, the formalism used in Ref. [172] uses a different ordering of the

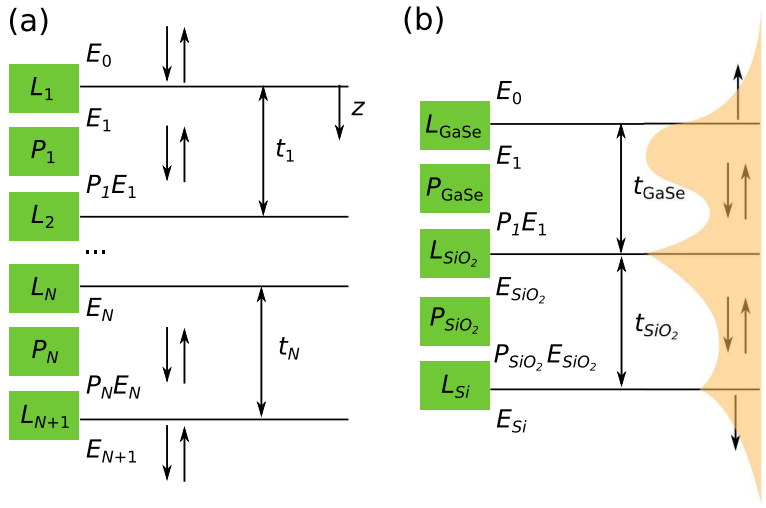

Figure 5.11 Schematic representation of the computation process using the 4×4 matrix formalism. (a) General case, where field $\boldsymbol{E}_0$ at the first interface is transformed into $\boldsymbol{E}_1$ by matrix $\boldsymbol{L}_1$, then propagated through layer 1 by matrix $\boldsymbol{P}_1$, the process being repeated for all N layers until the resulting field $\boldsymbol{E}_{N+1}$ is obtained. (b) Application of the model to guided modes in a slab of GaSe on a Si/SiO_2 substrate, where field amplitudes are sketched along with their allowed propagation directions.

electric field vectors defined as

$$\boldsymbol{E}^* = \begin{pmatrix} E_p^+ \\ E_p^- \\ E_s^+ \\ E_s^- \end{pmatrix}. \tag{5.102}$$

The transfer matrix must be reordered to correspond to that formalism using the following transformation

$$\boldsymbol{T}^* = \boldsymbol{\Lambda}^{-1}\boldsymbol{T}\boldsymbol{\Lambda}, \tag{5.103}$$

where the matrix Λ is defined as

$$\boldsymbol{\Lambda} = \begin{pmatrix} 1 & 0 & 0 & 0 \\ 0 & 0 & 1 & 0 \\ 0 & 1 & 0 & 0 \\ 0 & 0 & 0 & 1 \end{pmatrix}. \tag{5.104}$$

From the components of the reordered matrix $\boldsymbol{T}^*$, the reflection and transmission coefficients can be expressed as [172]

$$r_{pp} = \frac{T^*_{21}T^*_{33} - T^*_{23}T^*_{31}}{T^*_{11}T^*_{33} - T^*_{13}T^*_{31}}, \qquad t_{pp} = \frac{T^*_{33}}{T^*_{11}T^*_{33} - T^*_{13}T^*_{31}}, \tag{5.105}$$

$$r_{ss} = \frac{T^*_{11}T^*_{43} - T^*_{41}T^*_{13}}{T^*_{11}T^*_{33} - T^*_{13}T^*_{31}}, \qquad t_{ss} = \frac{-T^*_{11}}{T^*_{11}T^*_{33} - T^*_{13}T^*_{31}}, \tag{5.106}$$

$$r_{ps} = \frac{T^*_{41}T^*_{33} - T^*_{43}T^*_{31}}{T^*_{11}T^*_{33} - T^*_{13}T^*_{31}}, \qquad t_{ps} = \frac{T^*_{31}}{T^*_{11}T^*_{33} - T^*_{13}T^*_{31}}, \tag{5.107}$$

$$r_{sp} = \frac{T^*_{11}T^*_{23} - T^*_{21}T^*_{13}}{T^*_{11}T^*_{33} - T^*_{13}T^*_{31}}, \qquad t_{sp} = \frac{T^*_{13}}{T^*_{11}T^*_{33} - T^*_{13}T^*_{31}}, \tag{5.108}$$

which correspond to the ratios of incident and reflected (transmitted) components of the field form an incident field on interface $i = 1$ propagating towards positive z, with the first index denoting the s or p polarization of the incident field and the second index the reflected (transmitted) polarization.

5.3.3 Computed polariton dispersion curves

The reflectivity coefficient accurately describes the electrodynamics of the multilayer sample, as resonances in the reflectivity correspond to resonances in the system [172], with the imaginary part corresponding to the guided modes [4, 110, 173, 174]. This can be understood by considering that the poles of the reflectance correspond to eigenstates of energy and momentum in the multilayer system. The eigenstates that correspond to guided modes have imaginary wave vectors outside the layer, thefore they manifest as maxima of the imaginary component of the reflection coefficient. $\mathrm{Im}(r_{pp})$ corresponds to the dispersion of the guided TM and surface modes, while $\mathrm{Im}(r_{ss})$ describes the guided TE modes.

Using the definitions in equations (5.105) and (5.106), and the transformed transfer matrix $\boldsymbol{T}^*$, the polariton dispersion of a slab of GaSe can now be computed by calculating the transfer matrices and reflection coefficients for every frequency and tangential wave vector in a range of interest. In order to minimize computation time, the transfer matrices were computed over a logarithmically spaced wave vector range, ensuring high resolution at low wavenumbers, where highly dispersive behavior occurs, while minimizing computation time for the low dispersion regions at large wave vectors. This approach enables accurate modeling of the full dispersion relation within less than three hours on an average personal computer.

Fig. 5.12 illustrates the imaginary parts of r_{ss} and r_{pp} for a 5 µm thick GaSe slab in vacuum, calculated with damping parameters of $\Gamma_\perp = \Gamma_{/\!/} = 0.5\ \mathrm{cm}^{-1}$. The calculated polariton dispersion determined by the analytical model presented in §5.2 is superimposed onto the

calculated dispersion to verify the accuracy of the numerical model. Note that the s-polarized reflection coefficient corresponds to ordinary (TE) waves, and the p-polarized reflection coefficient corresponds to extraordinary (TM) waves. This result confirming the equivalency between the analytical and numerical results in the simple case of a GaSe slab in vacuum is used as a validating test before applying the numerical approach to more complex multilayer structures, which more accurately describe several of the samples used in this work.

The transfer matrix model makes it simple to take into account the effect of the SiO_2/Si substrate, with the dielectric function of the SiO_2 layer $\epsilon_{SiO_2}(\omega)$ taken from Ref. [175], and the permittivity of the silicon substrate $\epsilon_{Si} = 11.7$ in the modeled frequency range [176]. The resulting dispersion curves including the effect of the substrate are presented on Fig. 5.13. The principal effects of the substrate on the dispersion curves are threefold. First, the guided polariton modes are poorly guided below the light line in silicon, as evidenced by the reduced intensity and broadening of the computed reflection coefficients. Below the Si light line, the waves can propagate into the substrate, which results in a lossy waveguide. Secondly, only one of the two vacuum surface modes is visible in the $\mathrm{Im}(r_{pp})$ plot, corresponding to the vacuum interface of the layer. A weak mode is located above the Si light line, which corresponds to the second surface mode at the substrate interface. Since the SiO_2 layer is very thin, the evanescent field of the mode extends into the Si substrate, and so the mode is only apparent above the Si light line. Finally, the wave vectors of all guided modes are slightly higher (the curves are shifted to the right), since the higher permittivity of the substrate results in a higher confinement in the waveguide.

5.3.4 Guided-mode electric field distributions

Using the intermediate transfer matrices $\boldsymbol{A}_i$ and $\boldsymbol{L}_i$, the magnitude of the electric field can be computed at any position in the multilayer system for a given value of ω and k_x. First, the resulting field in layer $N+1$ is obtained from the system's transmission coefficients, and is then propagated backwards in incremental steps through the multiple layers to determine the field amplitudes at every step.

The effective transmission coefficient can be computed using the transfer matrix elements. Starting from the assumption that all fields outside the system are evanescent (the selection of an appropriate k_x, greater than $\sqrt{\epsilon}\frac{\omega}{c}$ in both of the external media, guarantees this), only fields propagating *away* from the outermost interfaces can be allowed to avoid diverging fields at $z = \pm\infty$ (see Fig. 5.11).

The coefficients t_{pp} and t_{ss} from equations (5.105) and (5.106) define the ratio between an

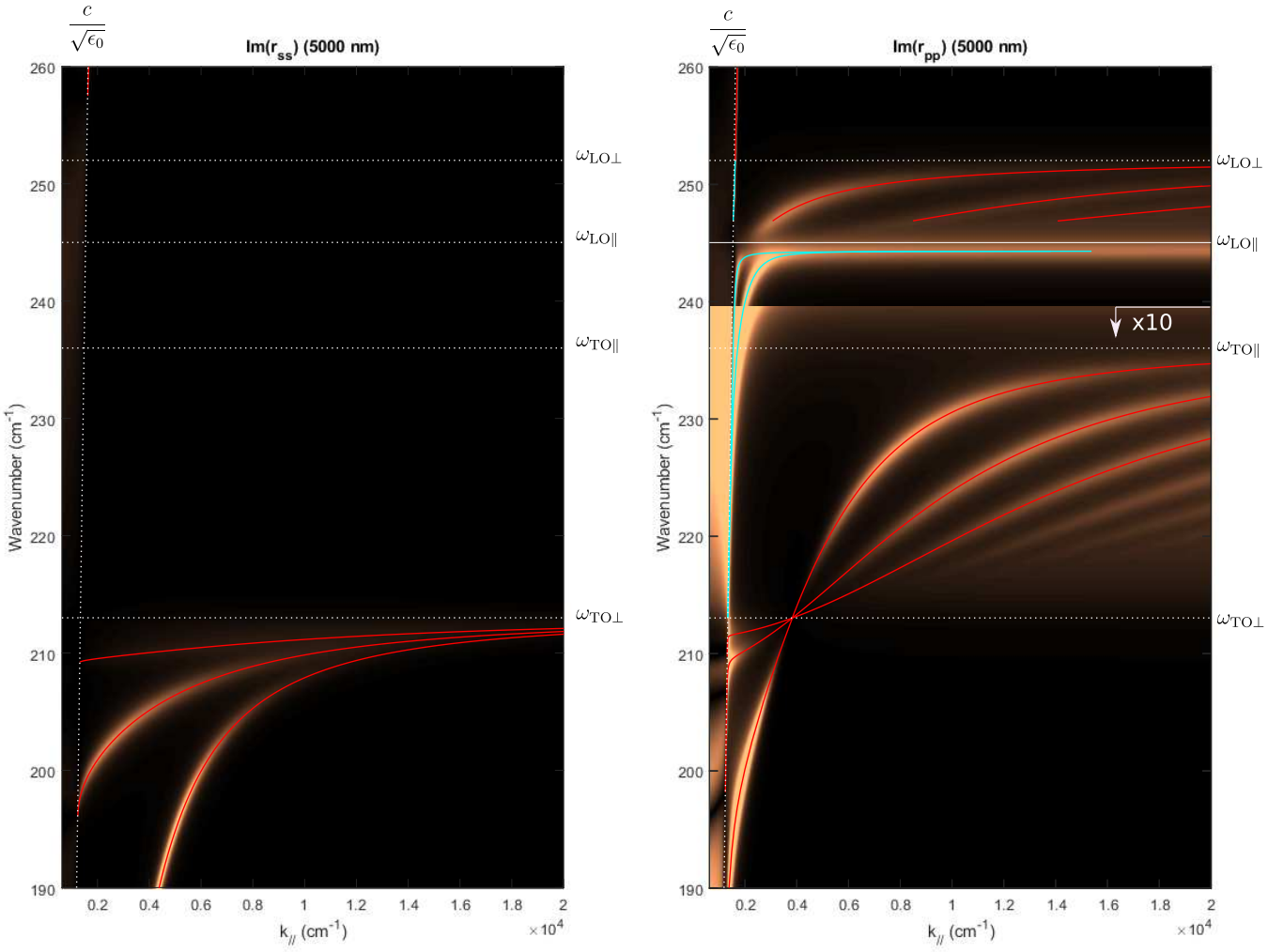

Figure 5.12 Imaginary part of the r_{pp} (right) and r_{ss} (left) reflectivity coefficients for a 5 µm thick slab of GaSe in vacuum. The intensity corresponds to the brightness of the orange color, on a normalized linear scale. The dispersion relations for the first three guided TE, TM (red curves) and surface modes (cyan curves) calculated in §5.2 are superimposed on the image confirming the validity of the computed dispersion relations. The lower portion of the $\mathrm{Im}(r_{pp})$ plot indicated by the arrow is scaled by a factor of 10 to enhance visibility of the weak TM modes. The light lines for vacuum is indicated by a dashed line on the left of each plot, revealing that no modes can be guided below the light line, as the waves can propagate into the vacuum. The energies of the longitudinal and transverse normal modes of GaSe are indicated by the horizontal dashed lines.

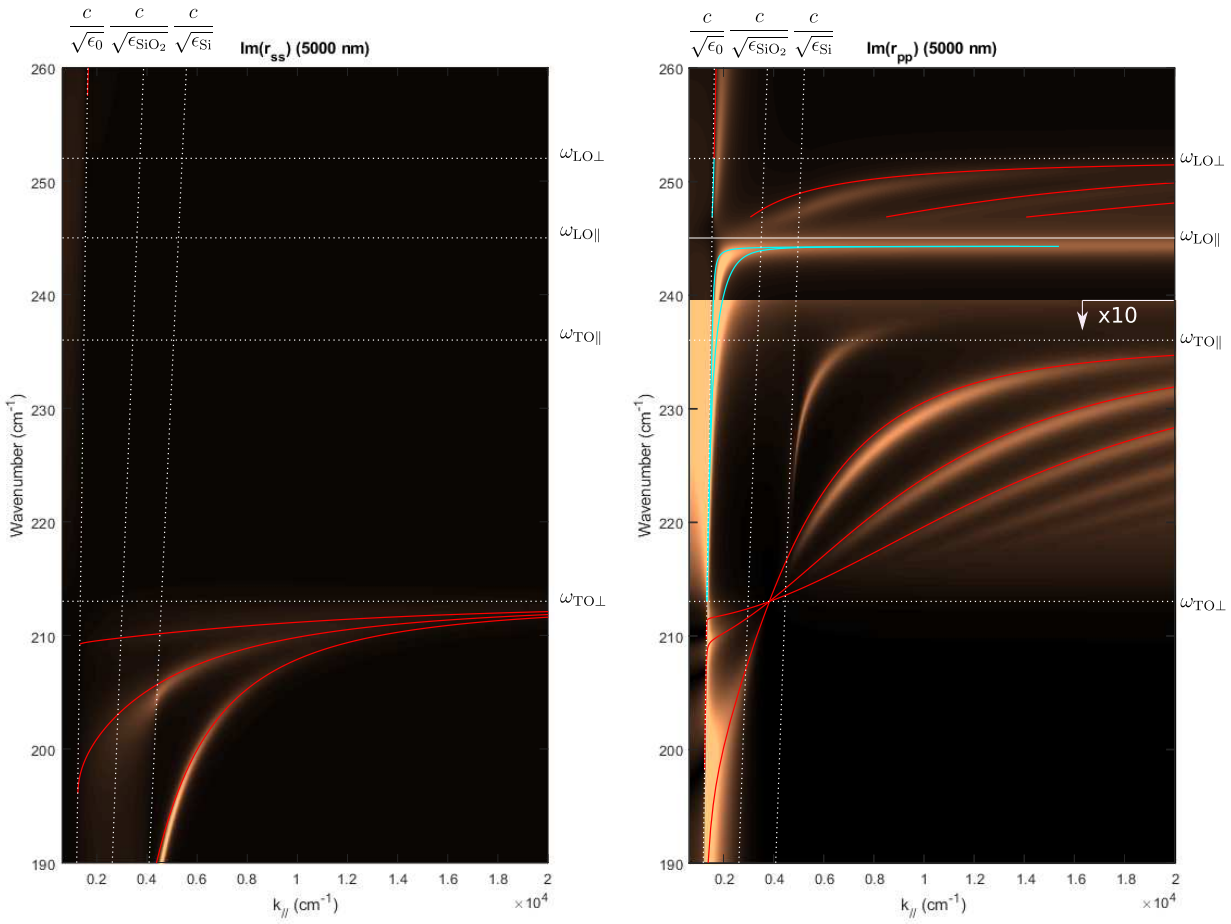

Figure 5.13 Imaginary part of the r_{ss} (left) and r_{pp} (right) reflectivity coefficients for a 5 µm thick slab of GaSe on a Si substrate with 300 nm of thermal oxide. The intensity corresponds to the brightness of the orange color, on a normalized linear scale. The dispersion relations for the first three guided TE, TM (red curves) and surface modes (cyan curves) for a sample in vacuum are superimposed on the image, highlighting the effect of the substrate on the dispersion. The lower portion of the $\mathrm{Im}(r_{pp})$ plot indicated by the arrow is scaled by a factor of 10 to enhance visibility of the weak TM and surface modes. The light lines for vacuum, Si and SiO_2 are indicated by the three dashed lines on the left of each plot. The energies of the longitudinal and transverse normal modes of GaSe are indicated by the horizontal dashed lines.

incident field at the air/GaSe interface and the transmitted field at the SiO_2/Si interface :

$$t_{pp} = \frac{T^*_{33}}{T^*_{11}T^*_{33} - T^*_{13}T^*_{31}} \qquad \text{and} \qquad t_{ss} = \frac{-T^*_{11}}{T^*_{11}T^*_{33} - T^*_{13}T^*_{31}}. \tag{5.109}$$

The electric field in layer $N+1$, which corresponds to the Si substrate, is then set to

$$\boldsymbol{E}_{\text{Si}} = \begin{pmatrix} E^+_{p,N+1} \\ E^-_{p,N+1} \\ E^+_{s,N+1} \\ E^-_{s,N+1} \end{pmatrix} = \begin{pmatrix} t_{pp} \\ 0 \\ t_{ss} \\ 0 \end{pmatrix}. \tag{5.110}$$

Using these initial field expressions, the fields amplitudes at all points in the system can be obtained using the interface matrices $\boldsymbol{A}_i$ between each layer and propagating the field between interfaces using an incremental version of the propagation matrix

$$\boldsymbol{P}_i(z) = \begin{pmatrix} e^{-\iota k^1_{z,i} z} & 0 & 0 & 0 \\ 0 & e^{-\iota k^2_{z,i} z} & 0 & 0 \\ 0 & 0 & e^{-\iota k^3_{z,i} z} & 0 \\ 0 & 0 & 0 & e^{-\iota k^4_{z,i} z} \end{pmatrix}. \tag{5.111}$$

Note that the treatment of the propagation matrix $\boldsymbol{P}_0(z)$ must be adapted, since only the two eigenmodes propagating towards positive z are allowed in the air above the layer (layer $i = 0$). $k^1_{z,0}$ and $k^2_{z,0}$ are set to $-k^1_{z,0}$ and $-k^1_{z,0}$ in order to define $\boldsymbol{P}_0(z)$ for evanescent fields away from the interface.

The resulting total field amplitudes in Cartesian coordinates are then [28]

$$E_x = E^+_p - E^-_p, \tag{5.112}$$

$$E_y = E^+_s + E^-_s, \tag{5.113}$$

$$E_z = \left(-\frac{k_x \epsilon_\perp}{k_{zi1}\epsilon_{/\!/}} E^+_p\right) - \left(-\frac{k_x \epsilon_\perp}{k_{zi3}\epsilon_{/\!/}} E^-_p\right), \tag{5.114}$$

where the negative sign applied to the p-polarized fields accounts for the phase change caused by the reflection of the field.

Fig. 5.14 illustrates the obtained spectral and spatial field distribution for $k_x = 6 \times 10^3\,\text{cm}^{-1}$ in a 5 µm thick GaSe slab on a Si/SiO_2 substrate. The first two guided To, Te and Le polariton modes are clearly visible, as well as the two surface modes. Note that the lower surface polariton (Sp_1) field is distributed throughout the slab with a concentration at the

substrate interface, whereas the upper Sp_2 mode is highly located at the air interface. This explains why only one of the surface modes is strongly affected by the presence of the substrate (see Fig. 5.13).

5.3.5 Modeled Raman spectrum

As presented in Chapter 4, the Raman scattering efficiency of polaritons can be expressed as a function of their electric field. Equation (4.58) derived in §4.3 and reproduced here :

$$I_N(\omega,\theta) = \frac{C(n_\omega+1)}{d}\left|(\hat{e}_i\cdot\widetilde{R}_N\cdot\hat{e}_s)\int_{-d/2}^{d/2} e^{\imath\Delta\boldsymbol{q}_\perp z}\langle E_N(z)\rangle \mathrm{d}z\right|^2 \delta(\Delta\boldsymbol{q}_{/\!/}-k_{/\!/})H_N^E(\omega,\theta) \quad (5.115)$$

enables a direct modeling of the relative scattering efficiency.

The effective Hopfield coefficients $H_N^E(\omega,\theta)$ can be obtained as a function of the polariton propagation direction θ and frequency (see equations (4.39)-(4.41)).

The effective Raman tensor $\widetilde{R}_N$ corresponds to (neglecting the $\boldsymbol{k}$-dependent Fröhlich contribution)

$$\widetilde{R}_N = \overset{\leftrightarrow}{R}_N + \frac{2}{K_N}\overset{\leftrightarrow}{\chi}{}_N^{(2)}, \quad (5.116)$$

which can be defined up to a constant using the Faust-Henry coefficients introduced in Chapter 4 :

$$\frac{R_{\lambda,ij}}{\chi^{(2)}_{\lambda,ij}} = C^{\mathrm{FH}}_{\lambda,ij}\frac{2\omega_{\mathrm{TO}\lambda}}{\sqrt{\epsilon_0(\epsilon_{s\lambda}-\epsilon_{\infty\lambda})}}. \quad (5.117)$$

The value of $C^{\mathrm{FH}}_{\lambda,ij}$ can be determined from the intensity ratio of the TO and LO modes along coordinate λ. Since only the E′ mode is Raman-active in GaSe, there is a single Faust-Henry coefficient $C^{\mathrm{FH}}_{\perp}$ which can be determined from equation (4.47). Using the ratio $I_{LO,\perp}/I_{TO,\perp} = 3.5$ from Ref. [24] yields the solutions $C^{\mathrm{FH}}_{\perp} = \{0.1324, -0.3651\}$. The positive solution corresponds to constructive interference between the mechanical and electro-optic scattering contributions, while the negative solution describes destructive interference. Only one of these solutions is physically valid [152], but the sign of C^{FH} cannot be determined from the LO/TO intensity ratio alone.

Irmer *et al.* [177] presented a method of obtaining the sign of C^{FH} through a detailed analysis of the scattering efficiency of transverse polaritons in near-forward geometry. Results that will be presented in Chapter 8 indicate that the electro-optic scattering contribution interferes

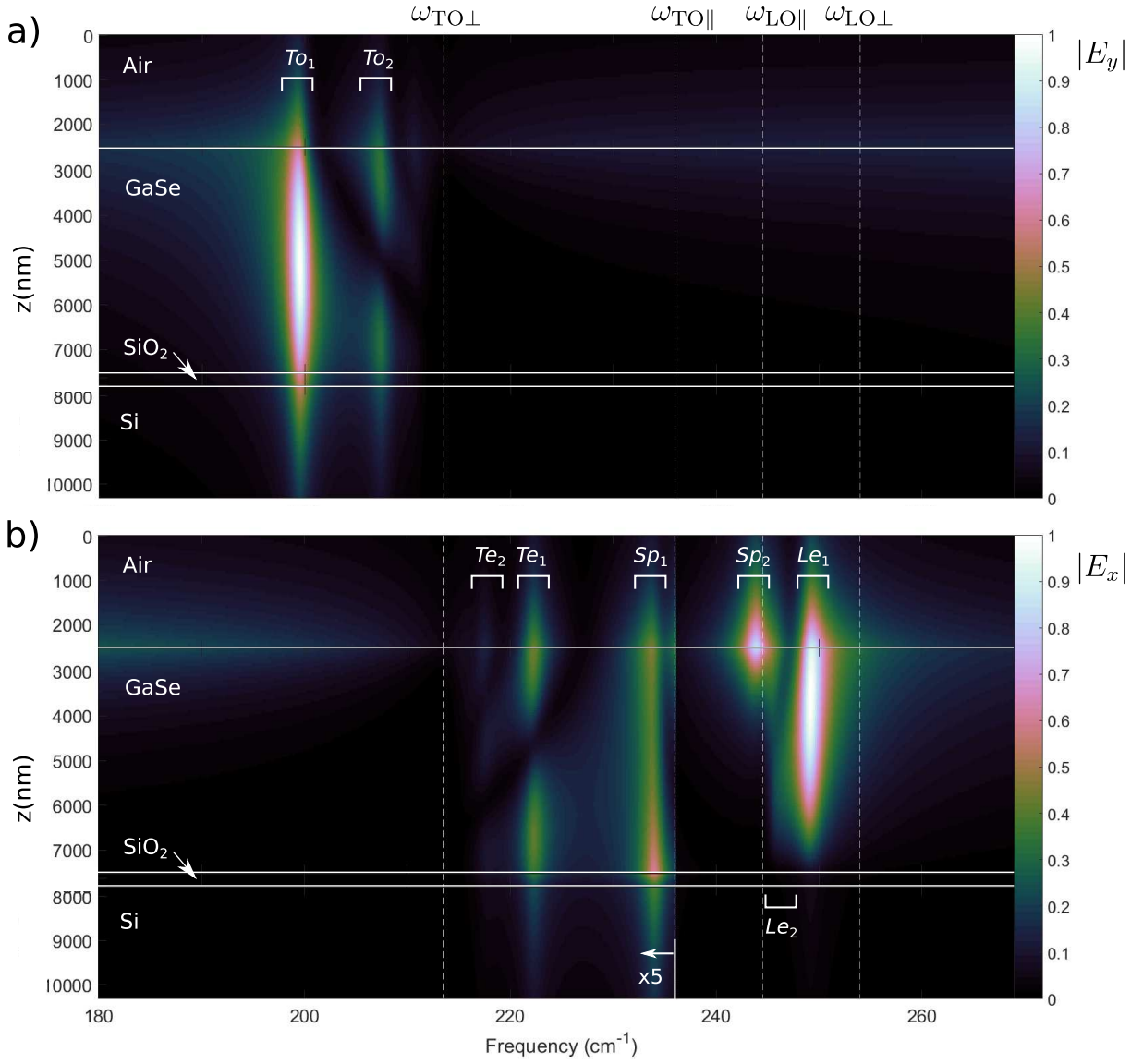

Figure 5.14 Normalized electric field magnitude distribution in a 5 µm thick GaSe slab on a Si/SiO_2 substrate for $k_x = 6 \times 10^3\,\mathrm{cm}^{-1}$. (a) Normalized magnitude of the y component of the electric field, corresponding to TE waves. The two guided transverse ordinary ($To_{1,2}$) polariton modes are indicated by the white brackets. (b) Normalized magnitude of the x component of the electric field, corresponding to TM waves. Field magnitudes below $\omega_{TO\parallel}$ are magnified by a factor of 5 as indicated by the arrow. Guided transverse extraordinary ($Te_{1,2}$) and longitudinal extraordinary ($Le_{1,2}$) as well as the two surface ($Sp_{1,2}$) polariton modes are indicated by the white brackets.

destructively with the mechanical deformation contribution, which corresponds to previous observations in GaSe [24], in GaP [152], and in α-GaN [177]. However, the thin samples used throughout this work often imply a relaxed wave vector conservation, along with the inability to measure scattering involving in-plane propagating photons. Therefore, an exhaustive symmetry analysis such as that proposed by Irmer *et al.* is not feasible here.

Note here that due to the relaxed wave vector conservation in some of the the thin films studied in this work, the scattered polariton propagation direction θ is not well defined. As a first approximation of θ, the momentum might be assumed to be conserved in the scattering process, but this approximation fails for very thin samples, and for large values of $k_{/\!/}$, especially in the case of hyperbolic modes, since propagation angles are restricted to

$$\theta(k \gg \omega/c) = \arctan\sqrt{\left|\frac{\epsilon_{/\!/}}{\epsilon_{\perp}}\right|}. \tag{5.118}$$

The field distributions in the slab are determined for each wavenumber in the range of interest and at every location in the multilayer system using the computational method presented in the previous section. Using the projection defined in §4.3.1 for a polariton wave vector $\boldsymbol{k} = k\,(\sin\theta, 0, \cos\theta)$, the field expressions for the three polariton branches expressed in the lattice cartesian coordinates are

$$\boldsymbol{E}_{To} = \begin{pmatrix} 0 \\ E_y \\ 0 \end{pmatrix}, \quad \boldsymbol{E}_{Te} = \begin{pmatrix} -\cos\theta E_x \\ 0 \\ \sin\theta E_z \end{pmatrix} \quad \text{and} \quad \boldsymbol{E}_{Le} = \begin{pmatrix} \sin\theta E_x \\ 0 \\ \cos\theta E_z \end{pmatrix}. \tag{5.119}$$

The electric field amplitudes then correspond to $\langle E_N \rangle = \sqrt{(E_N^*)^\top E_N}$, where $()^\top$ denotes transposition.

The scattering efficiency described by equation (5.115) has two terms that depend on θ, which can also be expressed as a function of the lattice coordinates. The effective Raman tensors are then

$$\widetilde{R}_{To} = \overset{\leftrightarrow}{\chi}{}^{(2)}_{\perp}\left(1 + \frac{C^{\mathrm{FH}}\omega^2_{\mathrm{TO}\perp}}{\omega^2_{\mathrm{TO}\perp} - \omega^2}\right), \tag{5.120}$$

$$\widetilde{R}_{Te} = \left[-\cos\theta\overset{\leftrightarrow}{\chi}{}^{(2)}_{\perp} + \sin\theta\overset{\leftrightarrow}{\chi}{}^{(2)}_{/\!/}\right]\left(1 + \frac{C^{\mathrm{FH}}\omega^2_{\mathrm{TO}\perp}}{\omega^2_{\mathrm{TO}\perp} - \omega^2}\right), \tag{5.121}$$

$$\widetilde{R}_{Le} = \left[\sin\theta\overset{\leftrightarrow}{\chi}{}^{(2)}_{\perp} + \cos\theta\overset{\leftrightarrow}{\chi}{}^{(2)}_{/\!/}\right]\left(1 + \frac{C^{\mathrm{FH}}\omega^2_{\mathrm{TO}\perp}}{\omega^2_{\mathrm{TO}\perp} - \omega^2}\right), \tag{5.122}$$

where $\overset{\leftrightarrow}{\chi}{}^{(2)}_{/\!/} = \overset{\leftrightarrow}{\chi}{}^{(2)}_{z} = 0$. Note that the second term in the parentheses diverges when $\omega \to$

$\omega_{\mathrm{TO}\perp}$, since the macroscopic electric field tends to zero, but this divergence is canceled out by the effective Hopfield coefficients,

$$H^E_{To}(\omega,\theta) = H^E_{\perp}(\omega) = \frac{h^E_{\perp}}{\epsilon_{\infty\perp}}, \tag{5.123}$$

$$H^E_{Te}(\omega,\theta) = \cos^2\theta H^E_{\perp}(\omega) + \sin^2\theta H^E_{/\!/}(\omega) = \frac{h^E_{\perp}\cos^2\theta}{\epsilon_{\infty\perp}} + \frac{h^E_{/\!/}\sin^2\theta}{\epsilon_{\infty/\!/}}, \tag{5.124}$$

$$H^E_{Le}(\omega,\theta) = \sin^2\theta H^E_{\perp}(\omega) + \cos^2\theta H^E_{/\!/}(\omega) = \frac{h^E_{\perp}\sin^2\theta}{\epsilon_{\infty\perp}} + \frac{h^E_{/\!/}\cos^2\theta}{\epsilon_{\infty/\!/}}, \tag{5.125}$$

$$h^E_{\perp} = \left(1 + \frac{\omega^2_{\mathrm{TO}\perp}(\omega^2_{\mathrm{LO}\perp} - \omega^2_{\mathrm{TO}\perp})}{(\omega^2_{\mathrm{TO}\perp} - \omega^2)^2}\right)^{-1} \qquad h^E_{/\!/} = \left(1 + \frac{\omega^2_{\mathrm{TO}/\!/}(\omega^2_{\mathrm{LO}/\!/} - \omega^2_{\mathrm{TO}/\!/})}{(\omega^2_{\mathrm{TO}/\!/} - \omega^2)^2}\right)^{-1}. \tag{5.126}$$

These coordinate projections can be used to express the total scattering efficiency from all polariton branches for a given scattering geometry relative to the lattice coordinates. Since only the xy plane has non-zero Raman tensors, the total scattering intensity is

$$I_{\perp}(\omega,\theta) = \frac{C(n_\omega+1)}{d}\left|\sum_{\lambda}(\hat{e}_i\cdot\widetilde{R}_{\lambda}\cdot\hat{e}_s)\int_{-d/2}^{d/2} e^{\iota\Delta\boldsymbol{q}_{\perp}z}\langle E_{\lambda}(z)\rangle \mathrm{d}z\right|^2 \delta(\Delta\boldsymbol{q}_{/\!/} - k_{/\!/})H^E_{\perp}(\omega,\theta). \tag{5.127}$$

Note that there is no contribution from the $H^E_{/\!/}$ Hopfield coefficient, as it applies to a forbidden Raman scattering geometry.

For numerical calculations, in order to avoid the diverging term in the effective Raman tensor mentioned above, the scalar component of the tensor $\left(1 + \frac{C^{\mathrm{FH}}\omega^2_{\mathrm{TO}\perp}}{\omega^2_{\mathrm{TO}\perp} - \omega^2}\right)$ is taken out of the squared term and multiplied to the effective Hopfield coefficient, thus avoiding any singularities in the numerical computation :

$$\Xi_{\perp}(\omega) \equiv \left|1 + \frac{C^{\mathrm{FH}}\omega^2_{\mathrm{TO}\perp}}{\omega^2_{\mathrm{TO}\perp} - \omega^2}\right|^2 H^E_{\perp}(\omega) = \frac{\left(\omega^2 - (C^{\mathrm{FH}}+1)\omega^2_{\mathrm{TO}\perp}\right)^2}{\epsilon_{\infty\perp}(\omega^2_{\mathrm{LO}\perp}\omega^2_{\mathrm{TO}\perp} - 2\omega^2_{\mathrm{TO}\perp}\omega^2 + \omega^4)}. \tag{5.128}$$

The scattering intensity from each polariton branch can then be computed as

$$I_N(\omega,\theta) = \frac{C(n_\omega+1)}{d}\left|\sum_{\lambda}(\hat{e}_i\cdot\overset{\leftrightarrow}{\chi}{}^{(2)}_N\cdot\hat{e}_s)\int_{-d/2}^{d/2} e^{\iota\Delta\boldsymbol{q}_{\perp}z}\langle E_N(z)\rangle \mathrm{d}z\right|^2 \delta(\Delta\boldsymbol{q}_{/\!/} - k_{/\!/})\Xi_{\perp}(\omega). \tag{5.129}$$

The overlap integral between the photon and polariton fields of eq. (5.129) can be computed numerically with a trapezoidal approximation using the calculated electric field distributions. In order to correlate the calculated spectra to an experimental configuration, care must be taken when defining the angles $\theta_{i,s}$. Owing to GaSe's optical anisotropy, the incident and scattered photon wave vectors outside the material correspond to ordinary (s) and extraor-

dinary (p) photons inside the material, thus incident and scattered photon polarizations and propagation directions must be taken into account. Example computed Raman spectra for different sample thicknesses and scattering configurations are presented in figures 5.15 and 5.16, assuming photon and polariton propagation in the xz plane.

For near-forward scattering configuration, the exponential term in the integral describes a slowly-varying oscillation, since $\Delta\boldsymbol{q}_\perp = q_i \cos\theta_i - q_s \cos\theta_s \sim 0$, and $q_i \sim q_s$ and $\theta_i \sim \theta_s$. In the case of backscattering, $\theta_s \sim \pi + \theta_i$, and $\Delta\boldsymbol{q}_\perp = 2q_i$, resulting in rapid oscillations with a period of $\sim \pi/q_i$ along z, significantly reducing scattering efficiency from the slowly-varying polariton electric field distribution in the layer, as was pointed out by Mills *et al.* [166]. However, modes that are strongly confined spatially can exhibit efficient backscattering cross-sections if the spatial extent of the field distribution is similar to or smaller than the period of the exponential term.

The value of $k_{/\!/}$ in the backscattering geometry is controlled experimentally by varying the incidence angle θ^{out}, as $k_{/\!/} = \Delta\boldsymbol{q}_{/\!/} = q_i \sin\theta_i - q_s \sin\theta_s = (q_i^{\text{out}} + q_s^{\text{out}}) \sin\theta^{\text{out}}$. The backscattering efficiency from weakly-confined polaritons is low due to the large $\Delta\boldsymbol{q}_\perp$, but reflections from the back surface allow observation of near-forward scattering with very small $\Delta\boldsymbol{q}_\perp$.

The demonstrated ability to model the separate contribution to the scattering efficiency from each polariton branch will prove an essential tool to interpret the experimental results wherein multiple factors contribute to the total scattered intensity. The particularities of the thickness dependency and reflection contribution to the backscattering efficiency will be discussed in further detail in the context of the experimental results presented in Chapter 8.

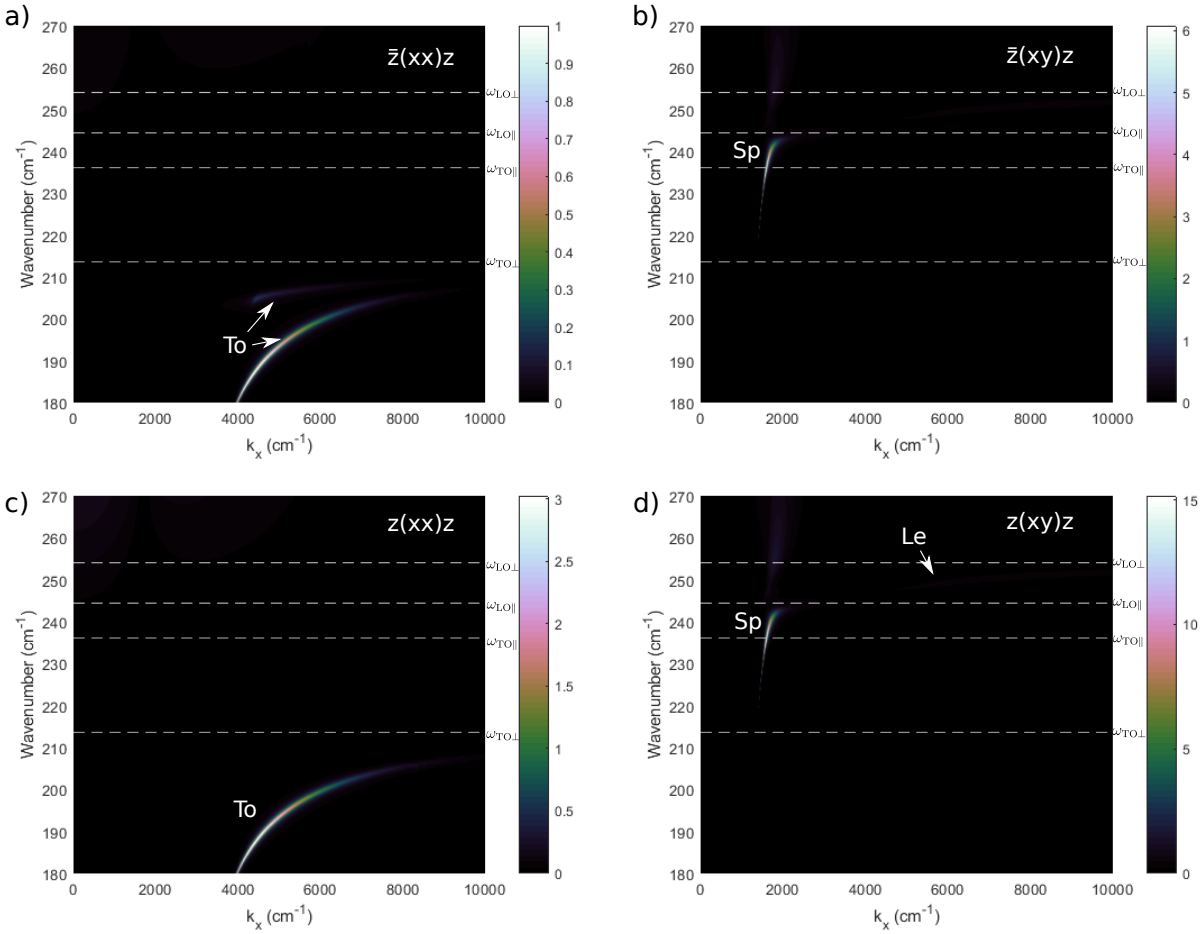

Figure 5.15 Computed Raman scattering efficiency $I_{To} + I_{Te} + I_{Le}$ as a function of k_x for a 5 µm slab of GaSe on a Si/SiO_2 substrate for various experimental configurations. Intensities are all normalized relative to the maximum intensity observed in the $\bar{z}(xx)z$ configuration. (a) Co-polarized backscattering, (b) cross-polarized backscattering, (c) co-polarized reflected backscattering and (d) cross-polarized reflected backscattering. As expected from the effective Raman tensors, the To polariton branch is visible in co-polarized measurements, whereas extraordinary polariton branches are visible in the cross-polarized configurations. The dominant feature in the cross-polarized spectra is the upper surface polariton mode, and the Te and Le polariton branches are barely visible. Furthermore, the relatively large thickness of the sample results in weakly confined polaritons, which translates into a roughly 3:1 ratio between the reflected $(z()z)$ and direct $(\bar{z}()z)$ backscattering intensities.

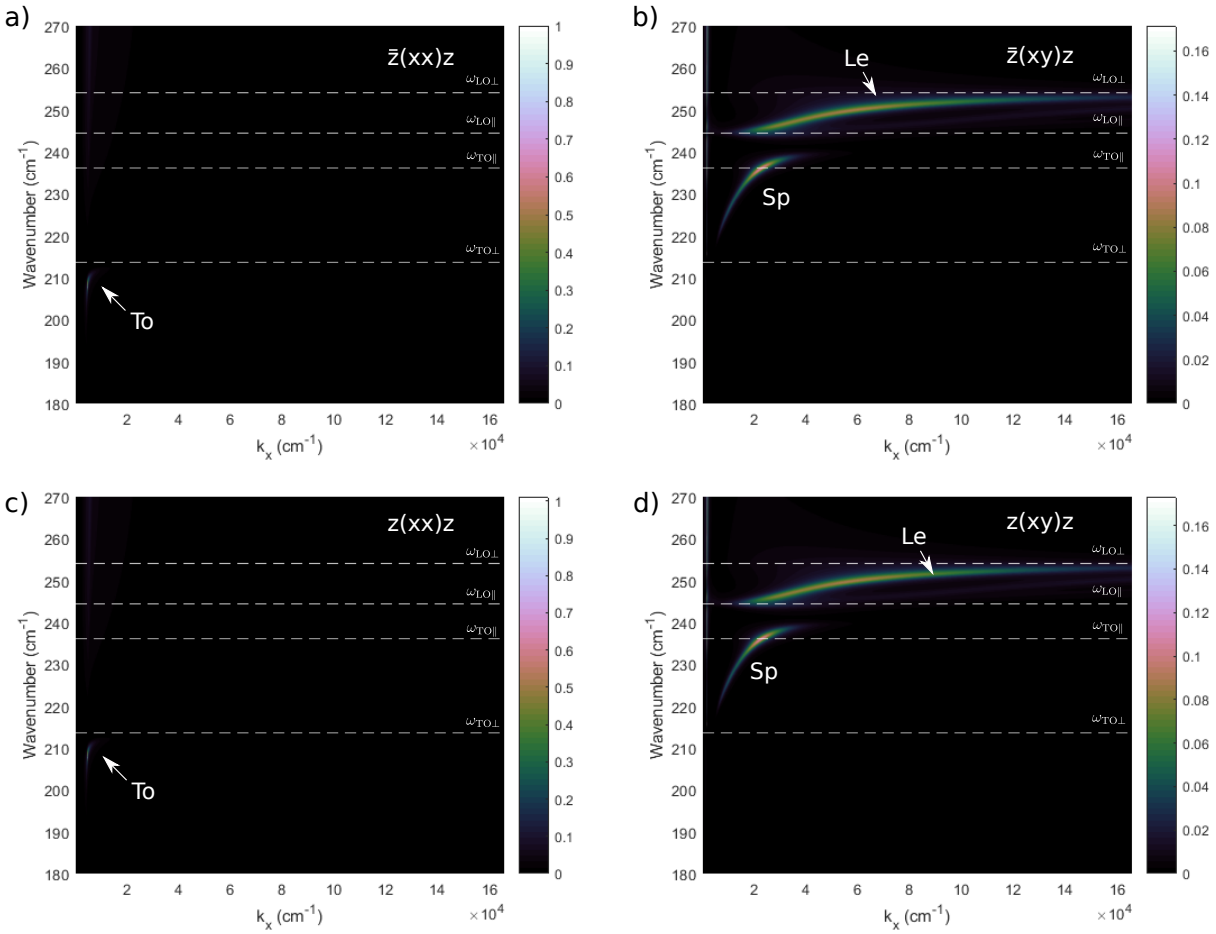

Figure 5.16 Computed Raman scattering efficiency as a function of k_x for a 500 nm slab of GaSe on a Si/SiO_2 substrate for various experimental configurations (note the x-axis scale). The cross-polarized spectra clearly show both the upper surface polariton and Le branch, while the Te polariton branch does not appear. Note how in this case, the small dimension of the sample results in highly confined polaritons, which translates into a roughly 1:1 intensity ratio between reflected and direct backscattering.

CHAPTER 6 SAMPLE PREPARATION AND EXPERIMENTAL TECHNIQUES

This chapter presents the different methods and experimental techniques utilized throughout the project in order to obtain and qualify the data needed to achieve the stated researched objectives and to confirm the validity of the theoretical models presented in chapter 3. The first section details the sample preparation, selection, and protection methods, and the next two section detail the optical techniques and setups used for the back-scattering Raman experiments and the k-resolved Raman imaging.

6.1 Sample preparation and characterization

This section presents the exfoliation method used to obtain nanometer-scale GaSe flakes, along with the different techniques used to evaluate sample thickness and crystalline orientation. Finally, the methods used to prevent unwanted sample oxidation are described.

6.1.1 Bulk crystal source

GaSe samples used throughout this project were sourced from Pr. Richard Leonelli and were produced at Université de Montréal by S. Jandl and J.L. Brebner in 1975 [178]. These crystals were produced by Bridgman growth [179], which yields predominantly crystals of the ϵ-GaSe polytype, although some authors report admixture of a small proportion of the γ-GaSe polytype in such grown crystals [18, 140, 145, 178]. However, the electronic and vibrational properties of these two polytypes are extremely similar, the one major difference relevant to the present work being the Raman selection rule of the A_2'' modes, which are Raman active in γ-GaSe and forbidden in ϵ-GaSe , which will be considered during data analysis.

Sample crystals were cleaved to expose pristine, optically clear and non-oxidized layers several millimeters below the original surface, such as the one shown in Fig. 6.1.

6.1.2 Micromechanical exfoliation

Small flakes were then cleaved off using tweezers and a razor blade and transferred onto a polydimethylsiloxane (PDMS) pad. The tweezers and PDMS pads were thoroughly cleaned with a lint-free wipe and acetone then rinsed with isopropanol and blow-dried with filtered compressed air to minimize the contamination of the samples.

Figure 6.1 (Left) Bulk Bridgeman-grown GaSe crystals used in this work. (Right) Example of a cleaved off flake from the main crystal before exfoliation.

The flakes were then thinned down further via the method of mechanical exfoliation described in Refs. [180] and [181]. It consists in repeatedly pressing down a PDMS stamp onto the flake and transferring part of it to an adjacent location on the pad, and after several cycles of this process, applying the stamp to a silicon wafer with 300 nm of thermal oxide, depositing a large number of GaSe flakes of varying thicknesses at random locations onto the substrate. This process involves a lot of hands-on manipulation, and the resulting flake yield depends significantly on operator technique and experience. Samples thicknesses down to the monolayer were obtained during this work, although their weak optical response and sensitivity to oxidation precluded any significant Raman analysis on the thinnest samples.

6.1.3 Flake thickness evaluation

Optical contrast microscopy was then used to rapidly screen the samples and identify flakes of the required thickness for various experiments. By sweeping over the whole surface of the sample, one can rapidly identify flakes within a certain thickness range by their apparent color, as interference of light reflected within the silicon oxide layer and through the flake yields significant color contrast, enabling almost transparent flakes to be observed optically with relative ease [45]. On the image shown in Fig. 6.2, the various flake colors correspond to different flake thicknesses. The locations of selected flakes were then mapped by a series of reference photos allowing localization for further characterization.

Optical contrast yields rough estimates of the flake thickness, but in order to determine precisely the number of GaSe monolayers in a thin sample, a tapping-mode atomic force microscope (AFM) was used, as it can resolve topography features of less than 1 nm (see Fig. 6.3).

For much thicker samples, on the order of several microns and more, or for freestanding flakes, optical contrast and AFM are not well-suited tools to evaluate their thickness. To

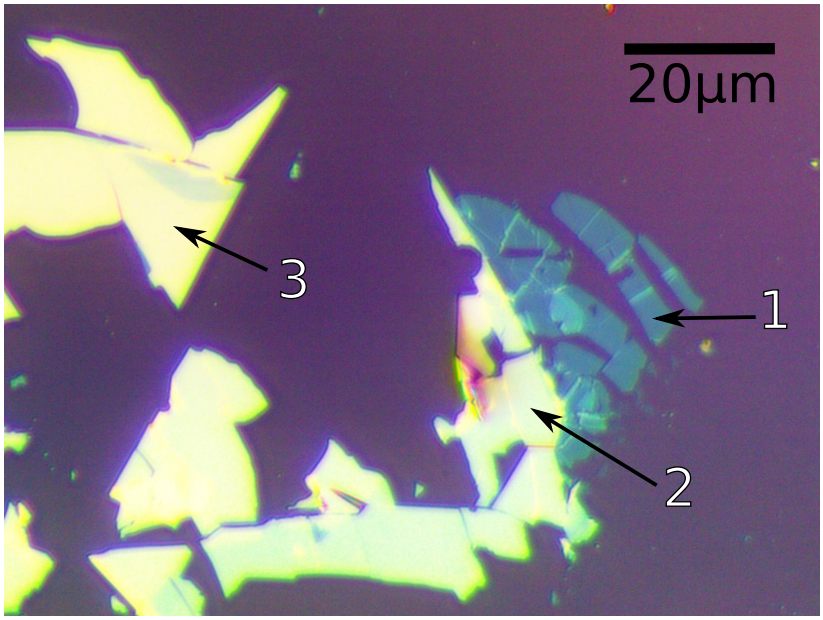

Figure 6.2 Typical result of the micro-mechanical exfoliation process onto a Si/SiO_2 substrate as seen through an optical microscope with a 40x magnification objective. The different observed colors correspond to different thicknesses. Regions 1, 2 and 3 identified by the arrows have thicknesses of 8 nm, 25 nm and 65 nm, respectively, as verified by AFM measurements.

do so, broadband transmission interferometry was used. Samples were illuminated with a broadband incandescent light source and the wavelength-resolved transmittance from 400 to 1200 nm was measured using a fiber-coupled spectrometer. The oscillations of the resulting transmittance spectrum (see Fig. 6.4) were then analyzed to obtain the sample thicknesses [182, 183]. The interference extrema positions are given by $2n_0d = m\lambda_0$, but determination of the order number m is not trivial. By using a second measurement at a known incidence angle θ, with interference extrema following $2n_id\cos\theta = m\lambda_i$, one can determine the order number, along with the sample thickness.

6.1.4 Crystalline orientation

Raman spectroscopy is not a useful tool to determine the in-plane orientation of GaSe flakes as there is an isotropic behavior in the ab plane. In order to determine more precisely the crystalline orientation, the cleaving directions can be used to some degree, but the random nature of mechanical exfoliation does not always cleave samples along well-defined crystal axes.

The second order polarization response can then be modeled as a function of the incident

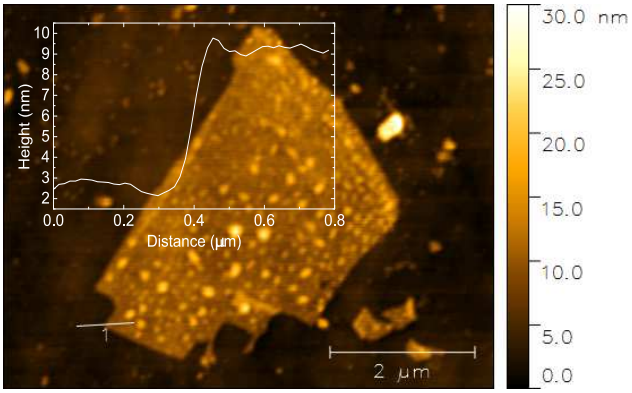

Figure 6.3 Typical AFM topographical image of an exfoliated GaSe flake. Overlaid on the image is a height profile along the white line indicated on the image, revealing the flake has a thickness of approximately 6 nm, which corresponds to 6 GaSe monolayers. The surface of the flake shows an uneven mottling of raised 'bumps', which are caused by accumulation of oxidation byproducts on the sample surface, as the sample was measured in air.

light polarization

$$P_i(2\omega) = \chi_{ijk} E_j(\omega) E_k(\omega). \tag{6.1}$$

For normal incidence of linearly polarized light onto the ab plane of GaSe, this yields a polarization-dependent SHG response of the form $I^{/\!/}_{SHG} \propto d_{22} \sin^2(3\phi)$ for a direct polarization configuration and $I^{\perp}_{SHG} \propto d_{22} \sin^2(3[\phi + \pi/2])$ for a crossed polarization, with ϕ representing the angle between the crystalline a axis and the incident linear polarization [31].

Using these expressions, polarization-resolved second harmonic generation enables rapid determination of a GaSe sample orientation, modulo a $\pi/3$ factor [184]. Figure 6.5 shows the polarization-resolved second-harmonic intensity obtained from a ∼100 nm thick GaSe flake.

6.1.5 Sample protection

In order to avoid sample oxidation, which we discuss in detail in chapter 7, most samples were prepared in a dry nitrogen environment using a positive-pressure glovebox. The exfoliation, optical contrast characterization and AFM measurements could all be performed within this inert atmosphere to guarantee good crystalline and surface quality. Once the flakes were selected and mapped by photographs, the substrate was mounted inside a custom-built optical vacuum cell.

In order to minimize refraction aberrations, the window of the vacuum cell is made from a 16 mm diameter No. 3 (∼300 µm thick) UV fused silica microscope coverslip glass. This

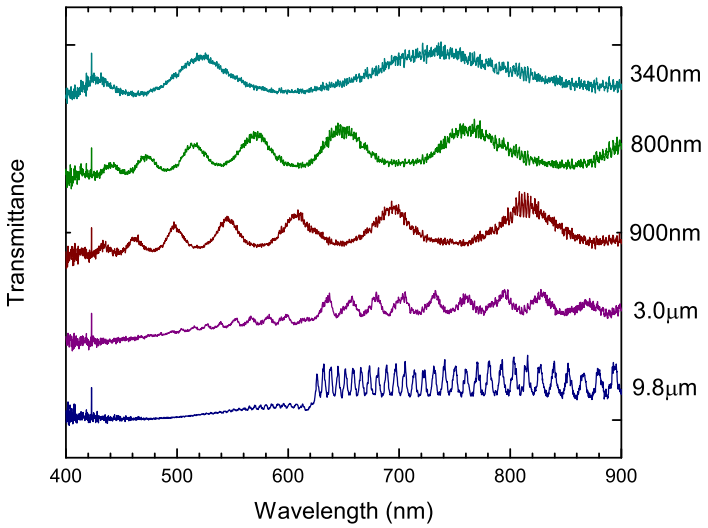

Figure 6.4 Spectral transmission curves obtained for various freestanding flakes at normal incidence. Estimated thicknesses are indicated on the right hand side of each flake. On the lower two curves, the bandgap absorption edge around 620 nm is clearly visible in addition to the interference fringes whereas it is not apparent for thinner samples. This difference is due to the very low absorption coefficient of GaSe for in-plane polarized light.

window is glued with JB-Weld epoxy to the aluminum body of the vacuum cell, in the center of which a circular opening is drilled to a diameter of 6 mm. This opening diameter was determined using a uniformly-loaded plate deflection model [185], restricting maximum deflection under full vacuum to $\leq$1 % of the window thickness to avoid excessive strain-induced polarization response. A spring-loaded adjustable post-mount allows the sample to be positioned less than 1 mm from the window in order to maximize the usable numerical aperture of the system.

Finally, a second custom vacuum cell, presented on Fig. 6.6, was designed for angle-resolved transmission measurements, using the same coverslip glass windows positioned less than 5 mm apart to maximize numerical aperture. The upper window is glued to the aluminum body, and the lower one is clamped onto an elastomer 'o-ring' to provide a vacuum seal while enabling the use of the window itself as a disposable sample substrate.

Once loaded with the sample, the vacuum cell was pumped down to a pressure of $\sim 10^{-3}$ mbar and then rapidly transferred to the optical bench while keeping the window covered with aluminum foil to prevent light exposure. The vacuum cell was then connected to a turbo-molecular vacuum pump and pumped continually during experiments, reaching a steady-state

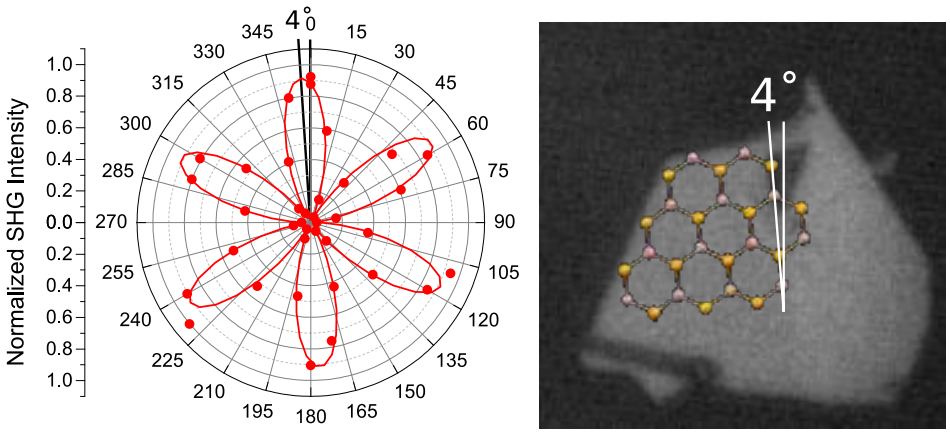

Figure 6.5 (Left) Polarization map of parallel polarization second harmonic generation from ∼300 fs laser pulses from a Ti:Sapphire laser at 875 nm. The solid line is a fit of the data, which shows good agreement with the measured intensity. One of the three symmetry axes of the SHG response (Right) Greyscale optical image of the measured flake with one of the two possible crystalline orientations superimposed on the image.

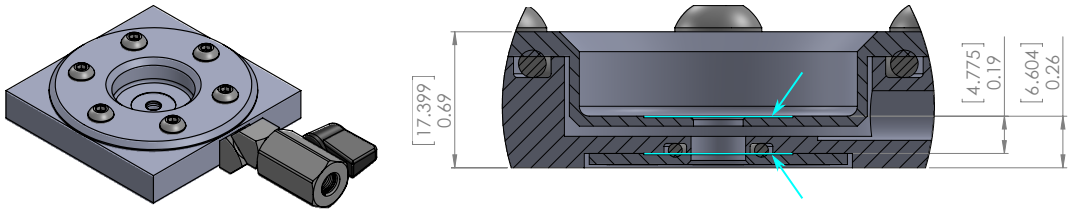

Figure 6.6 Technical drawing of the custom-designed transmission optical vacuum cell. Marked dimensions are in inches [millimeters]. The location of both 300 µm glass coverslip windows is indicated by the cyan arrows.

pressure of approximately $\sim 10^{-5}$ mbar.

6.2 Momentum conservation in Raman scattering

Owing to conservation of momentum, Raman spectroscopy can probe phonons with wave vector magnitudes k in the range $q_i - q_s > k > q_i + q_s$, depending on the experimental configuration, where q_i and q_s are the incident and scattered photon wave vector magnitudes inside the material. Indeed, conservation of momentum imposes that the observed phonon's wave vector be $\boldsymbol{k} = \boldsymbol{q_i} - \boldsymbol{q_s}$, or $k = \sqrt{q_i^2 + q_s^2 - 2q_i q_s \cos(\psi)}$, with ψ being the angle between $\boldsymbol{q_i}$ and $\boldsymbol{q_s}$. For visible incident light, the magnitude of $\boldsymbol{q_i}$ and $\boldsymbol{q_s}$ is approximately $10^5\,\mathrm{cm}^{-1}$, which is roughly 1 % of the size of the material's Brillouin zone.

The polariton dispersion relations presented in the previous section only affect the phonon energies at very low wave vectors, near the Brillouin zone center. For typical polariton energies, with wavenumbers ranging from $\sim 200{-}2000\,\mathrm{cm}^{-1}$, the corresponding wave vectors where polaritonic dispersion effects are observed are in the $k \sim 10^3 - 10^4\,\mathrm{cm}^{-1}$ range, near the lower range of the observable wave vectors in Raman spectroscopy, which are usually accessed through near-forward measurement configurations.

In most Raman measurement configurations, where the incident and scattered photons propagate in significantly different directions, the wave vector $\boldsymbol{k}$ must be large in order to redirect the scattered photon. Only for very small values of ψ (near-forward scattering) will the probed phonon have a wave vector close enough to the Brillouin zone center to observe polaritonic effects. For any other scattering geometry in bulk crystals the observed energies correspond to the non-dispersive regions of the LO and lower TO branches at the extreme right of Fig. 3.4. For high k values beyond this figure, the branches are purely mechanical phonons and show a slowly varying dispersion up to the edge of the Brillouin zone. A schematic depiction of different Raman geometries is illustrated on Fig. 6.7. Note that near-forward scattering conditions can be met in a backscattering experimental configuration if the incident or scattered light is reflected on the rear interface of the sample, which is illustrated on the right of Fig. 6.7.

6.2.1 Momentum conservation in an anisotropic medium

The magnitude of the incident and scattered wave vectors inside the medium are $q_i = 2\pi n_i \sigma_i$ $q_s = 2\pi n_s \sigma_s$, with $\sigma_s = \sigma_i - \sigma_p$ representing the wavenumbers of the scattered photon, incident photon and polariton, respectively. Assuming $\boldsymbol{q}_i /\!\!/ c$, and defining θ_s as the angle between $\boldsymbol{q}_s$ and the c axis, the polariton wave vector can be expressed for arbitrary $\boldsymbol{q}_i$, with angle θ_i relative to the c axis, the resulting expressions for $\boldsymbol{k}$ are then

$$k_{/\!/} = 2\pi \left(n_i \sigma_i \sin\theta_i - n_s(\sigma_i - \sigma_p)\sin\theta_s\right), \tag{6.2}$$

$$k_{\perp} = 2\pi (n_i \sigma_i \cos\theta_i - n_s(\sigma_i - \sigma_p)\cos\theta_s). \tag{6.3}$$

These momentum conservation relations can be used to determine the geometrical selection rules for any scattering geometry and polarization configuration of the slab, by selecting the appropriate values of the refractive indices n_i and n_s, considering the propagation direction and polarization of the incident and scattered photons. The observed propagation angles in the air outside the sample θ_{oi} and θ_{os} can be determined using the method based on the Huygens principle described in Ref. [186]. The relationship between incident and scattered

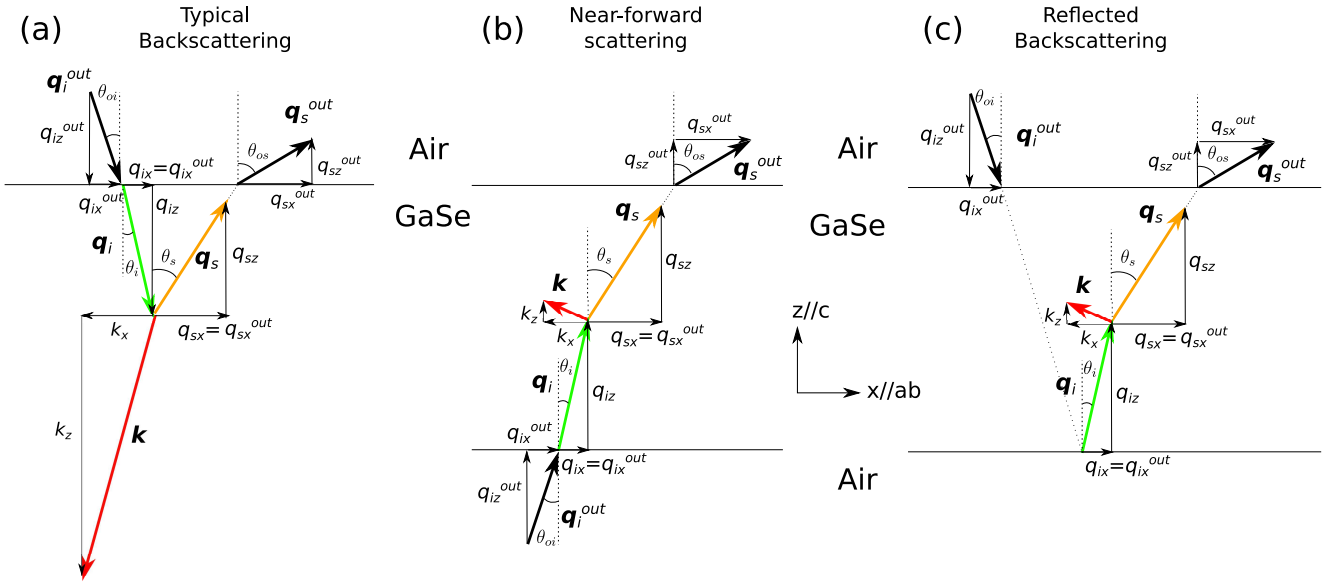

Figure 6.7 Schematical representation of three possible Raman scattering geometries at arbitrary laser incidence angle. $\boldsymbol{q_i}$, $\boldsymbol{q_s}$ and $\boldsymbol{k}$ represent the incident, scattered, and polariton wave vectors, respectively. θ and θ_o are the angles of the incident and scattered beams relative to the z or c axis, with the o indices added to the propagation angles outside the sample. $\boldsymbol{q_i^{out}}$ and $\boldsymbol{q_s^{out}}$ are the photon wave vectors outside the sample. (a) Typical backscattering configuration, where the scattered photon $\boldsymbol{q_s}$ is redirected toward the upper surface of the sample by the large vertical component k_z of the probed polariton wave vector. (b) Near-forward geometry, where the scattered photon's propagation direction is only slightly altered by the small $\boldsymbol{k}$ and exits the sample through the opposing interface. (c) Model of reflected backscattering, wherein the incident photon is first reflected by the lower surface of the sample, which reverses its propagation direction along z, allowing near-forward scattering behavior to be observed in a backscattering experimental configuration. Note that in all cases, the tangential component k_x is can be directly obtained from the external photon wave vectors by evaluating the difference $\vec{k}_x = \vec{q}_{ix}^{\,\text{out}} - \vec{q}_{sx}^{\,\text{out}}$.

angles for GaSe using the refractive index model of Ref. [187] is shown on figure 6.8

For direct backscattering, the polariton wave vector is colinear with the incident and scattered light, and has a magnitude $k = q_i + q_s$ for polarization-maintaining scattering, or $k = \sqrt{q_i^2 + q_s^{\dagger 2} - 2q_i q_s^{\dagger} \cos^2 \psi}$ for cross-polarized scattering, with † indicating the opposite polarization of the two light waves and ψ the angle between the incident and scattered photons inside the sample. The tangential component of $\boldsymbol{k}$ for parallel excitation and detection is given by

$$k_{/\!/} = (q_i^{\text{out}} + q_s^{\text{out}}) \sin \theta_o, \tag{6.4}$$

where $\theta_o = \theta_{io} = \theta_{so} + \pi$. The transverse component $k_\perp$ is given by

$$k_\perp = 2\pi(n_i \sigma_i \cos \theta_i - n_s(\sigma_s) \cos \theta_s), \tag{6.5}$$

which can be computed using the method of Ref. [186]. Both angles and refractive indices are equal for co-polarized measurements but differ for cross-polarized scattering.

For parallel reflected backscattering, the polariton tangential wave vector is the same, but the transverse component and overall momentum is generally much smaller since the sign of $\cos \theta_i$ is changed by the reflection on the bottom surface (see Fig. 6.7), and the transverse component tends to be very small since $\theta_i \sim \theta_s$ and $\sigma_i \sim \sigma_s$. However, in the case of cross-polarized scattering, the birefringence can cause a significant difference between the two angles.

6.3 Backscattering Raman experiments

The modular spectroscopy setup used for backscattering Raman experiments is shown on figure 6.9. The laser sources used are a helium-neon laser at 633 nm with a $\leq$1.5 GHz linewidth [188] and 35 mW nominal output power, which is filtered with a narrow bandpass (1 nm bandwidth) filter to eliminate parasitic cavity modes, and a diode-pumped Nd-YAG single-mode laser at 532 nm with a 1 MHz bandwidth. The laser power is controlled using a broadband half-wave plate and a polarizing cube and measured using a wavelength-calibrated Si diode at the sample position.

The excitation laser (green line on Fig. 6.9) is deflected by a non-polarizing beamsplitter cube with 90% transmission and 10% reflection, with 10% of the intensity being redirected toward the microscope objective. This choice of beamsplitter ensures that a the majority of the collected scattered light reached the spectrometer, at the expense of limited maximum

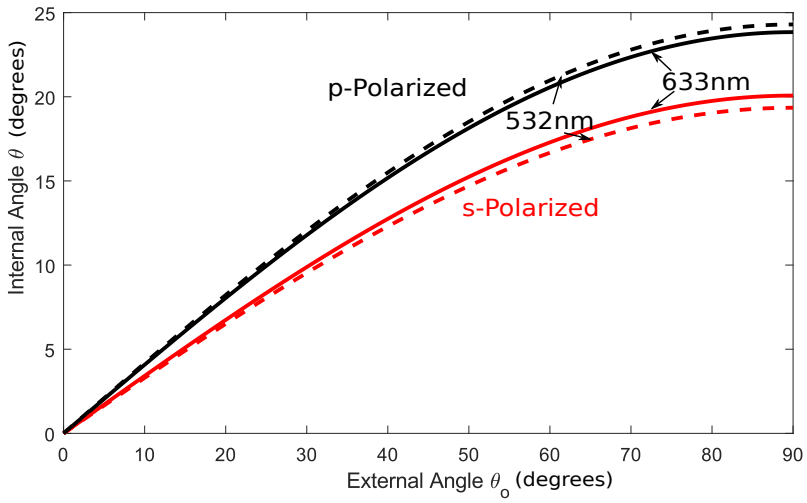

Figure 6.8 Relationship between the internal and external propagation angles (in degrees) for normal incidence of 532 nm (dashed curves) and 633 nm (solid curves) light. The red curves represent s-polarized, or ordinary rays and the black curves correspond to p-polarized or extraordinary rays.

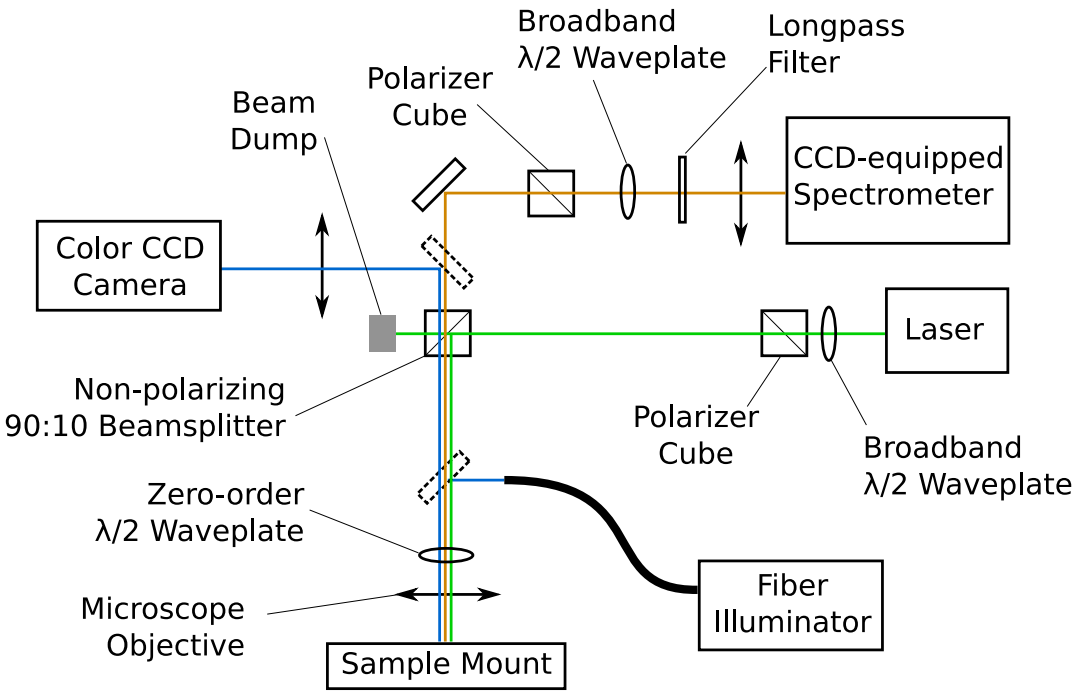

Figure 6.9 Experimental setup used for backscattering Raman experiments.

excitation power.

The light then passes through a zero-order $\lambda/2$ waveplate designed for each laser wavelength, which ensures that the wave retardance at the working wavelength is precisely 0.5λ, to ensure accurate polarization control, which is detailed later in this section.

A 50x 0.55 NA microscope objective with a 9.1 mm working distance is used to focalize the laser onto the sample. The rear entrance pupil of the objective has a 5 mm diameter, and is not entirely filled by the incident laser beam, which must be taken into account when estimating the effective numerical aperture of the excitation laser reaching the sample.

The laser beam has a Gaussian profile with a beam diameter of 1.7 mm, thus the entrance pupil of the microscope objective is 34 % filled, which yields a reduced effective excitation numerical aperture of approximately $\mathrm{NA}_{532} = 0.19$.

The microscope objective is mounted on a vertical translation stage above the sample mount, equipped with a motorized actuator enabling the objective to be moved co-axially along the laser beam, adjusting the focal point onto the sample surface below it.

Scattered light from the sample (orange line on Fig. 6.9) is collected by the same objective. The non-polarizing beamsplitter cube transmits 90% of the collected scattered light, which is then analyzed by a polarizer cube. The linear polarization of the light is then rotated using a broadband half-wave plate to align it with the spectrometer's highest efficiency polarization axis. It is then filtered by a Raman filter. For the 532 nm laser, a steep longpass filter was used, with a 2.7 nm wide transition at 533.3 nm from an optical density greater than 6 to a 93 % transmission, enabling effective observation of Raman scattering down to $\sim$120 cm^{-1}. For the 633 nm laser, a notch filter with a 25 nm wide blocking region centered at 633 nm was used.

The filtered light is then focused onto the entrance slit of the spectrometer using a 35 mm focal length achromatic doublet lens, which slightly underfills the spectrometer's input numerical aperture, minimizing stray light inside its enclosure while maximizing the exposed area of the grating to increase resolving power.

The spectrometer has a 550 mm focal length and a 1800 mm^{-1} holographic grating and is equipped with a 2048x512-13.5 µm pixel liquid nitrogen-cooled CCD camera. The spectral resolution of the system is approximately 0.02 nm.

6.3.1 Calibration

Preliminary calibration was derived from the 532 nm laser peak and the Si single-phonon peak at 520.2(5) cm^{-1} [189], which corresponds to 547.14 nm for 532.00 nm excitation, which were

both simultaneously visible on the CCD detector. A simple linear interpolation was used between these two wavelengths, yielding a general approximation of the measured wavelengths. However, the laser wavelength stability has at times proven unreliable due to thermal fluctuations of the laser head. Furthermore, linear interpolations over a wide wavelength range are inherently inaccurate, as the grating angular dispersion is linear, and the CCD detector is planar, thus a linear interpolation over the detector pixels will introduce a sinusoidal error.

In order to minimize the linear interpolation error, most Raman spectra presented in this work were calibrated using the A_1^1 and A_1^4 GaSe Raman peaks, located at $134\,cm^{-1}$ and $308\,cm^{-1}$, respectively. These wavenumbers correspond to wavelengths of 536 nm and 541 nm (assuming a 532 nm excitation laser), spanning a narrow range of about 5 nm which minimizes interpolation error. The energies of these peaks are well-documented in the literature as is discussed in the next chapter, and they generally exhibit the most intense Raman signal. They are non-polar vibrational modes thus do not exhibit directional dispersion. Their energies do vary slightly as a result of laser-induced sample heating (see §7.3), but this variation was shown to be lower than $0.2\,cm^{-1}$ at the maximal laser intensities used in this work.

Raman intensity calibration was referenced either to the area of the A_1^4 GaSe Raman peak or of the Si single-phonon peak according to the specific purpose of the calibration. Calibration against the A_1^4 peak allows for precise analysis of the relative intensities of the multiple GaSe peaks in order to compare the intensity ratios across several samples or on a single sample over time. The Si peak intensity, on the other hand, enables an absolute intensity reference, as all Si substrates used come from the same source. It could be utilized both as a system alignment yardstick by verifying the signal strength for a given excitation power and as an absolute intensity reference to be compared to the GaSe signal.

6.3.2 Sample identification

A semi-reflective mirror (shown as a dashed outline on Fig. 6.9) positioned on a swing arm above the microscope objective was used to redirect white light (blue line on Fig. 6.9) from an illuminated fiber bundle towards the sample, yielding a broadband off-axis illumination of the sample. An imaging color CCD camera fitted with a zoom lens was used to collect the scattered light, enabling sample observation to locate various regions of interest and sample flakes, along with direct observation of laser focal point location on the sample surface.

6.3.3 Polarization-resolved measurements

Control of the excitation and detection polarizations was achieved using two fixed polarizer cubes and a single zero-order half-wave plate, as shown on Fig. 6.9. This configuration enables acquisition of polarization scans by rotating the half-wave plate while maintaining a constant relative orientation of the excitation and detection polarizations. In the case of this work, both direct(parallel)-polarization and cross-polarization were used. For direct polarization scans, both polarizer cubes are parallel to each other, and the half wave plate rotates the excitation polarization by a certain angle. The collected light scattered by the sample travels through the wave plate backwards, and is thus counter-rotated by the same angle. The collection polarizer (or analyzer) then only lets through scattered light with parallel polarization to the excitation laser for all positions of the half wave plate. Conversely, rotating the analyzer by 90° selects only cross-polarized scattered light.

Polarization control requires precise adjustment of the relative orientation of the polarizer and analyzer cubes and a precisely half-wave plate for polarization rotation. All other optical components were chosen and tested as to have a polarization-independent response to ensure reliable polarization control throughout the experiment.

The polarization-dependent Raman response of the [100] silicon substrate is expected to display a four lobed pattern $I_{\mathrm{Si}} \propto \sin^2(\alpha - 2\phi)$, where α is the angle between the incident and scattered polarizations and ϕ is the rotation angle of the polarization around the [100] axis [190]. The symmetry and intensity contrast obtained from a polarization scan on the Si substrate was used as a performance benchmark of the polarization control system, as can be seen in Fig 6.10. The phase offset between the two polarization configurations is 6.5° smaller than the expected 90°, which is caused by an offset from the desired 90° angle between the polarizer and analyzer during the cross-polarized measurement. The contrast ratios between the fitted curves' maxima and minima confirms the misalignment of the polarizers in the cross-polarized scan, as it is about three times smaller than for the direct polarization scan. The 22:1 contrast observed on the direct scan demonstrates the robustness of the setup, where a single half wave plate rotates both the incident and scattered light. The analyzer cube being orthogonal to the maximal sensitivity polarization of the spectrometer causes a lower overall intensity of the cross-polarized scan, as the grating efficiency is about half its maximum in this configuration, which highlights the necessity of adding a half wave plate before the spectrometer to rotate the polarization to the grating's maximum response. These results demonstrate both the sensitivity of polarization-resolved Raman scattering on silicon to the alignment of the polarization optics, and the setup's ability to precisely control incident and scattered polarizations.

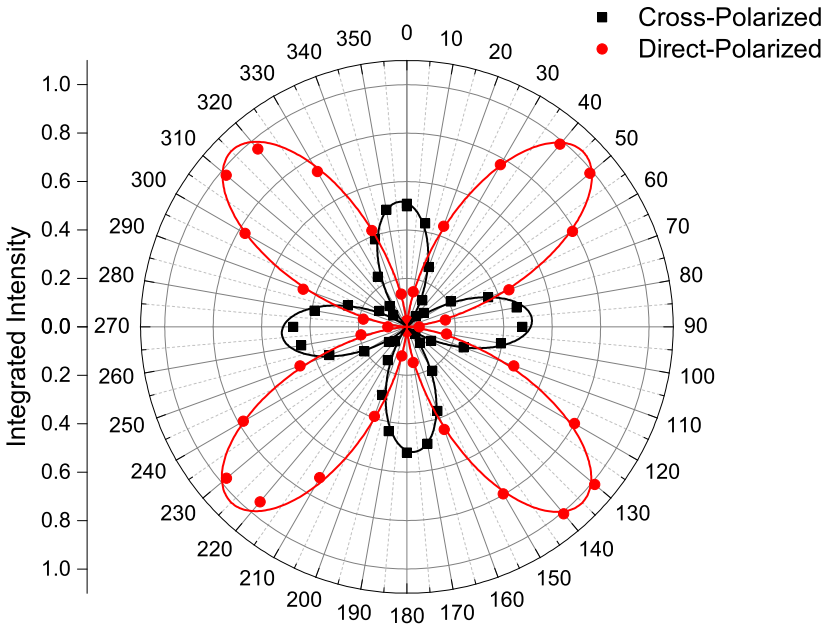

Figure 6.10 Integrated Raman intensity polarization scan for direct (red circles) and cross-polarized (black squares) configurations on a [100] silicon substrate. The intensity is normalized to the direct scan maximum intensity. Solid lines are fits of squared sines, showing a 83.5° phase offset and a 22:1 and 7:1 contrast ratio for the direct and cross-polarized curves, respectively.

6.3.4 Angle-resolved measurements

Several optical measurements in this work were made in the standard backscattering geometry, with the optical axis normal to the sample surface, but extensive work was also done to study the various angular dependencies of GaSe's optical properties.

The sample stage was equipped with an in-plane x-y translation stage, along with a two-axis gimbal rotation platform, with the θ and ψ axes of rotation tangent to the sample surface and co-linear with the optical axis respectively to allow the sample to remain in view and in focus when rotated (see Fig. 6.11). The mount could also be adapted to fit the custom vacuum cell, retaining θ adjustment ability only.

Precise control of the laser spot location was impaired at high incidence angles for several reasons. At high incidence angles, the laser spot becomes laterally spread perpendicular to the tilt axis, as the sample intersects the focal region diagonally, and accurate location of its center can prove difficult. For extreme angles, larger than $\sim$30°, the specular reflection of the

laser beam and illumination light land outside the acceptance cone of the objective. The laser spot can be located on a sample using its diffuse reflection and/or reflections on the sample edges or surface defects, at a cost in accuracy. Also, illumination through the microscope objective for imaging becomes impossible at these angles, and an LED flashlight was used to illuminate the sample so that the reflected light could be collected by the objective. Imaging quality using this technique is inferior to in-line illumination through the objective, which also hinders accurate positioning of the laser spot on the sample.

Considering these limits on the attainable laser position precision at high incidence angles, only large-area flakes were used for detailed angle-resolved measurements, in order to minimize the effects of positioning errors.

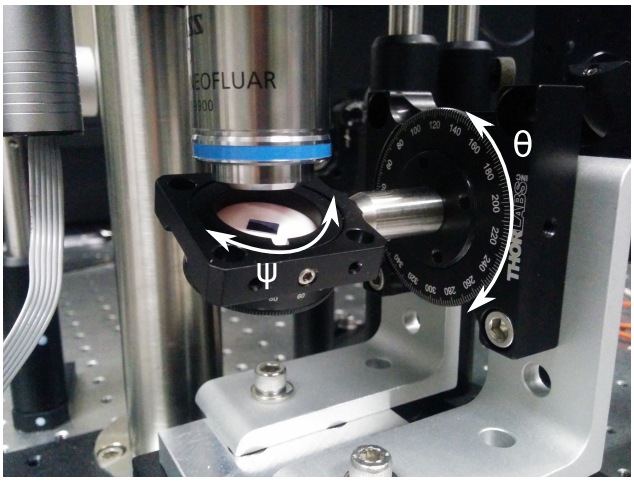

Figure 6.11 Rotational mount used for angle-resolved measurements allowing independent control of two angles θ and ψ.

6.4 Near-Forward scattering

In order to probe low wave vector phonons with Raman spectroscopy, the difference between the incident and scattered photon wave vectors must be small. Indeed, momentum conservation implies that the phonon wave vector $\boldsymbol{k}$ must be equal and opposite to the momentum variation between the incident and Raman-scattered phonons $\Delta\boldsymbol{q} = \boldsymbol{q}_L - \boldsymbol{q}_S$. Therefore, a given scattering geometry will involve phonons in specific regions of the Brillouin zone. More precisely, for a visible (∼500-600 nm) excitation laser and a medium (such as GaSe) with a permittivity of approximately $\epsilon = 3$, backscattering Raman measurements probe phonons with $\boldsymbol{k} \sim 2\boldsymbol{q}_L \sim 5 \times 10^6$ cm^{-1}.

In order to probe lower wave vector phonons, thus minimize $\Delta\boldsymbol{q}$, the incident and scattered

phonons must be almost co-linear, with the laser entering the sample from one side and the scattered light exiting on the other. This configuration of near-forward Raman spectroscopy involves low-$\boldsymbol{k}$ phonons, with wave vectors ranging from 0 to $\sim 5 \times 10^4$ cm^{-1} depending on the scattering angle.

Since the photons need to propagate through the whole thickness of the sample to be detected, the working wavelength needs to be chosen so that the sample will be mostly transparent to it. The sample also needs to be either freestanding or mounted onto a transparent substrate. In this work, freestanding samples with thicknesses between 10 and 100 µm were used for near-forward scattering experiments. The laser source was a 15 mW He-Ne laser emitting at 632.8 nm, which is below the optical band gap of GaSe and thus propagates through the sample with minimal absorption losses.

6.4.1 k-space imaging

In order to resolve the different wave vectors of the scattered phonons, a k-space imaging optical setup was used for the collection of scattered light. The laser, with a beam diameter of 1.22 mm, was first passed through a narrow bandpass filter to eliminate any harmonics of the laser cavity or weak discharge light, then was reduced to a diameter of ∼300 µm using an achromatic doublet pair beam reducer.

The collimated beam was aimed directly at the sample without focusing it to ensure all incident photons have the same wave vector. Scattered light was collected on the opposite side of the sample with a 10x, 0.25NA infinity-corrected microscope objective. The back focal plane (BFP), or Fourier plane, of this objective images each scattered wave vector orientation at a different spatial location. This k-space image of the scattered light is then magnified and projected onto the spectrometer entrance slit using four achromatic doublet lenses of focal lengths $f_1 = 100$ mm, $f_2 = 150$ mm, $f_3 = 75$ mm, and $f_4 = 150$ mm, as shown in Fig. 6.12.

Since the sample is isotropic in the ab plane, the scattering intensity pattern exhibits a rotational symmetry around the c axis, which is aligned with the optical axis of the setup. The projected image on the slit therefore also has a circular symmetry centered on the optical axis, with a proportional equivalence between the radius and the scattered photon wave vector angle relative to that axis. As is shown on the right of Fig. 6.12, the spectrometer entrance slit intersects the center of this circular image. The vertical position on the slit therefore corresponds to the scattering angle.

The microscope objective has an effective focal length of $f_O = 18$ mm, and the back focal

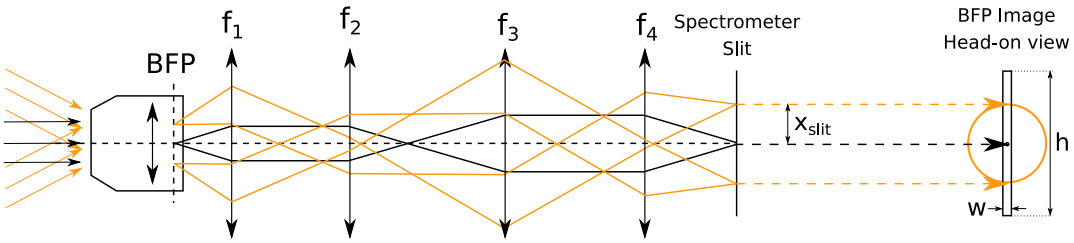

Figure 6.12 Schematic of the back focal plane imaging system used for k-space imaging near-forward Raman measurements. Black lines illustrate the imaging of incident rays parallel to the optical axis (corresponding to $k_{\parallel} = 0$) and orange lines illustrate the imaging of incident oblique rays. Due to the cylindrical symmetry of the system, the image on the spectrometer slit for a given incidence angle θ is a circle of radius x_{slit} as defined by equation (6.7), as is illustrated on the head-on view of the spectrometer slit of width w and height h.

plane spatial dispersion is

$$x_{\text{BFP}} = f_O \tan\theta_s, \tag{6.6}$$

with θ_s the scattering angle outside the sample with respect to the optical axis. The four lenses yield a total image magnification of $G_T = G_{12}G_{34} = f_2/f_1 \times f_4/f_3 = 3$. This results in a dispersion of

$$x_{\text{slit}} = G_T f_O \tan\theta_s \tag{6.7}$$

onto the entrance slit. Knowing that the tangential component of the wave vector is preserved by refraction through an interface, we can determine the tangential component of the scattered photon inside the sample

$$q_{s/\!/}^{(\text{GaSe})} = q_{s/\!/}^{(\text{air})} = |\boldsymbol{q}_{\boldsymbol{s}}^{(\text{air})}| \sin\theta_s. \tag{6.8}$$

Since the incident laser beam is colinear to the optical axis, it possesses no tangential momentum. Therefore, the tangential component of the scattered photon is exactly equal and opposed to that of the scattered phonon $k_{/\!/} = q_{s/\!/}^{(\text{air})}$.

Using the above relationships, a direct correspondence between the vertical position on the slit and the phonon tangential wave vector component can be calculated. Then, since the Czerny-Turner spectrometer configuration images the vertical entrance slit onto the CCD detector (taking into account the spectrometer's magnification factor of 1.1), the vertical axis of the obtained image directly corresponds to the phonon $k_{/\!/}$ (which corresponds to k_x in the models presented in the previous chapter), and the horizontal axis is the wavelength

dispersion. The resulting images are single-acquisition maps of the dispersion relation over a particular wave number and wave vector range.

The signals obtained with this measurement technique are very weak compared with standard backscattering measurements due to several reasons. The laser energy at 632.8 nm, being lower than the bandgap of GaSe, along with the forbidden electronic transition for in-plane polarized light, has a low scattering efficiency. Also, the masking of the vast majority of the 5 mm disc of collected light by the 100 µm wide and 5 mm tall entrance slit only lets about 2.5 % of the light into the spectrometer. In order to obtain satisfactory signal to noise ratios, the 512 vertical pixels of the CCD detector were binned into 32 16-pixel high bands, each corresponding to a specific tangential wave vector range. Total acquisition times up to 10 hours were needed to obtain satisfactory signal to noise ratios, averaging several hundred distinct 100 s acquisitions. In order to minimize readout noise of the CCD array, the analog-to-digital converter was set to its minimum speed.

In order to evaluate the reliability of the imaging system and to rule out any image-deforming effects that would skew the values of the measured wavenumbers, a thin layer < 1 mm of carbon disulfide (CS_2), a compound with a well-known strong Raman line at aroud 650 cm^{-1} [191] was sealed between two fused silica glass slides using silicone grease and placed on the sample mount. CS_2 being a liquid, the averaged Raman response for any observed mode must have complete rotational symmetry around the optical axis, therefore any observed directional dispersion observed in in its spectrum is artificially induced by the instrumental response. Back focal plane Raman scattering images revealed a lateral shear deformation of the image plane, possibly due to a slight misalignment between the collection optics and the spectrometer optical axis, or a radial or angular misalignment between the illumination laser beam and the collection system. Due to the very low scattering intensity from the small probed volume and low acquisition time, the Raman signal from the CS_2 sample, highlighted by a dotted red line, is barely visible on Fig. 6.13a. In order to guarantee the robustness of the results, a krypton arc calibration lamp placed in the focal plane of the microscope objective. The vertical discharge tube of the lamp spanned a length of approximately 10 cm, guaranteeing that the objective's back focal plane was completely and uniformly filled by the tube's illumination. Using this bright source with narrow spectral features enabled high contrast images to be acquired in a few seconds for calibration purposes (see Fig. 6.13c). The resulting images were then analyzed to determine the appropriate coefficients to use in a 2D shear affine transformation matrix to correct the shear distortion. Resulting corrected images are shown on Fig. 6.13b and 6.13d, revealing that the applied shear transformation significantly reduces image deformation.

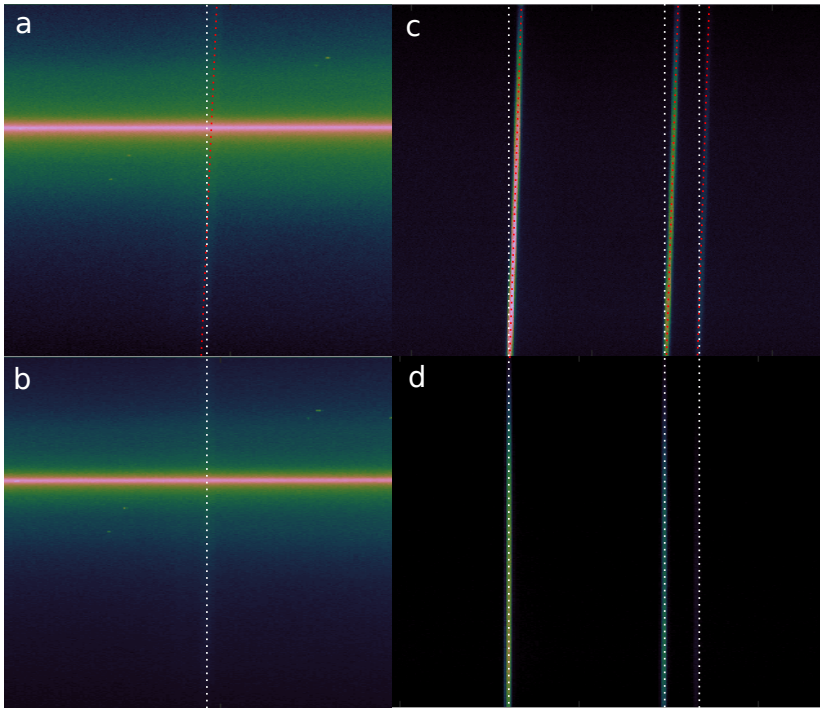

Figure 6.13 Image plane distortion observed for (a) CS_2 Raman scattering and (b) Kr calibration lamp, indicating a deformation of the back focal plane image (see red dotted lines). The images illustrate narrow vertical bands of the CCD detector, about 100 pixels wide, and span the full 512 pixel height of the detector. Using this data, the measured spectra were corrected using a shearing 2D affine transformation matrix, yielding the images presented in (b) and (d). Vertical white dotted lines were added as a guide to the eye to illustrate the expected position of the observed spectral lines on the camera detector.

Closer inspection of the linearly-corrected images reveals another subtle deformation in the image plane, as evidenced by the curvature of the CS_2 wavenumber offset shown as blue stars in Fig. 6.14. This effect, although much smaller than the first-order shear described in the previous paragraph, also has to be corrected in order to extract useable data from the back focal plane imaging data. In order to guarantee an accurate correction for each measurement, and assuming that the observed deformations are caused by slight misalignments of the various elements in the setup, a reliable non-dispersive calibration etalon for each individual signal acquisition is desired. The A_1^1 totally symmetric vibrational mode of GaSe, which has a strong signal in all near-forward measurements presented in this work, proves to be an ideal reference line for calibration, exhibiting a very similar wavenumber offset as the CS_2 reference line as shown by the black squares in Fig. 6.14. A second-order polynomial fit on the observed A_1^1 wavenumbers (see solid black line in Fig. 6.14) was thus used as an accurate second-order image plane correction for each individual data acquisition.

Repeated measurements revealed that the exact amount of shear deformation is highly sensitive to minute changes in the alignment, highlighting the need for a calibration reference in each measurement. This is evidenced by the slight linear offset seen in the laser sideband line in Fig. 6.14, which is expected to show no angular dispersion but was not fully corrected by the application of the shear transformation using the parameters derived from previous measurements on CS_2 and the Kr lamp.

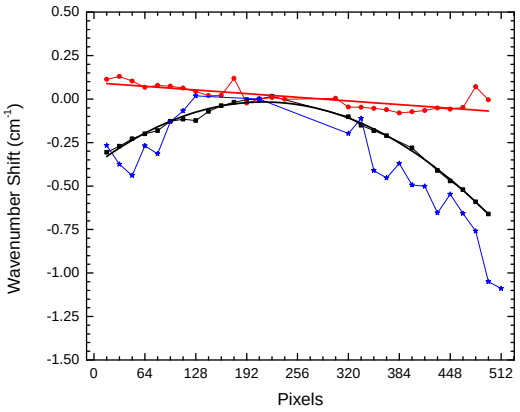

Figure 6.14 Wavenumber offset relative to the center ($\theta = 0$) wavenumber for Raman scattering of CS_2 (blue stars), and GaSe A_1^1 vibrational mode (black squares, black solid line illustrates a second-order polynomial fit of the data). The wavenumber offset from one of the He-Ne laser sidebands from a different acquisition is also illustrated as red circles, along with a linear regression on these data points (solid red line). All illustrated data points were previously corrected using the first-order shear transformation matrix method described earlier using the parameters obtained from the CS_2 Raman and Kr lamp measurements.

CHAPTER 7 PHOTO-OXIDATION OF THIN GALLIUM SELENIDE

Like most 2D materials, the properties of GaSe sensitively depend on the interaction of its surface with its chemical environment. In bulk form, GaSe is generally considered as a stable material and is known to have a high laser damage threshold suitable for non-linear optics applications [44,192]. Nonetheless, bulk GaSe is also known to naturally form a native oxide [193] and thermally- and photo-induced oxidation has been reported [194–196]. More recently, exposure to intense laser light was found to degrade optical properties and lead to chemical transformations [66, 197, 198]. In order to probe phonon-polaritons in GaSe using Raman spectroscopy, it is critical to understand the oxidation dynamics of the material when exposed to the laser light used for such measurements and to determine the conditions in which this oxidation can be suppressed or at least minimized.

In this chapter, we monitor the complex oxidation dynamics of thin GaSe exposed to laser irradiation and identify the emergence of several oxidation products using Raman spectroscopy. Indeed, in addition to the complex Raman spectrum of pristine GaSe presented in the previous chapter, several unassigned Raman features were observed on a large number of exfoliated samples. These Raman peaks, discussed in detail in this chapter, are linked to various oxidation products of gallium selenide, and can serve as a precise fingerprint of sample oxidation.

7.1 Evidence of laser-induced sample damage

GaSe samples were exposed to $6\,\mathrm{mW\,\mu m^{-2}}$ of radiation at 532 nm, about 230 meV above the bandgap of GaSe. This illumination fluence corresponds to about 6 % of the established laser damage threshold for nanosecond pulses at 620 nm [199], which corresponds to the excitonic absorption edge of GaSe [44].

7.1.1 Raman signature of laser damage

Fig. 7.1 presents the evolution of the Raman spectrum as a function of exposure time for a 45 nm thick GaSe sample in air. Freshly exfoliated GaSe measured in vacuum (pristine GaSe) presents the usual dominant Raman modes expected from bulk GaSe for normal-incidence backscattering measurements [18, 47, 178]: A_1^1 at $134\,\mathrm{cm^{-1}}$, $E_1'(TO)$ at $214\,\mathrm{cm^{-1}}$, and A_1^4 at $308\,\mathrm{cm^{-1}}$. Two other vibrational modes associated to bulk GaSe are located between $236\,\mathrm{cm^{-1}}$ and $246\,\mathrm{cm^{-1}}$ are also observed in some pristine samples, and they are linked to phonon-polariton thin slab modes, which will be discussed in the next chapter.

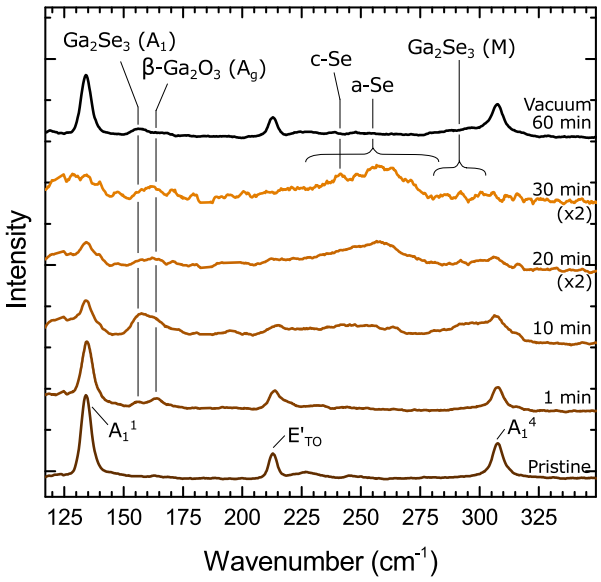

Figure 7.1 Evolution of the Raman spectrum of a 45 nm-thick GaSe sample in air as a function of exposure time to a 6 mW µm^{-2} radiation at 532 nm. Pristine refers to a second sample measured in vacuum immediately after exfoliation; the topmost curve is a spectrum obtained after 60 min of 6 mW µm^{-2} exposure in vacuum of the same sample. Reprinted from [29] published by AIP Publishing.

The Raman spectrum evolves significantly as a function of laser exposure time. The intensity of all features associated with GaSe rapidly decreases and several additional Raman modes appear at frequencies of 155 cm^{-1}, 161 cm^{-1}, 257 cm^{-1} and 282 cm^{-1}. All GaSe vibrational modes are already accounted for [18, 47] and none of these additional features can be related to any of the known GaSe polytypes. They are attributed to a photo-induced chemical transformation of GaSe and corresponds to Raman scattering from several oxidation by-products of GaSe: Ga_2Se_3, Ga_2O_3 and selenium.

7.1.2 Photoluminescence signature of laser damage

The observed degradation of the Raman intensity is also accompanied by a complete loss of the photoluminescence intensity as shown in Fig. 7.2. The well-defined and relatively narrow emission decreases in intensity and is gradually replaced by a very broad emission uncharacteristic of a high-quality semiconductor. After 30 min of laser exposure in air, the initial luminescence signal has disappeared, as the crystal structure has been greatly affected by the oxidation process.

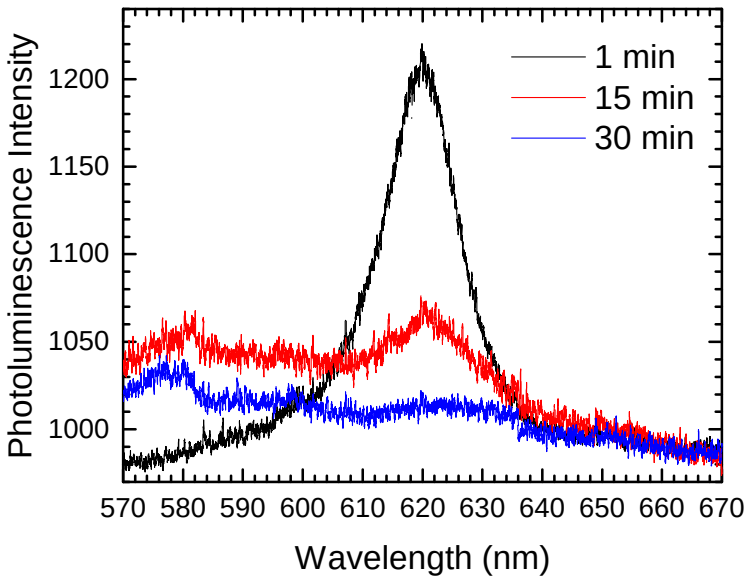

Figure 7.2 Photoluminescence from a 45 nm thick sample of GaSe after 1, 15 and 30 min exposure to 6 mW µm^{-2} of 532 nm laser light in air.

7.1.3 Visual and topographical evidence of laser damage

Along with significant changes in the Raman scattering spectra and photoluminescence, exposure to laser light in air also affects the observed optical contrast of the sample, as can be seen in Fig. 7.3(a-c). AFM topographical images reveal that these optical contrast changes are linked to some form of material ablation, as is evidenced by the ∼12 nm deep, sharply defined hole caused by the laser induced oxidation in the region highlighted by the red circle. That crater has a diameter of approximately 1.1 µm, which roughly corresponds to the size of the diffraction-limited laser spot on the surface sample (1.4 µm for an effective NA of 0.19). The crater is surrounded by bubble-shaped distortions in a region of several micrometers around the crater, indicating a long-range effect of the laser-induced damage, which is discussed in §7.1.4.

Extended laser exposure at higher powers causes more dramatic topographical changes, as evidenced by the region highlighted by the rectangle, showing a larger crater-like depression, along with sharp ripples along the bottom edge of the sample, which are likely a sign of inter-layer delamination.

The observation that laser exposure of GaSe flakes in air has significant effects on the degradation of the Raman signal, the photo-luminescence, the optical contrast, and topography,

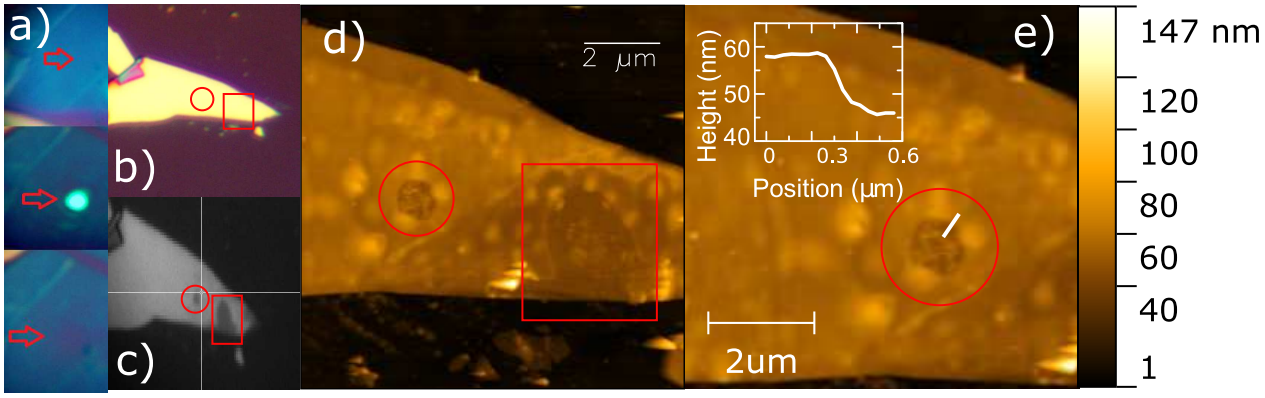

Figure 7.3 (a) Visual evidence of laser-induced damage after 60 min of exposure to 500 µW µm^{-2} 532 nm radiation on a ∼35 nm thick flake. The area indicated by the red arrow changes from green before exposure (top image) to purple-blue, which is the color of the bare Si/SiO_2 substrate, after exposure (bottom image). (b-e) Topographical evidence of 532 nm laser exposure induced damage to a 58 nm thick GaSe flake. The flake was exposed in two locations, identified by a red circle and a square, which were exposed to 6 mW µm^{-2} for 30 min, and up to 12 mW µm^{-2} for several hours, respectively. (b) Optical microscope image of the pristine GaSe flake after exfoliation onto a Si/SiO_2 substrate. (c) Monochrome optical image of the same flake after exposure. (d) AFM topography of the flake after exposure. (e) Close up view of the red circle region with inset topographical profile along the white line marked on the edge of the crater caused by the laser exposure.

along with the appearance of the Raman signature of several known oxidation by-products of GaSe clearly indicate the presence of a photo-oxidative process taking place.

7.1.4 Long-range effects of laser exposure

As can be seen in the topographical AFM data presented in Fig. 7.3, exposure of GaSe flakes to laser radiation in air affects surface topography beyond the immediate exposure area. Using the Raman signal intensity as a sensitive probe of sample degradation enables a more precise evaluation of the range of the laser-induced damage to the crystalline structure of the sample. Fig. 7.4 presents the long-range effects of low-fluence laser exposure onto a GaSe flake. No change is visible optically on the sample surface after exposure, but the A_1^1 Raman signal intensity is affected beyond the directly exposed area. The data indicate that the sample was affected on a much larger area than the size of the illumination spot. The origin of this long-rage degradation will be discussed in §7.7.

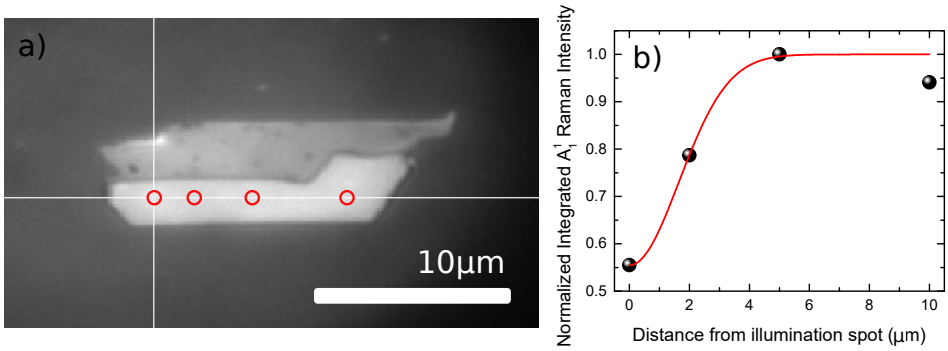

Figure 7.4 (a) Monochrome image of a bulk (∼150 nm thick) GaSe flake (pale region). The white cross indicates the location that was exposed to 500 µW µm^{-2} of 532 nm laser radiation in air. The photo-induced degradation at such low laser fluence did not result in any significant optical contrast change in the sample, but its effects are evidenced by the Raman signal loss. (b) Integrated Raman intensity of the A_1^1 mode normalized against the pristine flake signal as a function of the distance away from the laser exposure location (measurement locations indicated by red circles on the image). The red curve represents a gaussian fit of the data, which reveals a full width at half maximum of 3.87 µm

7.2 Thermal oxidation dynamics of GaSe

Although the laser-induced oxidative process discussed in this chapter will be demonstrated to be an photoelectrochemical process rather than a thermally-activated process, it is instructive to bring our attention to the work done on the thermal oxidation dynamics to better

understand the chemistry at play. The dominant thermal oxidation pathways involving GaSe and oxygen are well known [200],

$$\mathrm{GaSe} + \tfrac{3}{4}\mathrm{O_2} \rightarrow \tfrac{1}{2}\mathrm{Ga_2O_3} + \mathrm{Se}, \tag{7.1a}$$

$$\mathrm{GaSe} + \tfrac{1}{4}\mathrm{O_2} \rightarrow \tfrac{1}{3}\mathrm{Ga_2Se_3} + \tfrac{1}{6}\mathrm{Ga_2O_3}, \tag{7.1b}$$

$$\mathrm{Ga_2Se_3} + \tfrac{3}{2}\mathrm{O_2} \rightarrow \mathrm{Ga_2O_3} + 3\mathrm{Se}. \tag{7.1c}$$

Experimental studies have found that reaction (7.1a) is enabled around 150-250 °C and that it dominates the other two at low temperatures. The production of Ga_2Se_3 through reaction (7.1b) has been observed at temperatures above 450 °C [200–202]. Reaction (7.1c) is known to be active at temperatures around 600-700 °C [200–202] and eventually consumes all the α-Ga_2Se_3 produced through reaction (7.1b). The final oxidation products are β-Ga_2O_3 and Se. Due to its high vapor pressure, Se produced through (7.1a) and (7.1c) is easily be lost by sublimation and is rarely observed in thermally oxidized samples [201, 202]. The Ga_2O_3 formed at these high temperatures is either amorphous, suboxidized (GaO, Ga_2O), or of poor crystalline quality [201, 202].

7.3 Estimation of laser-induced sample heating

Since the known chemical reactions leading to oxidation only occur above at least 150 °C and severe sample damage has been observed with samples at room temperature, the localized laser-induced heating of the sample was investigated. Figure 7.5 shows the evolution of A_1^4 measured from a thin GaSe flake as a function of exposure power in vacuum, where convective sample cooling is at a minimum. The maximum observed energy variation is $0.6\,\mathrm{cm^{-1}}$ between the lowest and highest excitation powers. If this variation were attributed only to thermal effects, the net resulting change in temperature ΔT calculated from the first-order temperature dependence of $-0.014\,\mathrm{cm^{-1}\,K^{-1}}$ reported in Ref. [203] would be 43 K over more than 1.5 orders of magnitude of excitation power. Since the increase in temperature is largely independent of sample thickness for thin supported samples [204], these results clearly establish that thermally activated mechanisms are of secondary importance in the behavior observed here.

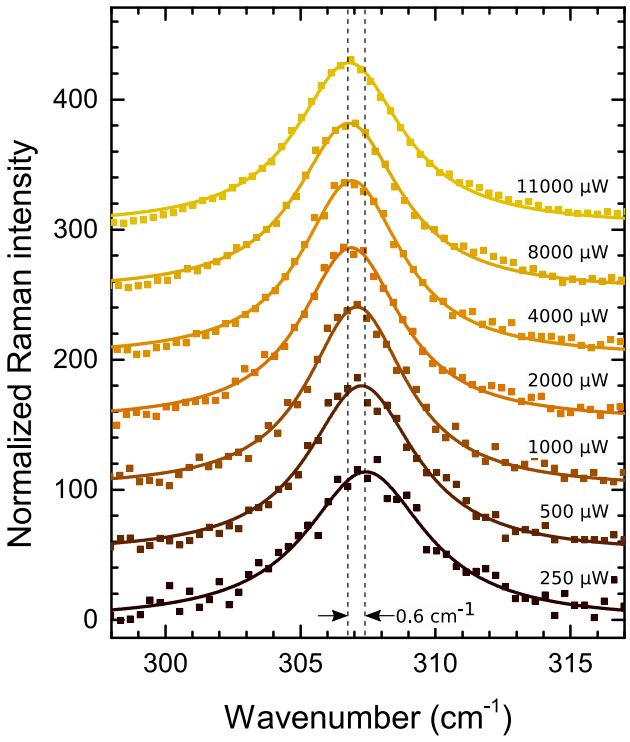

Figure 7.5 Evolution of the energy position of GaSe (A_1^4) as a function of excitation power. Solid lines are Lorentzian fits used to extract the peak energy and points represent the measured data. The dashed lines shows the largest peak position shift observed, between the lowest and highest excitation powers used. Data for different excitation powers is shifted vertically for clarity.

7.4 Identification of GaSe oxide-related Raman peaks and their crystalline origins

The frequency and width of the first mode at 155 cm^{-1} corresponds to the vibrational mode A_1 of Ga_2Se_3 [205]. Although Ga_2Se_3 exhibits several Raman-allowed modes, the one at 155 cm^{-1} is the narrowest and most intense [205–207] and thus the more likely to be observed. Ga_2Se_3 has a defect zinc-blende structure in which Ga vacancies may or may not be ordered. The polarization-resolved Raman measurements presented in Fig. 7.6 suggest that the photo-induced α-Ga_2Se_3 phase is polycrystalline, as will be discussed in §7.4.1.

Another feature related to Ga_2Se_3 is observed at 292 cm^{-1} after a 10 min photoexposure. This broad ($\sim$10 cm^{-1}) feature actually corresponds to a group of at least three vibrational modes with various symmetry representations (A_1, B_1, B_2) that have been assigned to localized vibrational modes of vacancy-disordered Ga_2Se_3 [206]. For its connection with multiple vibrational modes, this feature is labeled Ga_2Se_3 (M). Its presence suggests a high level of

disorder in the Ga_2Se_3 phase.

After exposure of 20 min and more, the Raman signal is dominated by two even broader features. The first at $130\,cm^{-1}$ likely corresponds to SeO_2 or SeO_3 Raman modes [208, 209], but a quantitative analysis of this feature has proven difficult as it partly overlaps with the more intense A_1^1 peak from GaSe and is also at the very limits of the transmission band of the longpass filter, which shows an oscillatory behavior.

The other feature at $257\,cm^{-1}$ matches the characteristics of a mode associated to selenium [197, 210] and its width ($\sim$20 cm^{-1}) suggests an amorphous phase (a-Se) [211, 212]. The narrower peak ($\sim$5 cm^{-1}) at $241\,cm^{-1}$ appears last and is associated [213] to a selenium crystalline phase (c-Se). As it has been often demonstrated, a-Se easily photo-crystallizes [214, 215].

The feature observed at $161\,cm^{-1}$ does not correspond to any modes belonging to GaSe, α-Ga_2Se_3 , or Se and its oxides. However, its frequency and width match the characteristics of the A_g vibrational mode of β-Ga_2O_3 [216,217]. According to Ref. [217], this feature should be the second most intense Raman feature from β-Ga_2O_3 ; the most intense one, found in single crystals at $199\,cm^{-1}$, has not been unambiguously observed in this work.

7.4.1 Polarization dependencies

The space group symmetry of the vacancy-ordered crystal α-Ga_2Se_3 is C_{2v}^{20}. As a function of linear polarization angle θ, the scattering efficiency of this A_1 mode is

$$I_{\parallel}(\theta) = (\alpha_i \cos^2\theta + \alpha_j \sin^2\theta)^2 \tag{7.2}$$

$$I_{\perp}(\theta) = (\alpha_i - \alpha_j)^2(\alpha_i \cos^2\theta \sin^2\theta), \tag{7.3}$$

for co-polarized $k(\theta,\theta)\bar{k}$ and cross-polarized $k(\theta,\theta+\pi/2)\bar{k}$ configurations, respectively. In these equations, α_i and α_j are two of three diagonal Raman tensor elements selected by the measurement axis k. The polarization-resolved Raman intensity shown in Fig. 7.6(a) reveals a uniform response where no θ dependence can be identified in both configurations. This uniform response and the lack of extinction in cross-polarized configuration strongly suggests that the photo-induced α-Ga_2Se_3 phase is polycrystalline, with a grain size significantly smaller than the measurement area.

Fig. 7.6(b) presents the polarization-resolved signal of the A_g vibrational mode of β-Ga_2O_3 observed at at $161\,cm^{-1}$. In a co-polarized configuration, the signal does not explicitly depend on the angle of polarization and in a cross-polarized configuration, the signal is too weak to

be analyzed. The point group of β-Ga_2O_3 is C_{2h}^3, thus the A_g mode is expected to exhibit two lobes for direct polarization scans and four lobes for cross-polarization [218]. From these results, no definitive conclusion can be drawn regarding the crystalline structure of the β-Ga_2O_3 , although it likely exhibits small crystalline domains.

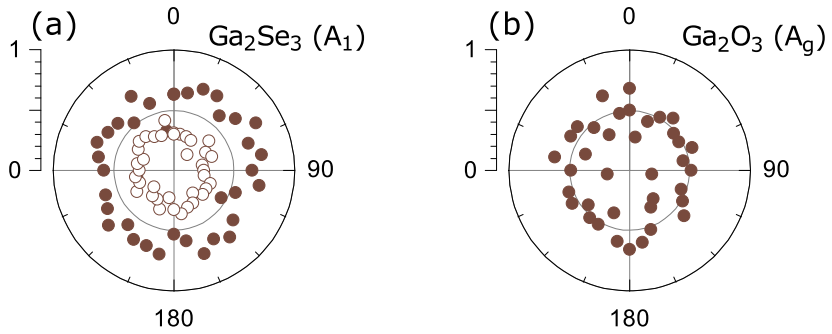

Figure 7.6 Polarization-resolved Raman intensity from (a) Ga_2Se_3 A_1 and (b) Ga_2O_3 A_g modes for co-polarized (full circles) and cross-polarized (empty circles) configurations.

7.5 Oxidation dynamics of GaSe

The formation of these oxidation products can be monitored as a function of time through the intensity of their Raman modes, which is in first approximation proportional to the amount of material in the probed volume, modulated by its crystalline quality. Fig. 7.7 (a) shows that the relative integrated intensity of all GaSe modes (A_1^1, E'_{TO}, A_1^4) along with the photoluminescence rapidly decreases with time under laser exposure. After 25 min of exposure, relative Raman intensities have dropped to ∼15% of their initial values, revealing that the integrity of the GaSe layer is severely compromised by photo-induced oxidation mechanisms.

Fig. 7.7 (b) shows the integrated intensity of the oxidation products mentioned in §7.4. After only one minute of exposure, the intensity of these modes is substantial and easily measurable. α-Ga_2Se_3 (A_1) and $Ga_2Se_3(M)$ increase to a maximum value after 5-10 min and then decrease below the detection limit after 30 min. β-Ga_2O_3 (A_g) appears and then retains a relatively constant intensity throughout the oxidation process. In contrast, the intensity of a-Se rapidly increases and eventually plateaus at an intensity significantly higher than that of all other observed Raman modes, as can be seen in Fig. 7.1.

Direct oxidation of GaSe into Ga_2O_3 and Se has been shown to dominate at low temperatures [193, 200, 219] and, after complete oxidation involving high temperatures, only Ga_2O_3 and elemental selenium should remain [201]. The rapid initial increase in intensity of all

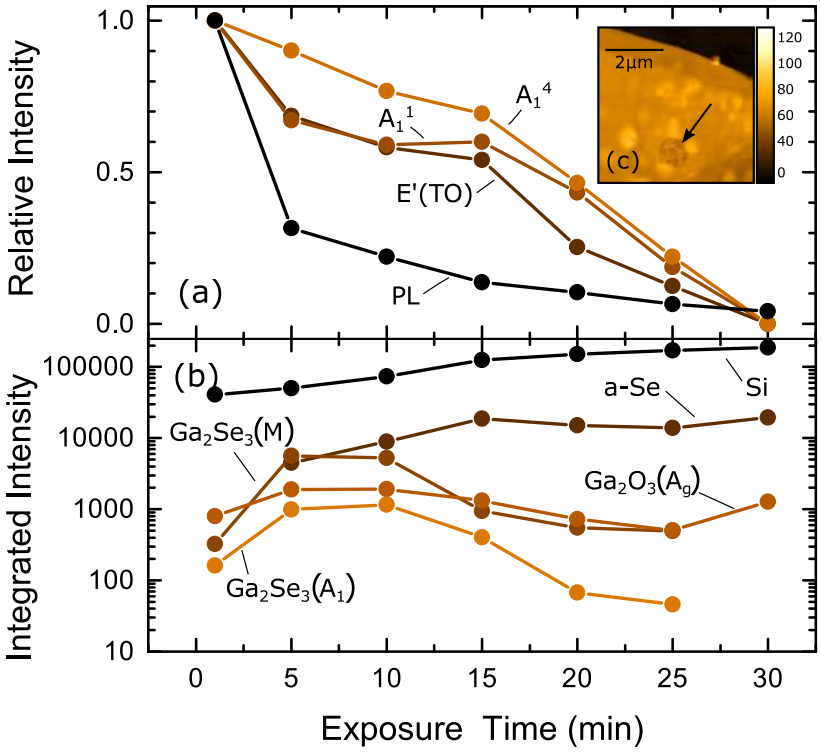

Figure 7.7 Integrated Raman intensity and luminescence as a function of exposure time of a 45 nm thick GaSe flake in air. (a) Relative intensity of GaSe Raman modes and photoluminescence (PL). (b) Integrated intensity of Raman modes associated to the oxidation products and Silicon. (c) AFM surface profile (color scale in nm) of the laser damage on a 58 nm thick flake after 30 min of 6 mW μm^{-2} laser exposure. A black arrow indicates the ∼12 nm deep, sharply defined hole caused by the laser induced oxidation. Reprinted from [29] published by AIP Publishing.

modes associated to Ga_2Se_3, Ga_2O_3 and Se suggests that more than one oxidation pathway is activated and that thermal oxidation is not the dominant mechanism due to the low temperatures involved. As detailed in §7.3, the temperature increase occurring in the experiment presented in Figs 7.1 and 7.7 is less than 40 K above ambient temperature.

The Raman intensity is proportional to the quantity of material in the probed volume, but it is also sensitive to its structural quality. It is therefore difficult to establish the concentrations of crystalline oxidation products, as, for example, the decrease of both Ga_2Se_3 modes could be related to its oxidation into Ga_2O_3 or to the degradation of its crystalline structure as the oxidation progresses. During oxide formation, excess Se segregates at the surface [193]. As seen from Fig. 7.7(b), its intensity quickly increases at short exposure times and mirrors the drop of intensity of GaSe Raman modes and luminescence signal. Because its response is much less sensitive to its structural quality, *a*-Se is believed to be the most reliable Raman

marker of oxidation amongst the various products.

The Raman signal from the Si substrate located underneath the GaSe flake steadily increases with time even though the excitation conditions are rigorously controlled. This is explained by the generation of a large-gap oxide and localized ablation. Oxidation leads to the formation of β-Ga_2O_3 with a gap of 4.9 eV [220], which is transparent at the excitation energy of 2.33 eV. Also, post-exposure AFM measurements indicate a layer-by-layer thinning induced by the laser exposure. This is explained by the high volatility of Se and the high atomic mobility of the remaining metallic Ga [207]. As a net result, the absorption from the GaSe flake decreases.

As suggested by the data presented in Fig. 7.1 (topmost curve), placing the sample in a vacuum environment protects GaSe samples from photo-induced oxidation. Curve A presented in Fig. 7.8 shows the evolution of the A_1^1 Raman intensity of a 10 nm thick flake as a function of time for an excitation power of 250 µW. For such thin layers, this power yields a weak but measurable Raman signal. The intensity of GaSe Raman modes is only marginally affected after an exposure of more than 60 min in vacuum. At the time indicated by the vertical dashed line, the sample was exposed to ambient air. After a few minutes, the Raman intensity has dropped by two orders of magnitude and the signal is completely lost after 10 min. This clearly shows that thin GaSe flakes are unstable in ambient conditions and that minimal laser illumination is sufficient to induce significant degradation, establishing that no safe above-gap excitation power exists for atomically-thin samples.

Curve B presented in Fig. 7.8 shows the Raman intensity of A_1^1 of a 150 nm flake exposed to 1000 µW of laser intensity. For the first data point, the sample is in vacuum. The sample is then exposed to ambient air without any illumination. After 12 hours, the sample is again measured under vacuum conditions and the Raman intensity is very similar to that initially measured, indicating that exposure to oxygen and water vapor alone does not induce significant chemical changes. After 60 min of laser illumination in vacuum, no appreciable change in intensity is observed, even though residual H_2O is present in the sample chamber and on the sample. Then, dry oxygen (<3 ppm H_2O) is introduced in the optical cell and the sample is exposed to radiation for another 60 min. A slight change in Raman intensity is observed, but the overall signal loss is minor because of the limited amount of H_2O available at the sample. Finally, the sample is exposed to ambient air and continually illuminated for another 60 min. It takes about 15 min for the intensity to change significantly. This delay is attributed to a relatively slow nucleation and initial growth of degradation by-products for thicker samples. From that point on however, a rapid decline of intensity takes place, losing more than one order of magnitude within less than one hour.

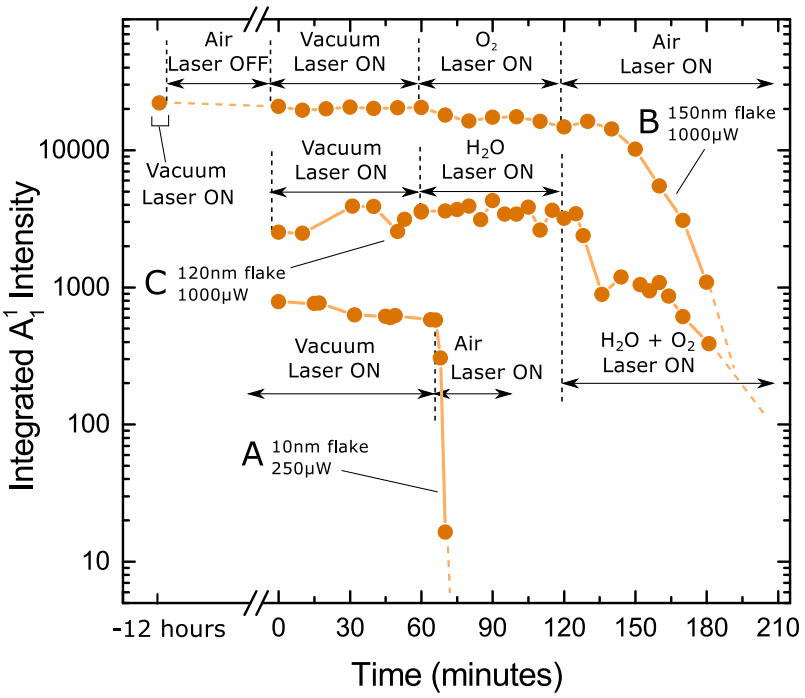

Figure 7.8 Integrated Raman intensity of the A_1^1 peak of GaSe flakes as a function of exposure time to a 532 nm laser in vacuum and in different environments. Flake thickness and exposure power are indicated on the curves. Reprinted from [29] published by AIP Publishing.

Curve C in Fig. 7.8 shows the Raman intensity from a 120 nm flake measured in vacuum and then in deoxygenated water vapor obtained from deionized water repeatedly frozen then thawed in vacuum. The Raman intensity does not show any appreciable change after 1 hour in each environment. Introduction of oxygen in the chamber at the 120 min mark leads to a rapid decrease in the Raman intensity. These experiments establish that continuous above-gap illumination, water vapor and oxygen alone do not support the photo-oxidation process, but that the simultaneous presence of all three is required.

7.6 Photoelectrochemical charge transfer oxidation model

Although the observed oxidation byproducts largely correspond to those produced by thermally-activated oxidation, the photo-oxidation process observed here is not temperature driven as discussed previously. This result suggest that the above gap illumination is not contributing significant heat, but rather generating a charge carrier density $\delta\eta$ in the conduction band which enables the oxidation process.

At first glance, the presence of optically excited carriers in the material might seem unrelated to its accelerated oxidation, but if these excited charges can be transferred to oxygen molecules at the sample surface, they can form highly reactive oxygen ions known as superoxide anions ($O^{\cdot-}_{2(aq)}$). For this charge transfer to happen, the energy levels of the excited charge carriers and of the empty electronic states of the oxygen must overlap [221].

Fig. 7.9 illustrates the energy position of these O_2 acceptor states relatively to GaSe, which is characterized by an electron affinity of 3.4 eV [222]. The gaseous molecular oxygen electron affinity is about 0.45 eV [223], almost 3 eV above the bottom of the GaSe conduction band, therefore the charge transfer to gaseous oxygen at the surface is unlikely.

However, when oxygen is solvated in water, its electron affinity is modified and the constant reorganization of the polar H_2O molecules around the molecules induces an effective broadening of about 1 eV of the electronic states [221, 224], allowing for a significant overlap with the lower conduction band of GaSe, as is shown in Fig. 7.9. Note that these states are not directly equivalent to energy bands in a solid, but a charge transfer can nonetheless occur if they align with energy states in the semiconductor substrate.

The charge transfer between the photo-excited carriers and aqueous oxygen (Eq. (7.5b)) can be modeled in the framework of the Marcus-Gerischer theory, where the rate of charge

transfer is described by [224] :

$$\frac{d[O_2^{\cdot-}]}{dt} \propto \delta\eta[O_2] \exp\left[-\frac{\left(\chi_{\mathrm{GaSe}} - E^0_{F,redox} - \lambda\right)^2}{4k_BT\lambda}\right], \tag{7.4}$$

where $\delta\eta$ is the conduction band electron density, $[O_2]$ and $[O_2^{\cdot-}]$ are the concentrations of neutral oxygen and superoxide in the water at the sample surface, χ_{GaSe} is the GaSe electron affinity, $E^0_{F,redox}$ is the Fermi level of the oxygen-water solution and λ is the solvent reorganization energy around oxygen molecules [221]. Since GaSe has an electron affinity which positions the lower conduction band in line with the aqueous oxygen acceptor states, the exponential function in Eq. 7.4 enables charge transfer towards the aqueous O_2. The generated aqueous superoxide anions ($O^{\cdot-}_{2(aq)}$) at the surface then rapidly react with the GaSe substrate to produce the observed oxidation byproducts at a much faster rate than non-ionized molecular oxygen, which will in turn decrease the observed GaSe Raman intensity.

This process can be modeled using the following equations:

$$\mathrm{GaSe} + h\nu \rightarrow \mathrm{GaSe}^* \tag{7.5a}$$

$$\mathrm{GaSe}^* + \mathrm{O}_{2(aq)} \rightarrow \mathrm{O}^{\cdot-}_{2(aq)} + \mathrm{GaSe} + h^+ \tag{7.5b}$$

$$\mathrm{O}^{\cdot-}_{2(aq)} + \mathrm{GaSe} + h^+ \rightarrow \{\mathrm{GaSe}\}_{\mathrm{ox}}, \tag{7.5c}$$

where GaSe^* represents GaSe with photoexcited electron hole pairs, and $\{\mathrm{GaSe}\}_{\mathrm{ox}}$ represents GaSe oxidation byproducts.

7.7 Experimental evidence of the proposed model

In the thickness regime studied here, the band gap variation is negligible, [37, 226] and the absorption coefficient is independent of thickness. The penetration depth of the 532 nm laser is about 5 µm, therefore there is carrier generation throughout the whole thickness of the flake along the laser beam path. Charge transfer towards oxygen can only occur at the sample surface, and so photoexcited carriers need to diffuse to the surface for this process to occur. Knowing that the charge transfer is a rather slow process, diffusion in all directions and superoxide anion formation at the surface away from the laser illumination spot is expected, which may explain the observed long-range effects of photo-oxidation presented in §7.1.4.

Assuming samples much thinner than the carrier diffusion length and laser penetration depth, we expect the photo-excited carrier concentration for a given excitation laser power to be uniform throughout the sample thickness, decreasing gradually away from the excitation

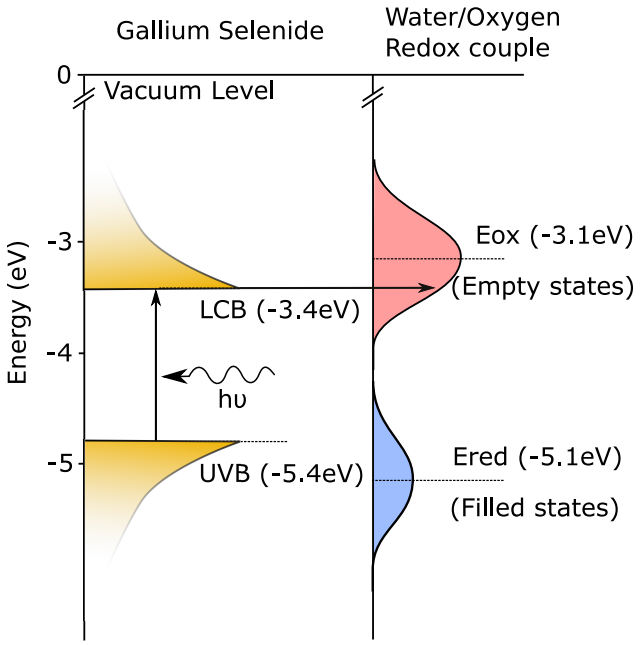

Figure 7.9 Schematic of the charge transfer process from GaSe to aqueous oxygen. The schematical electronic density of states of GaSe and aqueous oxygen molecules are illustrated relatively to vacuum energy [222, 225]. The vertical arrow represents the photoexcitation of a carrier from the upper valence band (UVB) to the lowest conduction band (LCB) of GaSe. The horizontal arrow indicates electron transfer from the LCB to the aqueous oxygen.

spot, regardless of sample thickness. The rate at which superoxide anions are generated is thus proportional to the exposure power, $d[O_2^{\cdot -}]/dt \propto \delta\eta \propto P_{\text{exp}}$, as revealed by Eq. (7.4). Fig 7.10 shows the intensity of the A_1^1 Raman signal obtained after an exposure of 15 min at the indicated exposure power in ambient air for samples of varying thicknesses. As predicted by Eq. (7.4), the observed degradation rate increases linearly with exposure power and is independent of sample thickness. The observed slopes vary between -0.27 and -0.38, but the smallest slope is only derived from two data points thus bears a higher uncertainty. The other slopes are all very similar, despite the wide range of flake thicknesses observed, which strongly points to a linear power dependency of the oxidation for all flake thicknesses in the assumed thickness range. This confirms the role of the linear dependence of the photo-oxidation mechanism on above gap illumination and further rules out thermal processes.

7.8 Summary

In all 2D materials, surfaces can be subject to oxidation and photo-oxidation. GaSe, in contrast, exhibits relatively complex oxidation dynamics. First, it involves several components : oxygen, humidity, and above-gap illumination, and results in the generation of several ox-

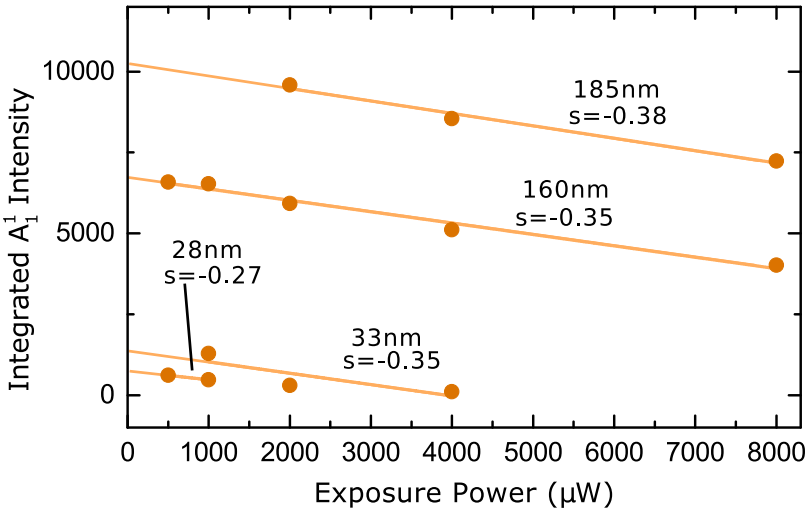

Figure 7.10 Integrated Raman intensity of A_1^1 as a function of exposure power for samples of varying thicknesses. Each data point represents a 15 min exposure at the specified power before a Raman spectrum was measured using a 500 µW laser excitation. Linear regression slopes s are shown. Reprinted from [29] published by AIP Publishing.

idation products, Ga_2Se_3, Ga_2O_3, and amorphous and crystalline selenium. Luminescence and Raman measurements in ambient conditions are found to severely degrade the optical and electronic characteristics of GaSe, indicating that no safe illumination threshold exists, especially for thin layers of GaSe. Hence, the study of the intrinsic characteristics of 2D GaSe requires a controlled environment at all stages of processing and characterization, especially so for optical measurements involving above-bandgap illumination. Consequently, most of the Raman experiments presented in this work were done with the sample inside a vacuum optical cell to avoid oxidation. The lack of any of the oxidation products Raman signatures in the measured spectra confirms the effectiveness of these precautions.

CHAPTER 8 RAMAN STUDY OF PHONON-POLARITONS IN GaSe SLABS AND FLAKES

One of the main challenges associated with the study of confined polaritons stems precisely from their confined nature. Indeed, confined polaritons can only strongly couple to their environment via evanescent electromagnetic waves coupling in the near-field. In this section, several experimental results are shown that showcase the use of Raman spectroscopy as a powerful tool to access and characterize highly confined phonon-polariton states without the need for direct near-field coupling.

Raman scattering from polaritons is usually only observable in a near-forward scattering configuration, owing to the very small wave vectors of phonon-polaritons, which lie in the vicinity of the light line. Such measurements often pose several challenges and limitations. They require the sample to be transparent to the incident and scattered light, and separating the very intense transmitted laser light from the scattered signal can prove difficult. The use of microscopy systems for spatially resolved transmission measurements on small samples is also complex. Fortunately, severely confining polaritons into sub-wavelength cavities dramatically increases their wave vector and relaxes scattering momentum conservation rules, enabling multiple polariton Raman scattering geometries. This makes Raman scattering a potentially very useful tool to study highly-confined polaritons, alleviating the requirement for near-field optical coupling through gratings of scanning probes.

In the first part of this chapter, results from near-forward scattering in thin slabs of GaSe are presented and discussed, showing evidence of phonon polariton dispersion, as well as multiple forbidden Raman modes associated to resonance scattering. The weak signal and high residual laser intensity are shown to limit the usefulness of the technique.

The second section describes how scattering from polariton modes, which normally can only be observed in near forward geometry, can be observed in backscattering configuration from thin samples. This backscattering from polariton states in thin GaSe flakes is then presented in the next section, where the polariton scattering numerical model is shown to accurately describe the observed scattering angle and thickness dependency, when taking into account the optical setup's numerical aperture. These results show clear evidence of confined and surface polariton modes in the Raman scattering spectrum of thin exfoliated GaSe flakes.

The following section presents evidence of resonant enhancement of these polariton states when excitation energy approaches the GaSe free exciton energy. This resonant enhancement is then used in the last section to study the effects of lateral confinement on the polariton

states in small exfoliated GaSe flakes.

8.1 Weakly confined polaritons : near-forward measurements

In this section, the polariton dispersion of a 70 µm thick slab of GaSe is studied via near-forward k-space imaging. For such a thick sample, momentum conservation is largely respected, and the polariton Raman scattering can only be observed in near-forward scattering geometry. As has been described in §6.4, k-space imaging enables direct measurement of the polariton over a section of the Brillouin zone determined by the numerical aperture of the system. In order to ensure transparency of the sample to laser light, this experiment was conducted using a 12 mW continuous 633 nm He-Ne laser source, whose energy lies 60.7 meV below the 2.02 eV bandgap of GaSe [227]. As configured, the experimental setup could collect scattered rays with angles between approximately $-4°$ and $4°$.

8.1.1 Data analysis

Before presenting the results, it is important to consider the data processing procedure that was used to extract the spectral information. The raw data are obtained by a 13 h exposure of the CCD detector, yielding an image as the one shown on Fig. 8.1. The lateral dimension of the image corresponds to the spectral dispersion of the spectrometer grating, spanning a wavenumber range from 72 to 554 cm^{-1}. The vertical axis, on the other hand, corresponds to the vertical scattering angles (θ_s) from $-4°$ to $4°$, which can be directly equated to an in-plane polariton wave vector using Eq. (6.2) with an incidence angle $\theta_i = 0$. The first order shear and second-order deformation in the image are corrected as described in chapter 6. The spectra are then binned vertically into 32 bands that are 16 pixels high, that each cover approximately 0.23° of the microscope objective's numerical aperture. This binning is necessary in order to increase the signal-to-noise ratios of the intrinsically weak signal. The resulting spectra, an example of which is shown on Fig. 8.2 for a 70 µm-thick sample, were analyzed using eight Lorentzian peak functions after baseline removal. An example of the fitted curves is shown on Fig. 8.3. A final wavenumber calibration is applied by fitting Lorentz peaks on the $\mathrm{A}_1'^{\,1}$ and $\mathrm{A}_1'^{\,4}$ Raman modes, and computing a linear regression on the fitted wavenumbers.

Note that due to the relatively rich structure observed over a relatively narrow energy range (see inset in Fig. 8.3), this peak fitting approach sometimes fails to identify uniquely the exact structure of the measured spectrum, as several overlapping polariton modes are expected. Nonetheless, the resulting peak positions and linewidths are a useful tool to identify and

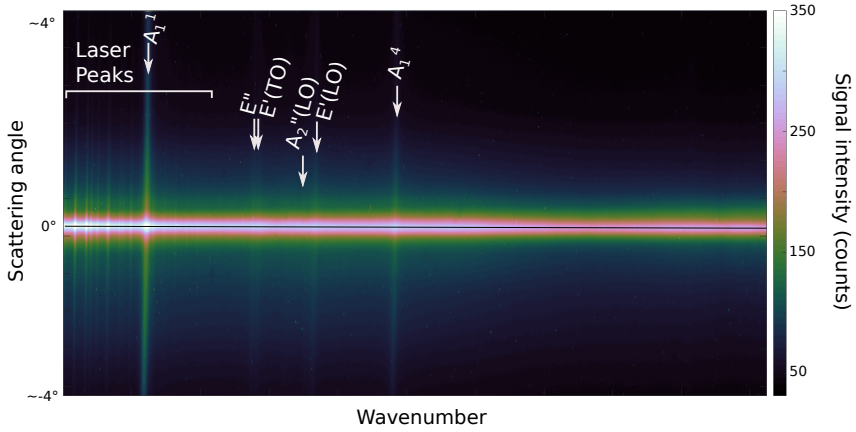

Figure 8.1 Typical k-space Raman 2048×512 pixel imaging data. The horizontal dimension corresponds to the spectrometer wavelength dispersion, while the vertical dimension corresponds to the angular k dispersion that is imaged on the vertical entrance slit. The bright horizontal band in the middle of the image results from the direct transmission of the laser beam through the sample and is centered on $k = 0$ or $\theta = 0$. The bright vertical bands correspond to Raman lines from GaSe as indicated by the white arrows, along with some weak emission lines, attributed to the laser, on the left side of the image. The various bright specks are caused by cosmic muons hitting the CCD detector over the extended acquisition period.

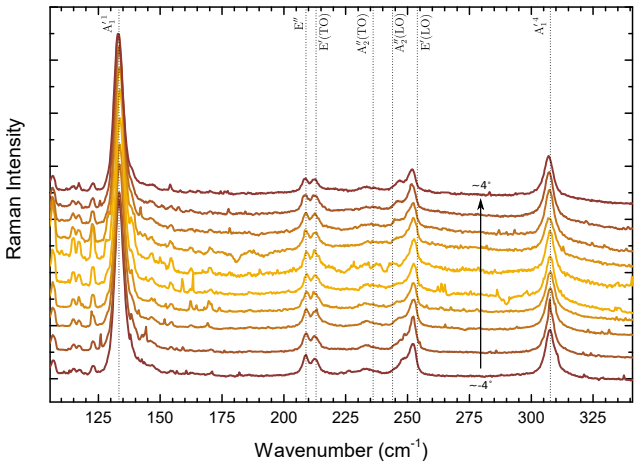

Figure 8.2 Processed data for a 70 µm thick sample for a 13 h integration time. Curves are offset vertically corresponding to the vertical position on the camera sensor. Each curve corresponds to the vertical integration of a 16-pixel high band, spanning approximately 0.23° of scattering angle.

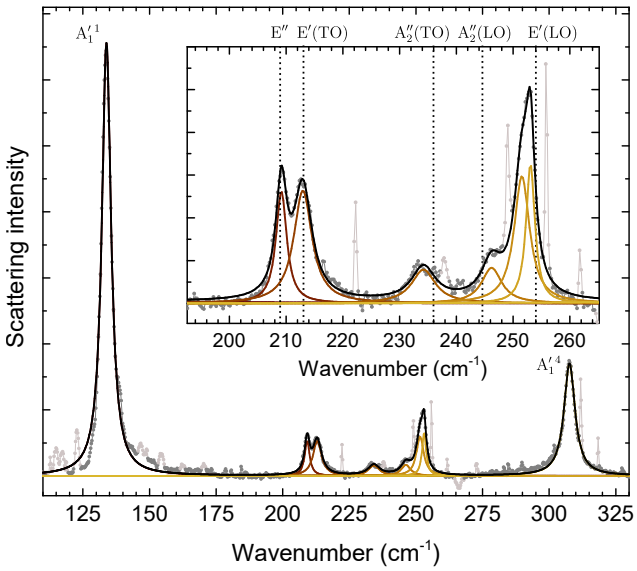

Figure 8.3 Example of fitting curves for near-forward spectra for a scattering angle of 1.6°. Measured data points are indicated by the dark gray points, the orange-colored curves represent the eight fitted Lorentzian peaks, and the black curve is their resulting sum. The pale gray points were ignored as they correspond to laser or muon peaks. The energies of the pure phonon modes are indicated by vertical dashed lines in the enlarged inset.

describe subtle variations in the spectrum as a function of scattering angle.

8.1.2 Results and discussion

As was discussed in the previous chapter, the Raman scattering tensor and geometrical selection rules for near-normal scattering should only allow the observation of $\mathrm{A}_1'^1$, $\mathrm{A}_1'^4$ and E′(TO). However, results from near-forward scattering reveal a multitude of additional features whose origin requires a more detailed examination.

Fig. 8.4 illustrates the peak positions and their full widths at half maximum as a function of the scattering angle, overlaid onto the polariton Raman scattering response computed using the model presented in §5.3.5, with a damping constant of $\Gamma = 1.8\,\mathrm{cm}^{-1}$. The computed spectra are displayed in a scaled logarithmic fashion in order to highlight their structure using

$$I_{\mathrm{tot}} = \frac{\log_{10}\left(1 + \sum_N S I_N\right)}{\log_{10}(S)}, \tag{8.1}$$

where I_N represents the scattering intensities for each tensor component ($N = \{To, Te, Le\}$) and S is a scaling factor. This logarithmic scaling adjustment, while not quantitatively ac-

curate, drastically increases the effective dynamic range of the color scale plot, which allows strong and weak modes to be seen simultaneously on a single plot. For large sample thicknesses, there are many guided polariton modes in the flake, and thus the Te and Le polariton branches are expected to form a quasi continuum, as can be observed in the simulation results presented in Fig. 8.4.

At first glance, the measured peaks do not appear to display significant dispersive behaviors, and two sharp, well-defined peaks that match the energies of the E″ and E′(TO) are identified, as well as four other features between 225 and 260 cm^{-1}. If E′(TO) is Raman active and expected for this geometry, none of the other five peaks can be interpreted using the basic mechanical Raman tensor, since they are either forbidden in this geometry or do not directly correspond to any known vibrational mode. The potential assignments of these five Raman features will now be discussed, keeping in mind that the fitted peaks may in fact be composed of multiple modes. Spectra for angles below 0.7° (indicated by the vertical dashed line on Fig. 8.4) were not analyzed due to the scattered laser light dominating the spectrum in this forward configuration.

Guided polariton modes

The computed Raman scattering from the To, Te and Le polariton tensor elements, shown on Fig. 8.4, predicts multiple features in the studied scattering angle range.

The lower To branch features multiple distinct modes below 2° and converges to approximately 210 cm^{-1} at higher angles. This branch coincides with the measured 209 cm^{-1} peak around scattering angles of 3°, but the observed lack of dispersion in the data at small angles differs from the strongly dispersive behavior of that branch, which effectively eliminates the possibility that this peak comes from that polariton branch. It might be interpreted as a resonant scattering process allowing scattering from the E″ mechanical mode, but this interpretation by itself fails to explain some of the observed behaviors of that Raman feature, which will be discussed in more detail in the following sections.

The Te branch covers a continuum band between 215 and 233 cm^{-1}. Although it may contribute in part to the broad feature observed around 234 cm^{-1}, it does not appear conclusively in the measured data. More interestingly, the Te polariton generates an intense scattering band between the A_2''(LO) and E′(LO) modes, which coincides very well with the dispersive feature increasing from 246.3 cm^{-1} to 248.4 cm^{-1} over the observed scattering angles. The dispersive behavior of this branch is the strongest evidence of polariton scattering in this data and will be studied in detail in the following sections.

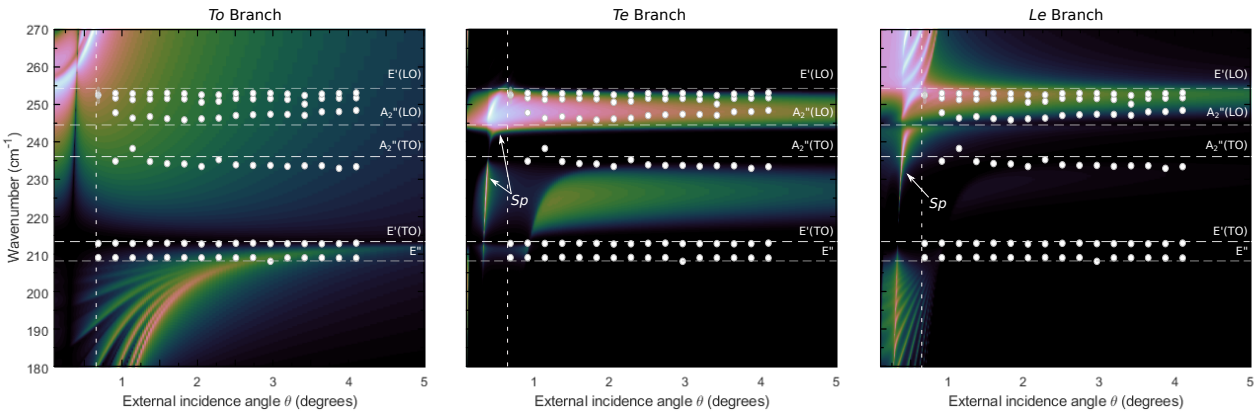

Figure 8.4 Comparison between numerical model and near-forward scattering experimental results for a 70 µm sample. Computed Raman scattering intensity (with $S = 10^4$) is illustrated by the color map, clearly showing the To, Te and Le polariton branches, as well as the surface polariton modes. Fitted Lorentzian peak positions and are indicated by the white circles (standard deviations are smaller than the circles). The energies of the pure mechanical phonon modes are indicated by the dashed white lines. The vertical dashed lines indicate the lowest scattering angle with a signal above the laser noise.

The surface polaritons Sp appearing in the Te and Le are highly dispersive along the light line below 0.5°, and rapidly converges to 244 cm^{-1} in the measured range. They may contribute some intensity to the peaks around 246.3 cm^{-1} between 1° and 2°, but cannot be uniquely identified in the data.

Finally, the Le branch shows barely resolved modes immediately beyond the light line that become a continuum band above 1°. The behavior of this branch corresponds to the two barely-resolved peaks observed around 251.5 cm^{-1} and 253 cm^{-1}, in the upper region of the Le polariton branch. For such a thick sample, the dispersive behavior in this upper region is only expected for scattering angles below 0.5°, which cannot be observed with the experimental setup used in this work due to the insufficient rejection of the scattered laser light at the center of the CCD image.

Fig. 8.5 shows a comparison between the computed and measured spectra for three scattering angles. In order to reproduce the measured polariton scattering in the 240-260 cm^{-1} range, the computed scattering from the Te and Le branches are scaled independently, with the Te intensity being multiplied by a factor of 3 for all scattering angles. This independent intensity adjustment can be justified by the understanding that polarization selection rules and resonant enhancement processes may differ for the three polariton tensor components, although it is not immediately clear why the observed scattering intensity is proportionally

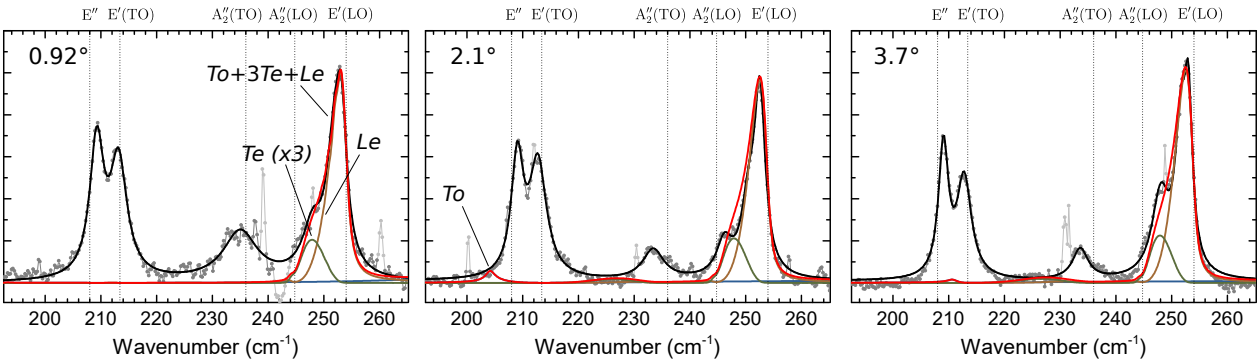

Figure 8.5 Comparison between measured, fitted and computed near-forward scattering spectra for selected scattering angles. Computed Raman scattering intensities from the To, Te and Le polariton branches, which have been linearly scaled to match the measured peak intensity as indicated, are illustrated by the blue, green and orange curves, respectively. The red curve is the summed computed spectrum, the gray points are the measured data and the black curve is the fitted Lorentzian peaks curve. Muon features that were ignored in the analysis are shown as pale gray points.

higher from the Te branch than from the two other branches. The resulting computed spectra (red curves) and suggest that the features observed below $240\,\mathrm{cm}^{-1}$ may not be assigned to polariton scattering, since neither the predicted energies nor intensities match the data. In the 240-260 cm^{-1} range, there is good agreement between the simulated and measured scattering intensity.

These discrepancies, features below $240\,\mathrm{cm}^{-1}$ and deviations from the calculated spectra, can be explained by another phenomenon, owing to the near-resonance between the 633 nm He-Ne laser source and the exciton energy of $E_g - E_R = 2.00\mathrm{eV}$ (where $E_R = 19.2\mathrm{meV}$ [227, 228] is the exciton Rydberg energy). The laser excitation is 40.7 meV below the $1s$ exciton resonance, and this near-resonance may lead to a significant Raman cross-section enhancement, as well as breakdown of selection rules [18, 140, 229, 230]. This is discussed next.

Resonance-mediated enhancement and selection rule breaking

The non-dispersive peaks located at $209\,\mathrm{cm}^{-1}$ and $234\,\mathrm{cm}^{-1}$ closely match the energies of the E'' and $\mathrm{A}_2''(\mathrm{TO})$ vibrational modes reported in the literature, respectively. However, the E'' mode should only be observable for an in-plane scattering geometry (corresponding to $\theta = 90°$), and the A_2'' is Raman-forbidden for all geometries in ϵ-GaSe. The presence of these peaks can be explained by resonant scattering processes, which can in some cases break selection rules and yield intense Raman features from forbidden modes. The lack of dispersion

observed from these modes suggests that they do not originate from polariton scattering, but rather from normal vibrational modes of the lattice. The broad nature of the A_2''(TO) mode could be ascribed to the fact that this mode is *doubly* forbidden, as not only is the Raman tensor vanishing for the A_2'' vibrational mode in $\epsilon-$GaSe, the scattering geometry also forbids the observation of a transverse A-type mode. It can be expected that lattice defects may play a part in its observation, which could explain some spectral broadening. Hoff [18] reports linewidths of about $4.2\,\mathrm{cm}^{-1}$ for the A_2''(TO) mode in γ-GaSe, where it is Raman-active. Most of the observed linewidths measured here for A_2''(TO) are around $10\,\mathrm{cm}^{-1}$. This broadening indicates the possibility impurity- or defect-mediated selection rule breakdown of the A_2''(TO) phonon, possibly enhanced by resonance conditions, as a major contribution to the observed scattering intensity of this mode. However since the linewidth varies somewhat erratically as a function of scattering angle and most of the peaks display an asymmetrical lineshape, there may also be a dispersive element, such as the surface or guided Te polaritons, contributing to the observed mode.

The longitudinal polar phonon modes are expected to exhibit the strongest exciton resonance enhancement [140, 231], and thus the polaritonic nature of the scattering observed between 240 and $260\,\mathrm{cm}^{-1}$ needs to be contrasted with the presence of the long-wavelength mechanical phonons A_2''(LO) at $244.5\,\mathrm{cm}^{-1}$ and E′(LO) at $254\,\mathrm{cm}^{-1}$. Owing to the observation of likely resonant enhancement of the E″ and A_2''(TO) modes, it is very probable that at least some of the observed scattering intensity in the higher energy range could also be linked to resonant scattering from A_2''(LO) and E′(LO). However, this assignment cannot explain the dispersive behavior observed from the lower mode, which increases from $246.3\,\mathrm{cm}^{-1}$ to $248.4\,\mathrm{cm}^{-1}$ over the observed scattering angle range, as resonant effects only affect scattering intensity, not energy. The $\sim 0.7\,\mathrm{cm}^{-1}$ per degree dispersion observed in Fig. 8.4 at very small angles greatly differs from the long-wavelength phonon dispersion predicted by the anisotropic dispersion model (see §3.1.1) that was verified experimentally in $\gamma-$GaSe by Hoff [18], wherein a shift of at most $\sim 0.005\,\mathrm{cm}^{-1}$ per degree is reported for external scattering angles below 45 deg for the LO branch. The strong dispersion observed in the current data can therefore positively be linked to guided polariton dispersion in the sample slab rather than to the lattice anisotropy.

In summary, the observed non-dispersive Raman features coincide rather closely with GaSe vibrational modes that are forbidden according to off-resonance Raman selection rules. In light of these observations, it is concluded that resonant processes may contribute to a significant degree to the observed Raman features, but there is some clear evidence of polariton dispersion in the 240-260 cm^{-1} range. The concomitant polariton and resonant effects hinder unambiguous mode assignment, therefore the usage of a 633 nm laser source might be considered as less than ideal to identify polariton modes in GaSe, but it was the only readily

available below-bandgap laser source to conduct this experiment. The results of near-forward scattering from 3-7 µm thick samples reported by Sasaki [24] show a better agreement with the modeled intensity, as they were done using a 514.5 nm argon-ion laser, which is further from the exciton resonance but has a large enough penetration depth to realize near-forward scattering measurements. The only other available laser in this work was a 532 nm Nd-YAG source, which has a penetration depth of approximately 5 µm in GaSe, which would limit the maximal thickness of the measured samples. Attempts were made to obtain near-forward scattering data from a thinner 10 µm flake with both the 633 nm and 532 nm lasers, but the low signal intensity resulted in poor quality spectra that were often dominated by laser noise. On the other hand, the resonant scattering process certainly increased the Raman cross section of the longitudinal polariton modes, facilitating their observation.

The results presented in this section confirm the presence of polariton features in the Raman spectrum of GaSe, but they also highlight the difficulty and the restrictive nature of near-forward measurements. In the following sections, it will be shown that these issues can be solved by exploiting the relaxation of momentum selection rules and the strong polariton confinement effects in thin films.

8.2 Momentum conservation and scattering geometry

In samples with large thicknesses compared to the laser wavelength, there are stringent momentum selection rules, and the conventional near-forward Raman scattering geometry is the only one in which polaritons should be observed. However, as can be seen in Fig. 8.6, a polariton scattering feature between the $A_2''(LO)$ and $E'(LO)$ frequencies is visible in Raman backscattering from a 70 µm GaSe flake excited with a 633 nm laser, but is absent under 532 nm excitation. Given the large penetration depth of 633 nm light in GaSe relative to the flake thickness, light may easily propagate through the layer and be reflected by the sample's rear face back toward the collection objective. Therefore, the measured spectrum can in principle be composed of both direct backscattered and reflected near-forward Raman signals, as mentioned in §6.2. In both cases, the tangential polariton wave vector is the same, but there is a significant difference in the magnitude of the probed transverse wave vector. For direct backscattering, the measured k are on the order of $6 \times 10^5\,\mathrm{cm}^{-1}$, and for near-forward scattering, polaritons can be probed down to the light line at $k = \omega/c$.

In order to discriminate between backscattering and reflected near-forward scattering, the focal point of the excitation beam was gradually lowered from the front surface, effectively probing different focal volumes along the sample thickness as illustrated in Fig. 8.7. Isotropic scattering, such as that from the totally symmetric phonons ${A_1'}^1$ and ${A_1'}^4$, exhibits maximal

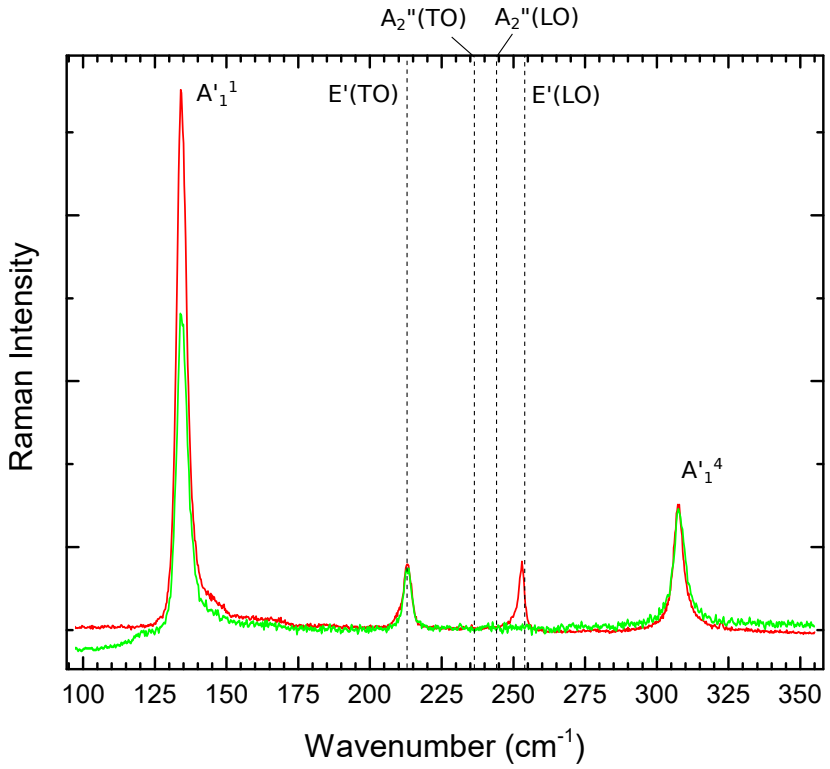

Figure 8.6 Raman backscattering from a freestanding 70 µm sample under 633 nm (red curve) and 532 nm (green curve) excitation at normal incidence. The expected long-wavelength phonons $A_1'^1$, E′(TO) and $A_1'^4$ are indicated on the spectrum, but an additional mode is observed at 252 cm^{-1} for 633 nm excitation, slightly below the forbidden E′(LO) mode. This mode is assigned to resonant polariton Raman scattering in near-forward measurements, and is absent from the 532 nm spectrum since the sample is much thicker than the penetration depth of light at that wavelength, and forward-scattered light reflected by the rear sample surface is absorbed before exiting the sample and cannot reach the detector.

scattering intensity when the laser is exciting the center of the sample, maximizing the probed sample volume. Directional forward scattering, on the other hand, is expected to be maximal when the focal plane coincides with the rear surface of the sample, as all reflected rays are within the collection optics aperture. The resulting depth-resolved scattering intensities, shown in Fig. 8.7, indeed reveal a stark contrast between the intensity profiles of the mechanical phonon modes and that of the *Le* resonant polariton mode. This highlights the fact that the resonant polariton scattering is highly selective to near-forward scattering geometries, as it reaches a maximal intensity when the collection acceptance cone exactly matches the recflected light cone from the excitation laser. Therefore, backscattering measurements can include a significant reflected near-forward signal component which has to be taken into consideration when assigning Raman modes.

In thinner samples, relaxation of wave vector conservation (see §4.3.4), along with confinement-induced wave vector increases, can alter the resulting scattering directivity of Raman scattering from polaritons. The numerical model described in Chapter 5 can be used to calculate the relative values of the forward and backward scattering intensities for any given wavenumber and scattering angle. In order to provide an estimate of the general scattering directivity for a given thickness, the ratios of the maxima of the forward and backward scattered intensities between 180 and 270 cm^{-1} were computed for 15 logarithmically spaced angle values between 0.1 and 45° then averaged. This process was then carried out for multiple sample thicknesses to obtain an estimate of the scattering directivity as a function of sample thickness. Fig. 8.8 presents the resulting scattering directivities, defined as the ratio $I_F/(I_F + I_B)$, where I_F and I_B are the maxima of the forward and back-scattered intensities, revealing that for samples below approximately 1 µm, the polariton scattering anisotropy becomes negligible. This underscores the fact that the commonly understood association between polaritons and near-forward scattering geometries only applies to thick samples, and that sub-micron sample sizes, commonplace among exfoliated Van der Waals materials, enable Raman observation of polariton modes in any scattering geometry.

8.3 Strongly confined polaritons : backscattering results

In contrast to weakly confined polariton modes in large crystals, observed at small wave vectors thus in the vicinity of the light line, strong confinement in sub-wavelength cavities greatly increases the polariton mode parallel momenta. Along with perpendicular momentum conservation rule relaxation, this enables observation of polariton Raman scattering in the backscattering geometry as discussed in the previous section, provided that the penetration depth at the excitation wavelength is large compared to the sample thickness. This

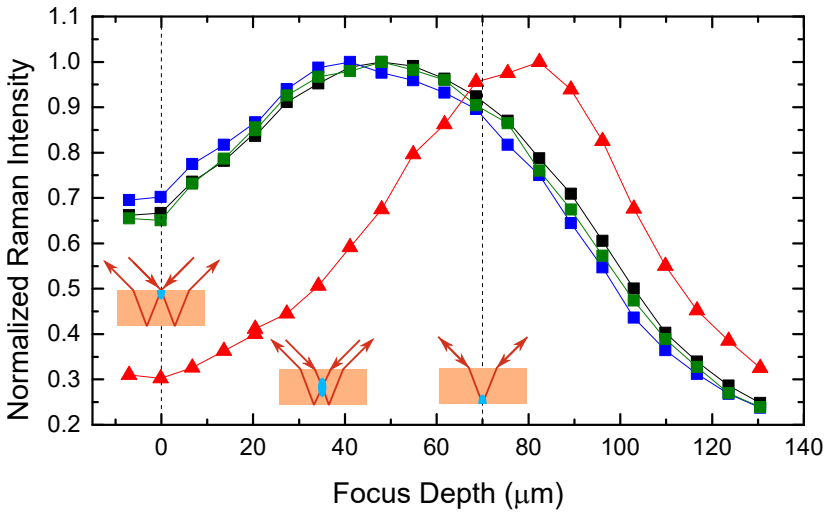

Figure 8.7 Normalized Raman backscattering intensity of the $A_1'^1$ (black squares), E′(TO) (blue squares), *Le* resonant polariton (red triangles), and $A_1'^4$ (green squares) modes as a function of focal depth within a 70 µm sample under 633 nm excitation. Estimated location of the interfaces are indicated by the vertical dashed lines. Schematic representations of the incident and scattered rays (red arrows) and of the probed volume (blue ovals) in the sample illustrate the scattering configuration for various focus depths.

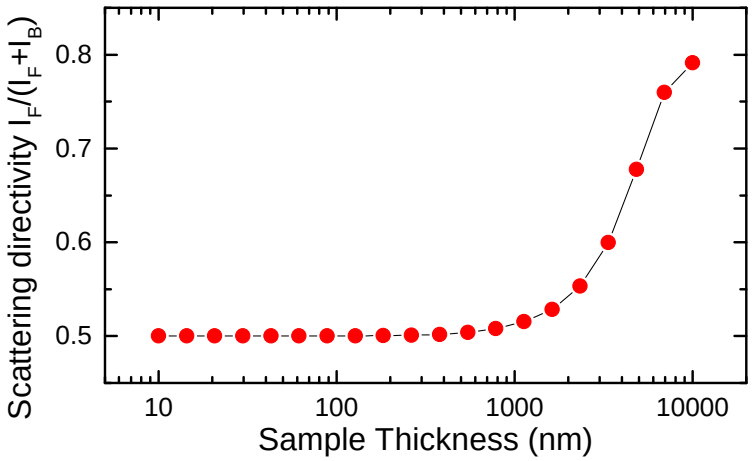

Figure 8.8 Computed polariton scattering directivity of GaSe as a function of sample thickness.

is especially crucial to the study of polaritons in 2D materials, that are often exfoliated or grown into few-nanometer flakes on opaque substrates such as Si/SiO_2, precluding forward scattering experiments. Their intrinsic small thickness and natural hyperbolicity make them ideal candidates for the study of polariton states through Raman backscattering experiments.

In this section, angle-resolved Raman backscattering data from sub-micrometer GaSe flakes on Si/SiO_2 substrates are demonstrated to exhibit strong scattering from guided polariton modes. These highly dispersive modes coincide closely with several Raman features often reported in the literature with conflicting interpretations. These results demonstrate the powerful simplicity of Raman scattering, using a technique that is already a standard 2D material characterization tool to probe highly confined surface and hyperbolic polariton states, which can conveniently be observed in a backscattering configuration.

8.3.1 Angle-resolved backscattering

Angle-resolved backscattering measurements were performed on multiple thin exfoliated GaSe flakes, and in several instances, dispersive modes were observed in the Reststrahlen bands between 220 and 260 cm^{-1}, corresponding to surface and hyperbolic polariton branches. Fig. 8.9 illustrates the angle-resolved backscattering data obtained from a 650 nm thick flake with 15 min exposure time to a 532 nm laser with a fluence of 210 $\mu\mathrm{W}\,\mu\mathrm{m}^{-2}$. Raman mode wavenumbers and Full widths at half maximum (FWHM) were extracted from the data using Lorentzian lineshapes, as illustrated in Fig. 8.10 for a sample tilt angle of 30°.

Long-wavelength phonon scattering

At normal incidence ($\theta = 0°$), the expected Raman-active long-wavelength phonon modes $A_1'^{\,1}$, E′(TO) and $A_1'^{\,4}$ dominate the spectrum, and two additional broad and strongly dispersive features appear between 225 and 255 cm^{-1}. For higher incidence angles, a 209 cm^{-1} mode, which coincides with E″, appears below the E′(TO) mode. Its appearance is expected from off-normal geometry, as it is Raman-allowed for in-plane scattering geometries, and z-axis momentum conservation is relaxed due to the small sample dimension along that axis.

One of these features shows an energy that corresponds to the A_2''(TO) phonon mode at normal incidence, and one might be tempted to attribute the observed dispersion to lattice anisotropy (see §3.1.1). However, this assignment fails to explain the observed dispersion in multiple regards. Firstly, this dispersive branch, starting near A_2''(TO) at 236.4 cm^{-1} for $\theta = 0°$ and increasing toward 241.6 cm^{-1} for $\theta = 45°$, does not correspond to an expected phonon dispersive branch. Indeed, not only is the A_2'' mode Raman-inactive, the electrostatic

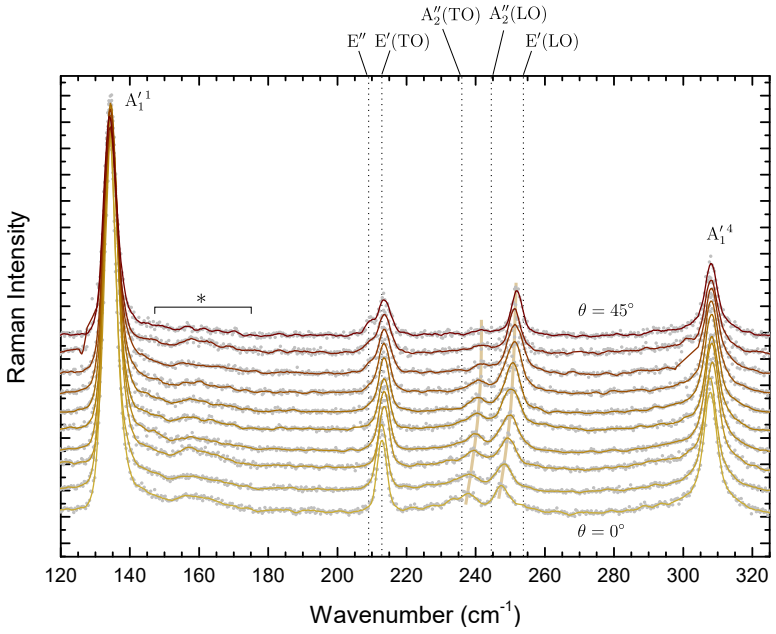

Figure 8.9 Raman backscattering from a 650 nm thick sample of GaSe on a Si/SiO_2 substrate as a function of sample tilt angle θ. Measured data are represented by the gray points, and solid lines are 5-point Savitzky-Golay filtered spectra. The 532 nm laser is p-polarized and the angle θ is varied between 0° (bottom curve) and 45° (top curve) in 5° increments. The nonpolar A_1^1 and A_1^4 modes show no dispersive behavior, but several features in the 200-250 cm^{-1} Restralhen bands show some degree of angular dispersion. The vertical curved lines are added as guides to the eye. Note that the signal between 150 and 175 cm^{-1} marked by the asterisk ($*$) comes from weak oxide peaks due to short exposure of the sample to air during handling.

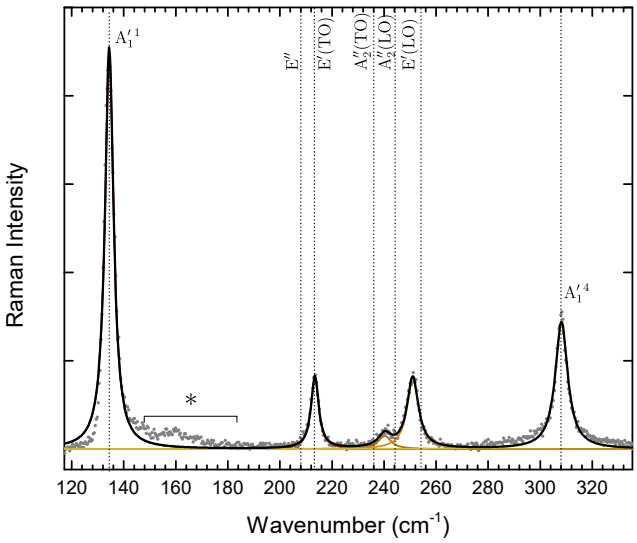

Figure 8.10 Example of fitting curves for backscattering spectra for an sample tilt angle of 30°. Measured data points are indicated by the gray points, the orange colored curves represent the five fitted Lorentzian peaks (E″ is too weak to be modeled here), and the black curve is their resulting sum. The features in the region marked by the asterisk (*) originate from slight oxide formation at the sample surface and were ignored. Energies of the pure mechanical phonon modes are indicated by vertical dashed lines.

anisotropy is dominant in GaSe and the phonon branches retain their TO/LO character [46,140]. This means that the only two long-wavelength phonon dispersion branches go from E′(TO) to A_2''(TO) and from A_2''(LO) to E′(LO), ruling out the possibility that the lower of the observed features corresponds to lattice dispersion of long-wavelength phonons.

The second dispersive branch, with wavenumbers from 247.8 to 251.9 cm^{-1}, does coincide with a lattice dispersion branch, but the high angular dispersion over the observed angle range (5.2 cm^{-1} for the lower branch and 4.1 cm^{-1} for the upper branch) cannot be explained by the crystalline anisotropy. Indeed, for a sample tilt angle $\theta = 45°$, the lattice dispersion model [140,232] predicts a wavenumber shift of at most 0.9 cm^{-1} for the A_2''(LO) → E′(LO) branch. This is illustrated in Fig. 8.11, where the lattice-induced mode dispersion is compared to the observed dispersion. As will be shown the next section, all of these behaviors can be explained by the confined polariton model.

Confined polariton branches

In order to understand the nature of the polaritons involved in the observed scattering features, the backscattering Raman cross section of polaritons in a 650 nm GaSe slab was calculated as a function of sample tilt angle using the numerical model described in Chapter 5.

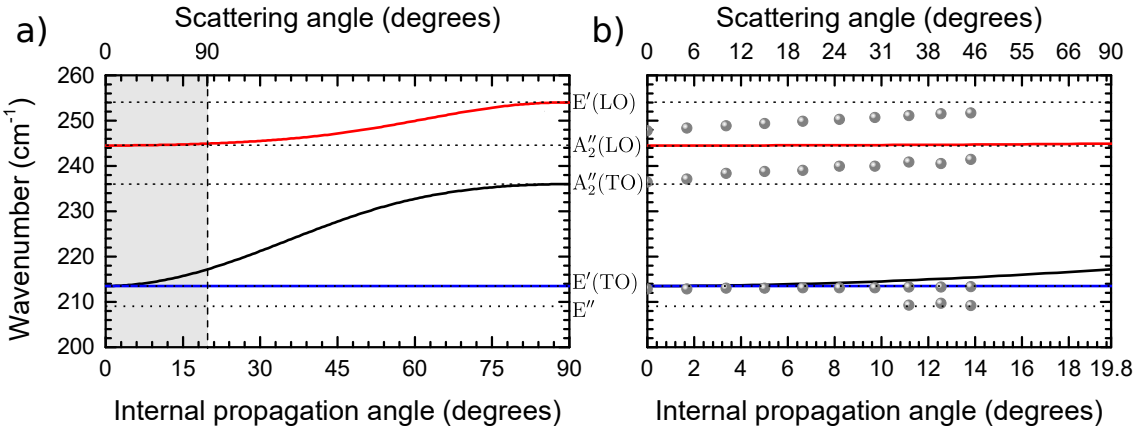

Figure 8.11 Comparison between the calculated lattice-induced dispersion and observed angular dispersion. (a) Complete lattice dispersion curve as a function of internal phonon propagation angles with the lattice c axis. Red and black curves illustrate the extraordinary LO and TO dispersive phonon branches, and the ordinary non-dispersive TO branch is represented by the blue curve. The upper scale indicates the corresponding external optical scattering angle, with the shaded area illustrating the accessible internal propagation angles below the total internal reflection angle of 19.8°. Lattice mode energies are indicated by the horizontal dotted lines. (b) Enlarged view of the shaded region in (a), with the measured data points from Lorentzian fitting superimposed as gray circles (standard deviations are smaller than the circles)

The polariton scattering response from each of the polariton normal coordinates is shown on Fig. 8.12. Note here the subtle distinction between the polariton normal coordinates (To, Te and Le) as defined in §4.3 and their associated polariton branches of the same name as defined in chapter 5. The computed spectra in Fig. 8.12 are obtained from the polariton tensor elements projected onto each of the normal coordinates, but just as in the case of mechanical dispersive polar phonons, dispersive branches can exhibit mixed character when they do not propagate along their respective symmetry axes, as is the case here for oblique propagation angles.

The two dominant polariton branches correspond to a surface polariton branch (labeled Sp) and a to guided Le mode between A_2''(LO) and E′(LO), and both involve contributions from the Te and Le polariton tensor components. The guided To branches only involve the To tensor component. They are highly dispersive and only have appreciable intensity for angles below 5°. This is explained by the fact that they are ordinary polaritons, and the slab cannot support strongly confined ordinary modes as opposed to the extraordinary surface and hyperbolic modes (see §5.1). Due to this high dispersion rate and limited angular selectivity of the experimental setup, these polariton branches are expected to appear in measurements as very broad feature, and are masked by the noise of the measurement. In order to facilitate

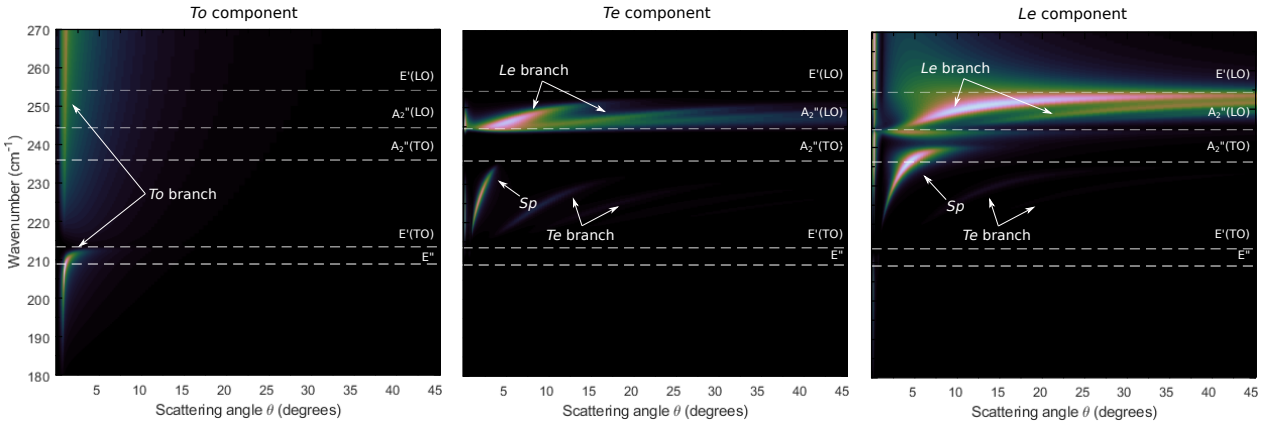

Figure 8.12 Comparison between numerical model and near-forward scattering experimental results for a 650 nm sample. Computed Raman scattering intensity for each of the polariton normal coordinates (logarithmically scaled with $S = 10^2$) is illustrated by the color map, with the guided To, Te and Le polariton branches, as well as a surface polariton mode (Sp) indicated by white arrows. The energies of the pure phonon modes are indicated by the dashed white lines.

comparison with measured data, it is omitted in Fig. 8.13, where the sum of the computed scattering intensity resulting from the Te and Le tensor components is overlaid with the fitted modes from the experimental data.

For angles above 10°, the upper dispersive branch of the measured data generally matches the simulated spectrum for the Le guided branch, exhibiting linewidths between 3 and 6 cm^{-1}, likely due to the multiple unresolved guided modes. Fig. 8.14 illustrates the comparison between the computed and measured spectrum at an angle of 45°, where the experimentally measured mode for the upper branch is clearly shown to be composed of multiple unresolved guided modes as seen in the modeled spectrum. This remarkable correlation between the experimental and measured scattering from the Le polariton branch does not hold as well for smaller scattering angles (see Fig. 8.13), as the high dispersion cannot be resolved by the limited angular selectivity of the optical system, which will be considered in detail the next section.

The second polariton feature in the data is the surface polariton mode located in the double Reststrahlen band, between the $\mathrm{A}_2''(\mathrm{TO})$ and $\mathrm{A}_2''(\mathrm{LO})$ frequencies. In order to determine the nature of this polariton mode, the spatial field distribution as a function of wavenumber was computed in the sample for various scattering angles. The results, shown in Fig. 8.15, highlight that this polariton is a surface mode, and is located spatially at the interface between the GaSe crystal and SiO_2 substrate (labeled $Sp(SiO_2)$). Its energy at high angles

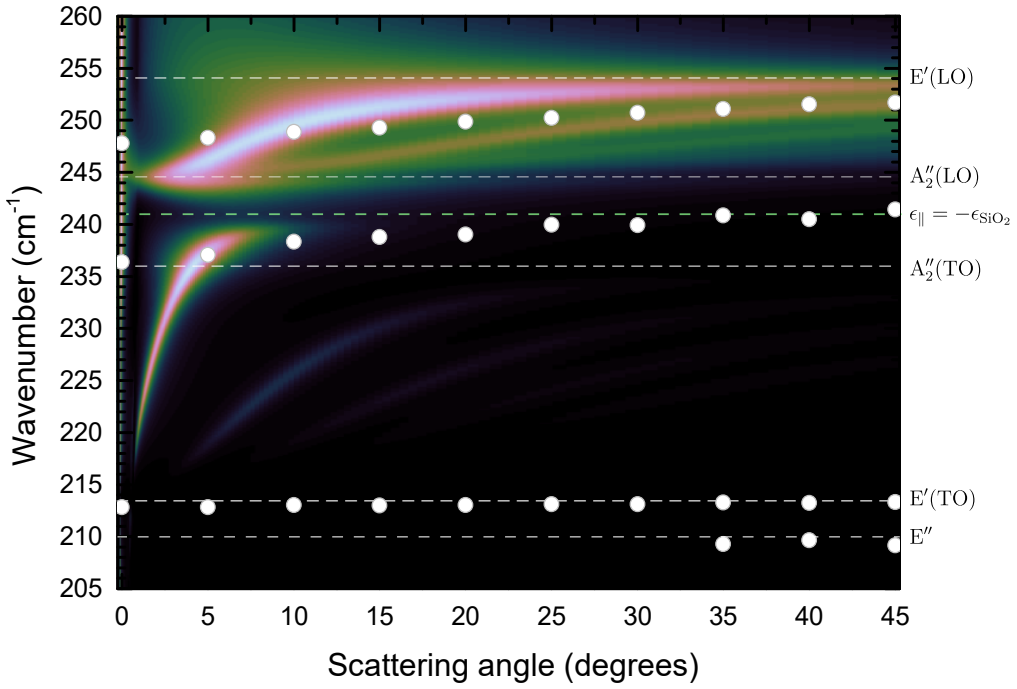

Figure 8.13 Modeled Raman spectra for angle-resolved colinear ($\theta_i = -\theta_s$) backscattering from a 650 nm thick sample of GaSe on a Si/SiO_2. Fitted Lorentzian peak positions from measured data are illustrated by the white circles, which are larger than the uncertainty of the fitted wavenumbers.

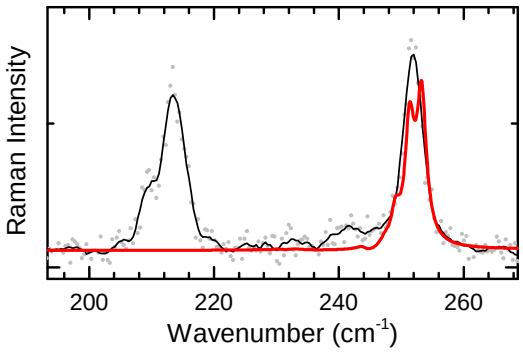

Figure 8.14 Comparison between computed and measured backscattering spectra from a 650 nm thick sample at a sample angle of 45°. Computed Raman scattering intensities from the *Le* and *Te* polariton branches, which has been linearly scaled to match the measured peak intensity, is illustrated by the red curve. The gray points are the measured data and the solid black curve is the smoothed data.

is bound by the surface mode confinement criterion of $\epsilon_{/\!/}(\omega_{Sp}) \leq -\epsilon_{\mathrm{SiO_2}}(\omega_{Sp})$, as indicated by the dashed green line at $\omega_{Sp} = 241\,\mathrm{cm}^{-1}$ in Fig. 8.13. The experimentally observed dispersion quite accurately matches the predicted behavior, with the exception of the data point at 0° due to the low angular selectivity of the measurement system (more on this later). Also, this mode remains visible for scattering angles way beyond what the model predicts, which might be linked to the presence of a thin oxide layer at the sample surface, as will be discussed in §8.3.3. The upper surface polariton Sp(Air) is not clearly visible in the measured and calculated spectra, as it only occurs as a low-energy shoulder below the intense Le branch.

The guided Te polariton branches between A_2''(TO) and E′(TO) are predicted to have very low scattering cross-sections, barely visible on Fig. 8.12, and thus do not appear in the data.

Finally, the mode below $\mathrm{E_{TO}}$ at $209\,\mathrm{cm}^{-1}$ could be associated to scattering from the To polariton branch, as was speculated in Ref. [233], but the results presented here indicate otherwise, as that polariton should only be observed for angles below $\theta \sim 10°$ in this sample (see Fig. 8.12), whereas it only becomes apparent in the measured spectra above $\theta \sim 30°$. This confirms that the observed feature corresponds to the E'' phonon mode, as is reported by several authors in the literature [18, 46].

8.3.2 Angular broadening

The angular resolution of the system is limited by the combined effect of wide excitation and collection numerical apertures. Simply adding both apertures yields an effective scattering range of almost ±45° on either side of the optical axis. The actual angular broadening is much lower, as the laser has a Gaussian beam profile that does not fill the entrance pupil of the objective and the collection imaging optics and filters act as a limiting aperture, preventing some off-axis rays from reaching the detector. As is shown below, it is crucial to interpret the results in light of the nonzero angular acceptance of the optical detection system.

Indeed, comparing the experimental data with the computed broadened spectra, there is a rather good agreement between the predicted and measured lineshape and energies for the Le branch. Indeed, the detailed comparison between the computed and measured spectra shown on Fig. 8.14 shows maximal measured peak width in the highly dispersive region at lower angles, whereas the non-broadened computed spectrum predicts a narrow peak width at a lower energy. For a scattering angle of 45°, the measured FWHM is $3.2\,\mathrm{cm}^{-1}$, which closely matches the non-broadened computed peak width, since the dispersion is very low at this angle.

In order to accurately model the measured signal at low scattering angles where dispersion

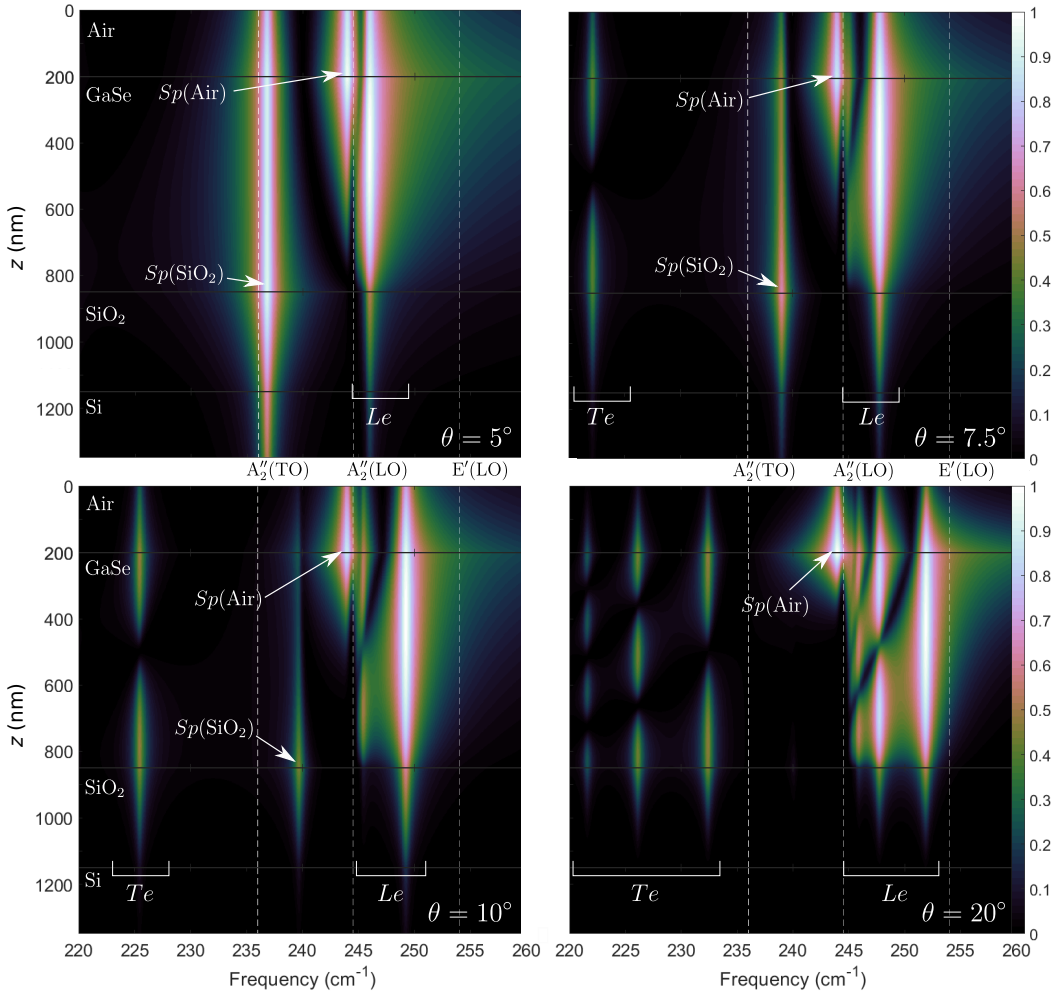

Figure 8.15 Spatial field distribution in a 650 nm thick sample of GaSe on a Si/SiO_2 substrate for different scattering angles θ, indicated in the bottom right corner of each graph. The guided Te and Le polariton branches are indicated by the white brackets and both surface polariton modes are indicated by $Sp(\mathrm{Air})$ and $Sp(\mathrm{SiO_2})$. Lattice normal modes are indicated by the vertical dashed lines. Color scale represents the extraordinary $|E_x|^2$ field component, with a logarithmic scaling factor of $S = 10$. The broadening parameter is set to $\Gamma = 0.5$ cm^{-1} to help discriminate nearly-degenerate modes.

is important, it is necessary to include a broadening factor in the numerical model, since multiple scattering geometries contribute simultaneously to the observed signal owing to the numerical aperture of the confocal measurement optics. The collection objective has a numerical aperture of 0.55, which corresponds to a collection angle of $\pm 33\,^{\circ}$. The objective is fitted with an exit pupil with a diameter of 5 mm, which limits the collection angle to approximately $\pm 13\,^{\circ}$. Supposing a Gaussian beam profile, with the collection angle defining the $1/e^2$ intensity angular beam width, the expected acceptance FWHM is $w = 15°$.

Fig. 8.16 illustrates the computed angle-dependent spectra with an acceptance angle $w = 15°$, which is the FWHM of a symmetrical Gaussian broadening around the optical axis. Applying this angular broadening correction to the computed spectra yields a more accurate representation of the measured energies for both observed polariton branches. The guided *Le* branch appears as a broad feature at low angles, evolving into a narrow mode below E′(LO) at high scattering angles, which accurately corresponds to the experimental data. The surface polariton *Sp* branch starts around $236\,\mathrm{cm}^{-1}$ and slowly rises towards $241\,\mathrm{cm}^{-1}$. Although the intensity of the computed *Sp* mode drops off rapidly for increasing sample tilt angles, the energy dispersion closely reproduces the observed dispersion in the experimental data. The lower than expected intensity decay rate of the *Sp* mode may be explained by the high sensitivity of surface polariton modes to the sample surface quality and dielectric environment, which can be affected by the presence of surface roughness, trapped charges, or oxide layers. The effects of the surrounding dielectric environment on the *Sp* branch will be discussed in more detail in the next section.

Fig. 8.17 shows the measured and computed spectra for an incidence angle of 5°, revealing the significantly better agreement with the data for broadened spectra (solid lines) than for the previously obtained unbroadened results (dotted lines). Comparing these results as well as those in Fig. 8.13 and Fig. 8.16 highlights the critical importance of the numerical aperture of the optical system when measuring the angular dispersion of polariton modes using confocal Raman scattering. Small numerical apertures yield higher angular resolution, which can prove essential when studying highly dispersive modes such as these.

In the following sections, all calculated spectra directly compared to experimental data will take into account the effect of the angular aperture of the optical system, unless specified.

8.3.3 Dielectric environment : lossy substrates and coupled polaritons

The surface polariton observed in Fig. 8.16 between 230 and $241\,\mathrm{cm}^{-1}$ is located at the substrate interface (see Fig. 8.15), which has been modeled as a perfect SiO_2/Si planar interfaces. However, it is well-known [234] that SiO_2/Si substrates can trap non-uniform

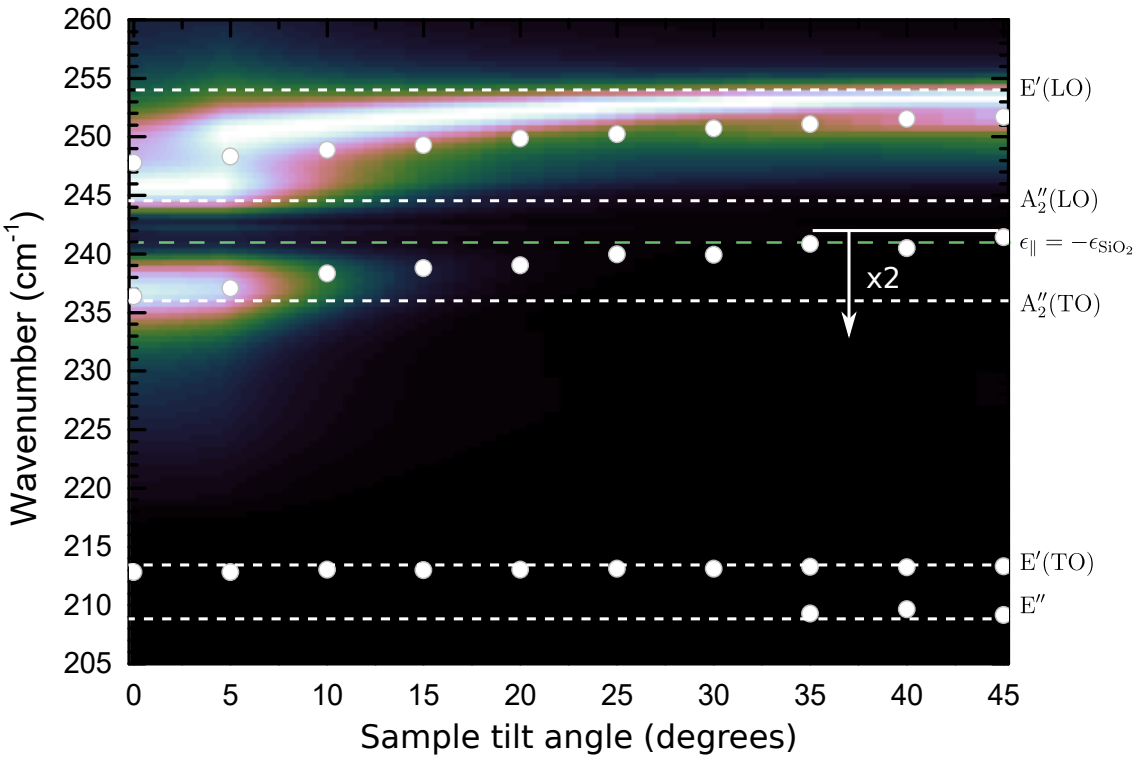

Figure 8.16 Comparison between computed and measured angle-resolved colinear backscattering from a 650 nm thick sample. The computed spectrum includes an angular resolution modeled as a Gaussian curve with a FWHM of $w = 15\,^{\circ}$. For each sample tilt angle value, the spectrum has been normalized by its maximum value in order to illustrate spectral distribution. As indicated by the white arrow, calculated scattering intensity below $242\,\mathrm{cm}^{-1}$ was multiplied by a factor of 2 to make the *Sp* branch more visible. Fitted Lorentzian peak positions from measured data are illustrated by the white circles, which are larger than the uncertainty of the fitted wavenumbers.

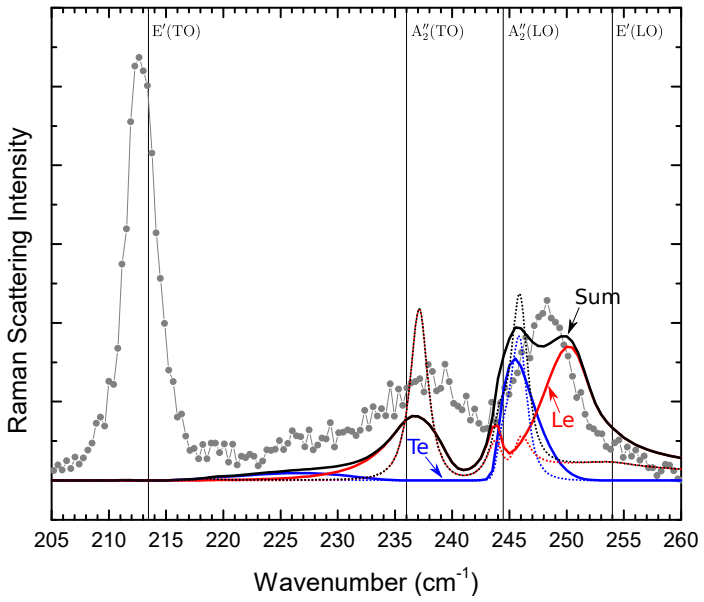

Figure 8.17 Comparison between computed and measured backscattering spectra from a 650 nm thick sample for a sample tilt angle of 5°. The solid black curve illustrates the computed polariton spectrum with an angular broadening modeled as a Gaussian curve with a FWHM of $w = 15\,°$. Contributions from the Te and Le polariton tensor elements are illustrated by the blue and red solid curves, respectively. The dotted curves illustrate the same results without accounting for angular broadening.

charge densities due to adsorbed water and surface irregularities, and can harbor leftover contaminants from the exfoliation process. It is also important to keep in mind that GaSe samples were modeled as a perfect infinite slab waveguide, without any surface oxide layers or defects. However, the work presented in Chapter 7 highlighted the possibility that oxidation byproducts may form on sample surfaces when exposed to air, even for brief periods of time. These oxide layers, although likely very thin due to the care taken when preparing the samples, alter the immediate dielectric environment at the surface of the slab, which can then significantly affect polariton modes in the slab. For example, in one of the first observations of surface polaritons [121], a benzene atmosphere was used to alter the surrounding dielectric medium in order to accentuate their dispersion (see Fig. 2.7). A recent work studying hyperbolic polariton propagation in h-BN slabs over multiple substrates such as quartz, monoclinic and rutile VO_2, silver, and silicon, as well as suspended over air, has highlighted the important effects of bulk and local substrate complex permittivity on both surface and guided polariton propagation and dispersion [235].

In the following section, the effects of charge trapping at the SiO_2 surface and of oxide layers at the GaSe surfaces are investigated using the multilayer transfer matrix numerical model.

SiO_2 charge trapping and permittivity

The complex permittivity of SiO_2 used in previous calculations is based on transmittance measurements on freestanding low-stress SiO_2 amorphous thin films [236]. Therefore, it is likely that the dielectric properties of the thermally-grown silicon oxide layer used in this work are not perfectly represented by this model. Indeed, dielectric properties of silicon oxide and silica glass are known to vary significantly due to impurities, defects, crystallinity, or synthesis processes [175], and surface charge trapping can further alter their properties [234].

In order to evaluate the potential impact of such deviations on the resulting Sp dispersion, Raman spectra were calculated for various constant offsets $\Delta\epsilon'$ and $\Delta\epsilon''$ (values used are detailed in caption of Fig. 8.18) added to the real (ϵ'_{SiO_2}) and imaginary (ϵ''_{SiO_2}) parts of the SiO_2 permittivity, respectively. The results are shown in Fig. 8.18. The main effect of the altered substrate permittivity is a slight reduction of the surface polariton scattering intensity for an increased ϵ''_{SiO_2}. The surface mode field being localized around the surface, this mode is more affected by losses in the substrate. Altering only the real part of the permittivity ϵ'_{SiO_2} has very little effect on the spectral distribution. Indeed, it does not affect the general symmetry of the system, but rather slightly alters the confinement factor thus the signal intensity, as seen on the blue curves in Fig. 8.18. Overall, it does not appear that the SiO_2 permittivity has a marked influence on the energy dispersion of either the surface or guided

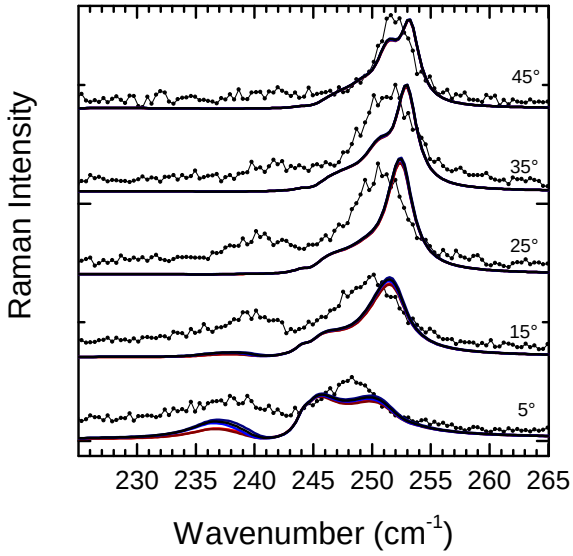

Figure 8.18 Modeled Raman spectra from a 650 nm GaSe slab on Si/SiO_2 for different SiO_2 dielectric parameters. The black curve shows the spectrum for unaltered SiO_2, the red curves correspond to permittivity changes of $(\Delta\epsilon' = 0, \Delta\epsilon'' = 0.5)$, $(\Delta\epsilon' = 0.5, \Delta\epsilon'' = 0.5)$, and the blue curves represent $(\Delta\epsilon' = 0.5, \Delta\epsilon'' = 0)$, and $(\Delta\epsilon' = -0.5, \Delta\epsilon'' = 0)$. On this scale, both red curves are almost indistinguishable.

polaritons.

Oxidation byproducts : coupled polariton resonance

In addition to the silicon oxide layer, thin layers of GaSe oxidation byproducts can be present at the sample interfaces. As described in Chapter 7, the first two oxidation species that form on a GaSe surface upon light exposure are α-Ga_2O_3 and β-Ga_2Se_3, and they can form in minutes under ambient conditions. These two compounds not only have significantly different static permittivities than GaSe, they also are anisotropic and they exhibit polar vibrational lattice modes in the 200 to 260 cm^{-1} energy range. Hence, they can sustain their own surface and hyperbolic polariton modes. An in-depth study of the coupled polariton states between the GaSe and oxide layer polariton modes is beyond the scope of this work, but the formalism used in this work (Chapter 5) conveniently allows integrating an an oxide layer into the modeled system. Using this model, the effect of a thin layer of α-Ga_2O_3 or β-Ga_2Se_3 on both slab interfaces can be included, fully taking into account coupled polariton states.

Fig. 8.19 illlustrates the overlap between the GaSe and oxidation species Resthrahlen bands. Note that the dielectric function for Ga_2O_3 comes from reflectance measurements on high-quality bulk β-Ga_2O_3 crystals with a monoclinic lattice symmetry (C_{2h} point group) [237], and thus the symmetry of the lattice mode involved in this Resthrahlen band is well-defined as a B_u mode, which is not Raman-active. However, it is very likely that the lattice of the oxidation species layer exhibits several defects, and thus some Raman-forbidden polar modes may be observed in Raman scattering. This is also the case of Ga_2Se_3, which exhibits a multitude of polar resonances between 221 and 255 cm^{-1} that are also visible in Raman scattering [205]. The lattice of Ga_2Se_3 is believed to have an orthorhombic defect zincblende structure [205], with a D_{2h} point group, but the exact nature of the observed vibrational modes is not well-established.

Hyperbolic materials can sustain guided and surface modes in deeply sub-wavelength waveguides, thus even thin layers of α-Ga_2O_3 or β-Ga_2Se_3 can greatly affect the electric field distribution near the GaSe interfaces, potentially altering the dispersion of surface modes significantly. In ultra-thin films, surface polariton modes become Epsilon Near Zero (ENZ) modes, which are a limiting case of the upper (high-frequency) surface polariton in polar dielectric films with a thickness smaller than $\lambda_0/100$, where λ_0 is the free-space wavelength of the polariton. In such thin films, the whole dispersion curve of the upper polariton is constrained to narrow energy interval just below the LO phonon energy, where the permittivity has a zero crossing (see Fig. 8.20). The near-zero permittivity leads to extremely high

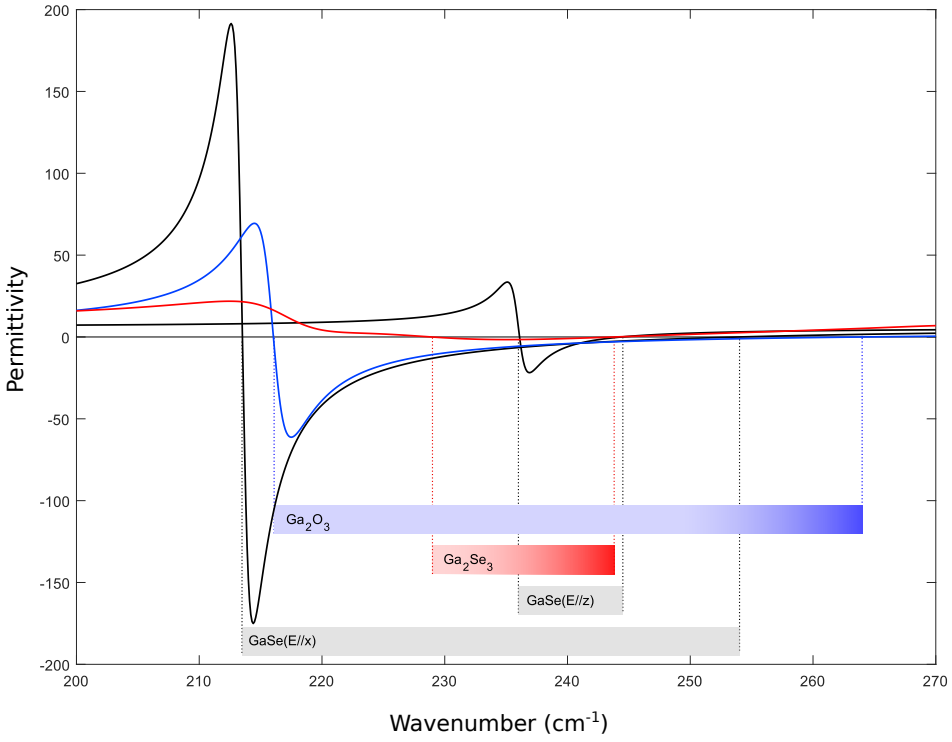

Figure 8.19 Resthrahlen band overlaps between GaSe (black curves), Ga_2O_3 (blue curve), and Ga_2Se_3 (red curve). The values for Ga_2O_3 come from reflectivity measurements from a bulk β-Ga_2O_3 crystal with the electric field along the c axis of its monoclinic lattice [237]. The Ga_2Se_3 data come from reflectance measurements on MOCVD-grown Ga_2Se_3 films on GaP substrates [238]. The two Resthrahlen bands of GaSe are indicated by gray bands, and those of both oxidation byproducts are indicated by red and blue bands.

field enhancement in the ENZ layer [239, 240]. Recent work by Passler *et al.* [114], revealed evidence of strong coupling and hybridization between surface polaritons of a slab of SiC with the ENZ polariton mode of an ultra-thin AlN film. Such ENZ modes in the oxidized layer could therefore significantly affect the dispersion of modes in the GaSe slab.

Since both oxidation byproducts are anisotropic, their crystalline lattice orientation relative to the layer geometry can have a major incidence on the resulting field distribution. A simplified uniaxial model of the permittivity tensor of these oxidized layers was defined in order to estimate their effect on the Raman spectrum. The permittivity tensor used is

$$\overleftrightarrow{\epsilon}^{\lambda} = \begin{pmatrix} \epsilon_o^{\lambda}(\omega) & 0 & 0 \\ 0 & \epsilon_o^{\lambda}(\omega) & 0 \\ 0 & 0 & \epsilon_e^{\lambda}(\omega) \end{pmatrix}, \tag{8.2}$$

which uses the same coordinate system used throughout. λ represents either Ga_2O_3 or Ga_2Se_3. Simplified expressions of $\epsilon_o^{\lambda}(\omega)$ and $\epsilon_e^{\lambda}(\omega)$ were defined using the dielectric function presented in Chapter 3. The lattice coordinate along which the resonance shown in Fig. 8.19 occurs ((001) and $(\bar{1}10)$ directions for Ga_2O_3 [237] and Ga_2Se_3 [241], respectively) is defined as the extraordinary (out-of-plane) axis, and all lattice modes along that direction are defining $\epsilon_e^{\lambda}(\omega)$. The remaining lattice modes are considered degenerate in the xy plane and included in the expression of $\epsilon_o^{\lambda}(\omega)$. This approximation can be justified when considering that most of the polar modes assigned to the ordinary axes have energies far above the energy range considered here and do not contribute significantly to the permittivity below their resonant frequency. Ga_2Se_3 does possess two distinct polar modes in the energy region of interest with very similar energies.

The resulting permittivities are illustrated in Fig. 8.21, where the Resthrahlen bands of both oxidation byproducts for z-oriented electric fields are indicated by red and blue bands. The in-plane permittivities of the oxidation byproducts, indicated by the two arrows, do not possess Resthrahlen bands in this energy range. In the case of Ga_2O_3, no active polar modes occur in this energy range, and the in plane permittivity is almost constant, whereas in the case of Ga_2Se_3, there is an infrared-active vibrational mode in this energy range, but its weak resonance does not cause the permittivity to become negative. Note that this could also be explained by an inaccurate evaluation of the high-frequency permittivity ϵ_∞.

Fig. 8.22 illustrates the resulting electric field distribution in the oxidized layer system for a 650 nm slab of GaSe with a 5 nm layer of Ga_2O_3 or Ga_2Se_3 on either interface. The sample tilt is set to 15° and 3°, respectively, as these are angles for which GaSe polariton mode energies coincide with the oxidation byproducts ENZ regions. Indeed, the E_z field

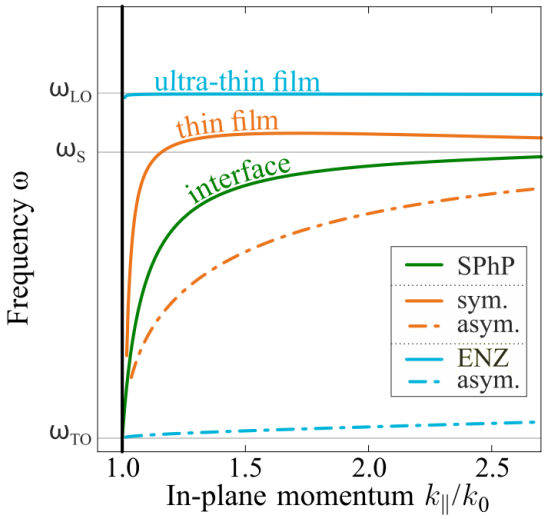

Figure 8.20 Schematical surface polariton mode dispersion for bulk (green curve), thin films (orange curves) and ultra-thin films (cyan curves). In the ultra-thin limit, the upper surface mode becomes non-dispersive, with an energy equivalent to ω_{LO}. Note that in this thesis, the two surface polariton branches are referred to as 'upper' and 'lower' surface polaritons, rather than the 'symmetric' and 'asymmetric' nomenclature used in this figure. Reprinted with permission from Ref. [114] © 2018 American Chemical Society.

magnitude is maximal between 245 and 260 cm^{-1} for Ga_2O_3, and between 225 and 235 cm^{-1} for the Ga_2Se_3 layer as indicated by the blue and red dotted rectangles, respectively, on Fig. 8.22. These wavenumber ranges are where ENZ modes occur in these materials, where strong field concentration is expected.

The presence of the oxidized layers affects the field distribution inside the GaSe slab, which affects the resulting scattering spectra. Fig. 8.23 illustrates the effect of the presence of oxidized layers at the GaSe slab interfaces. The rightmost panel presents the pristine GaSe Raman dispersion $I_{\mathrm{Pristine}}(\omega,\theta)$, whereas both panels on the right illustrate the difference between this pristine slab spectrum and the oxidized slab scattering for both oxidation byproducts, $\Delta_{\mathrm{Ga_2O_3}}(\omega,\theta) = I_{\mathrm{Ga_2O_3}}(\omega,\theta) - I_{\mathrm{Pristine}}(\omega,\theta)$ and $\Delta_{\mathrm{Ga_2Se_3}}(\omega,\theta) = I_{\mathrm{Ga_2Se_3}}(\omega,\theta) - I_{\mathrm{Pristine}}(\omega,\theta)$. The results show that the oxidized layers tend to mostly reduce the scattering intensity within their respective ENZ energy bands, along with inducing a slight blueshift and redshift of the scattering energies in the case of Ga_2O_3 and Ga_2Se_3 oxidized layers, respectively. This effect is unlikely to be significant in the data presented in Fig. 8.16, since the main discrepancy between measured and calculated spectra is the high intensity at high scattering angles in the experimental data.

The coupling of these ENZ modes affects the dispersion of the polariton modes in the GaSe

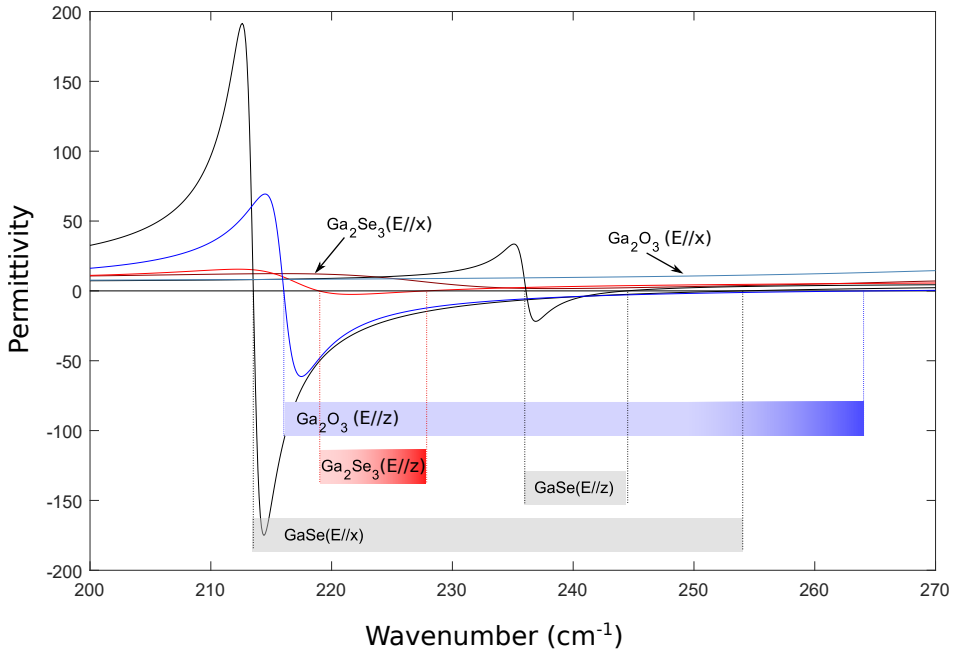

Figure 8.21 Resthrahlen band overlaps between GaSe (black curves), Ga_2O_3 (blue curves), and Ga_2Se_3 (red curves) for the simplified dielectric model. The permittivity as described by Eq. (8.2) was used to generate these curves. The two Resthrahlen bands of GaSe are indicated by gray bands, and those of both oxidation byproducts for z-oriented electric fields are indicated by red and blue bands. The in-plane permittivities of the oxidation byproducts do not possess Resthrahlen bands in this energy range, and are indicated by the two arrows.

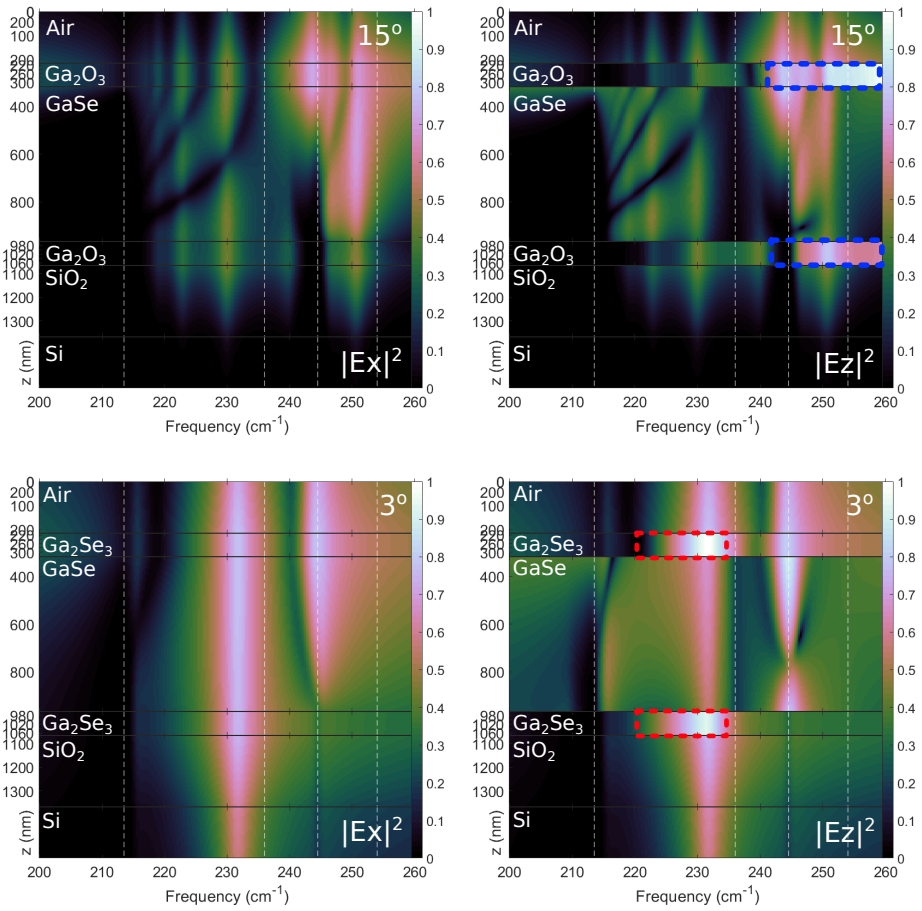

Figure 8.22 Field distribution in a 650 nm slab of GaSe with 5 nm-thick oxidized layers of Ga_2O_3 or Ga_2Se_3 at both interfaces. As indicated on the figures, sample tilt angles are 15° and 3°, respectively. Regions of significant ENZ field enhancement in the oxidized layers are indicated by the red and blue colored rectangles. Note that the oxidation product layer thicknesses have been magnified by a factor of 20 in the plots to help visibility.

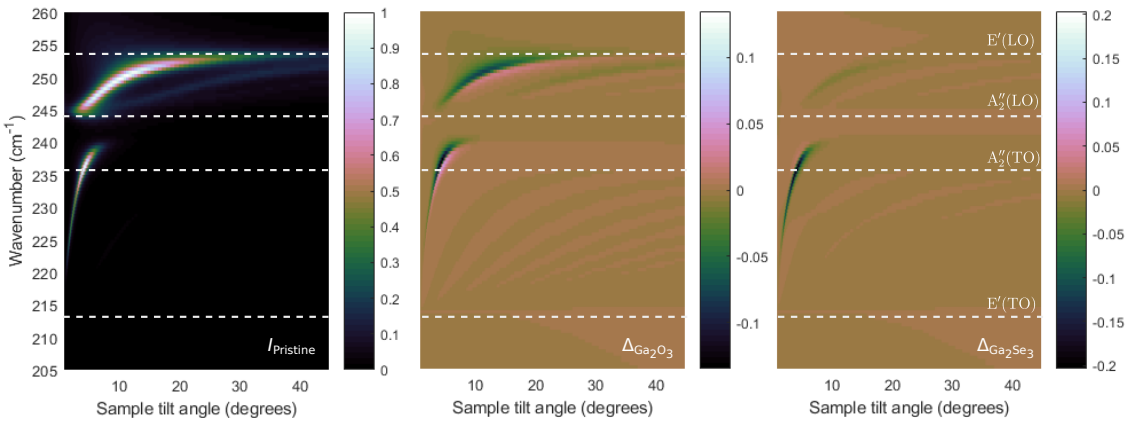

Figure 8.23 Computed un-broadened Raman scattering dispersion from an oxidized 650 nm GaSe layer, with 5 nm-thick oxidized layers of Ga_2O_3 or Ga_2Se_3 at both interfaces. The leftmost panel presents the non-broadened dispersion for a pristine GaSe layer, and both panels on the right represent the difference between this pristine slab spectrum and the oxidized slab scattering for both oxidation byproducts.

slab, but it may also directly contribute to the measured Raman scattering signal. Indeed, since both oxidation byproducts have polar lattice modes with energies located within the GaSe Reststrahlen bands, their polariton states can not only alter the GaSe polariton dispersion, but also directly scatter light, and this contribution has the potential to be significantly enhanced by the large ENZ field concentration. The Ga_2O_3 and Ga_2Se_3 polar modes considered here are Raman-forbidden, but as already discussed, these photo-oxidized layers are likely to have poor crystalline quality and scattering selection rules could be broken. The field enhancement in the oxidized layers could therefore directly contribute to Raman scattering in their respective ENZ regions.

In order to evaluate the direct Raman scattering contribution from the oxidized layers using the computed electric field, the numerical model presented in Chapter 5 is inadequate and would need to be significantly modified to include several additional elements. The Raman tensor elements of the defect-rich low-symmetry oxidation byproducts would need to be determined, as well as the Hopfield coefficients and Faust-Henry coefficients for each vibrational mode. Furthermore, in the case of Ga_2Se_3, the Resthrahlen band includes contributions from multiple coupled polar modes along the same axis, which cannot be adequately taken into account by the model of Chapter 4 as it assumes that each coordinate has only one active polar mode, thus the Hopfield coefficient definition used in this thesis would need to be adapted. Finally, as mentioned earlier, the crystalline lattice orientation of the oxidized layer could also significantly affect the result. Despite the complexity of such an approach, it would be

worthwhile to pursue it in further work. The direct Raman scattering from oxidized layers with polar lattice modes that lie within the GaSe Resthrahlen band could have an impact on the experimental results despite the small oxidized volume due to the large electric field magnitudes of these ENZ modes. Such ENZ enhanced Raman scattering might explain the larger than predicted scattering intensity from the *Sp* branch observed in the measured data at high tilt angles.

8.3.4 Thickness dependency

The effects of scattering angle and dielectric environment have been shown to affect the Raman spectrum in, and can be used to selectively probe certain regions of the polariton dispersion, and even to alter the dispersion relation in order to engineer polariton energies and propagative behavior. However, one of the most direct means of altering the confined polariton dispersion is to alter the 2D waveguide dimension, as discussed in Chapters 4 and 5.

The effects of waveguide thickness on polariton dispersion were calculated and are presented in Fig. 8.24. The effect of angular broadening has not been included here. For a 5° scattering angle, the *Sp* polariton scattering energy is highly dependent on sample thickness, spanning from 225 cm^{-1} for samples around 100 nm to about 240 cm^{-1} for samples that are 1000 nm or more. The *Le* branch varies more slowly, with frequencies around 245 cm^{-1} for thin layers and rising towards 254 cm^{-1} for samples of a few micrometers. When the sample tilt angle is increased, polaritons of larger transverse wave vectors are probed, and thus the scattering energies rise faster with thickness, with most of the energy variation of both polariton branches occurring in lower thickness regions.

This thickness dependence makes polariton Raman scattering a useful tool to rapidly determine sample thickness through Raman spectroscopy, especially for the *Sp* polariton branch since it spans a larger energy range. Furthermore, the sensitivity of the dispersion with the sample tilt angle enables rapid thickness determination over a wide range of sample dimensions. This method could be especially useful in the 50 to 1000 nm thickness range, since mechanical lattice mode shifts, commonly used to evaluate 2D material thicknesses, can generally only be used for samples below 10-30 layers thick depending on the material [45]. Therefore, polariton scattering energies might be used for rapid thickness evaluation above those thicknesses.

These results also highlight the fact that a narrow optical acceptance angle is necessary to precisely determine sample thickness from polariton Raman scattering, since the observed energies are highly sensitive to the sample angle, which can be directly equated to the trans-

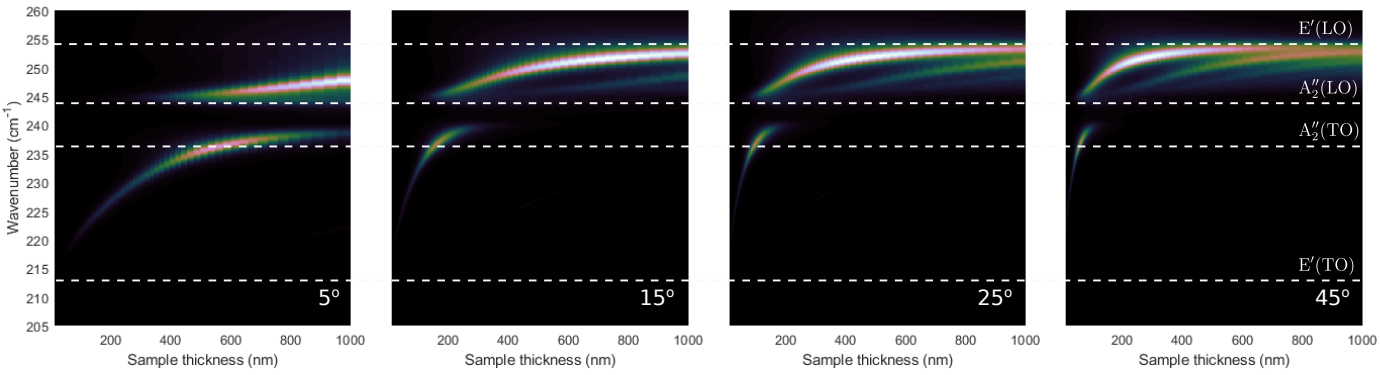

Figure 8.24 Computed thickness-dependent Raman scattering without angular broadening for multiple sample tilt angles, as indicated in the bottom right of each plot. Energies of the polar lattice modes are indicated by the horizontal dashed lines.

verse wave vector. In this work, a confocal Raman microscopy system was used, yielding a total acceptance angle estimated to 15°, and this low selectivity hinders accuracy from this approach to thickness determination. This effect is minimized in the normal incidence scattering configuration, since the effective acceptance angle is halved due to symmetry. Therefore, the measured normal incidence scattering data is expected to have the best predictive ability in regards to the thickness of the sample. Furthermore, as was previously mentioned, samples in the $\sim 1 \times 10^2$ nm thickness range, such as those studied in this work, are more easily differentiated by their near-normal *Sp* polariton scattering energy. Fig. 8.25 illustrates the computed Raman scattering spectrum as a function of sample thickness for a normal incidence, along with the fitted Lorentz peak positions from five different GaSe flakes. For each thickness value, the spectrum has been normalized by its maximum value in order to illustrate spectral distribution, rather than the thickness-related intensity dependence. The white symbols represent the *Sp* and *Le* polariton energies from samples of known 170, 190, and 650 nm thicknesses as measured by AFM. The orange and cyan symbols represent measured data from two flakes of unknown thickness, which were estimated by comparison with the computed spectra as being 300 and 400 nm thick, respectively.

The results presented in this section show an excellent agreement with the experimental data, indicating that Raman scattering from confined polaritons is a useful means of determining sample thickness in this thickness range. Use of a narrower angular aperture would enable higher precision from this technique.

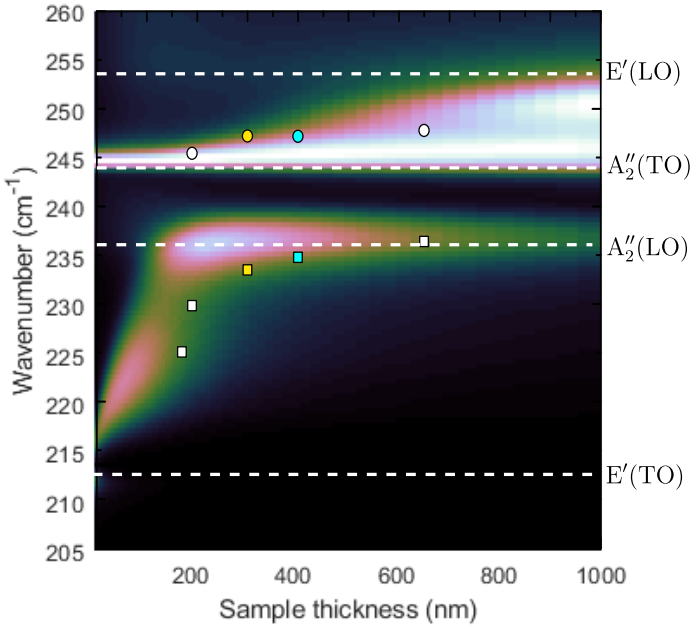

Figure 8.25 Computed Raman scattering as a function of sample thickness for normal incidence, with a 15° angular broadening value. For each thickness value, the spectrum has been normalized by its maximum value in order to illustrate spectral distribution. Experimental normal-incidence polariton Raman mode positions from 170, 190, and 650 nm flakes are overlaid on the plot as white squares and circles representing the *Sp* and *Le* polariton branches, respectively. Additional scattering data from two flakes whose thicknesses were estimated as 300 and 400 nm are indicated as orange and cyan symbols, respectively.

8.4 Resonant Raman

As mentioned in Chapter 4, Raman scattering can be significantly enhanced when either the incident or scattered photons are resonant with an electronic transition. This effect can be especially important for polar lattice vibrations since they can couple strongly to excitons through the Fröhlich interaction. In this section, resonant polariton scattering under excitation with 633 nm laser radiation is presented. The effects of this resonance on the Raman spectrum and angular dispersion are discussed, as well as their temperature dependency. Finally, polariton lateral confinement effects are shown to be strongly enhanced under resonant excitation through polarization-resolved Raman scattering measurements.

8.4.1 Low-temperature Raman scattering

In this section, cryogenic temperatures is used as a tool to tune the energy difference between the first exciton state and excitation laser. In order to accurately interpret the nature of the observed Raman modes, the energy variation of the lattice modes as a function of temperature must first be understood. Temperature-induced wavenumber shifts of all lattice mode frequencies are detailed in Table 8.1. Reliable data regarding the temperature shifts of the Raman-forbidden A_2'' mode energies could not be found in the literature and were thus inferred from the other reported values, assuming that the temperature-induced frequency shifts are proportional to each mode's frequency. The average observed shift from the A_1', E'', and E' modes is $\Delta\sigma/\sigma = 9.4 \times 10^{-3}$. This approximation accounts for the thermal expansion frequency shift, and although it does not take into account the three-phonon anharmonic coupling or Grüneisen parameter variance among modes [242], it provides a useful estimate of the temperature-induced energy shift for these Raman-forbidden modes.

Lattice mode	$\Delta\sigma$ (cm^{-1})
$A_1'^{\,1}$	1.4^a
E''	1.3^a
E'(TO)	2.5^b
A_2''(TO)	2.2^*
A_2''(LO)	2.3^*
E'(LO)	2.4^a
$A_1'^{\,4}$	2.8^a

Table 8.1 GaSe mechanical lattice mode energy shift $\Delta\sigma = \sigma_{\mathrm{GaSe}}(77\,\mathrm{K}) - \sigma_{\mathrm{GaSe}}(293\,\mathrm{K})$. ($a$) Values from Ref. [18] for ϵ-GaSe. (b) values from Ref. [242]. ($*$) Values estimated from the temperature frequency shifts observed in other modes.

Fig. 8.26 illustrates Raman scattering from a GaSe flake at room and liquid nitrogen temperatures measured with a 532 nm laser The flake thickness is estimated as ∼750 nm from the room temperature spectrum, as shown by the good agreement between the computed Raman spectrum (red curve) and measured data at 293 K. Using the low-temperature energies presented in Table 8.1, the low-temperature spectrum can be computed, and is shown by the top red curve of Fig. 8.26. Note that in this computation, only the polar E′ and A_2'' mode energies were altered, with all other parameters remaining fixed to their room temperature values. The upper Le_2 mode's energy and intensity are slightly underestimated by the model, which may be due to an erroneous estimation of the low-temperature A_2'' mode energies, but the overall resulting spectrum agrees well with the measured spectrum. These results demonstrate that no significant qualitative changes occur at different temperatures under 532 nm excitation.

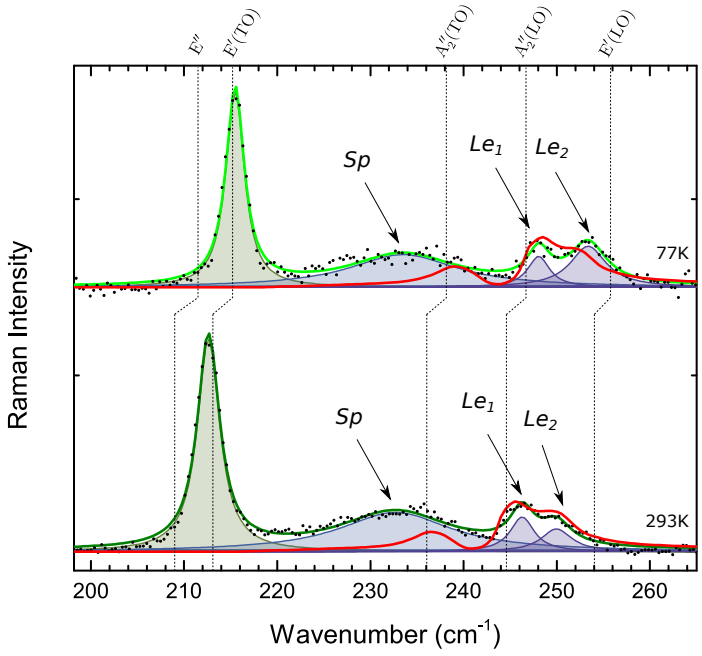

Figure 8.26 Low-temperature Raman scattering from a GaSe flake. Experimental data at room temperature and liquid nitrogen temperature are represented by the black points, along with the Lorentz peak fits as the shaded curves. Solid pale and dark green curves illustrate the resulting summed fitted spectra for 77 K and 2 93K sample temperatures, respectively. The red solid curved illustrate the computed Raman spectra at both temperatures for a 750 nm GaSe sample. Energies of the mechanical lattice modes at both temperatures are indicated by the vertical dashed lines.

8.4.2 Resonant phonon scattering in GaSe

Under resonant excitation, all Raman-active modes are exalted since the Raman tensor $\widetilde{R}$ includes near-vanishing denominators. In addition, the k-dependent Fröhlich exciton resonant mechanism [154,231] can also lead to a significant resonant enhancement of LO mode scattering for excitation energies near that of the $1s$ exciton. This LO-specific Fröhlich resonance was observed in Raman scattering for the allowed E'(LO) mode as well as the forbidden A_2''(LO) in ϵ-GaSe by multiple authors [18, 140, 229, 243, 244], including multi-phonon resonance up to the 6^{th} order for the E'(LO) mode [243, 244]. Here, it is interesting to note that the observed selection-rule breaking, as well as the multi-phonon resonant enhancement, means that longitudinal polar modes could be observed in Raman scattering from centrosymmetric crystals, where they are usually Raman-forbidden.

In order to contextualize the resonant polariton scattering results that are reported in the next sections, this section presents a brief overview of the results reported by Hoff [18]. In their work, results from resonant Raman scattering from large ϵ-GaSe samples in right-angle geometry are reported and interpreted using Martin's model [154, 231]. The sample size and scattering geometries that were used mean that no polariton dispersion effects should be apparent in their results. Indeed, low confinement and large scattering wave vectors only allow scattering from pure phonon modes. Nevertheless, the results and interpretations presented in this section provide valuable insight for the analysis of the resonant polariton scattering results reported in the following sections.

Fig. 8.27, reproduced from Ref. [18], shows the reported Raman scattering efficiency, S_{GaSe}, of several Raman modes of GaSe when the excitation laser approaches the $1s$ exciton energy E_{ex}, in reference to the scattering efficiency of α-quartz, S_{Q}. In the reported experiment, incident and scattered photons were polarized along the z axis and propagating in the GaSe xy plane, thus the E′ mode was Raman-forbidden in this configuration, but the results reported by Hoff can still translate to the scattering geometries used in this thesis since the observed resonance is accompanied by a selection rule breakdown. In the left panel, the nonpolar A_1' modes (both A_1' modes having similar behavior)) and the E′(TO) mode resonant behaviors are illustrated. In the case of the nonpolar modes, there is a marked anti-resonance around 45 meV below the first exciton level, which the authors could not explain using their model. A_1' and E′(TO) were reported as both exhibiting a strong resonance at the exciton energy. Although forbidden in this geometry, resonant excitation breaks selection rules and the intensity of E′(TO) becomes comparable to that of A_1'.

The right panel of Fig. 8.27 illustrates the resonant behavior of the E′(LO) and A_2''(LO) modes, for which scattering via k-dependent Fröhlich interaction with excitons is dominant.

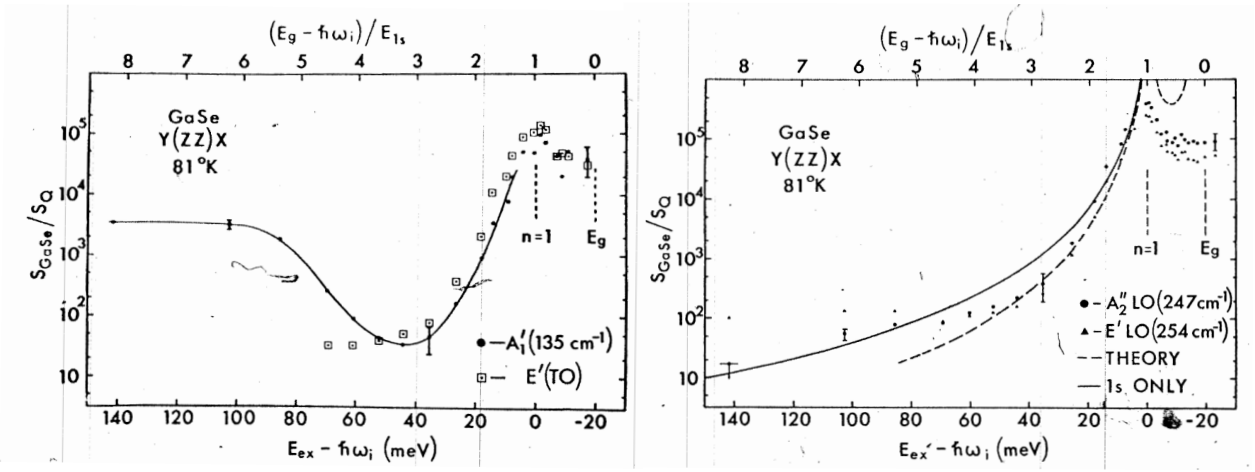

Figure 8.27 Scattering efficiency from nonpolar and TO phonon modes (left panel) and LO phonon modes (right panel) in GaSe as a function of the energy difference between the 1s exciton and the excitation laser. Scattering intensity is normalized relative to the scattering intensity, S_Q, from a quartz sample. The solid line on the left panel is a guide to the eye following the $A_1'^1$ antiresonant behavior. On the right panel, the dashed and solid lines illustrate the theoretical curves from Martin's model, and the isolated 1s exciton contribution, respectively.Adapted with permission from Ref. [18] © 1975 Canadian Science Publishing.

Both LO modes show similar resonant enhancement near the 1s exciton, which is more than an order of magnitude higher than for non-polar and TO modes, as predicted by Martin's model (see §4.3.3 and Ref. [18]). For lower excitation energies, there is a significant distinction between the two LO modes. The E′(LO) mode, which is Raman-allowed in other scattering geometries, includes a deformation potential resonant component with baseline at about 10^2 S_Q and which is dominant for excitation more than ∼100 meV below the 1s exciton. Conversely, the A_2''(LO) mode scattering efficiency does not plateau at low excitation energies, since there is no uncorrelated carrier contribution to the resonance, and its scattering efficiency only originates from the 1s exciton Fröhlich interaction selection rule breaking. The resonant enhancement of both these longitudinal modes has only been observed by the authors for zz-polarized geometries, which is attributed to the strong dipolar orientation of both the 1s exciton state and of the optical dipole of the direct bandgap, which is along the z axis in GaSe [140].

Overall, Hoff observes excellent agreement between his results and the proposed mechanical phonon dispersion and resonance models, which have been referred to throughout this thesis. However, major discrepancies between the reported results and those presented in this thesis indicate that the mechanical phonon-based model of Hoff does not provide a comprehensive

picture of Raman scattering in GaSe. Indeed, the large samples used in their work exhibit high polariton dispersion rates and the right-angle scattering geometry only probes large wave vectors, therefore all observed energies correspond in almost every case to the large-wave-vector asymptotic behavior of polariton modes, which converge toward mechanical phonon energies. However, when sample dimensions are comparable to or lower than the polariton wavelengths, which is the case for every sample studied in this work, polaritonic dispersion becomes significant and is clearly apparent in Raman scattering, including resonant Raman effects, as discussed next.

8.4.3 Resonant polariton scattering in GaSe

Fig. 8.28 illustrates the Raman scattering measured from a ∼750 nm GaSe flake under excitation from 532 nm and 633 nm lasers, at room temperature and liquid nitrogen temperatures. At room temperature, the exciton energy of $E_{\text{ex}} = E_g - E_R = 2.00\text{eV}$ (where $E_R = 19.2\text{meV}$ is the exciton Rydberg energy [227, 228]), and for liquid nitrogen temperatures, the exciton energy increases to 2.085 eV [245]. The energy differences between the excitation laser energy $\hbar\omega$ and exciton energy E_{ex} are indicated for each curve on the left of Fig. 8.28. It must be noted here that, although it is not in direct resonance with the $1s$ exciton, the 532 nm laser energy is above the bandgap and injects charge carriers in the sample, which can have an impact on polariton mode energies and dispersion [246, 247]. The 633 nm laser is strictly below the bandgap and cannot generate free carriers or excitons in the sample. If it is possible that some of the mode energy shift observed in spectra from both lasers originate from a carrier population difference, it should have has minimal effects on scattering intensity. The effects of resonance on Raman scattering efficiency is discussed next.

The two upper curves of Fig. 8.28 illustrate the Raman scattering data at ambient temperature for both excitation lasers, where the near-resonance from the 633 nm spectrum exhibits several marked differences compared to the off-resonance 532 nm spectrum. Under near-resonant conditions, the Sp surface mode becomes much broader, potentially due to additional contribution from resonance-enhanced guided Te modes. The E′(TO) mode does not shift significantly in energy, but its intensity is drastically reduced compared to the $\text{A}_1'^{\,4}$ nonpolar mode used here as an intensity reference. Conversely, the two Le polariton modes are greatly exalted, and the splitting between the two is increased, indicating that they are strongly affected by the near-resonant conditions. This correlates well with the Fröhlich exciton resonance model of Martin [154, 231] described in §4.3.3, since these two polariton modes possess a longitudinal character, thus can exhibit resonant k-dependent Fröhlich interaction with the $1s$ exciton.

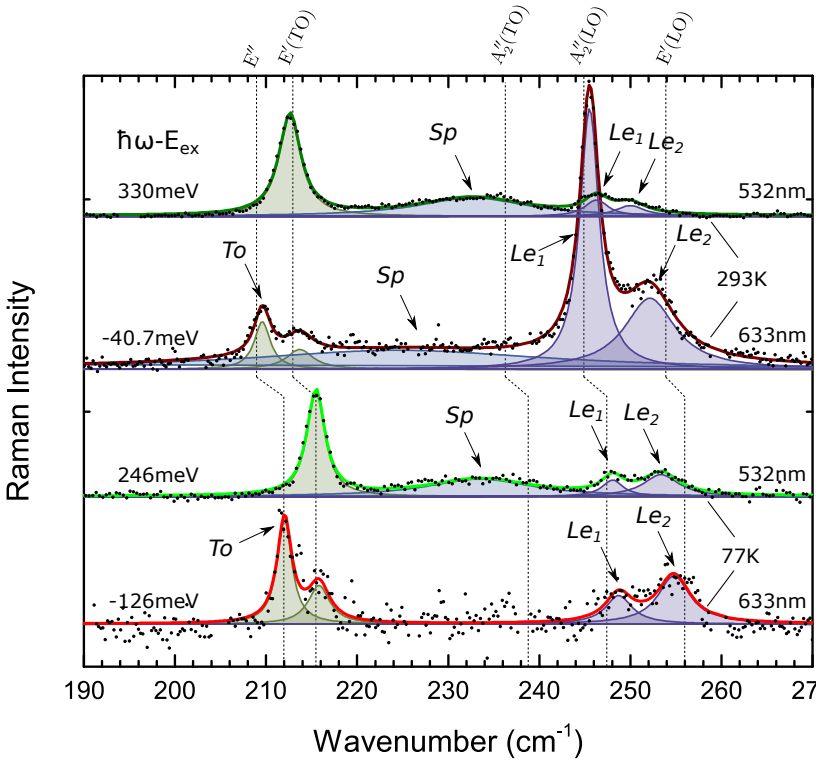

Figure 8.28 Raman spectra from GaSe at room temperature and liquid nitrogen temperature. Measured data are indicated by the black symbols, shaded areas correspond to the individual fitted Lorentzian peaks for each mode, and the solid green and red lines represent the resulting fitted spectra for 532 nm and 633 nm laser excitation, respectively. All spectra were normalized using the $A_1'^4$ integrated scattering intensity as a reference. Energies of the mechanical lattice modes are indicated by the vertical dashed lined for both temperatures.

Finally, a new mode near the E″ mechanical phonon is also exalted near resonance. The strong resonant enhancement observed here, along with the fact that the E″ mode is forbidden for this scattering geometry, indicates that this mode is likely a guided To polariton, as was reported in Ref. [233] for reflected forward scattering in a bulk sample. Even though this is a transverse polariton, it may possess some some longitudinal character, thus q-dependent Fröhlich matrix elements could contribute to its scattering efficiency. Other resonant terms may also cause selection rule breakdown for this polariton mode, as was observed by Hoff for the mechanical E′(TO) mode near the $1s$ exciton energy [18]. A similar Raman mode was observed in near-forward scattering measurements at $209\,\mathrm{cm}^{-1}$, although it did not match the computed angular dispersive behavior for the To polariton branch (see §8.1.2).

The bottom curves in Fig. 8.28 illustrate Raman scattering from the same GaSe flake cooled to liquid nitrogen temperature. At this temperature, the 633 nm laser is further away from the $1s$ exciton energy, and therefore resonant enhancement is diminished. This holds true for the two Le polariton modes, which exhibit similar intensities than for the 532 nm laser. In contrast, the To polariton mode remains exalted even at low temperatures and 633 nm excitation. This could be explained by the fact that the resonant scattering cross-section of this transverse mode does not involve the q-dependent Fröhlich term in a significant manner as is the case for the Le modes. Other resonant terms may exhibit a more gradual decrease away from resonance.

8.4.4 Second-order Resonant Raman scattering

Fig. 8.29 shows the observed second order resonant Raman scattering from the Le_2 polariton under near-resonant laser excitation. Conversely second order resonant Raman is not clearly observed for the lower Le_1 mode in Fig. 8.29, manifesting at most as a slight shoulder to the observed mode.

Overtone resonant Raman scattering has been reported for the $245\,\mathrm{cm}^{-1}$ mechanical E′(LO) phonon by several authors, up to the 6^{th} overtone [229,243,244], which correlates well with the data presented here. A_2''(LO) resonant overtones, however are also absent in data reported in the literature, despite exhibiting strong first-order resonances. This has been explained by the fact that the E′(LO) mode has stronger anharmonic forces than the the A_2''(LO) mode, based on two-phonon infrared absorption measurements [244].

A parallel can be drawn between these observations and the resonant Le polariton behavior observed here, since the energies of the Le_1 and Le_2 modes are very close to those of the mechanical A_2''(LO) and E′(LO) oscillators, respectively, therefore their lattice deformation components likely possess characteristics similar to these normal modes.

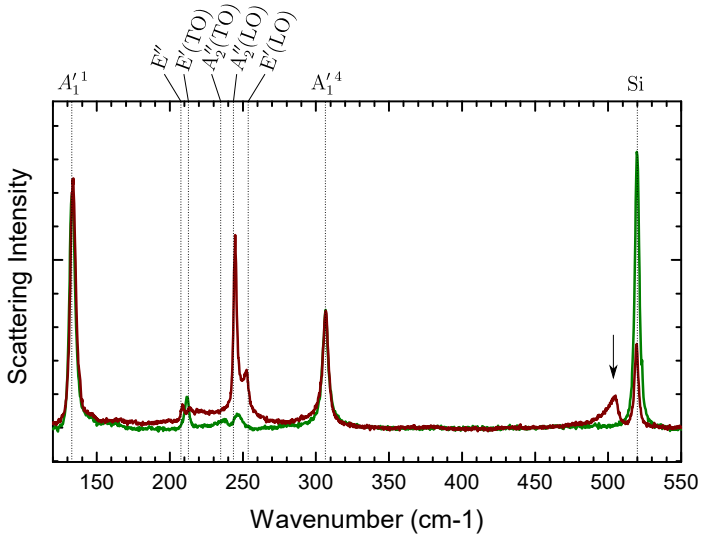

Figure 8.29 Resonant second-order Raman scattering from GaSe. Spectra for 532 nm and 633 nm excitation are represented bu the green and red curves, respectively. The second overtone of the resonantly-enhanced Le_2 polariton, visible in the 633 nm spectrum is indicated by the black arrow. Energies of the GaSe and silicon normal lattice modes are indicated by the vertical dashed lines.

The resonant Raman results presented in this section offer an interesting insight into the coupling between the electronic and polaritonic states in GaSe, and provide an interesting window into the rich band structure and exciton dynamics of GaSe. Furthermore, the extreme enhancement of the Raman cross-section near resonance enables a closer study of polaritonic effects which could not be observed away from resonance due to weak signals. This resonant behavior can indeed be used to study second-order Raman scattering, but also to reveal multi-dimensional polariton confinement effects, as is presented in the next section.

8.5 Lateral confinement effects

As has been established by numerical modeling and Raman scattering measurements, polaritons confined along the z dimension in 2D GaSe slabs below the polariton free-space wavelength (λ_0 ~40 µm) have thickness-dependent dispersion relations. Furthermore, mechanically exfoliated flakes are finite in all dimensions, often at a smaller scale than λ_0, yielding 3D confinement of the modes. In this section, lateral polariton confinement effects in mechanically exfoliated flakes are studied using resonant Raman scattering, demonstrating the great potential of the technique to probe subtle effects in confined polariton states.

Fig. 8.30 shows the polarization-resolved Raman spectra from a large (0.8× 1.2 cm) 70 µm thick GaSe slab, under excitation from 532 nm and 633 nm lasers. The leftmost panel shows

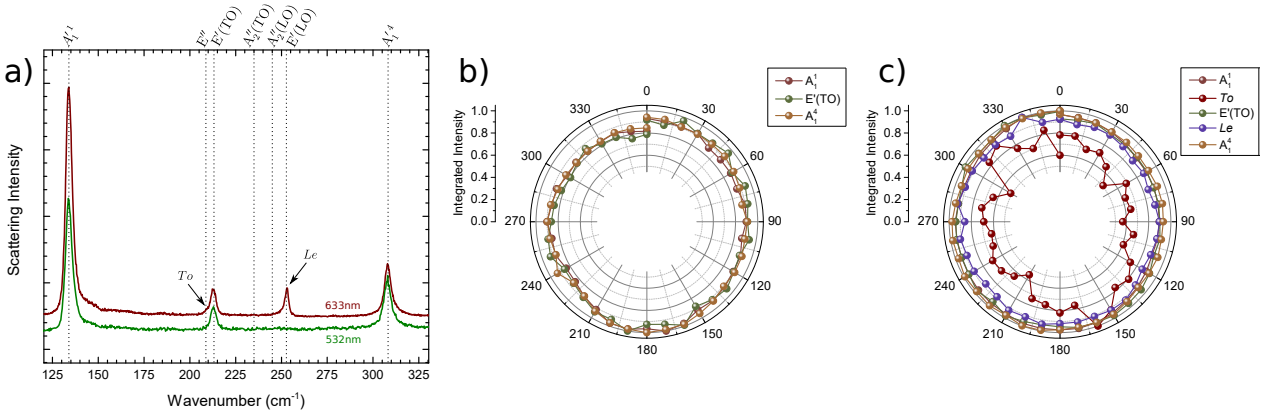

Figure 8.30 Polarization-resolved backscattering spectra from a bulk 70 µm GaSe sample. (a) Raman spectra for a polarization angle ϕ=0° under 532 nm and 633 nm laser excitation, normalized by the A'^4_1 scattering intensity. Energies of the mechanical lattice modes are indicated by the vertical dotted lines. Resonantly-enhanced *To* and *Le* polariton modes are indicated by the arrows. The polar plots illustrate the polarization dependency of the integrated intensity of all Raman modes from (b) 532 nm and (c) 633 nm laser excitation. All curves are normalized by their highest value.

typical spectra from both lasers, with 532 nm excitation showing strong signal from all Raman-allowed mechanical phonon modes for normal incidence : A'^1_1, A'^4_1, and E′(TO). As shown in Fig. 8.30(c), no polarization anisotropy is observed in this geometry, as is expected from the Raman tensor symmetries. Under 633 nm laser excitation, *To* and *Le* resonance-enhanced polariton modes are observed in addition to the same non-polarized mechanical phonon modes. The *Le* mode is clearly not polarized, while the *To* mode appears to be slightly polarized with a twofold symmetry.

In an infinite 2D slab, polariton states are fully defined by the sample interfaces and by the dielectric tensor, which in GaSe is isotropic in the xy plane. Therefore, in similar fashion to the in-plane mechanical modes, there is no expected favored scattering polarization direction for the polariton modes at normal incidence. However, finite samples have lateral boundaries that can reduce the in-plane symmetry of polariton field distribution, which can be observed in the Raman scattering data.

Since the sample measured in Fig. 8.30 is quite large, no significant lateral confinement effects are expected, although interference with reflected waves from a sample boundary might affect the field distribution near its edges. The observed polarisation of the *To* mode likely results from the combined effect of a very weak scattering signal (one order of magnitude lower than the overlapping E′(TO) mode), and of a slight anisotropy in the collection efficiency.

While the intensity of the *Le* polariton mode scattering for near resonant excitation (633 nm) is comparable to the allowed mechanical phonon modes, it is important to note here that no polariton signal could be observed in the backscattering Raman spectrum at 532 nm. This resonant enhancement proves to be a crucial element for the observation of lateral confinement, which is discussed next.

8.5.1 Polarization anisotropy

Fig. 8.31 illustrates the resonant polarization-dependent scattering intensity from four exfoliated flakes with different geometries and aspect ratios. Optical images of the flakes are shown the leftmost column, with white dashed flake outlines highlighted for clarity. Sample (c) has a thicker triangular region in its center, indicated by the green outline. The position of the measurement location is indicated by the visible red laser beam spot or red circle. The center column indicated the polarization dependency of the mechanical phonons from GaSe, and the Si 520 cm phonon, which has a symmetrical four-fold polarization response. The symmetry of this Si Raman mode can be used as a gauge of the quality of the polarization control and measurement. As can be seen from the Si mode in Fig. 8.31(d-f), the system's polarization response is excellent, and mechanical phonon modes show the expected isotropic polarization behavior.

The rightmost column illustrates the polarization-dependent intensity of the visible polariton modes in all flakes. In the case of flake (a), which has an aspect ratio close to 1, there is no significant polarization from any of the visible modes, which is expected since the lateral confinement has a high symmetry. High aspect ratio flakes (b) and (c), however, show strong polarization effects from all polariton modes, with the maximal intensity being aligned with the samples' long axis. These results are clear evidence that lateral confinement on the order of 10 µm to 20 µm in thin flakes affects polariton mode field distribution, which in turns affects Raman scattering intensity. This results indicates that guided polariton modes in these flakes can propagate a minimum distance l_p of 5 µm to 10 µm, since reflected waves at each lateral interface need to reach each other for confinement anisotropy to be observable. For a 15° collection numerical aperture, the average probed transverse wave vector k_p is $1.6 \times 10^4\,\mathrm{cm}^{-1}$, therefore the polariton propagation loss figure of of merit [14] $\gamma^{-1} = l_p/\lambda_p = 2\pi l_p/k_p$ can be estimated as $\gamma^{-1} = 16$ for flake (c), with a confinement factor of $\lambda_0/\lambda_p = 10$. This value approaches those reported for hyperbolic polaritons in high-quality *h*-BN samples [14, 101], and points to great potential for low-loss far-infrared polaritonic devices in GaSe.

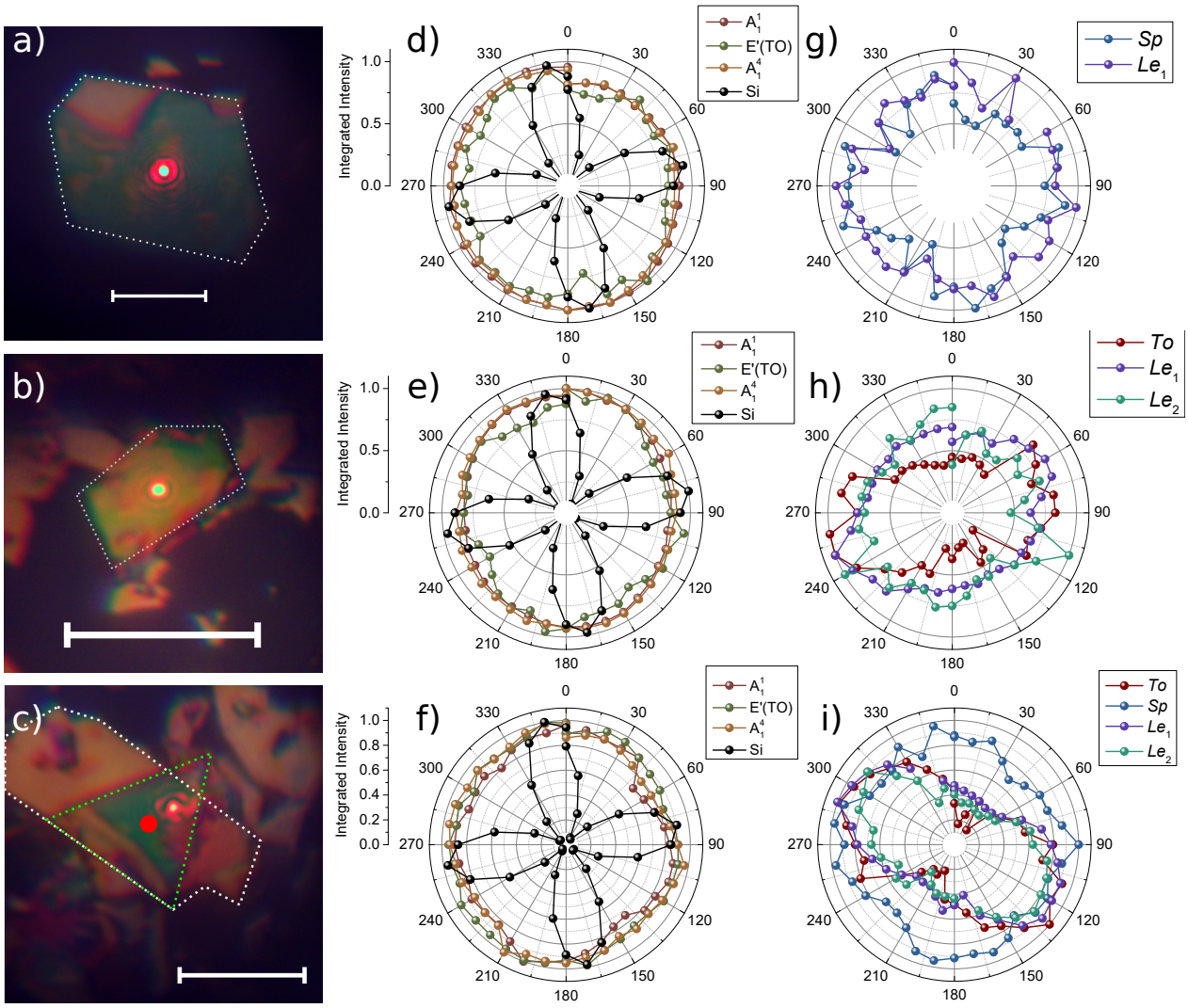

Figure 8.31 In-plane polarization of GaSe and Si modes under 633 nm laser excitation with co-polarized excitation and detection as a function of polarization angle ϕ. (a-c) Optical images of the flakes, with the measurement location indicated by the red laser dot. All white scale bars are 20 µm. (d-f) GaSe (A'_1 and E′(TO)) and Si (520 cm^{-1}) mechanical phonon mode intensities as a function of polarization. All intensities are normalized by their highest observed value. (g-i) Normalized GaSe polariton scattering intensities as a function of polarisation angle. Sample images and polar plots are mutually aligned.

8.5.2 Lateral confinement energy shifts

Controlling the scattering polarization enables selective probing of the long-axis or short-axis confined polariton modes. Since the confinement dimension is different along these two axes, the probed polariton modes are expected to have slightly different energies. Fig. 8.32 illustrates the wavenumber shift as a function of the measurement polarization angle for the flake presented in Fig. 8.31(b). The Le_1 mode, which is the most intense, shows a clear $0.4\,\mathrm{cm}^{-1}$ increase in energy for polarizations along the sample short axis, where confinement is highest, when compared to the energy along the sample's longest axis. Based on the 2D confined polariton model developed in this work, stronger confinement pushes the Le modes towards lower energies, since it reduces the dispersion rate. This is not the observed behavior here, where Le_1 is seen to exhibit higher energies in the strongest confinement direction. This could be explained by the fact that the Le_1 mode may actually include a significant contribution from the upper surface polariton mode. Indeed, this mode is expected to show an asymptotic increase toward the $\mathrm{A}_2''(\mathrm{LO})$ energy for diminishing thicknesses, as it tends toward an ENZ mode as described in §8.3.3. Note that the model does not apply to laterally-confined modes, but it gives insights for understanding the behavior observed here.

The polarization and energy anisotropies observed in the last two sections provide a clear demonstration of the potential of Raman spectroscopy as a tool to probe confined and guided polariton states with a high degree of selectivity and control. They clearly reveal the existence of 3D confined polariton states, which indicate a very high propagation loss figure of merit of $\gamma^{-1} \geq 39$, which similar to values reported in high-quality h-BN samples. However, in order to exploit the technique to its full potential, there is still a need for a more sophisticated modeling framework, which can take into account not only three-dimensional confinement of polariton modes, but also resonant scattering behavior. Indeed, near-resonant scattering is demonstrated to be a powerful technique, but it also dramatically alters scattering selection rules, which affects the observed dispersion relations.

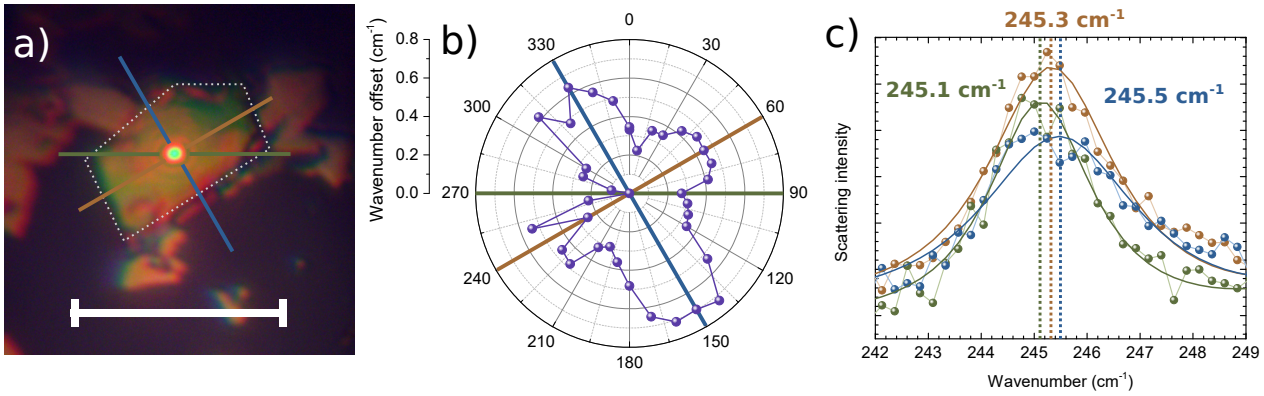

Figure 8.32 Observed polariton mode energy shift as a function of polarization angle ϕ. (a) Optical flake image, as described in Fig. 8.31. Selected polarization directions are indicated by the orange, green and blue lines, corresponding to the sample's long axis, short axis, and longest dimension, respectively. (b) Observed mode wavenumber offsets ΔN relative to lowest observed wavenumber as a function of polarization angle ϕ. Selected polarizations are indicated using the same polarization as in (a). (c) Selected fitted curves for scattering polarizations following the same color scheme as in (a) and (b)

CHAPTER 9 CONCLUSION

In this thesis, polariton Raman spectroscopy, which Henry and Hopfield used for the first experimental observation of phonon-polariton states in 1965, is brought back to the forefront of material research with the demonstration that it can be a convenient and powerful tool to study confined phonon-polariton states in 2D materials.

9.1 Summary of Contributions

The first original contribution of this work is the study of oxidation dynamics of GaSe using Raman scattering, which offers valuable insight into the photo-chemical processes involved in the rapid photo-oxidation of thin GaSe flakes, which is a common issue with 2D materials. Experimental results reveal that simultaneous exposure to above-bandgap illumination, moisture, and oxygen causes rapid sample degradation. Earliest signs of GaSe sample degradation are also reported as Ga_2Se_3 and Ga_2O_3 Raman modes at $155\,cm^{-1}$ and $161\,cm^{-1}$, respectively. These original results already have had an impact on research involving 2D GaSe flakes, providing clear guidelines regarding the protection of GaSe samples, as well as identifying the Raman fingerprint of early oxidation.

The second and probably the most significant original contribution of this thesis is the demonstration that sub-micron thin GaSe flakes exhibit strong polariton backscattering signal due to momentum conservation relaxation. In most of the literature, polariton modes are understood to be observable only in near-forward configuration owing to their low wave vectors. However, this is not the case in thin samples. This phenomenon is especially important in hyperbolic materials given the deep subwavelength confinement of polaritons, wherein polaritons modes can propagate with extremely large wave vectors. The compounded effect of relaxed momentum conservation and hyperbolic confinement yields a strong backscattering Raman signal. Even extremely thin flakes may support multiple confined polariton modes exhibiting highly dispersive behaviors. This mode dispersion means that off-normal scattering can probe wide regions of the dispersion curve. This result could have a significant impact in the 2D materials scientific community for two reasons.

The first reason is that in addition to direct experimental demonstrations pertaining to gallium selenide, the original work presented here is a clear demonstration that the simple, rapid, and accessible technique of Raman scattering is a powerful tool to study highly-confined hyperbolic polariton states in 2D materials. Just like the commonly used s-SNOM technique,

it provides high spatial resolution and energy resolution. In addition, high wave-vector resolution can be achieved through scattering geometry adjustment, without the requirement for spatial imaging of s-SNOM. Scattering geometry selection also allows observation both of in-plane and out-of-plane polarized modes, whereas s-SNOM is only sensitive to out-of-plane electric fields. Other major advantages of Raman scattering over most currently popular techniques used to study hyperbolic polaritons are that it requires neither high-quality sources and detectors at the polariton wavelength, nor near-field to far-field coupling schemes. Indeed, Raman scattering only requires lasers, optics, spectrometers, and detectors which are already commonplace in most, if not all, research labs studying 2D materials.

The second reason is that, given that all polar 2D materials are naturally hyperbolic due to their intrinsically anisotropic lattice structure, polariton scattering has to be taken into account when analyzing their Raman spectra even in backscattering configuration. For instance, experimental scattering results presented in this work have demonstrated for the first time that polariton scattering in GaSe likely has been wrongly assigned the the $A_2''(TO)$ Raman-forbidden mode in the literature. This work may also help resolving other conflicting assignment of phonon modes in other polar 2D materials, where the presence of polaritons may have gone unsuspected. Finally, the dispersion of confined polariton states is thickness-dependent, which extends the range where Raman spectra can be used to estimate the sample thickness up to 1000 nm.

The third major contribution of this work is the development of a numerical model which allows computation of Raman scattering spectra from confined hyperbolic polaritons states in multi-layer anisotropic media. This model exploits the direct relation between the lattice displacement and electromagnetic field of polaritons that is defined using the Hopfield and Faust-Henry coefficients, as was originally described by Mill and Burstein [25]. The polariton scattering spectrum can thus be completely determined from the distribution of the electric field in the sample. A 4×4 transfer matrix optical waveguide model, which was developed by Passler [28], was used to provide a complete description of the electromagnetic field in complex multi-layered anisotropic media. The electric field distribution obtained using this numerical model was then used to determine Raman spectra using a generalization for uniaxial crystals of the polariton Raman tensors and matrix elements determined by Irmer [26]. The resulting original numerical model is a powerful tool to analyze scattering spectra from complex anisotropic multilayer structures, such as exfoliated 2D materials supported by various substrates, as well as complex layered materials heterostructures.

The fourth major contribution is the use of near-resonant Raman scattering to study 3D-confined polariton states in exfoliated GaSe flakes. The original results presented show

evidence of anisotropic laterally confined polariton states. From these results, very low polariton propagation losses in GaSe were estimated, and a lower bound on the propagation figure of merit of $\gamma^{-1} \geq 39$ is reported for the first time in GaSe, which is as high as state of the art values reported in other 2D materials [14, 101]. This indicates that GaSe is a very promising material for applications in far-infrared subwavelength nanophotonic devices.

9.2 Limitations and Future Research

Many of the results presented in this thesis involve were not based on well-established measurement and analysis methods, and these novel approaches deserve to be subject to additional scrutiny. Due to a multitude of factors including the randomness inherent to sample preparation, experimental limitations, and sample degradation, some data acquired throughout the years had to be dismissed and could not be directly used to support the contributions presented in this work. Given the novelty of the reported results, it appears imperative to build larger datasets in order definitively identify and control all parameters influencing polariton behavior in 2D GaSe cavities. Four directions in particular would benefit from additional work.

The first aspect concerns the thickness dependence of the modeled polariton scattering. In this regard, a relatively low number of samples were characterized using AFM in order to establish their exact thickness, and polariton scattering data from a larger number of flakes should be obtained to reproduce calculated dispersion curves. Also, a rigorous study of the thickness dependence could help rule out potential effects from substrate charge accumulation or surface oxidation. Furthermore, care should be taken in this study to select flakes with large lateral dimensions and near-unity aspect ratios in order to mitigate effects related to lateral confinement.

The second aspect pertains to the angular resolution of the optical system used in backscattering experiments. The high numerical aperture objective used in this work was selected for the excellent spatial resolution and high collection efficiency it provides given the intrinsically weak Raman signals. However, this high numerical aperture induces significant angular broadening of the measured spectra, which turns out to be particularly detrimental to the study of highly dispersive modes such as confined polaritons, since a broad range of wave vectors are probed simultaneously. The use of low-numerical aperture optics, or independently adjustable excitation and collection aperture-shaping systems such as irises and annular apertures, would provide a significant improvement in the angular selectivity of the system, which could reveal the confined mode dispersion relations in a more precise and direct fashion. Such an improvement would reduce Raman scattering intensity from isotropic

scatterers, but should not affect the intensity from highly anisotropic polariton modes.

The third aspect concerns the photon energy of the excitation lasers that were used in this work. At the time of the experimental measurements, the only two wavelengths for which the appropriate laser source, optical filters and polarization control elements were available were 532 nm and 633 nm. While these two wavelengths proved adequate to attain the objectives of this works, there remains a possibility that some of the observed polariton scattering behavior originates from unaccounted-for phenomena. In particular, the 532 nm laser, while not in resonance with the free exciton state of GaSe, generates significant charge carrier populations in the sample. These populations are known to affect polariton states. The 633 nm laser, on the other hand, shows clear evidence of strongly resonant scattering processes, which the numerical model does not consider. Therefore, in order to clearly discriminate intrinsic polariton mode scattering from resonance- and carrier-modulated effects, Raman scattering measurements should be performed using a non-resonant, below-bandgap laser source. Such results would provide a more robust test of the proposed model, and help identify the precise origin of all scattering processes.

The fourth aspect relates to the limitations of the developed numerical model, in that it cannot take into account resonant scattering nor 3D confinement of polariton states. Lateral confinement is likely rather straightforward to implement since material dielectric properties are already well known, leaving an electromagnetic cavity boundary problem to be solved. The laterally confined polariton modes observed in this work could not be characterized beyond a cursory analysis of the anisotropic behavior of their scattering cross-section and energy. Implementation of lateral confinement in the numerical model would provide valuable insight on the nature and properties of these volume-confined polaritons. Additionally, the inclusion of resonant terms to the Raman model would require the development of a more sophisticated theoretical model, taking into account several anisotropic resonant scattering processes, as well as the associated selection rule breakdown. Such an improved model would provide an essential tool to interpret the effects of resonant Raman scattering in the reported results, which often could not be unambiguously distinguished from concomitant nonresonant scattering processes.

Building upon the significant findings reported in this work, several further research avenues appear very promising to further both the use of Raman spectroscopy and GaSe as a material, in the field of polaritonics. The first research direction concerns the use of Raman scattering to study confined polariton not only in *h*-BN, where they already have been the subject of through analysis using other techniques, but also in other common polar 2D materials, such as transition metal dichalcogenides, which could not only reveal interesting hyperbolic

polariton physics in these materials, but also introduce potential new interpretations of their Raman spectra.

The second research direction could be an expansion of the last section of this thesis by including spatially-resolved Raman scattering measurements in order to quantitatively assess the propagative properties and spatial distribution of the observed volume-confined polariton states.

Finally the last research direction could be a more ambitious venture into development of infrared polaritonic devices using micro-fabricated GaSe waveguides, mirrors, and nonlinear emitters. These could also be coupled to other 2D material optoelectronic components for signal injection, manipulation or readout by creating multifunctional layered material heterostructures.

BIBLIOGRAPHY

[1] J. Kasprzak, M. Richard, S. Kundermann, A. Baas, P. Jeambrun, J. M. Keeling, F. M. Marchetti, M. H. Szymánska, R. André, J. L. Staehli, V. Savona, P. B. Littlewood, B. Deveaud, and L. S. Dang, "Bose-Einstein condensation of exciton polaritons," *Nature*, vol. 443, no. 7110, pp. 409–414, 2006.

[2] S. Christopoulos, G. B. H. Von Högersthal, A. J. Grundy, P. G. Lagoudakis, A. V. Kavokin, J. J. Baumberg, G. Christmann, R. Butté, E. Feltin, J. F. Carlin, and N. Grandjean, "Room-temperature polariton lasing in semiconductor microcavities," *Physical Review Letters*, vol. 98, no. 12, pp. 1–4, 2007.

[3] H. Lee, Z. Liu, Y. Xiong, C. Sun, and X. Zhang, "Development of optical hyperlens for imaging below the diffraction limit," *Optics Express*, vol. 15, no. 24, p. 15886, 2007.

[4] S. Dai, Z. Fei, Q. Ma, A. S. Rodin, M. Wagner, A. S. McLeod, M. K. Liu, W. Gannett, W. Regan, K. Watanabe, T. Taniguchi, M. Thiemens, G. Dominguez, A. H. Castro Neto, A. Zettl, F. Keilmann, P. Jarillo-Herrero, M. M. Fogler, and D. N. Basov, "Tunable phonon polaritons in atomically thin van der Waals crystals of boron nitride," *Science*, vol. 343, no. 6175, pp. 1125–1129, 2014.

[5] J. D. Caldwell, A. V. Kretinin, Y. Chen, V. Giannini, M. M. Fogler, Y. Francescato, C. T. Ellis, J. G. Tischler, C. R. Woods, A. J. Giles, M. Hong, K. Watanabe, T. Taniguchi, S. A. Maier, and K. S. Novoselov, "Sub-diffractional volume-confined polaritons in the natural hyperbolic material hexagonal boron nitride," *Nature Communications*, vol. 5, pp. 1–9, 2014.

[6] A. Poddubny, I. Iorsh, P. Belov, and Y. Kivshar, "Hyperbolic metamaterials," *Nature Photonics*, vol. 7, no. 12, pp. 958–967, 2013.

[7] J. Sun, N. M. Litchinitser, and J. Zhou, "Indefinite by Nature: From Ultraviolet to Terahertz," *ACS Photonics*, vol. 1, no. 4, pp. 293–303, 2014.

[8] W. Ma, B. Shabbir, Q. Ou, Y. Dong, H. Chen, P. Li, X. Zhang, Y. Lu, and Qiaoliang Bao, "Anisotropic polaritons in van der Waals materials," *InfoMat*, no. February, pp. 777–790, 2020.

[9] W. Ma, P. Alonso-González, S. Li, A. Y. Nikitin, J. Yuan, J. Martín-Sánchez, J. Taboada-Gutiérrez, I. Amenabar, P. Li, S. Vélez, C. Tollan, Z. Dai, Y. Zhang, S. Sri-

ram, K. Kalantar-Zadeh, S. T. Lee, R. Hillenbrand, and Q. Bao, "In-plane anisotropic and ultra-low-loss polaritons in a natural van der Waals crystal," *Nature*, vol. 562, no. 7728, pp. 557–562, 2018.

[10] Z. Zheng, N. Xu, S. L. Oscurato, M. Tamagnone, F. Sun, Y. Jiang, Y. Ke, J. Chen, W. Huang, W. L. Wilson, A. Ambrosio, S. Deng, and H. Chen, "A mid-infrared biaxial hyperbolic van der Waals crystal," *Science Advances*, vol. 5, no. 5, pp. 1–9, 2019.

[11] C. Wang, S. Huang, Q. Xing, Y. Xie, C. Song, F. Wang, and H. Yan, "Van der Waals thin films of WTe2 for natural hyperbolic plasmonic surfaces," *Nature Communications*, vol. 11, no. 1, pp. 1–9, 2020.

[12] C. Luo, X. Guo, H. Hu, D. Hu, C. Wu, X. Yang, and Q. Dai, "Probing Polaritons in 2D Materials," *Advanced Optical Materials*, vol. 8, no. 5, pp. 1–18, 2020.

[13] M. Lewin, F. Gaussmann, K. S. Novoselov, T. Taubner, K. Watanabe, A. V. Kretinin, J. D. Caldwell, T. Taniguchi, and P. Li, "Hyperbolic phonon-polaritons in boron nitride for near-field optical imaging and focusing," *Nature Communications*, vol. 6, no. 1, pp. 1–9, 2015.

[14] T. Low, A. Chaves, J. D. Caldwell, A. Kumar, N. X. Fang, P. Avouris, T. F. Heinz, F. Guinea, L. Martin-Moreno, and F. Koppens, "Polaritons in layered two-dimensional materials," *Nature Materials*, vol. 16, no. 2, pp. 182–194, 2017.

[15] Z. Cai, Y. Xu, C. Wang, and Y. Liu, "Polariton Photonics Using Structured Metals and 2D Materials," *Advanced Optical Materials*, vol. 1901090, pp. 1–20, 2019.

[16] G. Hu, J. Shen, C. W. Qiu, A. Alù, and S. Dai, "Phonon Polaritons and Hyperbolic Response in van der Waals Materials," *Advanced Optical Materials*, vol. 1901393, pp. 1–19, 2019.

[17] T. G. Folland, L. Nordin, D. Wasserman, and J. D. Caldwell, "Probing polaritons in the mid- to far-infrared," *Journal of Applied Physics*, vol. 125, no. 19, 2019.

[18] R. M. Hoff, J. C. Irwin, and R. M. A. Lieth, "Raman Scattering in GaSe," *Canadian Journal of Physics*, vol. 53, no. 17, pp. 1606–1614, 2011.

[19] P. Tonndorf, R. Schmidt, P. Böttger, X. Zhang, J. Börner, A. Liebig, M. Albrecht, C. Kloc, O. Gordan, D. R. T. Zahn, S. M. de Vasconcellos, and R. Bratschitsch, "Photoluminescence emission and Raman response of monolayer MoS_2, $MoSe_2$ and WSe_2," *Optics Express*, vol. 21, no. 4, pp. 4908–4916, aug 2013.

[20] K. Ohtani, B. Meng, M. Franckié, L. Bosco, C. Ndebeka-Bandou, M. Beck, and J. Faist, "An electrically pumped phonon-polariton laser," *Science Advances*, vol. 5, no. 7, pp. 1–8, 2019.

[21] C. Kübler, R. Huber, S. Tübel, and A. Leitenstorfer, "Ultrabroadband detection of multi-terahertz field transients with gase electro-optic sensors: Approaching the near infrared," *Applied Physics Letters*, vol. 85, no. 16, pp. 3360–3362, 2004.

[22] C.-w. Chen, T.-t. Tang, S.-h. Lin, J. Y. Huang, C.-s. Chang, P.-k. Chung, S.-t. Yen, and C.-l. Pan, "Optical properties and potential applications of -GaSe at terahertz frequencies," *Journal of the Optical Society of America B*, vol. 26, no. 9, p. A58, sep 2009.

[23] C. H. Henry and J. J. Hopfield, "Raman Scattering by Polaritons," *Physical Review Letters*, vol. 15, no. 25, pp. 964–966, dec 1965.

[24] Y. Sasaki and S. Ushioda, "Guided-wave polaritons in thin films of the layered compound GaSe," *Physical Review B*, vol. 27, no. 2, pp. 1122–1135, jan 1983.

[25] D. L. Mills and E. Burstein, "Polaritons : The Electromagnetic Modes of Media," *Reports On Progress In Physics*, vol. 37, no. 7, pp. 817–926, 1974.

[26] G. Irmer, C. Röder, C. Himcinschi, and J. Kortus, "Phonon polaritons in uniaxial crystals: A Raman scattering study of polaritons in α-GaN," *Physical Review B - Condensed Matter and Materials Physics*, vol. 88, no. 10, 2013.

[27] S. Ushioda, "Light scattering spectroscopy of surface electromagnetic waves in solids," *Progress in Optics*, vol. 19, no. C, pp. 139–210, 1981.

[28] N. C. Passler and A. Paarmann, "Generalized 4×4 matrix formalism for light propagation in anisotropic stratified media: study of surface phonon polaritons in polar dielectric heterostructures," *Journal of the Optical Society of America B*, vol. 34, no. 10, p. 2128, 2017.

[29] A. Bergeron, J. Ibrahim, R. Leonelli, and S. Francoeur, "Oxidation dynamics of ultrathin GaSe probed through Raman spectroscopy," *Applied Physics Letters*, vol. 110, no. 24, 2017.

[30] W. Klemm and H. U. von Vogel, "Uber die Chalkogenide von Gallium und Indium," *Zeitschrift für Anorganische Chemie*, vol. 219, no. 1, pp. 45–64, 1934.

[31] D. N. Nikogosyan, "Nonlinear optical crystals: A complete survey," in *Nonlinear Optical Crystals: A Complete Survey*. Springer, 2005, ch. 3, pp. 108–114.

[32] A. Kenmochi, T. Tanabe, Y. Oyama, K. Suto, and J.-i. Nishizawa, "Terahertz wave generation from GaSe crystals and effects of crystallinity," *Journal of Physics and Chemistry of Solids*, vol. 69, no. 2-3, pp. 605–607, feb 2008.

[33] J. Guo, J.-J. Xie, D.-J. Li, G.-L. Yang, F. Chen, C.-R. Wang, L.-M. Zhang, Y. M. Andreev, K. A. Kokh, G. V. Lanskii, and V. A. Svetlichnyi, "Doped GaSe crystals for laser frequency conversion," *Light: Science Applications*, vol. 4, no. 12, p. e362, dec 2015.

[34] C. León, L. Kador, K. R. Allakhverdiev, T. Baykara, and A. A. Kaya, "Comparison of the layered semiconductors GaSe, GaS, and $GaSe_{1-x}S_x$ by Raman and photoluminescence spectroscopy," *Journal of Applied Physics*, vol. 98, no. 10, 2005.

[35] S. Lei, L. Ge, S. Najmaei, A. George, R. Kappera, J. Lou, M. Chhowalla, H. Yamaguchi, G. Gupta, R. Vajtai, A. D. Mohite, and P. M. Ajayan, "Evolution of the electronic band structure and efficient photo-detection in atomic layers of InSe," *ACS Nano*, vol. 8, no. 2, pp. 1263–1272, 2014.

[36] C.-H. Ho, M.-H. Hsieh, and C.-C. Wu, "Photoconductance and photoresponse of layer compound photodetectors in the UV-visible region," *Review of Scientific Instruments*, vol. 77, no. 11, p. 113102, 2006.

[37] P. Hu, L. Wang, M. Yoon, J. Zhang, W. Feng, X. Wang, Z. Wen, J. C. Idrobo, Y. Miyamoto, D. B. Geohegan, and K. Xiao, "Highly responsive ultrathin GaS nanosheet photodetectors on rigid and flexible substrates." *Nano letters*, vol. 13, no. 4, pp. 1649–54, apr 2013.

[38] M. Isik and N. Gasanly, "Ellipsometric study of optical properties of GaS_xSe_{1-x} layered mixed crystals," *Optical Materials*, vol. 54, pp. 155–159, 2016.

[39] D. J. Terry, V. Zólyomi, M. Hamer, A. V. Tyurnina, D. G. Hopkinson, A. M. Rakowski, S. J. Magorrian, N. Clark, Y. M. Andreev, O. Kazakova, K. Novoselov, S. J. Haigh, V. I. Fal'ko, and R. Gorbachev, "Infrared-to-violet tunable optical activity in atomic films of GaSe, InSe, and their heterostructures," *2D Materials*, vol. 5, no. 4, p. 041009, sep 2018.

[40] Y. Wu, H.-R. Fuh, D. Zhang, C. Ó. Coileáin, H. Xu, J. Cho, M. Choi, B. S. Chun, X. Jiang, M. Abid, M. Abid, H. Liu, J. J. Wang, I. V. Shvets, C.-R. Chang, and

H.-C. Wu, "Simultaneous large continuous band gap tunability and photoluminescence enhancement in GaSe nanosheets via elastic strain engineering," *Nano Energy*, vol. 32, no. December 2016, pp. 157–164, 2017.

[41] X. Zhou, J. Cheng, Y. Zhou, T. Cao, H. Hong, Z. Liao, S. Wu, H. Peng, K. Liu, and D. Yu, "Strong Second-Harmonic Generation in Atomic Layered GaSe," *Journal of the American Chemical Society*, vol. 137, no. 25, pp. 7994–7997, 2015.

[42] Y. Tang, W. Xie, K. C. Mandal, J. A. McGuire, and C. W. Lai, "Linearly Polarized Remote-Edge Luminescence in GaSe Nanoslabs," *Physical Review Applied*, vol. 4, no. 3, p. 034008, sep 2015.

[43] I. Appelbaum and P. Li, "Spin-Polarization Control in a Two-Dimensional Semiconductor," *Physical Review Applied*, vol. 5, no. 5, pp. 1–7, 2016.

[44] N. Fernelius, "Properties of gallium selenide single crystal," *Progress in Crystal Growth and Characterization of Materials*, vol. 28, no. 4, pp. 275–353, jan 1994.

[45] D. J. Late, B. Liu, H. S. S. R. Matte, C. N. R. Rao, and V. P. Dravid, "Rapid Characterization of Ultrathin Layers of Chalcogenides on SiO2/Si Substrates," *Advanced Functional Materials*, vol. 22, no. 9, pp. 1894–1905, may 2012.

[46] T. J. Wieting and M. Schlüter, *Electrons and phonons in layered crystal structures*. Dordrecht, Netherlands: Springer, 1979, vol. 3.

[47] T. J. Wieting and J. L. Verble, "Interlayer bonding and the lattice vibrations of ϵ-GaSe," *Physical Review B*, vol. 5, no. 4, pp. 1473–1479, 1972.

[48] T. J. Wieting, "Long-wavelength lattice vibrations of MoS2 and GaSe," *Solid State Communications*, vol. 12, no. 9, pp. 931–935, 1973.

[49] M. Hayek, O. Brafman, and R. M. A. Lieth, "Splitting and Coupling of Lattice Modes in the Layer Compounds GaSe, GaS, and $GaSe_xS_{1-x}$," *Physical Review B*, vol. 8, no. 6, pp. 2772–2779, sep 1973.

[50] R. Le Toullec, N. Piccioli, and J. C. Chervin, "Optical properties of the band-edge exciton in GaSe crystals at 10 K," *Physical Review B*, vol. 22, no. 12, pp. 6162–6170, 1980.

[51] V. K. Bashenov, I. Baumann, and D. I. Marvakov, "Lattice Dynamics of Gallium Selenide in the One-Layer Approach," *Physica Status Solidi (b)*, vol. 89, no. 2, pp. K115–K118, oct 1978.

[52] V. Y. Altshul, V. K. Bashenov, D. I. Marvakov, and A. G. Petukhov, "Lattice Dynamics and Elastic Properties of GaSe," *physica status solidi (b)*, vol. 98, no. 2, pp. 715–725, apr 1980.

[53] J. C. Irwin, R. M. Hoff, B. P. Clayman, and R. A. Bromley, "Long wavelength lattice vibrations in GaS and GaSe," *Solid State Communications*, vol. 13, no. 9, pp. 1531–1536, 1973.

[54] F. Meyer, E. E. de Kluizenaar, and D. den Engelsen, "Ellipsometric determination of the optical anisotropy of gallium selenide," *Journal of the Optical Society of America*, vol. 63, no. 5, p. 529, may 1973.

[55] L. Plucinski, R. Johnson, B. Kowalski, K. Kopalko, B. Orlowski, Z. Kovalyuk, and G. Lashkarev, "Electronic band structure of GaSe(0001):Angle-resolved photoemission and ab initio theory," *Physical Review B*, vol. 68, no. 12, p. 125304, sep 2003.

[56] N. Kuroda, I. Munakata, and Y. Nishina, "Exciton transitions from spin-orbit split off valence bands in layer compound InSe," *Solid State Communications*, vol. 33, no. 6, pp. 687–691, feb 1980.

[57] M. O. Camara, A. Mauger, and I. Devos, "Electronic structure of the layer compounds GaSe and InSe in a tight-binding approach," *Physical Review B - Condensed Matter and Materials Physics*, vol. 65, no. 12, pp. 1–12, 2002.

[58] E. Mooser and M. Schlüter, "The band-gap excitons in gallium selenide," *Il Nuovo Cimento*, vol. 18, no. 1, pp. 164–208, 1973.

[59] R. D. Rodriguez, S. Müller, E. Sheremet, D. R. T. Zahn, A. Villabona, S. a. Lopez-Rivera, P. Tonndorf, S. M. de Vasconcellos, and R. Bratschitsch, "Selective Raman modes and strong photoluminescence of gallium selenide flakes on sp 2 carbon," *Journal of Vacuum Science Technology B, Nanotechnology and Microelectronics: Materials, Processing, Measurement, and Phenomena*, vol. 32, no. 4, p. 04E106, jul 2014.

[60] M. Suzuki, M. Kohda, S. Takasuna, S. Matsuzaka, Y. Sato, T. Tanabe, Y. Oyama, and J. Nitta, "Effect of optical waveguide on photoluminescence polarization in layered material GaSe with millimeter scale," *Japanese Journal of Applied Physics*, vol. 57, no. 2, 2018.

[61] M. Brotons-Gisbert, R. Proux, R. Picard, D. Andres-Penares, A. Branny, A. Molina-Sánchez, J. F. Sánchez-Royo, and B. D. Gerardot, "Out-of-plane orientation of

luminescent excitons in two-dimensional indium selenide," *Nature Communications*, vol. 10, no. 1, pp. 1–10, 2019.

[62] A. Segura, J. Bouvier, M. Andrés, F. Manjón, and V. Muñoz, "Strong optical nonlinearities in gallium and indium selenides related to inter-valence-band transitions induced by light pulses," *Physical Review B - Condensed Matter and Materials Physics*, vol. 56, no. 7, pp. 4075–4084, 1997.

[63] X. Li, M.-W. Lin, A. a. Puretzky, J. C. Idrobo, C. Ma, M. Chi, M. Yoon, C. M. Rouleau, I. I. Kravchenko, D. B. Geohegan, and K. Xiao, "Controlled vapor phase growth of single crystalline, two-dimensional GaSe crystals with high photoresponse." *Scientific reports*, vol. 4, p. 5497, jan 2014.

[64] Z. Ben Aziza, D. Pierucci, H. Henck, M. G. Silly, C. David, M. Yoon, F. Sirotti, K. Xiao, M. Eddrief, J. C. Girard, and A. Ouerghi, "Tunable quasiparticle band gap in few-layer GaSe/graphene van der Waals heterostructures," *Physical Review B*, vol. 96, no. 3, pp. 1–8, 2017.

[65] O. D. Pozo-Zamudio, S. Schwarz, M. Sich, I. A. Akimov, M. Bayer, R. C. Schofield, E. A. Chekhovich, B. J. Robinson, N. D. Kay, O. V. Kolosov, A I Dmitriev, G. V. Lashkarev, D. N. Borisenko, N. N. Kolesnikov, and A. I. Tartakovskii, "Photoluminescence of two-dimensional GaTe and GaSe films," *2D Materials*, vol. 2, no. 3, p. 035010, 2015.

[66] D. Andres-Penares, A. Cros, J. P. Martínez-Pastor, and J. F. Sánchez-Royo, "Quantum size confinement in gallium selenide nanosheets: band gap tunability versus stability limitation," *Nanotechnology*, vol. 28, no. 17, p. 175701, apr 2017.

[67] N. B. Singh, D. R. Suhre, V. Balakrishna, M. Marable, R. Meyer, N. Fernelius, F. K. Hopkins, and D. Zelmon, "Far-infrared conversion materials: Gallium selenide for far-infrared conversion applications," *Progress in Crystal Growth and Characterization of Materials*, vol. 37, no. 1, pp. 47–102, 1998.

[68] S. a. Mikhailov, "Theory of the giant plasmon-enhanced second-harmonic generation in graphene and semiconductor two-dimensional electron systems," *Physical Review B*, vol. 84, no. 4, p. 045432, jul 2011.

[69] V. A. Margulis, E. E. Muryumin, and E. A. Gaiduk, "Optical second-harmonic generation from two-dimensional hexagonal crystals with broken space inversion symmetry," *Journal of Physics Condensed Matter*, vol. 25, no. 19, 2013.

[70] Y. Li, Y. Rao, K. F. Mak, Y. You, S. Wang, C. R. Dean, and T. F. Heinz, "Probing Symmetry Properties of Few-Layer MoS 2 and h-BN by Optical Second-Harmonic Generation," *Nano Letters*, vol. 13, no. 7, pp. 3329–3333, jul 2013.

[71] L. M. Malard, T. V. Alencar, A. P. M. Barboza, K. F. Mak, and A. M. de Paula, "Observation of intense second harmonic generation from $MoS_2 atomic crystals,'' Physical Review B, vol.\ 87, no.\ 20, p.201401, may2013$.

[72] C. Janisch, D. Ma, N. Mehta, A. Laura-Elias, N. Perea-Lopez, M. Terrones, and Z. Liu, "Harmonic generation in 2D layered materials," in *Proceedings of SPIE*, Z. Liu, Ed., vol. 9198, sep 2014, p. 91980L.

[73] D. J. Clark, V. Senthilkumar, C. T. Le, D. L. Weerawarne, B. Shim, J. I. Jang, J. H. Shim, J. Cho, Y. Sim, M. J. Seong, S. H. Rhim, A. J. Freeman, K. H. Chung, and Y. S. Kim, "Strong optical nonlinearity of CVD-grown MoS2 monolayer as probed by wavelength-dependent second-harmonic generation," *Physical Review B - Condensed Matter and Materials Physics*, vol. 90, no. 12, pp. 1–5, 2014.

[74] M. L. Trolle, G. Seifert, and T. G. Pedersen, "Theory of excitonic second-harmonic generation in monolayer MoS2," *Physical Review B*, vol. 89, no. 23, p. 235410, jun 2014.

[75] M. Grüning and C. Attaccalite, "Second harmonic generation in h-BN and MoS2 monolayers: Role of electron-hole interaction," *Physical Review B*, vol. 89, no. 8, p. 081102, feb 2014.

[76] Q. Hao, H. Yi, H. Su, B. Wei, Z. Wang, Z. Lao, Y. Chai, Z. Wang, C. Jin, J. Dai, and W. Zhang, "Phase Identification and Strong Second Harmonic Generation in Pure -InSe and Its Alloys," *Nano Letters*, vol. 19, no. 4, pp. 2634–2640, 2019.

[77] H. Zeng, G. B. Liu, J. Dai, Y. Yan, B. Zhu, R. He, L. Xie, S. Xu, X. Chen, W. Yao, and X. Cui, "Optical signature of symmetry variations and spin-valley coupling in atomically thin tungsten dichalcogenides," *Scientific Reports*, vol. 3, pp. 2–6, 2013.

[78] Z. Sun, A. Martinez, and F. Wang, "Optical modulators with 2D layered materials," *Nature Photonics*, vol. 10, no. 4, pp. 227–238, 2016.

[79] L. Hu, D. Wei, and X. Huang, "Second harmonic generation property of monolayer TMDCs and its potential application in producing terahertz radiation," *Journal of Chemical Physics*, vol. 147, no. 24, 2017.

[80] A. Autere, H. Jussila, Y. Dai, Y. Wang, H. Lipsanen, and Z. Sun, "Nonlinear Optics with 2D Layered Materials," *Advanced Materials*, vol. 30, no. 24, pp. 1–24, 2018.

[81] K. Tolpygo, "PHYSICAL PROPERTIES OF A ROCK SALT LATTICE MADE UP OF DEFORMABLE IONS," *Ukrainian Journal of Physics*, vol. 53, no. Special Issue, pp. 93–102, 2008.

[82] K. Huang, "Lattice vibrations and optical waves in ionic crystals," *Nature*, vol. 167, no. 4254, pp. 779–780, 1951.

[83] J. J. Hopfield, "Theory of the contribution of excitons to the complex dielectric constant of crystals," *Physical Review*, vol. 112, no. 5, pp. 1555–1567, 1958.

[84] D. N. Basov, M. M. Fogler, and F. J. Garcï¿a De Abajo, "Polaritons in van der Waals materials," *Science*, vol. 354, no. 6309, 2016.

[85] R. K. Fisher and R. W. Gould, "Resonance cones in the field pattern of a short antenna in an anisotropic plasma," *Physical Review Letters*, vol. 22, no. 21, pp. 1093–1095, 1969.

[86] M. Noginov, M. Lapine, V. Podolskiy, and Y. Kivshar, "Focus issue: hyperbolic metamaterials," *Optics Express*, vol. 21, no. 12, p. 14895, 2013.

[87] Y. Xiong, Z. Liu, C. Sun, and X. Zhang, "Two-dimensional imaging by far-field superlens at visible wavelengths," *Nano Letters*, vol. 7, no. 11, pp. 3360–3365, 2007.

[88] D. R. Smith, D. Schurig, J. J. Mock, P. Kolinko, and P. Rye, "Partial focusing of radiation by a slab of indefinite media," *Applied Physics Letters*, vol. 84, no. 13, pp. 2244–2246, 2004.

[89] J. Kim, V. P. Drachev, Z. Jacob, G. V. Naik, A. Boltasseva, E. E. Narimanov, and V. M. Shalaev, "Improving the radiative decay rate for dye molecules with hyperbolic metamaterials," *Optics Express*, vol. 20, no. 7, p. 8100, mar 2012.

[90] Y. He, S. He, and X. Yang, "Optical field enhancement in nanoscale slot waveguides of hyperbolic metamaterials," *Optics Letters*, vol. 37, no. 14, p. 2907, 2012.

[91] X. L. Chen, M. He, Y. X. Du, W. Y. Wang, and D. F. Zhang, "Negative refraction: An intrinsic property of uniaxial crystals," *Physical Review B - Condensed Matter and Materials Physics*, vol. 72, no. 11, pp. 1–4, 2005.

[92] A. J. Huber, B. Deutsch, L. Novotny, and R. Hillenbrand, "Focusing of surface phonon polaritons," *Applied Physics Letters*, vol. 92, no. 20, pp. 2–4, 2008.

[93] L. V. Alekseyev, V. A. Podolskiy, and E. E. Narimanov, "Homogeneous hyperbolic systems for terahertz and far-infrared frequencies," *Advances in OptoElectronics*, vol. 2012, 2012.

[94] Z. Jacob, "Nanophotonics: Hyperbolic phonon-polaritons," *Nature Materials*, vol. 13, no. 12, pp. 1081–1083, 2014.

[95] K. Korzeb, M. Gajc, and D. A. Pawlak, "Compendium of natural hyperbolic materials," *Optics Express*, vol. 23, no. 20, p. 25406, 2015.

[96] A. Y. Nikitin, E. Yoxall, M. Schnell, S. Vélez, I. Dolado, P. Alonso-Gonzalez, F. Casanova, L. E. Hueso, and R. Hillenbrand, "Nanofocusing of Hyperbolic Phonon Polaritons in a Tapered Boron Nitride Slab," *ACS Photonics*, vol. 3, no. 6, pp. 924–929, 2016.

[97] S. Dai, M. Tymchenko, Y. Yang, Q. Ma, M. Pita-Vidal, K. Watanabe, T. Taniguchi, P. Jarillo-Herrero, M. M. Fogler, A. Alù, and D. N. Basov, "Manipulation and Steering of Hyperbolic Surface Polaritons in Hexagonal Boron Nitride," *Advanced Materials*, vol. 30, no. 16, pp. 1–5, 2018.

[98] P. Pons-Valencia, F. J. Alfaro-Mozaz, M. M. Wiecha, V. Biolek, I. Dolado, S. Vélez, P. Li, P. Alonso-González, F. Casanova, L. E. Hueso, L. Martín-Moreno, R. Hillenbrand, and A. Y. Nikitin, "Launching of hyperbolic phonon-polaritons in h-BN slabs by resonant metal plasmonic antennas," *Nature Communications*, vol. 10, no. 1, pp. 1–8, 2019.

[99] P. Li, I. Dolado, F. J. Alfaro-Mozaz, A. Y. Nikitin, F. Casanova, L. E. Hueso, S. Vélez, and R. Hillenbrand, "Optical nanoimaging of hyperbolic surface polaritons at the edges of van der Waals materials," *Nano Letters*, vol. 17, no. 1, pp. 228–235, 2017.

[100] Z. Zheng, J. Chen, Y. Wang, X. Wang, X. Chen, P. Liu, J. Xu, W. Xie, H. Chen, S. Deng, and N. Xu, "Highly Confined and Tunable Hyperbolic Phonon Polaritons in Van Der Waals Semiconducting Transition Metal Oxides," *Advanced Materials*, vol. 1705318, p. 1705318, 2018.

[101] S. Dai, Q. Ma, T. Andersen, A. S. McLeod, Z. Fei, M. K. Liu, M. Wagner, K. Watanabe, T. Taniguchi, M. Thiemens, F. Keilmann, P. Jarillo-Herrero, M. M. Fogler, and D. N. Basov, "Subdiffractional focusing and guiding of polaritonic rays in a natural hyperbolic material," *Nature Communications*, vol. 6, pp. 1–7, 2015.

[102] J. D. Caldwell, I. Vurgaftman, J. G. Tischler, O. J. Glembocki, J. C. Owrutsky, and T. L. Reinecke, "Atomic-scale photonic hybrids for mid-infrared and terahertz nanophotonics," *Nature Nanotechnology*, vol. 11, no. 1, pp. 9–15, 2016.

[103] F. Zenhausern, M. P. O'Boyle, and H. K. Wickramasinghe, "Apertureless near-field optical microscope," *Applied Physics Letters*, vol. 65, no. 13, pp. 1623–1625, 1994.

[104] J. M. Atkin, S. Berweger, A. C. Jones, and M. B. Raschke, "Nano-optical imaging and spectroscopy of order , phases , and domains in complex solids," *Advances in Physics*, vol. 61, no. 6, pp. 745–842, 2012.

[105] J. Wessel, "Surface-enhanced optical microscopy," *Journal of the Optical Society of America B*, vol. 2, no. 9, p. 1538, 1985.

[106] B. Knoll and F. Keilmann, "Near-field probing of vibrational absorption for chemical microscopy," *Nature*, vol. 399, no. 6732, pp. 134–137, 1999.

[107] R. Hillenbrand, T. Taubner, and F. Keilmann, "Phonon-enhanced light-matter interaction at the nanometre scale," *Nature*, vol. 418, no. 6894, pp. 159–162, 2002.

[108] R. Hillenbrand and F. Keilmann, "Complex optical constants on a subwavelength scale," *Physical Review Letters*, vol. 85, no. 14, pp. 3029–3032, 2000.

[109] N. Ocelic, A. Huber, and R. Hillenbrand, "Pseudoheterodyne detection for background-free near-field spectroscopy," *Applied Physics Letters*, vol. 89, no. 10, pp. 1–4, 2006.

[110] Z. Fei, G. O. Andreev, W. Bao, L. M. Zhang, A. S. McLeod, C. Wang, M. K. Stewart, Z. Zhao, G. Dominguez, M. Thiemens, M. M. Fogler, M. J. Tauber, A. H. Castro-Neto, C. N. Lau, F. Keilmann, and D. N. Basov, "Infrared Nanoscopy of Dirac Plasmons at the Graphene–SiO 2 Interface," *Nano Letters*, vol. 11, no. 11, pp. 4701–4705, nov 2011.

[111] J. D. Caldwell, O. J. Glembocki, Y. Francescato, N. Sharac, V. Giannini, F. J. Bezares, J. P. Long, C. Owrutsky, I. Vurgaftman, J. G. Tischler, V. D. Wheeler, N. D. Bassim, L. M. Shirey, R. Kasica, and S. a. Maier, "Low-Loss, Extreme Subdiffraction Photon Confinement via Silicon Carbide Localized Surface Phonon Polariton Resonators," *Nano Letters*, vol. 13, pp. 3690–3697, 2013.

[112] A. Otto, "Excitation of nonradiative surface plasma waves in silver by the method of frustrated total reflection," *Zeitschrift für Physik*, vol. 216, no. 4, pp. 398–410, 1968.

[113] N. C. Passler, I. Razdolski, S. Gewinner, W. Schöllkopf, M. Wolf, and A. Paarmann, "Second-Harmonic Generation from Critically Coupled Surface Phonon Polaritons," *ACS Photonics*, vol. 4, no. 5, pp. 1048–1053, 2017.

[114] N. C. Passler, C. R. Gubbin, T. G. Folland, I. Razdolski, D. S. Katzer, D. F. Storm, M. Wolf, S. De Liberato, J. D. Caldwell, and A. Paarmann, "Strong Coupling of Epsilon-Near-Zero Phonon Polaritons in Polar Dielectric Heterostructures," *Nano Letters*, vol. 18, no. 7, pp. 4285–4292, jul 2018.

[115] N. C. Passler, A. Heßler, M. Wuttig, T. Taubner, and A. Paarmann, "Surface Polariton-Like s-Polarized Waveguide Modes in Switchable Dielectric Thin Films on Polar Crystals," *Advanced Optical Materials*, p. 1901056, 2019.

[116] L. Xiao and Z. D. Schultz, "Spectroscopic Imaging at the Nanoscale: Technologies and Recent Applications," *Analytical Chemistry*, vol. 90, no. 1, pp. 440–458, 2018.

[117] X. Chen, D. Hu, R. Mescall, G. You, D. N. Basov, Q. Dai, and M. Liu, "Modern Scattering-Type Scanning Near-Field Optical Microscopy for Advanced Material Research," *Advanced Materials*, vol. 31, no. 24, pp. 1–24, 2019.

[118] I. D. Barcelos, H. A. Bechtel, C. J. de Matos, D. A. Bahamon, B. Kaestner, F. C. Maia, and R. O. Freitas, "Probing Polaritons in 2D Materials with Synchrotron Infrared Nanospectroscopy," *Advanced Optical Materials*, vol. 1901091, pp. 1–16, 2019.

[119] H. Tornatzky, R. Gillen, H. Uchiyama, and J. Maultzsch, "Phonon dispersion in MoS2," *Physical Review B*, vol. 99, no. 14, p. 144309, 2019.

[120] D. J. Evans, S. Ushioda, and J. D. McMullen, "Raman scattering from surface polaritons in a GaAs film," *Physical Review Letters*, vol. 31, no. 6, pp. 369–372, 1973.

[121] J. Y. Prieur and S. Ushioda, "Raman scattering from the upper mode of surface polaritons in a layered structure," *Physical Review Letters*, vol. 34, no. 16, pp. 1012–1015, 1975.

[122] J. B. Valdez and S. Ushioda, "Selection Rules in Raman Scattering from Surface Polaritons," *Physical Review Letters*, vol. 38, no. 19, pp. 1098–1101, may 1977.

[123] K. Subbaswamy and D. Mills, "Light scattering spectra of guided wave polaritons in thin crystals: Theory," *Solid State Communications*, vol. 27, no. 11, pp. 1085–1088, sep 1978.

[124] J. Valdez, G. Mattei, and S. Ushioda, "Light scattering spectra of guided wave polaritons in thin crystals: Experiment," *Solid State Communications*, vol. 27, no. 11, pp. 1089–1092, sep 1978.

[125] D. H. Auston, K. P. Cheung, J. A. Valdmanis, and D. A. Kleinman, "Cherenkov radiation from femtosecond optical pulses in electro-optic media," *Physical Review Letters*, vol. 53, no. 16, pp. 1555–1558, 1984.

[126] T. P. Dougherty, G. P. Wiederrecht, and K. A. Nelson, "Impulsive stimulated Raman scattering experiments in the polariton regime," *Journal of the Optical Society of America B*, vol. 9, no. 12, p. 2179, 1992.

[127] C. Yang, Q. Wu, J. Xu, K. a. Nelson, and C. a. Werley, "Experimental and theoretical analysis of THz-frequency, direction-dependent, phonon polariton modes in a subwavelength, anisotropic slab waveguide." *Optics express*, vol. 18, no. 25, pp. 26 351–26 364, 2010.

[128] S. A. Holmstrom, T. H. Stievater, M. W. Pruessner, D. Park, W. S. Rabinovich, J. B. Khurgin, C. J. K. Richardson, S. Kanakaraju, L. C. Calhoun, and R. Ghodssi, "Guided-mode phonon-polaritons in suspended waveguides," *Physical Review B - Condensed Matter and Materials Physics*, vol. 86, no. 16, pp. 1–5, 2012.

[129] R. Frech, "Oblique phonons in uniaxial crystals," *The Journal of Chemical Physics*, vol. 67, no. 3, p. 952, 1977.

[130] R. Claus, "Light Scattering by Optical Phonons and Polaritons," *Physica Status Solidi b*, vol. 50, no. 11, pp. 11–32, 1972.

[131] R. Loudon, "The Raman effect in crystals," *Advances in Physics*, no. 13:52, pp. 423–482, 1964.

[132] L. Merten and G. Lamprecht, "Directional Dependence of Extraordinary Infrared Oscillator Parameters of Uniaxial Crystals (I)," *physica status solidi (b)*, vol. 39, no. 2, pp. 573–580, 1970.

[133] R. Claus, L. Merten, and J. Brandmuller, *Light Scattering by Phonon-Polaritons*, ser. Springer Tracts in Modern Physics, J. Brandmüller, R. Claus, and L. Merten, Eds. Berlin, Heidelberg: Springer Berlin Heidelberg, 1975, vol. 75.

[134] R. H. Lyddane, R. G. Sachs, and E. Teller, "On the Polar Vibrations of Alkali Halides," *Physical Review*, vol. 59, no. 8, pp. 673–676, apr 1941.

[135] T. Kurosawa, "Polarization Waves in Solids," *Journal of the Physical Society of Japan*, vol. 16, no. 7, pp. 1298–1308, 1961.

[136] A. Polian, K. Kunc, and A. Kuhn, "Low-frequency lattice vibrations of δ-GaSe compared to ϵ- and γ-polytypes," *Solid State Communications*, vol. 19, no. 11, pp. 1079–1082, sep 1976.

[137] A. Mercier and J. Voitchovsky, "Raman scattering from GaS_xSe_{1-x}," *Solid State Communications*, vol. 14, no. 8, pp. 757–762, apr 1974.

[138] H. Yoshida, S. Nakashima, and a. Mitsuishi, "Phonon Raman spectra of layer compound GaSe," *Physica Status Solidi (B)*, vol. 59, no. 2, pp. 655–666, 1973.

[139] N. Kuroda, Y. Nishina, and T. Fukuroi, "Phonon Structures in Optical Spectra of Layer Compounds GaSe and GaS," *Journal of the Physical Society of Japan*, vol. 28, no. 4, pp. 981–992, apr 1970.

[140] R. M. Hoff and J. C. Irwin, "Resonant Raman scattering in GaSe," *Physical Review B*, vol. 10, no. 8, pp. 3464–3470, 1974.

[141] P. Leung, G. Andermann, W. Spitzer, and C. Mead, "Dielectric constants and infrared absorption of GaSe," *Journal of Physics and Chemistry of Solids*, vol. 27, no. 5, pp. 849–855, 1966.

[142] E. Palik, *Handbook of Optical Constants of Solids Vol. III*. Academic Press, 1997.

[143] T. C. Damen, S. P. S. Porto, and B. Tell, "Raman Effect in Zinc Oxide," *Physical Review*, vol. 142, no. 2, pp. 570–574, feb 1966.

[144] R. S. Mulliken, "Report on Notation for the Spectra of Polyatomic Molecules," *The Journal of Chemical Physics*, vol. 23, no. 11, pp. 1997–2011, nov 1955.

[145] S. Jandl and J. L. Brebner, "Group Theoretical Analysis of Lattice Vibrations in GaSe Polytypes," *Canadian Journal of Physics*, vol. 52, no. 24, pp. 2454–2458, dec 1974.

[146] R. Longuinhos and J. Ribeiro-Soares, "Ultra-weak interlayer coupling in two-dimensional gallium selenide," *Physical Chemistry Chemical Physics*, vol. 18, pp. 25 401–25 408, 2016.

[147] R. W. Boyd, *Nonlinear Optics*, 2nd ed. San Diego, CA: Elsevier, 2003.

[148] P. Y. Yu and M. Cardona, *Fundamentals of Semiconductors : Physics and Materials Properties*, 4th ed. Springer-Verlag Berlin Heidelberg, 2010.

[149] W. D. Johnston, "Nonlinear optical coefficients and the raman scattering efficiency of LO and TO phonons in acentric insulating crystals," *Physical Review B*, vol. 1, no. 8, pp. 3494–3503, 1970.

[150] X. C. Long, R. A. Myers, S. R. Brueck, R. Ramer, K. Zheng, and S. D. Hersee, "GaN linear electro-optic effect," *Applied Physics Letters*, vol. 67, no. 1995, p. 1349, 1995.

[151] S. Wemple and M. Di Domenico, "Electrooptical and Nonlinear Optical Properties of Crystals," in *Applied Solid State Science*. Academic Press, 1972, vol. 3, pp. 263–383.

[152] W. L. Faust and C. H. Henry, "Mixing of visible and near-resonance infrared light in GaP," *Physical Review Letters*, vol. 17, no. 25, pp. 1265–1268, 1966.

[153] R. Loudon, "Theory of the first-order Raman effect in crystals," *Proceedings of the Royal Society of London. Series A. Mathematical and Physical Sciences*, vol. 275, no. 1361, pp. 218–232, sep 1963.

[154] R. M. Martin, "Theory of the One-Phonon Resonance Raman Effect," *Physical Review B*, vol. 4, no. 10, p. 3676, 1971.

[155] A. Cantarero, C. Trallero-Giner, and M. Cardona, "Excitons in one-phonon resonant Raman scattering: Deformation-potential interaction," *Physical Review B*, vol. 39, no. 12, pp. 8388–8397, apr 1989.

[156] J. Menendez and M. Cardona, "Allowed and forbidden scattering by LO phonons: interference effects," *Pure and Applied Chemistry*, vol. 57, no. 2, pp. 181–185, jan 1985.

[157] R. M. Martin and T. C. Damen, "Breakdown of selection rules in resonance Raman scattering," *Physical Review Letters*, vol. 26, no. 2, pp. 86–88, 1971.

[158] C. Trallero-Giner, A. Cantarero, and M. Cardona, "One-phonon resonant Raman scattering: Fröhlich exciton-phonon interaction," *Physical Review B*, vol. 40, no. 6, pp. 4030–4036, aug 1989.

[159] K. Gołasa, M. Grzeszczyk, M. R. Molas, M. Zinkiewicz, Ł. Bala, K. Nogajewski, M. Potemski, A. Wysmołek, and A. Babiński, "Resonant quenching of Raman scattering due to out-of-plane A1g/A1 modes in few-layer MoTe2," *Nanophotonics*, vol. 6, no. 6, pp. 1281–1288, jan 2017.

[160] A. Fainstein, M. Trigo, D. Oliva, B. Jusserand, T. Freixanet, and V. Thierry-Mieg, "Standing optical phonons in finite semiconductor superlattices studied by resonant Raman scattering in a double microcavity," *Physical Review Letters*, vol. 86, no. 15, pp. 3411–3414, 2001.

[161] A. Fainstein and B. Jusserand, "Raman spectroscopy of phonons in optically confined semiconductor nanostructures," *Semiconductor Science and Technology*, vol. 18, no. 10, 2003.

[162] B. Miller, J. Lindlau, M. Bommert, A. Neumann, H. Yamaguchi, A. Holleitner, A. Högele, and U. Wurstbauer, "Tuning the Fröhlich exciton-phonon scattering in monolayer MoS2," *Nature Communications*, vol. 10, no. 1, p. 807, dec 2019.

[163] Q.-H. Tan, Y.-j. Sun, X.-l. Liu, K.-x. Xu, Y.-F. Gao, S.-L. Ren, P.-H. Tan, and J. Zhang, "Breakdown of Raman Selection Rules By Fröhlich Interaction in Few-Layer WS_2," pp. 1–5, aug 2019.

[164] T. Sohier, M. Calandra, and F. Mauri, "Two-dimensional Fröhlich interaction in transition-metal dichalcogenide monolayers: Theoretical modeling and first-principles calculations," *Physical Review B*, vol. 94, no. 8, p. 085415, aug 2016.

[165] T. Sohier, M. Gibertini, M. Calandra, F. Mauri, and N. Marzari, "Breakdown of Optical Phonons' Splitting in Two-Dimensional Materials," *Nano Letters*, vol. 17, no. 6, pp. 3758–3763, 2017.

[166] D. L. Mills, Y. J. Chen, and E. Burstein, "Raman scattering of light by polaritons in thin films; surface polaritons and size effects," *Physical Review B*, vol. 13, no. 10, pp. 4419–4438, may 1976.

[167] S. Ushioda, "Light scattering spectroscopy of surface electromagnetic waves in solids," *Progress in Optics*, vol. 19, no. C, pp. 139–210, 1981.

[168] G. R. Fowles, *Introduction to Modern Optics*, 2nd ed. New York: Dover Publications, Inc., 1975.

[169] A. M. Jalaleddine, "Guided waves propagating in isotropic and uniaxial anisotropic slab waveguides," Master of Science, Ohio University, 1982.

[170] D. W. Berreman, "Optics in Stratified and Anisotropic Media: 4×4-Matrix Formulation," *Journal of the Optical Society of America*, vol. 62, no. 4, p. 502, 1972.

[171] W. Xu, L. Wood, and T. Golding, "Optical degeneracies in anisotropic layered media: Treatment of singularities in a 4×4 matrix formalism," *Physical Review B - Condensed Matter and Materials Physics*, vol. 61, no. 3, pp. 1740–1743, 2000.

[172] P. Yeh, "Electromagnetic propagation in birefringent layered media," *Journal of the Optical Society of America*, vol. 69, no. 5, p. 742, 1979.

[173] F. Keilmann and R. Hillenbrand, "Near-field microscopy by elastic light scattering from a tip," *Philosophical Transactions of the Royal Society A: Mathematical, Physical and Engineering Sciences*, vol. 362, no. 1817, pp. 787–805, 2004.

[174] A. Cvitkovic, N. Ocelic, and R. Hillenbrand, "Analytical model for quantitative prediction of material contrasts in scattering-type near-field optical microscopy," *Optics Express*, vol. 15, no. 14, p. 8550, 2007.

[175] R. Kitamura, L. Pilon, and M. Jonasz, "Optical constants of silica glass from extreme ultraviolet to far infrared at near room temperature," *Applied Optics*, vol. 46, no. 33, p. 8118, 2007.

[176] W. Karstens, D. C. Bobela, and D. Y. Smith, "Impurity and free-carrier effects on the far-infrared dispersion spectrum of silicon," *Journal of the Optical Society of America A*, vol. 23, no. 3, p. 723, 2006.

[177] G. Irmer, C. Röder, C. Himcinschi, and J. Kortus, "Raman tensor elements and Faust-Henry coefficients of wurtzite-type α -GaN: How to overcome the dilemma of the sign of Faust-Henry coefficients in α -GaN?" *Journal of Applied Physics*, vol. 116, no. 24, 2014.

[178] S. Jandl, J. L. Brebner, and B. M. Powell, "Lattice dynamics of GaSe," *Physical Review B*, vol. 13, no. 2, pp. 686–693, 1976.

[179] P. Schmid and J. P. Voitchovsky, "Electron–Lattice Interaction in Gallium Selenide," *Physica Status Solidi (B)*, vol. 65, no. 1, pp. 249–254, 1974.

[180] A. Castellanos-Gomez, M. Buscema, R. Molenaar, V. Singh, L. Janssen, H. S. J. van der Zant, and G. a. Steele, "Deterministic transfer of two-dimensional materials by all-dry viscoelastic stamping," *2D Materials*, vol. 1, no. 1, p. 011002, apr 2014.

[181] Y. Y. Huang, V. Kumar, X. Feng, R. G. Nuzzo, Z.-T. Zhu, M. A. Meitl, K. J. Lee, J. A. Rogers, and I. Adesida, "Transfer printing by kinetic control of adhesion to an elastomeric stamp," *Nature Materials*, vol. 5, no. 1, pp. 33–38, 2005.

[182] R. Swanepoel, "Determining refractive index and thickness of thin films from wavelength measurements only," *Journal of the Optical Society of America A*, vol. 2, no. 8, p. 1339, aug 1985.

[183] M. Kępińska, M. Nowak, P. Duka, and B. Kauch, "Spectrogoniometric determination of refractive indices of GaSe," *Thin Solid Films*, vol. 517, no. 13, pp. 3792–3796, may 2009.

[184] M. a. Van Der Veen, F. Vermoortele, D. E. De Vos, and T. Verbiest, "Point group symmetry determination via observables revealed by polarized second-harmonic generation microscopy: (1) theory," *Analytical Chemistry*, vol. 84, no. 15, pp. 6378–6385, 2012.

[185] H. D. Conway and K. A. Farnham, "Deflections of uniformly loaded circular plates with combinations of clamped, simply supported and free boundary conditions." *International Journal of Mechanical Sciences*, vol. 9, no. 9, pp. 661–671, 1967.

[186] M. Avendaño-Alejo, O. N. Stavroudis, and A. R. Boyain y Goitia, "Huygens's principle and rays in uniaxial anisotropic media I Crystal axis normal to refracting surface," *Journal of the Optical Society of America A*, vol. 19, no. 8, p. 1668, 2002.

[187] T. A. McMath and J. C. Irwin, "Indices of refraction of GaS and GaSe," *Physica Status Solidi (a)*, vol. 38, no. 2, pp. 731–738, dec 1976.

[188] T. M. Niebauer, J. E. Faller, H. M. Godwin, J. L. Hall, and R. L. Barger, "Frequency stability measurements on polarization-stabilized He–Ne lasers," *Applied Optics*, vol. 27, no. 7, p. 1285, 1988.

[189] J. H. Parker, D. W. Feldman, and M. Ashkin, "Raman scattering by silicon and germanium," *Physical Review*, vol. 155, no. 3, pp. 712–714, 1967.

[190] G. Kolb, T. Salbert, and G. Abstreiter, "Raman-microprobe study of stress and crystal orientation in laser-crystallized silicon," *Journal of Applied Physics*, vol. 69, no. 5, pp. 3387–3389, 1991.

[191] R. W. Wood and G. Collins, "Raman spectra of a series of normal alcohols and other compounds," *Physical Review*, vol. 42, no. 3, pp. 386–392, 1932.

[192] K. Allakhverdiev, "Interaction of laser light with the $A^{III}B^{VI}$ layered semiconductors: nonlinear optical applications," in *Proceedings of SPIE*, T. N. Dreischuh and A. T. Daskalova, Eds., vol. 8770, mar 2013, p. 877003.

[193] S. I. Drapak, S. V. Gavrylyuk, Z. D. Kovalyuk, and O. S. Lytvyn, "Native oxide emerging of the cleavage surface of gallium selenide due to prolonged storage," *Semiconductors*, vol. 42, no. 4, pp. 414–421, apr 2008.

[194] V. N. Katerynchuk, Z. R. Kudrynskyi, and Z. D. Kovalyuk, "Structure of oxidized and unoxidized end faces of GaSe layered crystals," *Inorganic Materials*, vol. 50, no. 4, pp. 339–343, mar 2014.

[195] H. Iwakuro, C. Tatsuyama, and S. Ichimura, "XPS and AES Studies on the Oxidation of Layered Semiconductor GaSe," *Japanese Journal of Applied Physics*, vol. 21, no. Part 1, No. 1, pp. 94–99, 1982.

[196] Z. Kovalyuk, V. Katerynchuk, a.I. Savchuk, and O. Lytvyn, "Surface topology of GaSe oxidized crystals," *Superlattices and Microstructures*, vol. 44, no. 4-5, pp. 416–419, oct 2008.

[197] T. E. Beechem, B. M. Kowalski, M. T. Brumbach, A. E. McDonald, C. D. Spataru, S. W. Howell, T. Ohta, J. A. Pask, and N. G. Kalugin, "Oxidation of ultrathin GaSe," *Applied Physics Letters*, vol. 107, no. 17, p. 173103, oct 2015.

[198] J. Susoma, J. Lahtinen, M. Kim, J. Riikonen, and H. Lipsanen, "Crystal quality of two-dimensional gallium telluride and gallium selenide using Raman fingerprint," *AIP Advances*, vol. 7, no. 1, p. 015014, jan 2017.

[199] M. May, S. Debrus, K. Zakrzewska, H. Benisty, and A. Chevy, "Room-temperature optical nonlinearities in bulk GaSe," *Journal of the Optical Society of America B*, vol. 14, no. 5, p. 1048, may 1997.

[200] O. Balitskii and V. Savchyn, "Thermodynamic study of AIIIBVI compounds oxidation," *Materials Science in Semiconductor Processing*, vol. 7, no. 1-2, pp. 55–58, feb 2004.

[201] N. Berchenko, O. Balitskii, R. Lutsiv, V. Savchyn, and V. Vasyltsiv, "Characteristics of phase formation during gase oxidation," *Materials Chemistry and Physics*, vol. 51, no. 2, pp. 125–129, nov 1997.

[202] V. P. Savchyn and J. M. Stakhira, "Cathodoluminescence studies of thermally oxidized cleaved surfaces of gallium selenide layered crystals," *Physica Status Solidi (a)*, vol. 156, no. 1, pp. 113–118, jul 1996.

[203] N. Gasanly, A. Aydınlı, H. Özkan, and C. Kocabaş, "Temperature-dependent Raman scattering spectra of ϵ-GaSe layered crystal," *Materials Research Bulletin*, vol. 37, no. 1, pp. 169–176, jan 2002.

[204] J. Judek, A. P. Gertych, M. Świniarski, A. Łapińska, A. Dużyńska, and M. Zdrojek, "High accuracy determination of the thermal properties of supported 2D materials," *Scientific Reports*, vol. 5, p. 12422, 2015.

[205] E. Finkman, J. Tauc, R. Kershaw, and A. Wold, "Lattice dynamics of tetrahedrally bonded semiconductors containing ordered vacant sites," *Physical Review B*, vol. 11, no. 10, pp. 3785–3794, may 1975.

[206] A. Yamada, N. Kojima, K. Takahashi, T. Okamoto, and M. Konagai, "Raman Study of Epitaxial Ga2Se3 Films Grown by Molecular Beam Epitaxy," *Japanese Journal of Applied Physics*, vol. 31, pp. 186–188, 1992.

[207] A. Märkl, M. von der Emde, C. Nowak, W. Richter, and D. Zahn, "Investigation of Se capping of epitaxial Ga2Se3 layers," *Surface Science*, vol. 331-333, pp. 631–635, jul 1995.

[208] A. Anderson, A. Sanders, and W. Smith, "Raman Spectra of Selenium Dioxide at High Pressures," *Journal of Raman Spectroscopy*, vol. 31, pp. 403–406, 2000.

[209] N. J. Brassington, H. G. M. Edwards, and V. Fawcett, "The vibrational Raman spectra of selenium trioxide ag," *Spectrochimica Acta Part A: Molecular Spectroscopy*, vol. 43, no. 3, pp. 451–454, 1987.

[210] O. A. Balitskii, V. P. Savchyn, and V. O. Yukhymchuk, "Raman investigation of InSe and GaSe single-crystals oxidation," *Semiconductor Science and Technology*, vol. 17, no. 2, pp. L1–L4, 2002.

[211] P. J. Carroll and J. S. Lannin, "Raman Scattering of amorphous selenium films," *Solid State Communications*, vol. 40, no. 1, pp. 81–84, 1981.

[212] A. Baganich, V. Mikla, D. Semak, A. Sokolov, and A. Shebanin, "Raman Scattering in Amorphous Selenium," *Phys. Stat. Sol.*, vol. 297, 1991.

[213] G. Lucovsky, A. Mooradian, W. Taylor, G. B. Wright, and R. C. Keezer, "Identification of the fundamental vibrational modes of trigonal, α-monoclinic and amorphous selenium," *Solid State Communications*, vol. 5, no. 2, pp. 113–117, 1967.

[214] V. V. Poborchii, A. V. Kolobov, and K. Tanaka, "An in situ Raman study of polarization-dependent photocrystallization in amorphous selenium films," *Applied Physics Letters*, vol. 72, no. 10, p. 1167, 1998.

[215] K. Ishida and K. Tanaka, "Photoinduced anisotropic crystallization of amorphous Se," *Physical Review B*, vol. 56, no. 1, pp. 206–209, 1997.

[216] T. Onuma, S. Fujioka, T. Yamaguchi, Y. Itoh, M. Higashiwaki, K. Sasaki, T. Masui, and T. Honda, "Polarized Raman spectra in β-Ga2O3 single crystals," *Journal of Crystal Growth*, vol. 401, pp. 330–333, sep 2014.

[217] D. Dohy, G. Lucazeau, and a. Revcolevschi, "Raman spectra and valence force field of single-crystalline β Ga2O3," *Journal of Solid State Chemistry*, vol. 45, no. 2, pp. 180–192, 1982.

[218] C. Kranert, C. Sturm, R. Schmidt-Grund, and M. Grundmann, "Raman tensor elements of β-Ga2O3," *Scientific Reports*, vol. 6, pp. 1–9, 2016.

[219] Y. Stakhira and N. Tovstyuk, "Analysis of the behaviour of chalcogen and oxygen in the system of GaSe–Ga2Se3–Ga2O3," *Materials Science and Engineering: B*, vol. 116, no. 2, pp. 112–118, 2005.

[220] H. H. Tippins, "Optical Absorption and Photoconductivity in the Band Edge of β–Ga2O3," *Physical Review*, vol. 140, no. 1A, pp. A316–A319, oct 1965.

[221] R. Memming, *Semiconductor Electrochemistry*, 2nd ed. Weinheim, Germany: WILEY-VCH Verlag GmbH Co. KGaA, 2015.

[222] R. H. Williams and A. J. McEvoy, "Electron Emission Studies from GaSe Surfaces," *Journal of Vacuum Science and Technology*, vol. 9, no. 2, p. 867, 1972.

[223] K. M. Ervin, I. Anusiewicz, P. Skurski, J. Simons, and W. C. Lineberger, "The Only Stable State of O_2^- is the $X^2\Pi_g$ Ground State and It (Still!) Has an Adiabatic Electron Detachment Energy of 0.45 eV," *Journal of Physical Chemistry A*, vol. 107, no. 41, pp. 8521–8529, 2003.

[224] A. Favron, E. Gaufrès, F. Fossard, A.-L. Phaneuf-L'Heureux, N. Y.-W. Tang, P. L. Lévesque, A. Loiseau, R. Leonelli, S. Francoeur, and R. Martel, "Photooxidation and quantum confinement effects in exfoliated black phosphorus." *Nature materials*, vol. 14, no. 8, pp. 826–832, 2015.

[225] P. L. Levesque, S. S. Sabri, C. M. Aguirre, J. Guillemette, M. Siaj, P. Desjardins, T. Szkopek, and R. Martel, "Probing charge transfer at surfaces using graphene transistors." *Nano letters*, vol. 11, no. 1, pp. 132–7, jan 2011.

[226] D. V. Rybkovskiy, N. R. Arutyunyan, a. S. Orekhov, I. a. Gromchenko, I. V. Vorobiev, a. V. Osadchy, E. Y. Salaev, T. K. Baykara, K. R. Allakhverdiev, and E. D. Obraztsova, "Size-induced effects in gallium selenide electronic structure: The influence of interlayer interactions," *Physical Review B*, vol. 84, no. 8, p. 085314, aug 2011.

[227] C. Ferrer-Roca, J. Bouvier, a. Segura, M. V. Andres, and V. Munoz, "Light-induced transmission nonlinearities in gallium selenide," *Journal of Applied physics*, vol. 85, no. 7, pp. 1–6, 1999.

[228] A. Budweg, D. Yadav, A. Grupp, A. Leitenstorfer, M. Trushin, F. Pauly, and D. Brida, "Control of excitonic absorption by thickness variation in few-layer GaSe," *Physical Review B*, vol. 100, no. 4, pp. 2–7, 2019.

[229] J. Reydellet and J. M. Besson, "Double resonance in Raman scattering on single phonon modes of GaSe," *Solid State Communications*, vol. 17, no. 1, pp. 23–26, 1975.

[230] J. Reydellet, M. Balkanski, and J. Besson, "Multiple-phonon resonant raman scattering processes in GaSe," *Journal de Physique Lettres*, vol. 37, no. 9, pp. 219–222, 1976.

[231] R. M. Martin and T. Damen, "Breakdown of Selection Rules in Resonance Raman Scattering," *Phys. Rev. Lett.*, vol. 26, no. 2, pp. 86–88, 1971.

[232] J. Hlinka, I. Gregora, and V. Vorlíček, "Complete spectrum of long-wavelength phonon modes in Sn2P2S6 by Raman scattering," *Physical Review B*, vol. 65, no. 6, p. 064308, jan 2002.

[233] A. Bianchini and H. G. Winful, "Ultrafast Optical Studies of Phonon Polaritons, Squeezed Modes and High Frequency Diamagnetism in Metamaterials," Ph.D. dissertation, University of Michigan, 2012.

[234] A. Tiwari and M. Syväjärvi, *Advanced 2D Materials*, A. Tiwari and M. Syväjärvi, Eds. Hoboken, NJ, USA: John Wiley Sons, Inc., jul 2016.

[235] A. Fali, S. T. White, T. G. Folland, M. He, N. A. Aghamiri, S. Liu, J. H. Edgar, J. D. Caldwell, R. F. Haglund, and Y. Abate, "Refractive Index-Based Control of Hyperbolic Phonon-Polariton Propagation," *Nano Letters*, vol. 19, no. 11, pp. 7725–7734, 2019.

[236] G. Cataldo, E. J. Wollack, A. D. Brown, and K. H. Miller, "Infrared dielectric properties of low-stress silicon oxide," *Optics Letters*, vol. 41, no. 7, p. 1364, 2016.

[237] E. G. Víllora, Y. Morioka, T. Atou, T. Sugawara, M. Kikuchi, and T. Fukuda, "Infrared reflectance and electrical conductivity of β-Ga2O3," *Physica Status Solidi (A) Applied Research*, vol. 193, no. 1, pp. 187–195, 2002.

[238] S. Morley, M. Von Der Emde, D. R. Zahn, V. Offermann, T. L. Ng, N. Maung, A. C. Wright, G. H. Fan, I. B. Poole, and J. O. Williams, "Optical spectroscopy of epitaxial Ga2Se3 layers from the far infrared to the ultraviolet," *Journal of Applied Physics*, vol. 79, no. 6, pp. 3196–3199, 1996.

[239] S. Vassant, J.-P. Hugonin, F. Marquier, and J.-J. Greffet, "Berreman mode and epsilon near zero mode," *Optics Express*, vol. 20, no. 21, p. 23971, 2012.

[240] I. Liberal and N. Engheta, "Near-zero refractive index photonics," *Nature Photonics*, vol. 11, no. 3, pp. 149–158, 2017.

[241] K. Ohmura, N. Aoki, and T. Nakayama, "Raman spectra calculation of ordered-vacancy Ga2Se3 compounds; origin of anisotropy," *Journal of the Physical Society of Japan*, vol. 69, no. 12, pp. 3860–3863, 2000.

[242] N. M. Gasanly, A. Aydnl, H. Özkan, and C. Kocabaş, "Temperature-dependent Raman scattering spectra of ϵ-GaSe layered crystal," *Materials Research Bulletin*, vol. 37, no. 1, pp. 169–176, 2002.

[243] J. Camassel, T. C. Chiang, Y. R. Shen, J. P. Voitchovsky, and N. M. Amer, "Multiphonon resonant Raman scattering in GaSe," *Solid State Communications*, vol. 19, no. 6, pp. 483–485, 1976.

[244] J. Reydellet, M. Balkanski, and J. Besson, "Multiple-phonon resonant raman scattering processes in GaSe," *Journal de Physique Lettres*, vol. 37, no. 9, pp. 219–222, 1976.

[245] M. Isik, E. Tugay, and N. M. Gasanly, "Temperature-dependent optical properties of GaSe layered single crystals," *Philosophical Magazine*, vol. 96, no. 24, pp. 2564–2573, 2016.

[246] A. D. Dunkelberger, C. T. Ellis, D. C. Ratchford, A. J. Giles, M. Kim, C. S. Kim, B. T. Spann, I. Vurgaftman, J. G. Tischler, J. P. Long, O. J. Glembocki, J. C. Owrutsky, and J. D. Caldwell, "Active tuning of surface phonon polariton resonances via carrier photoinjection," *Nature Photonics*, vol. 12, no. 1, pp. 50–56, 2018.

[247] A. D. Dunkelberger, D. C. Ratchford, A. B. Grafton, V. M. Breslin, E. S. Ryland, D. S. Katzer, K. P. Fears, R. J. Weiblen, I. Vurgaftman, A. J. Giles, C. T. Ellis, J. G. Tischler, J. D. Caldwell, and J. C. Owrutsky, "Ultrafast Active Tuning of the Berreman Mode," *ACS Photonics*, vol. 7, no. 1, pp. 279–287, 2020.